

Dipl.-Ing. K. H. Armin Fischer



Experimental and Numerical Investigation of Injector Tip Wetting in Modern Gasoline Engines as predecessor for particle emissions

Doctoral Thesis

to achieve the university degree of
Doktor der technischen Wissenschaften

AVL List GmbH



Submitted to the doctoral school of mechanical engineering
Graz University of Technology

Referees: Univ.-Prof. Dipl.-Ing. Dr.techn. Helmut Eichlseder
Em. Univ.-Prof. Dr.-Ing. Günter Hohenberg

Graz, Jan-18

Dipl.-Ing. K. H. Armin Fischer



Messung und Simulation der Kraftstoffbenetzung einer GDI Einspritzdüse als Ursache erhöhter Partikel Emission

Dissertation

zur Erlangung des akademischen Grades
Doktor der technischen Wissenschaften

AVL List GmbH



eingereicht an der Doctoral School für Maschinenbau
Technische Universität Graz

Gutachter: Univ.-Prof. Dipl.-Ing. Dr.techn. Helmut Eichlseder
Em. Univ.-Prof. Dr.-Ing. Günter Hohenberg

Graz, im Jan-18

Für meine Frau Clara

Abstract

With upcoming emission regulations particle emissions for GDI engines are challenging engine and injector developers. Despite the introduction of GPFs, engine-out emission should be optimized to avoid extra cost and exhaust backpressure. Engine tests with a state of the art Miller GDI engine showed up to 200% increased particle emissions over the test duration due to injector deposit related diffusion flames. No spray altering deposits have been found inside the injector nozzle.

To optimize this tip sooting behavior a tool chain is presented which involves injector multiphase simulations, a spray simulation coupled with a wallfilm model and testing. First the flow inside the injector is analyzed based on a 3D-XRay model. The next step is a Lagrangian spray simulation coupled with a wallfilm module which is used to simulate the fuel impingement on the injector tip and counter-bores. Lower injection pressures and a rounded edge at the nozzle inlet due to hydro-erosive grinding are increasing the wallfilm on the injector. The simulations are verified with measurements including high speed microscopic video analyzes of the injector tip during injection. The simulated wallfilm on the injector tip matches well with the measurement results.

As a last step, the tested engine is simulated in one operating point including the injector nozzle geometry for a full 720° CrA cycle. Variations of charge motion, injector and fuel temperatures are investigated to reduce the tip wetting and improve fuel evaporation. An increased fuel temperature and high tip temperatures show a promising reduction of the injector tip wallfilm. Further simulations performed with multi-component fuels allow a prediction of tip wetting for region based different gasoline distillation curves.

Kurzfassung

Eine zunehmende gesetzliche Limitierung der PN Emissionen für Benzin DI Motoren stellt Motoren- und Injektor-Entwickler vor neue Herausforderungen. Die beginnende Einführung des Otto Partikelfilters schafft Abhilfe, führt aber neben höheren Kosten zu gesteigertem Bauraumbedarf und erhöhtem Abgasgegendruck. Eine Reduktion der verbrennungsseitigen Partikelanzahl sollte deshalb angestrebt werden. Eine Versuchsreihe mit einem modernen Miller GDI Motor in dieser Studie ergab eine Erhöhung der Partikelanzahl von über 200% auf Grund rußender Diffusionsflammen auf der Injektorspitze ohne das Vorhandensein durchflussändernder Ablagerungen.

Die vorliegende Arbeit präsentiert eine Werkzeugkette zur Simulation und Optimierung der Injektorspitzenbenetzung welche als Vorstufe externer Ablagerung und in weiterer Folge der Diffusionsverbrennung gilt. Die vorgestellten Arbeitsschritte umfassen eine Injektor Multiphasen Simulation, eine Simulation der Einspritzung in Kombination mit einem Wandfilmmodell sowie verschiedene Messabläufe. Den ersten Schritt stellt die Injektor Simulation dar, welche die Bedingungen im Inneren der Düse simuliert. Dies erfolgte auf Basis von verschiedenen Messungen zur Erstellung einer exakten Modellgeometrie. In einem nächsten Schritt wird das Einspritzverhalten simuliert mit gleichzeitiger Modellierung der Wandbenetzung auf der Injektorspitze. Zum Abgleich der Simulation werden die Ergebnisse mit verschiedenen Messungen verglichen, u.a. mit Hochgeschwindigkeitsaufnahmen des Injektors während der Einspritzung. Der modellierte Wandfilm zeigt eine gute Übereinstimmung mit der Messung. Höhere Einspritzdrücke und ein scharfer Düseneintritt reduzieren den auftretenden Wandfilm.

In einem letzten Schritt wird ein Betriebspunkt aus den Motortestläufen über einen vollen Zyklus simuliert. Variationen der Einspritz- und Motorbedingungen zeigen Möglichkeiten zur Reduktion der Wandbenetzung bzw. zum schnelleren Verdampfen des Films. Eine erhöhte Kraftstofftemperatur sowie hohe Temperaturen auf der Injektorspitze vermindern die Kraftstoffbenetzung. Erste Simulationen mit Mehrkomponenten Kraftstoff geben einen Ausblick auf zukünftige Möglichkeiten zur weiteren Detaillierung des vorgestellten Modells.

Acknowledgment

The presented study was performed in AVL Graz and AVL Shanghai Tech Center as one of many global R&D projects to optimize combustion engine technology under Prof. Dipl.-Ing. Dr. techn. Theodor Sams. The research was supported by the institute of combustion engines and thermodynamics at the university of technology Graz under Univ.-Prof. Dipl.-Ing. Dr. techn. Helmut Eichlseder.

I want to specifically thank both Univ.-Prof. Dr. Helmut Eichlseder and Prof. Dr. Theodor Sams for their contribution, the continuous support over the last years and the countless interesting discussions.

I also want to thank em. Univ.-Prof. Dr. Günter Hohenberg as second examiner of this work.

Further I want to acknowledge the support of Dr. Klaus Denkmayr and Dr. Frank Beste as general manager of the AVL shanghai technical center who made the engine investigations of this study possible. Additionally, I want to thank Dr. Jiang Hong for the support during my working years in China.

The simulation part of the project was conducted in AVL Graz in the department DAC under Andreas Ennemoser who I want to thank for providing me the necessary hardware and knowledge to master AVL Fire. I appreciate the support by all members of the DAC department and especially by Marta Merida who spent countless hours with me optimizing simulation parameters.

I certainly want to thank my parents for making my education possible.

Finally, I want to thank my wife Clara for the encouragement and understanding over the years as well as my two sons Arthur and Albert always manage to put a smile on my face after a long working day.

Table of Content

Abstract	II
Kurzfassung	III
Acknowledgment	IV
Table of Content	V
Table of Figures	VIII
Abbreviations and Symbols	XV
1 Motivation	1
1.1 Current and Future Emission Regulation	1
1.2 GDI Vehicle Fleet Tests in China	2
1.3 Problems for Future Engine Technologies	3
2 Current Research and Deposit Investigations	4
2.1 Deposits in Combustion Engines	4
2.1.1 Deposit Models	4
2.1.2 Parameters influencing Deposits.....	7
2.1.3 Chemical Composition	13
2.1.4 Different Types of Injector Deposits	15
2.2 Influence of Injector Deposits	17
2.2.1 Injection Time and Spray Influence	17
2.2.2 Tip Coking – Diffusion Flames	19
3 Engine Deposit Cycle	24
3.1 Engine Description	24
3.1.1 Layout	25
3.1.2 Valve Lifts.....	26
3.1.3 Injector	27
3.1.4 Testbed Setup.....	28
3.2 Test Cycle Development	29
3.3 Test Fuels	34
3.4 Results	35
3.4.1 Shanghai RON 92	36
3.4.2 China M15.....	38

3.4.3	Indian RON 91	40
3.4.4	Shanghai RON 95	43
3.5	Injector Deposits as PN Source	45
3.5.1	Shanghai RON 92	45
3.5.2	China M15.....	46
3.5.3	Indian RON 91	48
4	Simulation Assumptions	51
4.1	Deposits Model Assumption.....	51
4.2	Wallfilm Module.....	51
4.3	Simulation Work Flow	55
5	Injector Simulation.....	57
5.1	Measurement Inputs	57
5.1.1	X-Ray Images	57
5.1.2	Cut Injector.....	59
5.1.3	Massflow Measurement	59
5.1.4	Needle Lift.....	61
5.2	Model description and boundaries	62
5.2.1	Mesh Setup.....	62
5.2.2	Boundaries and Simulation Setup	64
5.3	Variations	66
5.3.1	Single Component Fuel.....	66
5.3.2	Multi Component Fuel	67
5.4	Results	68
5.4.1	Massflow Results	68
5.4.2	Fuel Distribution and Velocity.....	70
5.4.3	Comparison sharp to rounded Edge with same Needle Lift	77
5.4.4	Conclusion from Results	79
6	Spray Simulation.....	81
6.1	Measurement Inputs	81
6.1.1	Spray Shape and Droplet SMD	81
6.1.2	Wallfilm on Injector Tip.....	82
6.2	Model Description and Boundaries	84
6.2.1	Mesh Setup.....	84
6.2.2	Boundaries and Simulation Setup	85
6.3	Results	87

6.3.1	Spray Shape and Penetration	87
6.3.2	Wallfilm on Injector Tip.....	92
6.3.3	Conclusion from Results	98
7	Engine Simulation.....	99
7.1	Measurement Inputs	99
7.1.1	Operating Point from Test Cycle	99
7.1.2	Crank Angle based Inlet and Outlet Boundaries	100
7.1.3	Deposit Pictures	102
7.1.4	Nozzle Files.....	103
7.2	Model Description and Boundaries	104
7.2.1	Mesh Setup.....	105
7.2.2	Boundaries and Simulation Setup	106
7.3	Variations	107
7.4	Results	108
7.4.1	Air Charge Motion from #E1	108
7.4.2	Base Engine Result #E2	112
7.4.3	Combustion Model Calibration using Case #E3	119
7.4.4	Variations Results	120
7.5	Conclusion from Results	130
8	Overall Conclusion and Outlook.....	131
8.1	Conclusion	131
8.2	Outlook.....	132
9	Appendix.....	133
9.1	Appendix I – Engine Sensors and Parameters.....	133
9.2	Appendix II - Injector Simulation.....	138
9.3	Appendix III - Spray Simulation	139
9.4	Appendix IV - Engine Simulation.....	141
10	Bibliography	144

Table of Figures

Figure 1: LTFT [%] values for 4 vehicles running a fleet test in Shanghai, China	2
Figure 2: Mechanisms of deposit formation and removal per Lepperhoff et al. [12]	5
Figure 3: Temperature dependency of deposit mass and composition [12]	5
Figure 4: Polymerization theory of deposit formation per Kinoshita et al. [28]	6
Figure 5: Boundaries and fuel composition favoring deposits per [16].	7
Figure 6: Injector Coking based on tip temperature measured by flow loss [40]	8
Figure 7: Injector coking based on engine operating conditions with different trends at same tip temperatures [39]	9
Figure 8: Schematic diagram of different injector design variants	10
Figure 9: Injector coking behavior due to different injector designs evaluated by stationary fuel rate loss per hour [39]	11
Figure 10: Change of deposit related flow reduction by increasing injection pressure from 50 to 100 bar [43].	12
Figure 11: Injector deposit composition based on the location of appearance [48]	14
Figure 12: Internal (left) and external (right) injector deposits	15
Figure 13: Deposits inside the injector nozzle (internal deposits) [39]	16
Figure 14: clean and coked Gasoline DI injector with external deposits [49]	16
Figure 15: Injectors with internal deposits (decreased flow rate) leading to longer penetration depths and smaller cone angles [51]	17
Figure 16: Coked injectors with internal deposits show an increase in HC and CO emission [19].	18
Figure 17: Increased particle number and mass emission for injectors with internal deposits (injector 1 & 2) compared to a clean injector (injector 3) at different engine loads [6]	19
Figure 18: Optical detection of sooting diffusion flame around the injector tip [9]	19
Figure 19: Increase in diffusion flame intensity and particle emission over engine running time [52]	20

Figure 20: Improved injector design leads to particle reduction caused by tip sooting [8]	21
Figure 21: Injector Coking leading to diffusion flames depended on injection pressure and injection strategy [52]	22
Figure 22: Influence of in Cylinder charge air motion and fuel pressure on tip sooting [7]	23
Figure 23: AVL HiEff Engine BSFC Map (2015) [54].....	25
Figure 24: AVL HiEff Engine Layout.....	26
Figure 25: AVL HiEff Valve Timing	27
Figure 26: Injector configuration used in the test engine	28
Figure 27: Engine Instrumentation before installation in the test cell	29
Figure 28: Speed, load, and coolant profile of the new developed test cycle	32
Figure 29: Shanghai RON 92 @ 3000 rpm / 10bar BMEP test result.....	36
Figure 30: Shanghai RON 92 @ 2000 rpm / 14bar BMEP test result.....	37
Figure 31: China M15 @ 3000 rpm / 10bar BMEP test result	38
Figure 32: China M15 @ 2000 rpm / 14bar BMEP test result	40
Figure 33: Indian RON 91 @ 3000 rpm / 10bar BMEP test result	42
Figure 34: Indian RON 91 @ 2000 rpm / 14 bar BMEP test result	43
Figure 35: Shanghai RON 95 @ 3000 rpm / 10bar BMEP test result.....	44
Figure 36: Deposits on Injector Tip after 60h Test Cycle with Shanghai RON 92	45
Figure 37: Shanghai RON 92 @ 3000 rpm / 10bar BMEP particle drop after injector ...	46
Figure 38: Deposits on Injector Tip after 50h Test Cycle with China M15	47
Figure 39: China M15 91 @ 3000 rpm / 10bar BMEP particle drop after injector cleaning	48
Figure 40: Deposits on Injector Tip after 50h Test Cycle with Indian RON 91.....	49
Figure 41: Indian RON 91 @ 3000 rpm / 10bar BMEP particle drop after injector cleaning	50

Figure 42: Spray/Wall Interaction based on dimensionless wall temperature (T^*) and droplet velocity (K) according to Kuhnke [59]	53
Figure 43: Schematic of the experimental setup used for nozzle tomography measurements [63].....	57
Figure 44: Injector STL File converted from X-Ray	58
Figure 45: Cut through the injector geometry before (left) and after conversion in a CAD program.....	58
Figure 46: Injector cut along needle	59
Figure 47: Measured injection rate and signal current for 2.1ms signal duration @ 150bar	60
Figure 48: example of a Bosch HDEV5 needle lift curve.....	61
Figure 49: Scaled and stretched needle lift curve for 2.1ms signal duration	62
Figure 50: Structural Hexagon Injector Mesh	63
Figure 51: Sharp edge between injector seat and nozzle.....	64
Figure 52: Rounded edge ($r=20\ \mu\text{m}$) between injector seat and nozzle	64
Figure 53: Injector Simulation Boundaries.....	65
Figure 54: Injector Nozzle Numbers	68
Figure 55: Injector Massflow @ 50 / 150 bar – Simulation vs. Measurement.....	69
Figure 56: Injector Massflow @ 150 bar lift factor 1 / 0.5 – Simulation vs. Measurement	70
Figure 57: Y-Cut Liquid Phase Volume Fraction for Case #1, #2, #4	71
Figure 58: Y-Cut Liquid Phase Velocity for Case #1, #2, #4	72
Figure 59: Y-Cut Liquid, Vapor and Air Phase for Case #1, #2, #4	73
Figure 60: Isometric surface (liquid volume fraction = 0.1) colored with velocity at constant needle lift for Case #1, #2, #4	74
Figure 61: Measurement area for nozzle file (left picture) and counter-bore exit at injector tip (right picture)	75
Figure 62: Liquid Volume Fraction in the Nozzle measurement area and counter-bore outlet for Case #1, #2, #4	76

Figure 63: Liquid Phase Velocity in the Nozzle measurement area and counter-bore outlet for Case #1, #2, #4.....	77
Figure 64: Y-Cut Liquid, Vapor Volume Fraction and Velocity for Case #2, #3	78
Figure 65: Liquid Volume Fraction in the Nozzle measurement area and counter-bore outlet for Case #2, #3	79
Figure 66: Injector Spray Imaging Capturing system.....	81
Figure 67: Test rig setup for high speed injector tip measurements during injection	83
Figure 68: Microscopic pictures of injector tip for two different injectors.....	83
Figure 69: Polyhedral Spraybox mesh with refinements in spray direction and modelled injector nozzles	85
Figure 70: Case #2, Nozzle #2 Liquid Volume Fraction. Area with min. 0.97 volume fraction for droplet introduction (left) and total liquid volume fraction	86
Figure 71: Spray Development and Shape for 50 bar, 1ms and sharp edge (Case #1)	88
Figure 72: Spray Development and Shape for 150 bar, 2.1ms and sharp edge (Case #2)	89
Figure 73: Spray Development and Shape for 150 bar, 2.1ms and rounded edge (Case #4).....	90
Figure 74: Particle Diameter Distribution Measurement vs. Simulation for 150bar, 2.1ms and sharp edge (Case #2).....	91
Figure 75: Particle Diameter Distribution Measurement vs. Simulation for 150bar, 2.1ms and rounded edge (Case #4)	91
Figure 76: Particle Diameter Distribution Measurement vs. Simulation for 50bar, 1ms and sharp edge (Case #1).....	92
Figure 77: Wallfilm Measurement and simulation (Case #4, rounded edge) on injector tip at 150 bar, 2.1ms injection. Sooted tip to increase visibility	93
Figure 78: Wallfilm Measurement and simulation (Case #2, sharp edge) on injector tip at 150 bar, 2.1ms injection. Sooted tip to increase visibility	94
Figure 79: Wallfilm development on injector tip and in holes during injection for Case #4 (Needle is closed at 2.2 ms).....	95
Figure 80: Wallfilm mass during and after injection for Case #4 in holes and on the tip	96

Figure 81: Overestimation of wallfilm thickness in simulation.....	97
Figure 82: Relative Wallfilm Mass for Case #1, #2, #4 & #5 and 300 bar.	97
Figure 83: Cut through the valves for the reference and HiEff engine.....	100
Figure 84: Intake and Exhaust Valve Timing for the HiEff and reference engine at 3000 rpm / 10 bar BMEP.....	101
Figure 85: Scaled and shifted intake mass flow over crank angle as simulation input @ 3000 rpm / 10 bar BMEP.....	102
Figure 86: Coked injectors from China 92 deposit test runs from cylinder 1 (left) and 2 (right).....	103
Figure 87: Fuel Mass Flow and fuel volume fraction for 110 bar and n-heptane (Case #5)	104
Figure 88: FIRE FEP mesh with detail in the injector area	105
Figure 89: Cylinder Boundary Conditions for the base setup	107
Figure 90: Air charge motion development during intake valve opening – cross section through intake valve (Case #E1)	109
Figure 91: Swirl break-up towards firing TDC – cross section through the center	110
Figure 92: Velocity and Temperature at the injector tip from end of injection to ignition timing (Case #E1).....	111
Figure 93: Gas Velocity Field development after end of injection (Case #E1).....	112
Figure 94: Unburnt Equivalence Ratio for simulated Engine Case #E2	113
Figure 95: Isometric Surface for $\Lambda=1$ overlaid with gas velocity during injection (Case #E2)	114
Figure 96: Equivalence ratio in the injector niche from end of injection until start of ignition for case #E2	114
Figure 97: Wallfilm development on injector tip and in holes during injection for Case #E2 (Needle is closed at 94°CrA after TDC).....	115
Figure 98: Wallfilm mass on injector tip and holes for Case #E2 as reference for the following variants.....	116
Figure 99: Wallfilm on injector from end of injection to start of ignition for case #E2...	117

Figure 100: Flame front during combustion with wallfilm thickness on the injector for Case #E2.....	117
Figure 101: Unburnt Equivalent Ratio for Case #E2	118
Figure 102: Heat Release rate and total heat release for case #E2	119
Figure 103: Heat release rate and accumulated heat release for case #E3 compared with the measurement MFB% points	120
Figure 104: Wallfilm area and thickness after injection (260°CrA before TDC) for Case #E2 to #E7	122
Figure 105: Relative wallfilm mass on injector tip after injection (260°CrA before TDC) for case #E2 to #E7	123
Figure 106: Wallfilm from end of injection to ignition for case #E2 to #E7	124
Figure 107: Total injector wallfilm over full cycle for single component fuel variants... ..	125
Figure 108: Comparison of coked injector with wallfilm simulation at spark timing	125
Figure 109: Distillation curves for gasoline surrogates	126
Figure 110: Multi-Component Wallfilm on Injector tip from start of injection to ignition	128
Figure 111: Wallfilm Area for Case #E2 (Fire 2017.0) and #E2b (Fire 2017.1)	129
Figure 112: Standard sensor location (example).....	133
Figure 113: EGR and ESC system sensor positions.....	135
Table 1: AVL HiEff Test Cycle Operating Points	31
Table 2: Fixed Injection pressure, intake VVT and EGR valve position for each test point	33
Table 3: Deposit Cycle Test Fuel Properties	35
Table 4: Injector massflow measurement variations	60
Table 5: Injector Mesh Data	63
Table 6: Simulation variants single component fuel	66
Table 7: Simulation variants multi component fuel	67
Table 8: Test Rig properties	84

Table 9: Spray Box mesh properties	85
Table 10: Primary and Secondary Break-up Model Constants.....	87
Table 11: Engine boundaries at 3000 rpm / 10 bar for simulation input	99
Table 12: Engine Cylinder mesh properties	106
Table 13: Simulation variants engine simulation	108
Table 14: ECFM-3Z combustion model parameters.....	120
Table 15: Standard engine testbed sensors.....	133
Table 16: Additional EGR and ESC related sensors	135
Table 17: Testbed and EMS signals	136
Table 18: Euler Multiphase Simulation parameters.....	138
Table 19: Lagrangian Spray Simulation parameters	140
Table 20: Engine Simulation parameters	141

Abbreviations and Symbols

Abbreviation

BDC	bottom dead center
BSFC	brake specific fuel consumption
CCD	combustion chamber ceposites
DVVT	(dual) variable valve train
ECFM-3Z	extended coherent flame model 3 zones
ECU	engine control unit
EVC	exhaust valve closing
EVO	exhaust valve opening
FAME	Fire automatic mesh engine
FEP	FAME engine plus
HDEV	high pressure injector (HochDruck EinspritzVentil)
HP EGR	(high pressure) exhaust gas recirculation
IVC	intake valve closing
IVD	intake valve deposits
IVO	intake valve opening
LTFT	long term fuel trend (OBD value)
MFB x%	mass fraction burned (x% of total fuel)
MIL	malfunction indication lamp
NEDC	new European driving cycle
OBD	on board diagnostics
RFF	roller finger follower
RON	research octane number
RP-EMS	rapid prototype engine management system
RTC	real time controller
T_W_O	Engine coolant out temperature
TDC	top dead center
TGDI	(Turbo) gasoline direct injection
WLTP	worldwide harmonized light vehicle test procedure

Symbols

c	(Fuel vapor) concentration
Ca	Dimensionless Capillary number
c_f	Dimensionless local friction factor
d	(Droplet) diameter

K	dimensionless velocity according to Kuhnke
La	Dimensionless Laplace number
P_m	Correction factor to consider the influence of the laminar sublayer on the mass transfer on rough surfaces
S	Scale factor
Sc_t	Turbulent Schmidt Number
St_m	Stanton number for mass transfer
T^*	dimensionless temperature according to Kuhnke
T_{sat}	Saturation temperature
T_W	Wall temperature
u	Velocity
u_τ	Wall shear velocity
V_h	Swept volume
We	Dimensionless Weber number
δ	Wallfilm thickness
η	Correction factor to consider rough wallfilm surface in the evaporation model
μ	Dynamic viscosity
ρ	Density
σ	(Droplet) surface tension
τ_w	Wall shear stress

1 Motivation

This chapter gives a short instruction about the background of this work and industry requirements

1.1 Current and Future Emission Regulation

Despite the current trend towards alternative transportation concepts like fuel cell or electric vehicle traditional combustion engines will still play a major role in the next century [1]. A base requirement for the coexistence is a continuous reduction of greenhouse gases and emissions over the next years to reduce global air pollution and global warming.

Increasingly stringent emission regulations are put in place around the globe to limit vehicle emission in special cycles or on the road. One of the most dangerous pollutants is the particle emissions which has been proven to cause cancer by the world health organization [2]. In the past particle emissions were mainly a problem of Diesel engines which lead to the introduction of particle filters to meet current emission legislations. Recent studies showed however that vehicles with modern gasoline DI engines where particle filters are not commonly used emit higher number of particles than Diesel engines in test cycles and real driving conditions. It is expected that in 2030 particle numbers from GDI vehicles will exceed those of Diesel vehicles [3].

As a result, the European emission regulations started to limit particle numbers also for gasoline vehicles. Starting with Euro 6b in 2014 gasoline DI vehicles were limited with a factor 10 higher particle number (6×10^{12} [# / km]) than Euro 5 Diesel vehicles in the NEDC. Beginning with end of 2017 both Diesel and Gasoline DI vehicles need to meet a limit of 6×10^{11} [# / km] in the new WLTP cycle for Euro 6c. Euro 6d in 2020 will additionally limit particle emissions in real driving conditions with a factor of 1.5 to 9×10^{11} [# / km] [4].

While a particle filter can help to meet the emission targets engine developers should also focus on reducing engine out emissions. Especially as these filters increase exhaust back pressure and add cost and package requirements to the engine [5]. As particles are mainly created during combustion in areas with a too high fuel to air ratio the engine fuel system plays an important role in the optimization. Small changes in the fuel distribution can cause significant changes in terms of particle emission [6] - [11]. The focus on this work is laid on the injector itself and its behavior under different fuel and engine conditions.

1.2 GDI Vehicle Fleet Tests in China

Vehicle fleets tests in recent years which have been conducted in AVL China with state of the art GDI engines showed a severe fuel influence on the injection system. The investigated vehicles were equipped with German OEM 1.6l TGDl engines while driving a Shanghai mixed city/highway cycle. A special gasoline blend was used with 15% Methanol and very high levels of sulfur and washed/unwashed gums to accelerate coking effects. The distillation curve was also higher than a typical European RON95 fuel.

During the mileage accumulation, the engine injectors had to be exchanged several times as the long-term fuel trend (LTFT) OBD threshold activated the MIL. The LTFT is a diagnostic value which represents the deviation between calibrated injection time and necessary injection time to reach requested lambda values. An increasing LTFT value indicates a coked injector with reduced mass flow rate as the ECU must inject longer to introduce the same fuel mass as a clean one. Figure 1 shows the LTFT values for 4 vehicles from the mentioned fleet test over 15.000km driving distance.

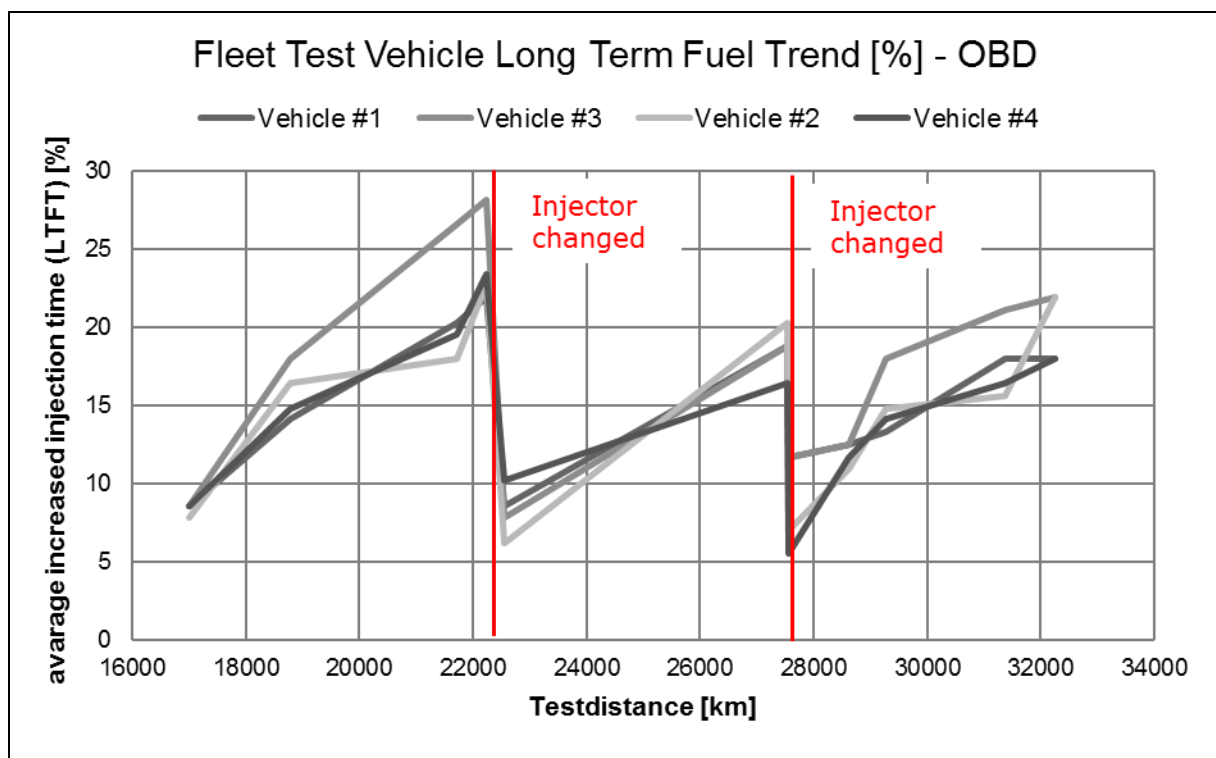


Figure 1: LTFT [%] values for 4 vehicles running a fleet test in Shanghai, China

At the beginning of the test the LTFT values were already at 8% due to a lower heat value of the used M15 gasoline fuel. Within just 5000km one of the vehicles already exceeded a LTFT value of 28% which activated the MIL. Compared to the start of the

test runs this is an 18% increase of injection time or a 15% reduction of injector mass flow rate due to deposits. As the focus of this project was not on injector coking it has been decided to exchange the injectors every 5000km.

1.3 Problems for Future Engine Technologies

Although the fuel used in the vehicle fleet tests exceeded current Chinese fuel regulations by far and leads to unrealistic fast coking phenomena even a 10 times longer injector change interval would not be accepted by the customer. Additionally, the emission levels would exceed every regulation causing more pollution and health problems. Therefore, its crucial for engine and injector developers to understand the mechanisms behind.

While current GDI engines are well covered in recent research next-gen technologies will increase the complexity of the system and mechanisms further. Technologies like Miller valve trains and (forced) EGR systems are changing the gas and combustion boundaries around the injector. In this project, a gasoline engine with innovative technologies optimized for CO₂ emission is run in a controlled environment to investigate the injector behavior under changing conditions and the influence on the emissions.

In times of continuous digitalization and shorter development times simulation of engines and their behavior plays a major role in engine development. Based on the findings from the engine test runs the second part of the presented research is focusing on the accurate simulation of the injector as a possible source of particles and its optimization. The findings can be used to develop cleaner gasoline DI engines in the future with stable emission levels over the vehicle lifetime.

2 Current Research and Deposit Investigations

Responsible for changes of injector behavior (e.g. mass flow rate) during engine operation are mainly deposits which build up on the injector parts which are exposed to the combustion chamber. This chapter gives an overview about how and where deposits are created, how they affect the injector and their influence on engine emission.

2.1 Deposits in Combustion Engines

Deposits in combustion engines are commonly defined as residues caused by (partly) burnt fuel or lubrication components on the surface of engine components such as valves, piston rings, heat exchangers and injectors [12] - [15]. They cause unwanted and normally negative effects on the specific parts which has effects on engine wear, performance, emission, and fuel consumption [16] - [19]. As deposits occur in all combustion engines, research in the last centuries was focused on avoiding or reducing deposit build-up.

2.1.1 Deposit Models

Already back in 1993 Lepperhoff and Houben developed a theory regarding the build-up and removal of engine deposits based on fundamental mechanisms [12]. While their research didn't distinguish between Diesel or Gasoline engines or certain engine components their results allow to understand basic influence factors. In the performed experiment a gas with deposit able components was guided through a cooled tube and despite the parallel flow of the fluid to the wall deposits accumulated.

According to their model (Figure 2) deposit build-up starts with condensation [20] [21] and adsorption [22] of hydrocarbons on the cold wall . In this sticky layer particles are caught by sticking, incorporation and impaction [23] - [25] leading to a continually growth. With growing deposit thickness the temperature on the surface increases due to the insulation effect of the particles. Higher temperatures avoid further condensation and lead to other effects such as abrasion due to lower adhesive forces limiting the thickness. Gaseous components then diffuse through the porous layer and increase the density. Once deposits are built they can be removed by physical, mechanical or chemical effects (see Figure 2, right) [13] [26] [27].

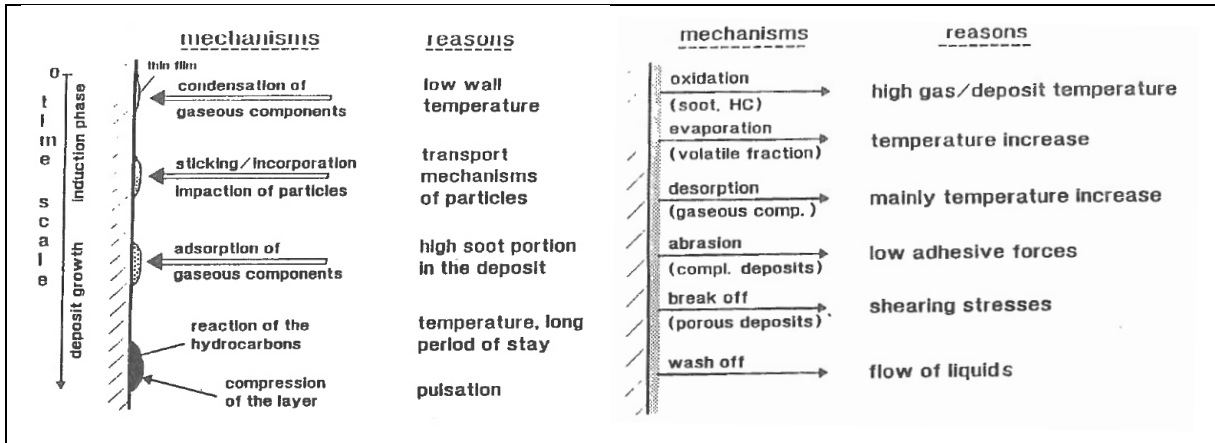


Figure 2: Mechanisms of deposit formation and removal per Lepperhoff et al. [12]

The study identified thermophoresis as main driver for particle impactation with the wall if the gas flow is parallel to the wall. Thermophoresis describes the movement of particles in a fluid due to a temperature difference - the particles tend to move towards a colder area or wall. This effect is explained by the statistically higher impacts of gas molecules on the particles at the high temperature side moving the particle towards the cold side.

A higher temperature difference leads to more particles impacting the wall and sticking to the condensed hydrocarbons. The diagram in Figure 3 on the left displays the deposit mass for a cooled tube where exhaust gases were streamed through. Where the wall temperature matches the gas temperature no deposits can be measured. With decreasing coolant temperature, the mass increases due to thermophoresis and below a certain level condensation of volatile components can be observed.

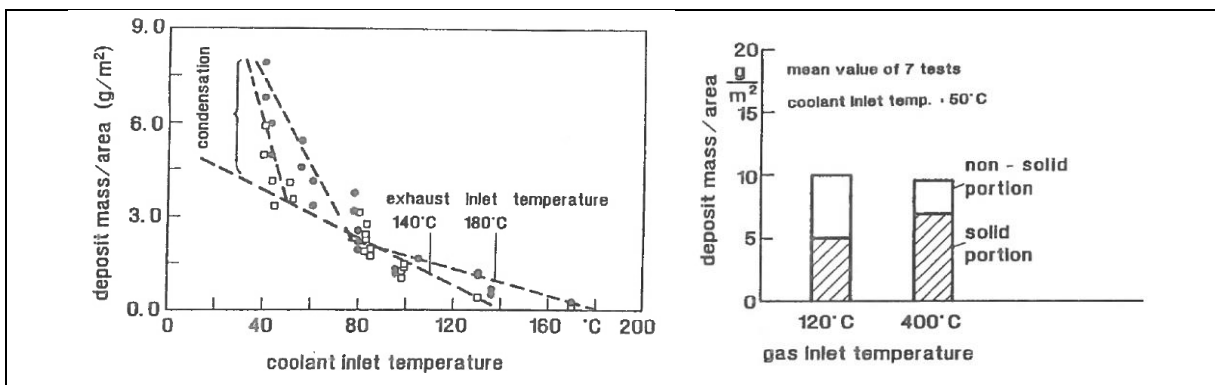


Figure 3: Temperature dependency of deposit mass and composition [12]

The diagram on the right compares two different gas temperatures using the same low wall temperature. While the total mass is the same the deposits of the high gas temperature case consist of more solid components, mainly carbon, due to higher

thermophoresis effects and lower non-solid components due to reduced condensation of hydrocarbons.

Further tests investigating the influence of the flow turbulence on the particle concentration showed that higher turbulence decreases the thermophoresis effect.

While the model of Lepperhoff and Houben is not considering any specific engine component a later deposit model by Kinoshita et al. is focusing on the gasoline DI injector [28]. According to their polymerization theory high boiling fuel components are left on the hot nozzle walls leading to a waxy residue due to polymerization. Figure 4 shows the 3 stages of the deposit build-up starting with fuel at the nozzle wall. After the injection fuel is trapped in the nozzle and deposit precursors (e.g. metals, sulfur etc.) are dispersed in the fuel (a) they start to agglomerate and move towards the wall during evaporation of the fuel (b). The precursors and particles stick together and form the residue after most of the fuel is evaporated (c). If the nozzle temperature is low or the distillation curve of the fuel is high the process stops in stage 2 (b) and a following injection washes the deposit precursors away before they adhere to the wall. A higher injector temperatures increased the deposit build-up in this study.

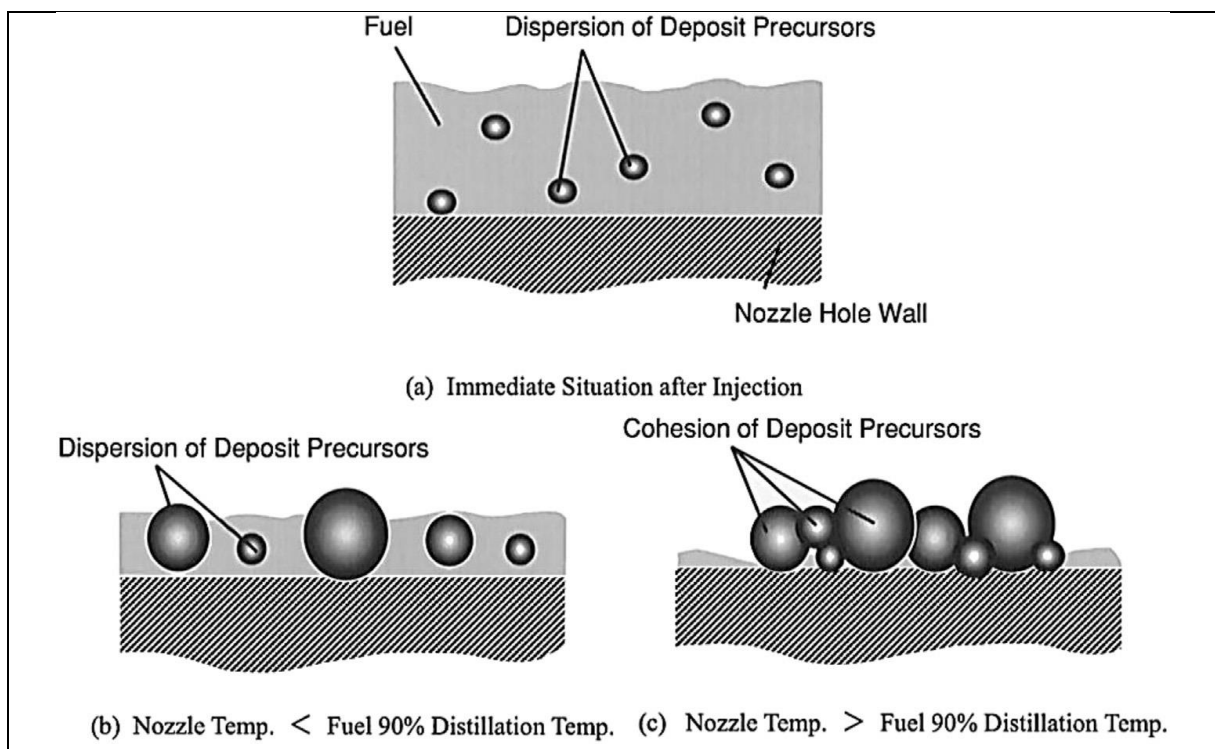


Figure 4: Polymerization theory of deposit formation per Kinoshita et al. [28]

As both models show a dependency of temperature and other boundaries it is expected that the engine operating point has a big impact on the deposits. Further the

composition of the fuel or lubricant which is a predecessor for the residuals will influence the mechanisms.

2.1.2 Parameters influencing Deposits

The influence of different boundaries on GDI injector deposits is commonly evaluated by comparing the stationary flow through the injector before and after coking. Residuals inside the injector nozzle reduce the hydraulic diameter which results in a reduced mass flow rate. The difference between initial flow rate and reduced flow rate is called “flow loss” or “(lean) flow shift” in different studies. Another way is to monitor the LTFT of the engine control unit as described in chapter 1.2.

Figure 5 gives an overview of engine boundaries and fuel or lubricant composition which favor deposits in combustion engines.

Element	Notable Technological Features
Injector Deposit	+High Temperature at Injector Tip +Low T90 of Fuel +High Aromatics of Fuel +High Sulfur of Fuel +Detergent
CCD	+High Aromatics of Fuel +High T90 of Fuel +Stratified Charge Combustion +Detergent
IVD	+Fuel Effect (Aromatics, T90) +Stratified Charge Combustion (High EGR) +Oil Properties (Blow-by Gas& Stem Seal Design) +Detergent

Figure 5: Boundaries and fuel composition favoring deposits per [16].

The areas are split in injector deposits, combustion chamber deposits (CCD) and intake valve deposits (IVD). As the focus of this study is laid on the injector the CCD and IVD are not further discussed. Detailed investigations for gasoline and diesel combustion chamber deposits including IVD confirming Figure 5 can be found e.g. in [29] - [31] for operating point and in [16], [32]- [36] for fuel and lubricant composition.

In terms of Gasoline DI Multi-Hole Injectors current studies show four influence groups on deposit build-up:

- Injector Tip Temperature which is a function of injector geometry, location, and engine operating point
- Injector Design in terms of nozzle geometry and surface quality
- Injection pressure

- Fuel composition

Injector Tip Temperature

Studies on GDI injector coking show a big influence of tip temperature on coking phenomena [28], [37] - [41]. If the tip temperature is below a certain level no coking can be observed which can be explained by too much residual fuel between injections washing any deposits away. As soon as a certain temperature level is exceeded the deposits increase with higher tip temperature. Figure 6 shows a coking test with different tip temperatures indicating a higher flow loss due to deposits in the nozzle with increasing temperature. However, there is also a temperature threshold at which the flow loss trend is reversed indicating deposit removal effects at very high temperatures.

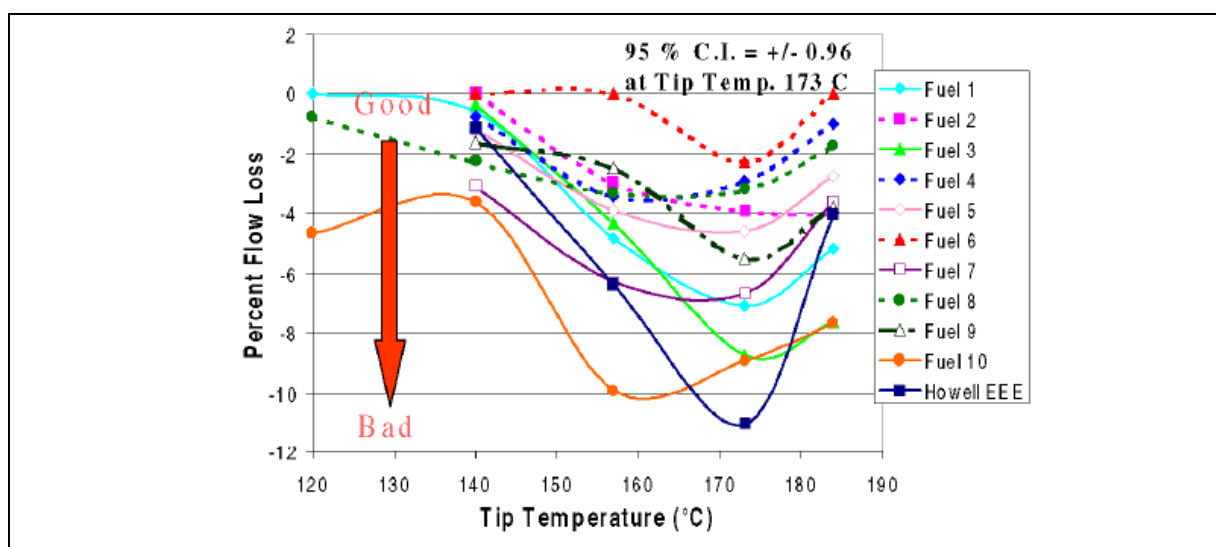


Figure 6: Injector Coking based on tip temperature measured by flow loss [40]

Test performed by Imoehl et al. [39] indicate that tip temperature alone can't predict coking conditions. In Figure 7 several operating points are evaluated and despite the same tip temperature high load points show a deposit removal state while low load points form deposits.

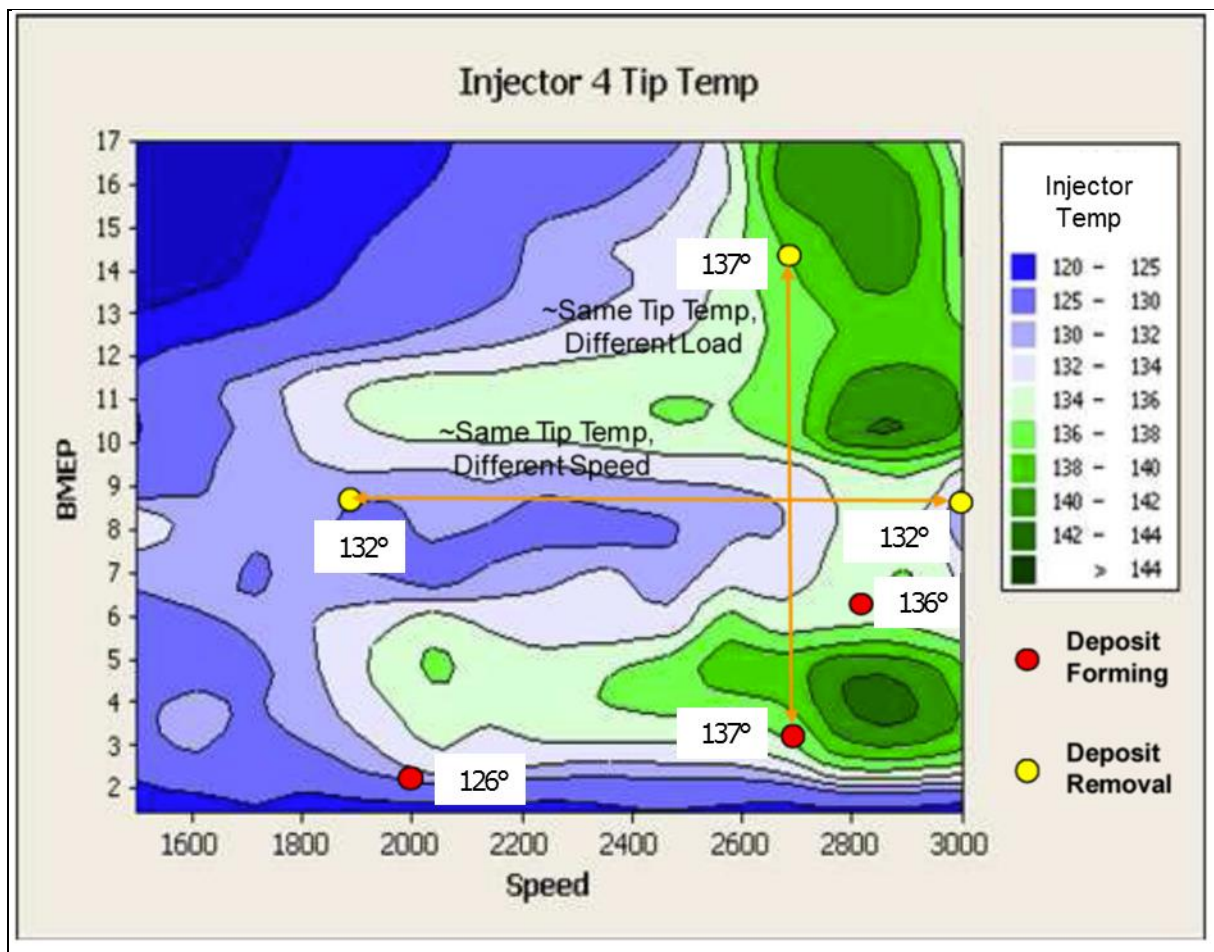


Figure 7: Injector coking based on engine operating conditions with different trends at same tip temperatures [39]

This behavior can probably be explained with increasing injection pressure at higher engine loads which leads to deposit wash off and break off. Unfortunately, the injection pressure is not mentioned in this study.

Injector design

The injector design, mainly the shape of the nozzle holes and the surface quality have been proven to influence the injector coking tendencies [11] [39]. The investigation done in [39] by Imoehl et al. investigates different GDI injector design variants and their influence on coking from tip shape to combustion sealing position. Figure 8 shows the principle of different GDI design features.

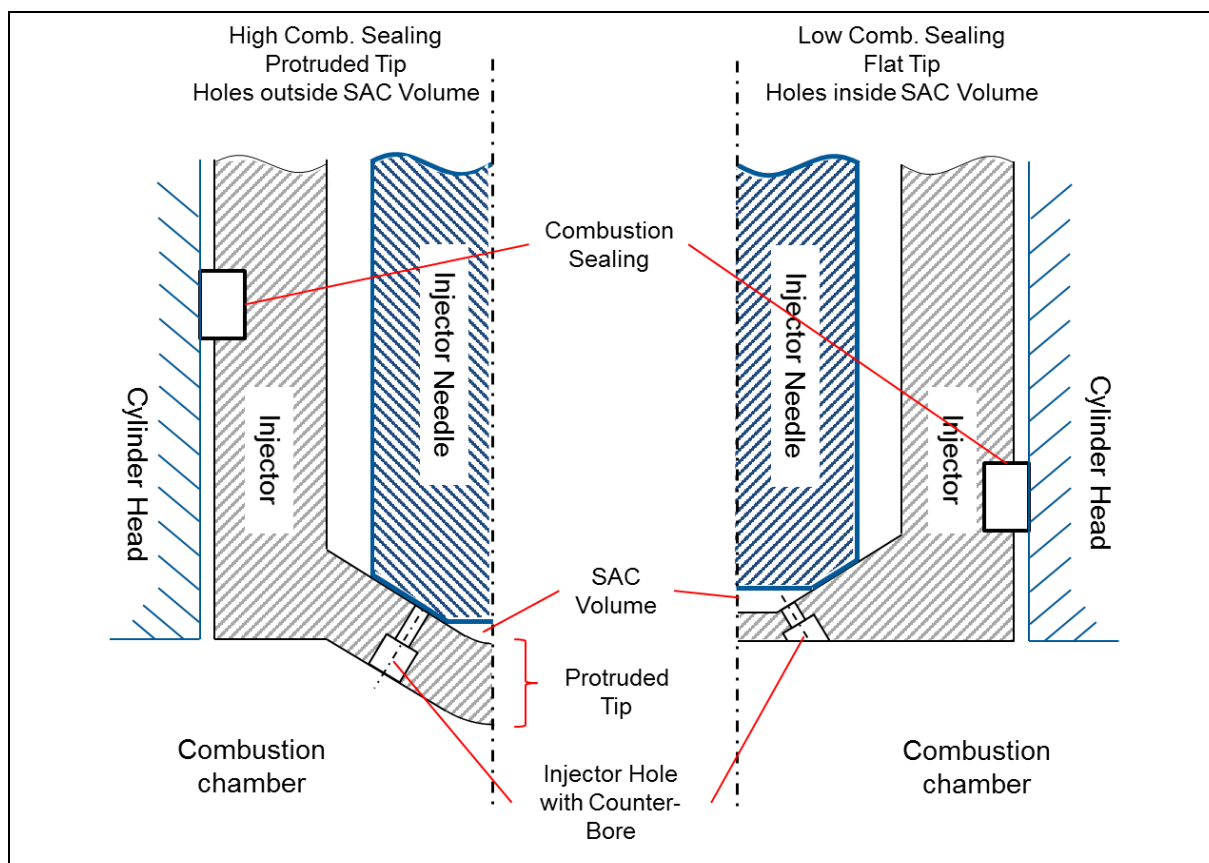


Figure 8: Schematic diagram of different injector design variants

The results in Figure 9 on top evaluate basic injector design features for an inward opening multi-hole GDI injector. The least coking tendencies are achieved by an injector design featuring a separated Sac volume after needle closing, a protruded tip and a sealing further away from the combustion chamber (left sketch in Figure 8).

For this design, which also uses a counter-bore, the hole itself is further optimized in the lower diagram by investigating the influence of a conical shape of 3° , surface roughness due to different machining methods, coating and the effect of a rounded edge at the hole entry due to hydro-erosive grinding. The best design uses a straight hole where the hole itself and the counter-bore are mechanically drilled and the entry from the seat area into the nozzle is not rounded by hydroerosive-grinding.

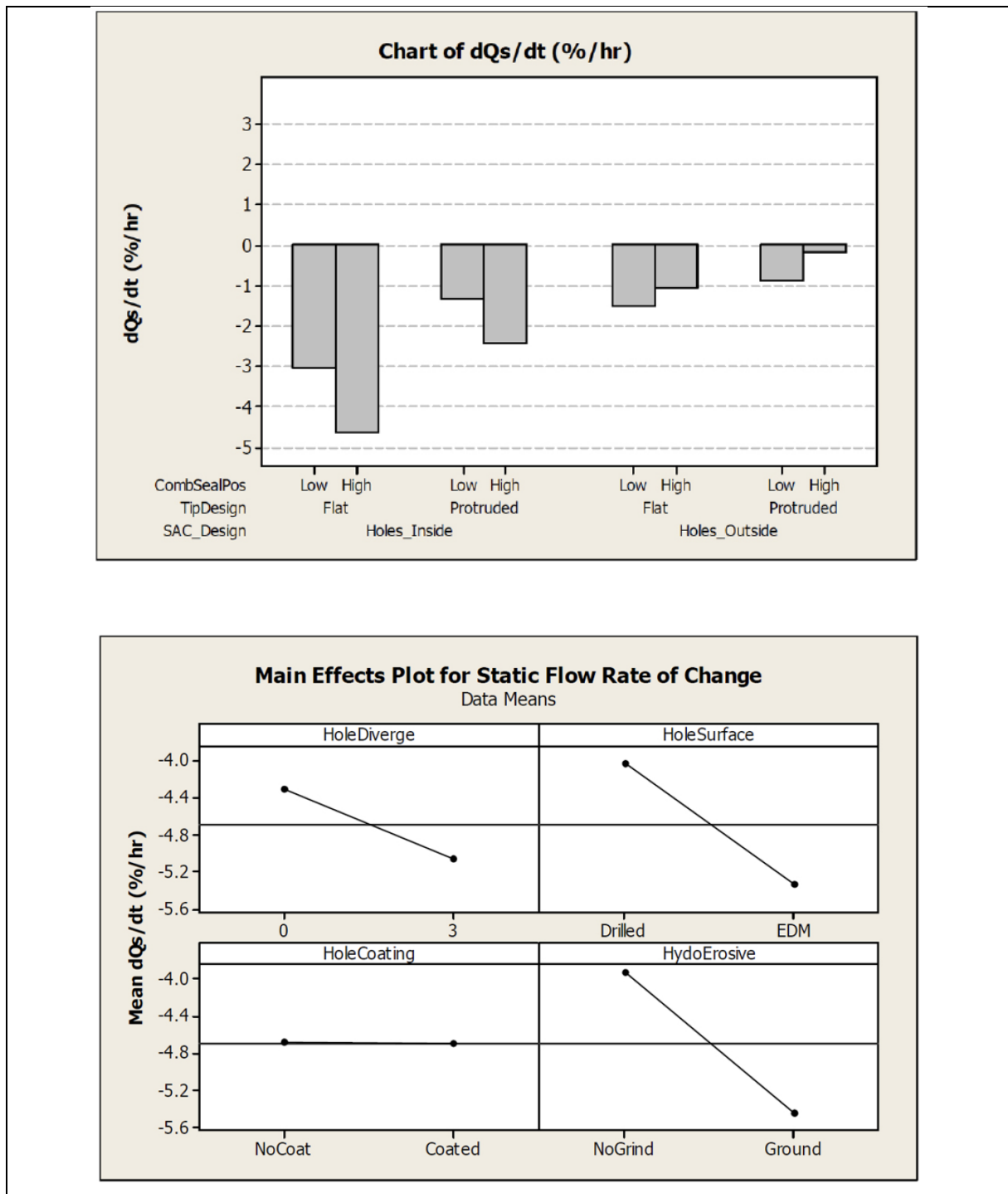


Figure 9: Injector coking behavior due to different injector designs evaluated by stationary fuel rate loss per hour [39]

In [11] new hole designs like a slot show potential to further reduce injector coking. Additionally, cavitation inside the nozzle which is based on nozzle design and injection pressure can improve coking behavior [42].

Injection pressure

A higher injection pressure has been linked to improved coking behavior in a few studies [37] [40] [43]. Figure 10 shows an average reduction of 50% of the lean flow shift by increasing the injection pressure from 50 to 100bar. A possible reason is the higher wash off effect of higher flow velocities as well as reduced residual fuel in the nozzle after needle closing due to increased inertia of the fuel. This would also match with the observations from [39] where the injector design with the connected Sac volume has the worst coking behavior as more residual fuel is available.

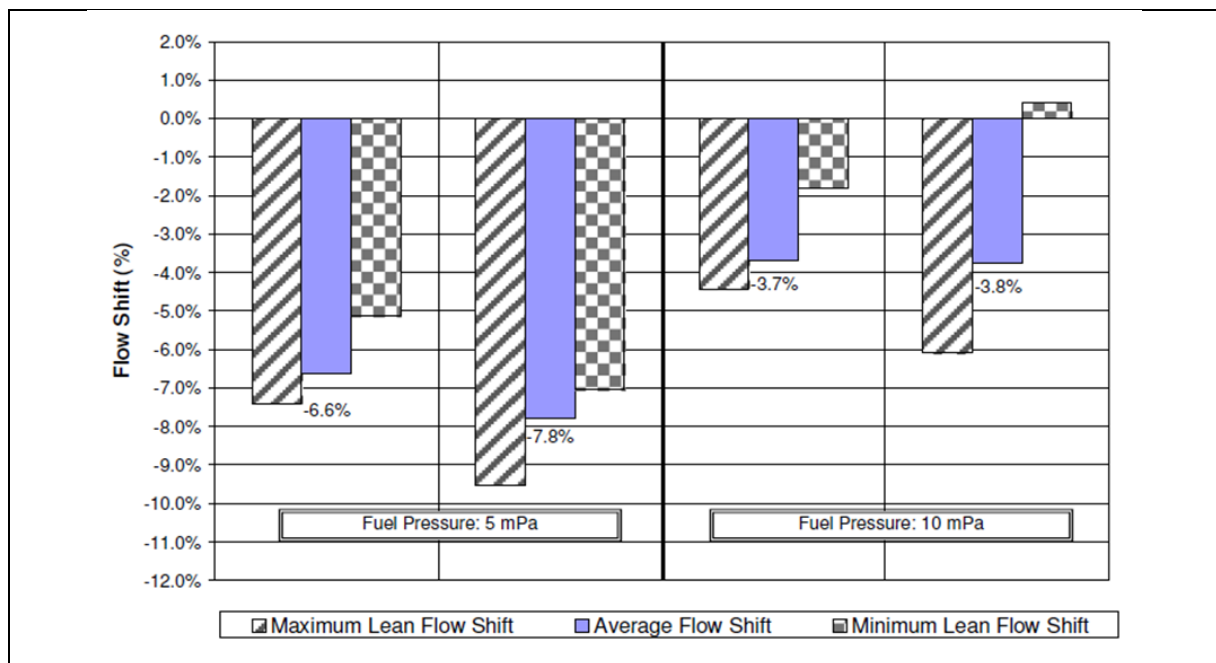


Figure 10: Change of deposit related flow reduction by increasing injection pressure from 50 to 100 bar [43].

Recent studies also showed a big improvement of particle emissions due to injector coking with increased fuel pressure. The results are discussed in chapter 2.2.2.

Fuel Composition

As injector design is done by injector suppliers and injection pressure and engine operating conditions are different for each engine most of the studies investigating GDI injector coking focus on the influence of fuel properties and additives.

Tests with different distillation curves of the test fuels show a dependency between the T90 value (temperature at which 90% of the investigated fuel is evaporated) and the flow shift. Tests performed with fuels which have a lower T90 level show higher flow loss than fuels with high T90 level [28] [33] [44].

High Sulfur levels increase the coking effects [16] [41] while the level of aromatics is not clear. In [16] high levels of aromatics are associated with increased injector coking while in [45] low aromatic levels are worse. Higher olefin levels seem to increase the flow shift [41].

In all studies fuel additives are the most effective way to avoid injector deposits and are even able to clean heavily coked injectors [19], [40], [45] - [47].

2.1.3 Chemical Composition

Dearn et al. [48] performed a detail investigation of the chemical composition of coked Gasoline DI injectors based on the location of appearance. Depending on the location the composition of the deposits highly varies. Regions closer to the combustion chamber show high contents of carbon while residuals inside the injector have high levels of elements like Sulfur, Calcium, Natrium, Iron, and Oxygen.

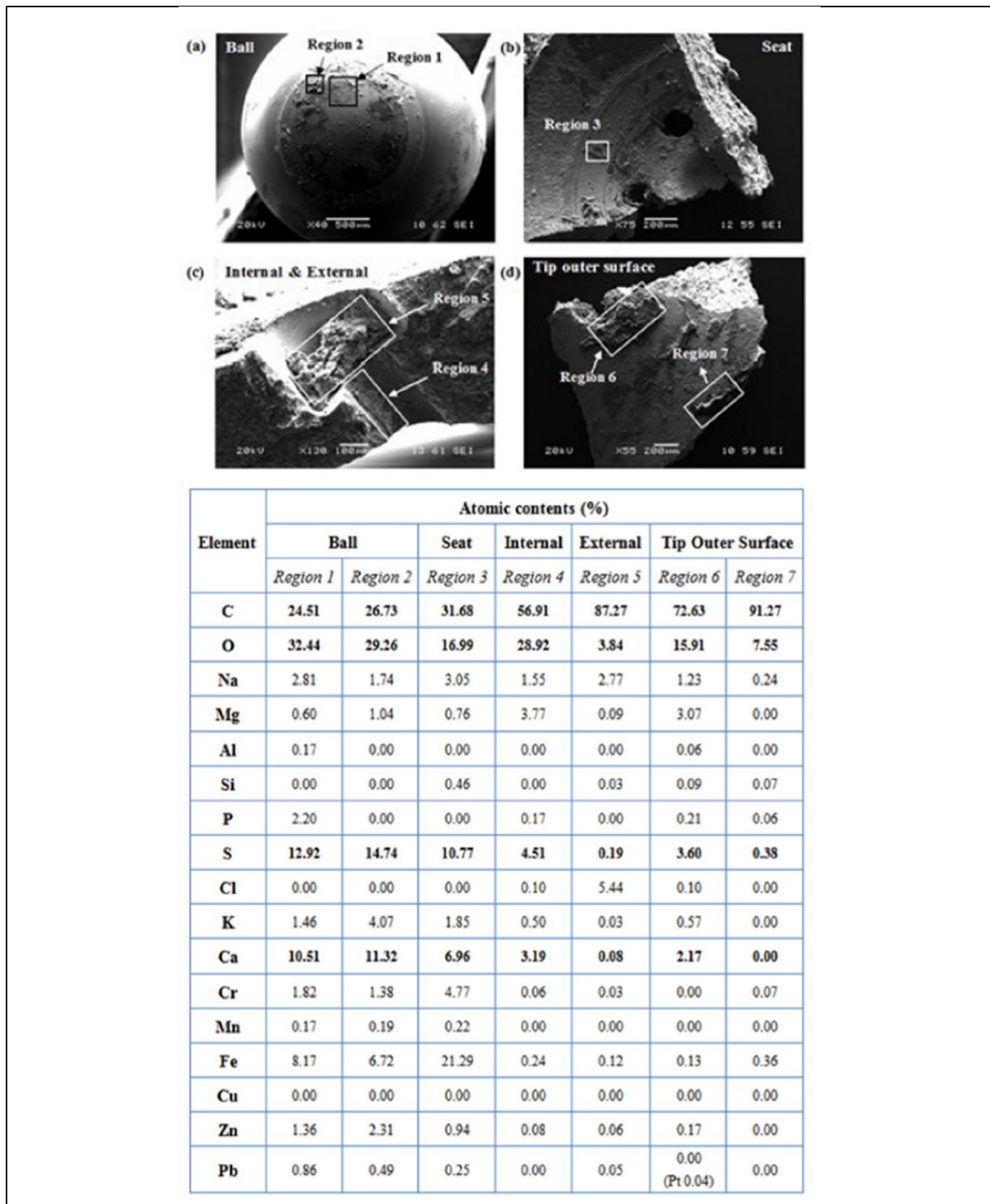


Figure 11: Injector deposit composition based on the location of appearance [48]

The difference of composition could be explained by the two models introduced in chapter 2.1.1. Deposits inside the nozzle and on the ball are created according to the polymerization model by Kinoshita et al [28] where the volatile fuel components evaporate and deposit precursors like metals which are already dispersed in the fuel accumulate on the wall.

Deposits on the injector tip and counter-bore are created based on the model by Lepperhoff et al. [12] by condensation or remaining of high boiling hydrocarbons on high temperature surfaces building a sticky layer where carbon particles from the combustion accumulate. The model would also explain the higher carbon content in region 7 compared to region 6 (Figure 11) as areas closer to the nozzle outlet have lower temperatures due to the evaporation of the fuel.

2.1.4 Different Types of Injector Deposits

In the present study, the GDI injector deposits are split in two different categories. Internal deposits which are located inside the nozzle and reduce the hydraulic diameter and external deposits which can be found in the counter-bore (if present) and on the injector tip. In Figure 12 both types are schematically shown with the blue areas representing the residuals.

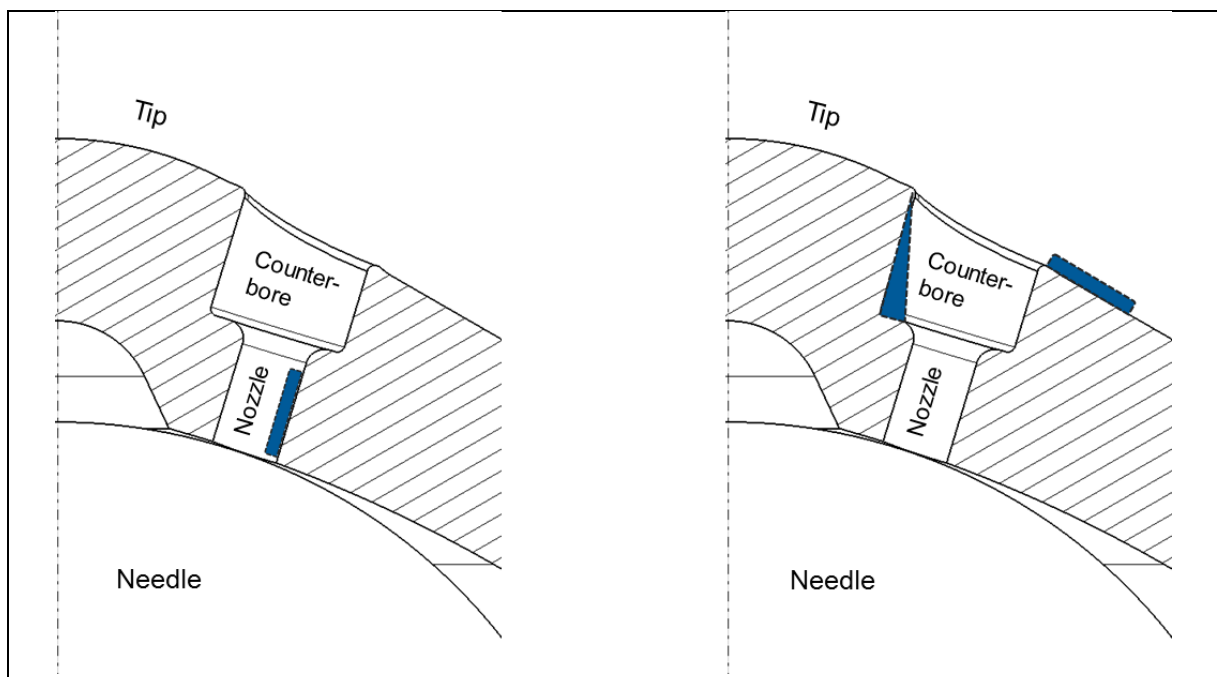


Figure 12: Internal (left) and external (right) injector deposits

All previous mentioned studies were focused on the internal deposits as this type causes the flow shift which was used to evaluate coking behavior. Therefore also all presented influencing factors are mainly valid for the first type and could have a different effect on the second type.

For example, measures to reduce the tip temperature and the request for fuel with a high T90 level had the purpose to keep the fuel in the nozzle liquid until the next

injection event to avoid accumulation of deposit precursors on the wall (polymerization model – internal deposits). Such internal deposits are shown in Figure 13.



Figure 13: Deposits inside the injector nozzle (internal deposits) [39]

For parts, which are exposed more to the combustion chamber like the counter-bore and the injector tip a low wall temperature and high boiling fuel (high T90) lead to increased condensation or residuals of hydrocarbons and increased thermophoresis effects (Lepperhoff model – external deposits). The result are external deposits as shown in Figure 14.

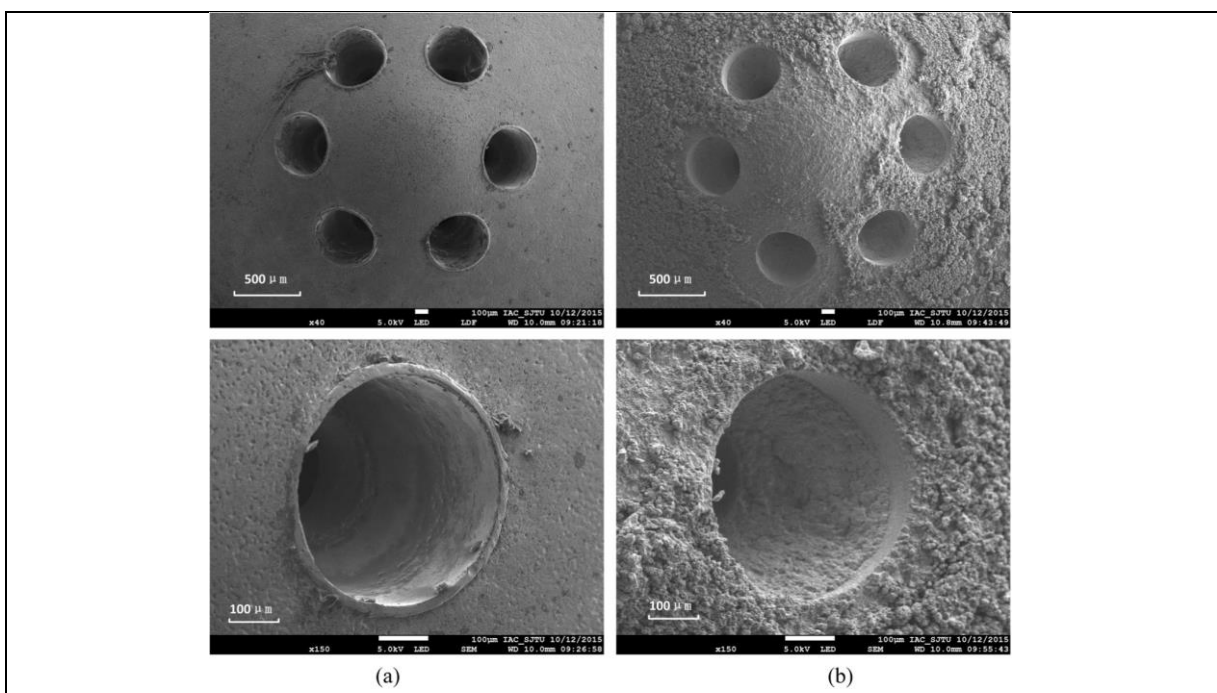


Figure 14: clean and coked Gasoline DI injector with external deposits [49]

2.2 Influence of Injector Deposits

The following chapter describes the influences of gasoline DI injector deposits on engine behavior, emission, and fuel consumption

2.2.1 Injection Time and Spray Influence

Gasoline DI injectors have a big influence on the air/fuel mixture inside the cylinder. Changed spray behavior due to injector deposits can lead to rich and lean zones during the combustion affecting emission and engine performance.

A reduction of the hydraulic diameter inside the nozzle (internal deposits) leads to a higher velocity of the fuel droplets which causes increased penetration depth and smaller plume cone angles [50] [51]. Further a larger droplet size is observed for coked injectors [6] [51]. However, one study found opposite effect with shorter penetration and smaller droplets [49] which leads to the conclusion that spray altering effects by deposits depend on the injector geometry. Figure 15 shows the difference of spray development for a clean and coked injector.

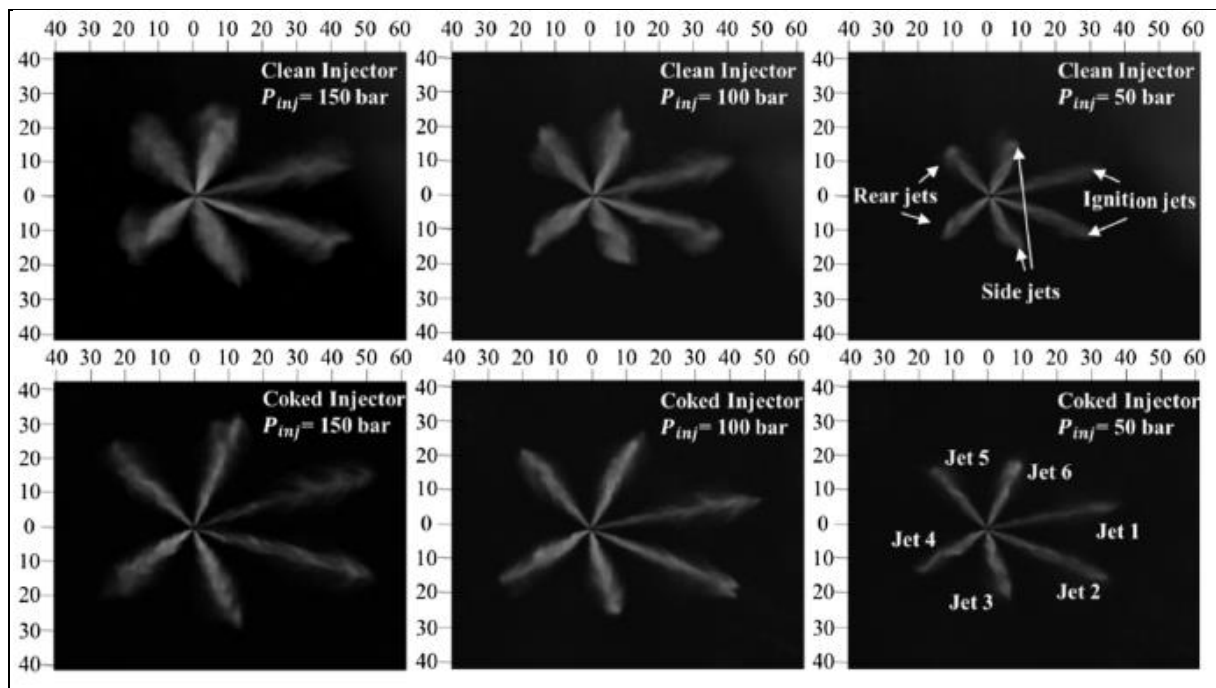


Figure 15: Injectors with internal deposits (decreased flow rate) leading to longer penetration depths and smaller cone angles [51]

Deviations from the optimized spray pattern like mentioned above all have a negative impact on engine emission and performance due to increased fuel impingement on the cylinder liner and piston and inhomogeneous air/fuel mixture. The longer injection

duration which is required to compensate the reduced flow rate also influences the mixture process.

As expected studies showed a clear correlation between the grade of injector coking measured by flow shift and engine emissions [6] [19]. Figure 16 shows the HC and CO emission increase during the injector coking phase and a drop to the base level once the injectors are cleaned using additives.

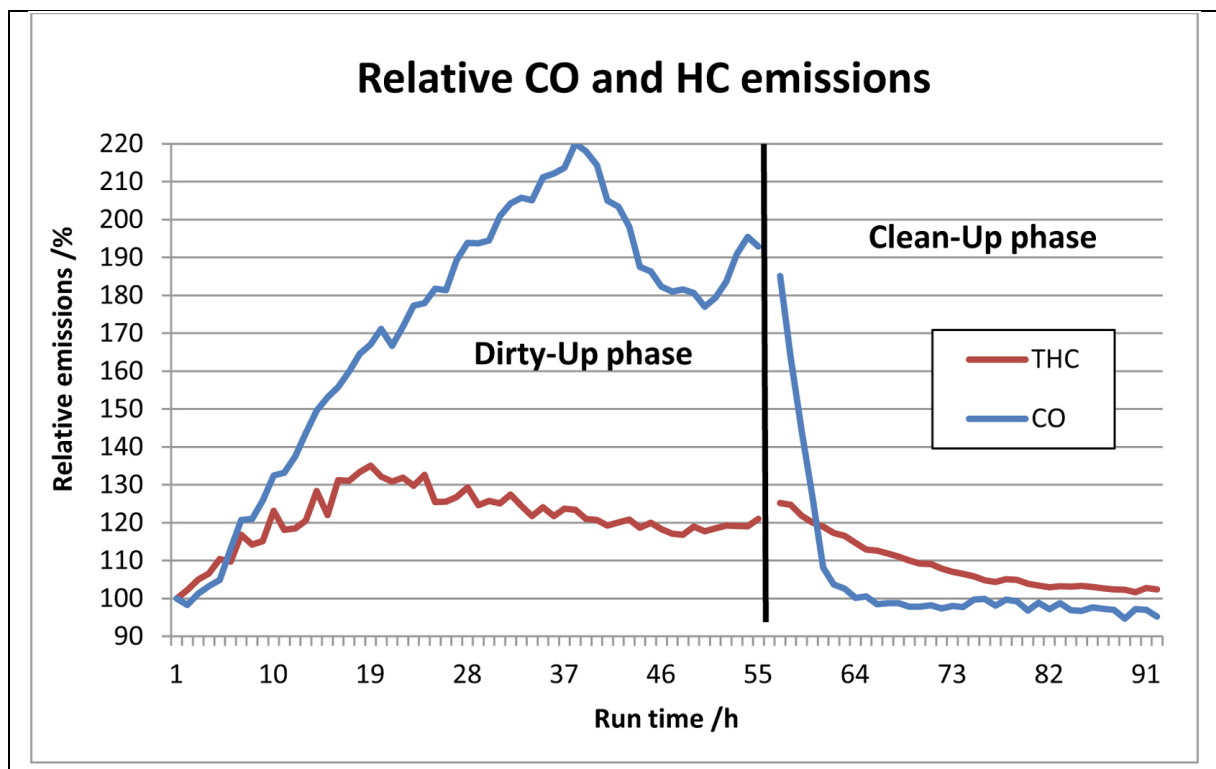


Figure 16: Coked injectors with internal deposits show an increase in HC and CO emission [19].

Both studies also observed a longer combustion duration with coked injectors which resulted in increased fuel consumption and lower engine performance. Additionally, pre-ignition events occurred when using coked injectors in [19].

A 3D-CFD simulation investigating the mixture process showed higher fuel impingement on the piston and more areas with rich mixture for a coked injector with internal deposits. The effects got worse with later injections [51].

Wang et al. [6] compared the particle number and mass emission for 3 injectors at different engine loads. Injector 1 and Injector 2 had internal deposits resulting in 8.5% and 5.3% flow shift while injector 3 was clean. For all engine loads injector 1 lead to the highest particle emissions and injector 3 to the lowest, see Figure 17.

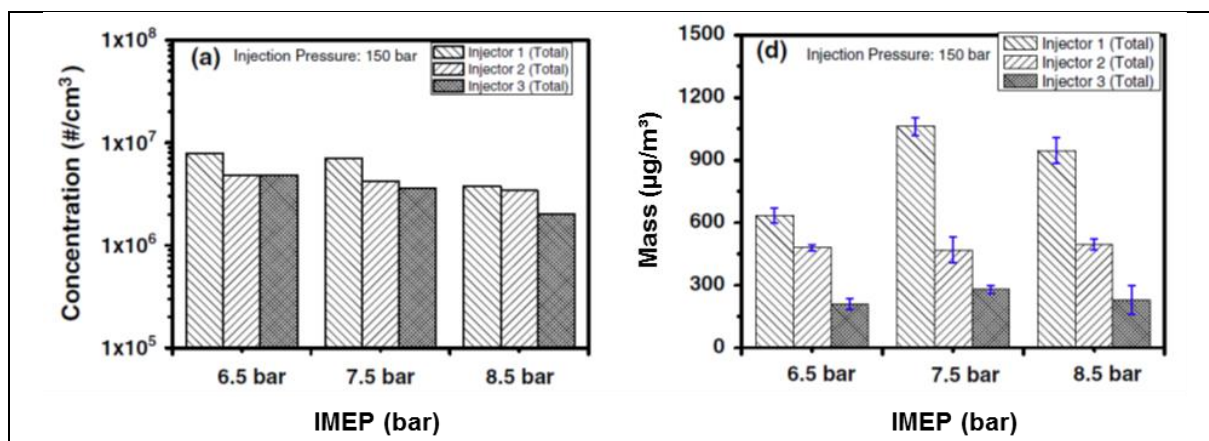


Figure 17: Increased particle number and mass emission for injectors with internal deposits (injector 1 & 2) compared to a clean injector (injector 3) at different engine loads [6]

Higher injection pressure reduced the overall particle mass emissions for both the clean and coked injector but increased the difference between clean and coked [6].

2.2.2 Tip Coking – Diffusion Flames

External deposits in the counter-bores and on the injector tip are normally not interfering with the spray pattern due to their location. Therefore, they should show no influence on engine performance and emission as described in the previous chapter. However, recent studies regarding GDI injector deposits revealed an increase in particle number and mass emission despite no obvious flow shift [7] [9] [52].

Optical measurements with fiber-optic sensors and endoscopes identified a bright yellow diffusion flame on the injector tip indicating rich air/fuel conditions as seen in Figure 18.

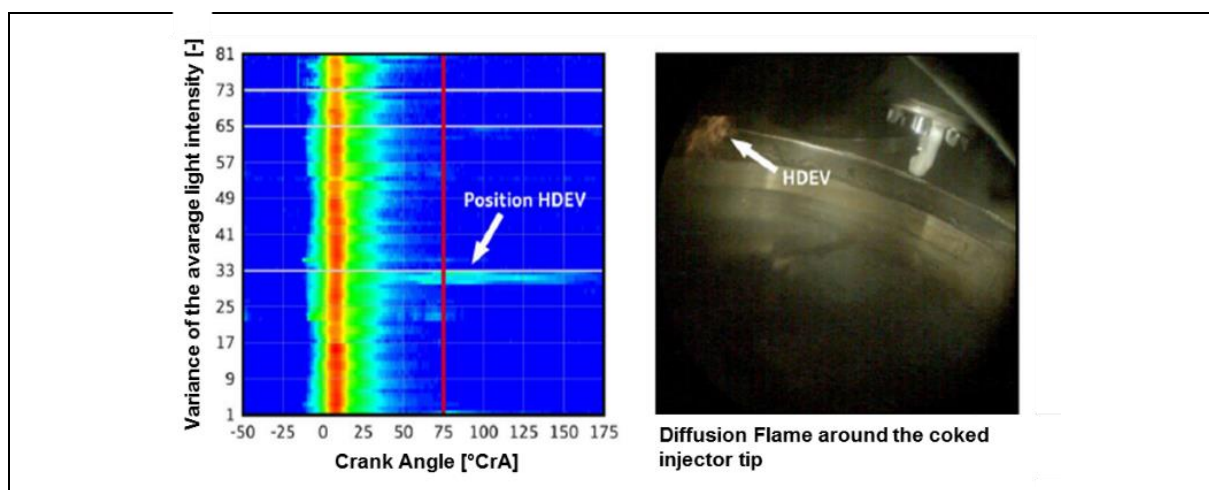


Figure 18: Optical detection of sooting diffusion flame around the injector tip [9].

The diffusion flame occurs after the main combustion explaining the lack of air around the injector. This phenomenon is also referred to as “tip sooting”. All injectors experiencing tip sooting show external deposits [7] [8] [9] [11] [52].

Experiments conducted by Berndorfer et al. [52] suggest that fuel remains on the injector tip and in the counter-bores after the injection event. When the flame front of the main combustion reaches the injector, the fuel produces particles due to the local rich air/fuel mixture. A part of the particles build up a porous deposit layer which is able to store more fuel during and after the injection leading to even higher particle emissions. This self-amplifying effect is shown Figure 19 where the diffusion flame intensity and particle emission increase over time until they reach a stable state where deposit cleaning factors avoid further build-up.

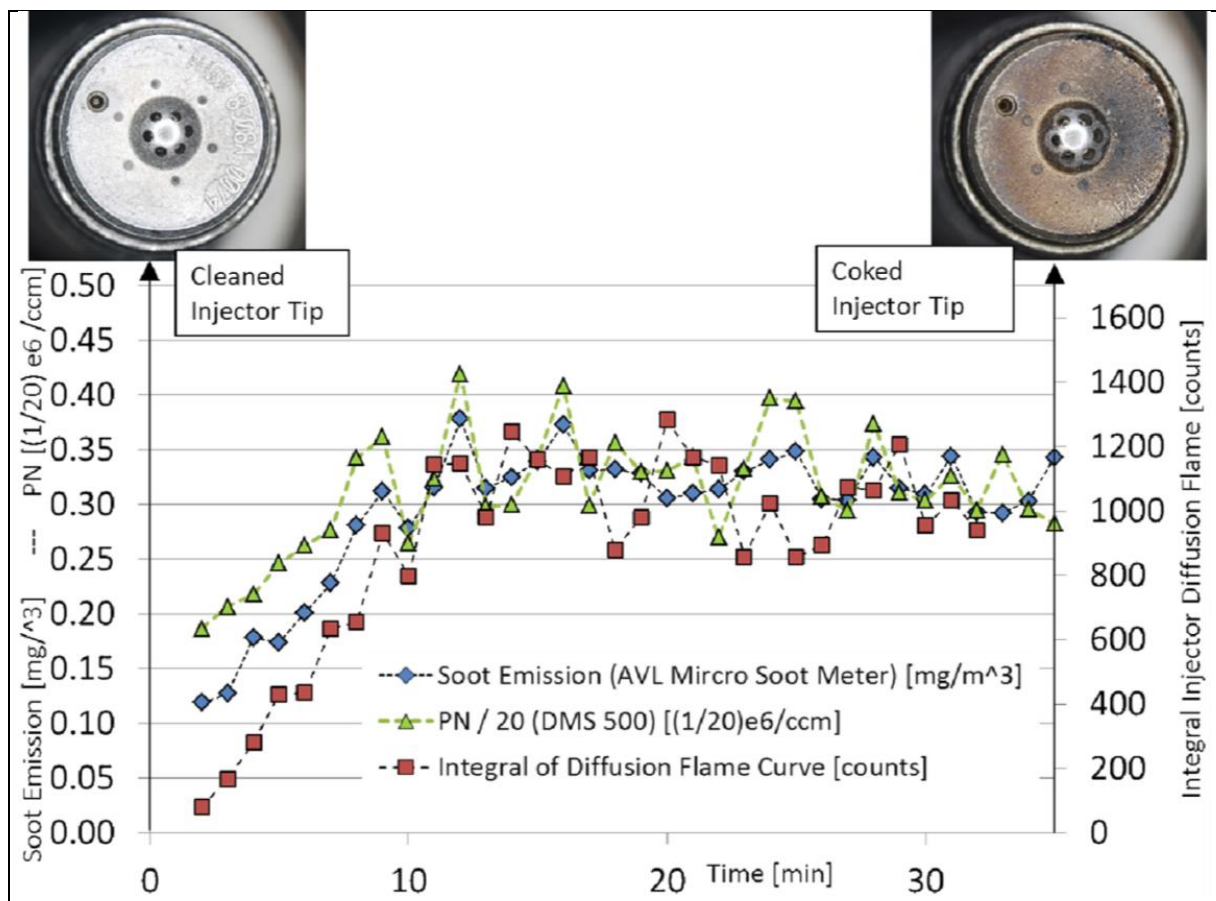


Figure 19: Increase in diffusion flame intensity and particle emission over engine running time [52]

After stabilization Berndorfer et al. switched to a port fuel injection while keeping the heavily coked injector in the combustion chamber. The particle emissions dropped to the state of a clean injector and no diffusion flames were observed [52]. This leads to

the conclusion that the external deposits don't have a negative influence but the fuel stored inside which comes directly from the injector due to the injection event.

The key to reduce particle emissions due to tip sooting is therefore to reduce or avoid conditions which transport fuel to the counter-bore walls and the injector tip or evaporate the fuel before the flame front reaches the injector. Reduced tip wetting will increase the stabilization time but will eventually lead to the same thickness of external deposits, however the amount of fuel stored after each injection is less.

Injector tip wetting is depending on flow conditions inside the injector, nozzle and counter-bore geometry and their relationship, fuel pressure, flow and temperature conditions inside the cylinder and injection strategy [8].

Improvement of the nozzle and tip design which reduced fuel impingement in the counter-bores and on the tip proved to reduce particle emissions as less fuel was stored in the external deposits during each injection [8] [9] [52]. Optimization of the injector design is in responsibility of the injector supplier; the result is shown in Figure 20. Bosch used 3D-CFD to reduce the tip wetting of their HDEV5-injector (Basis). The new HDEV6-injector (optimised) nearly reaches the PN emission levels of a clean injector (Figure 20) after stabilization.

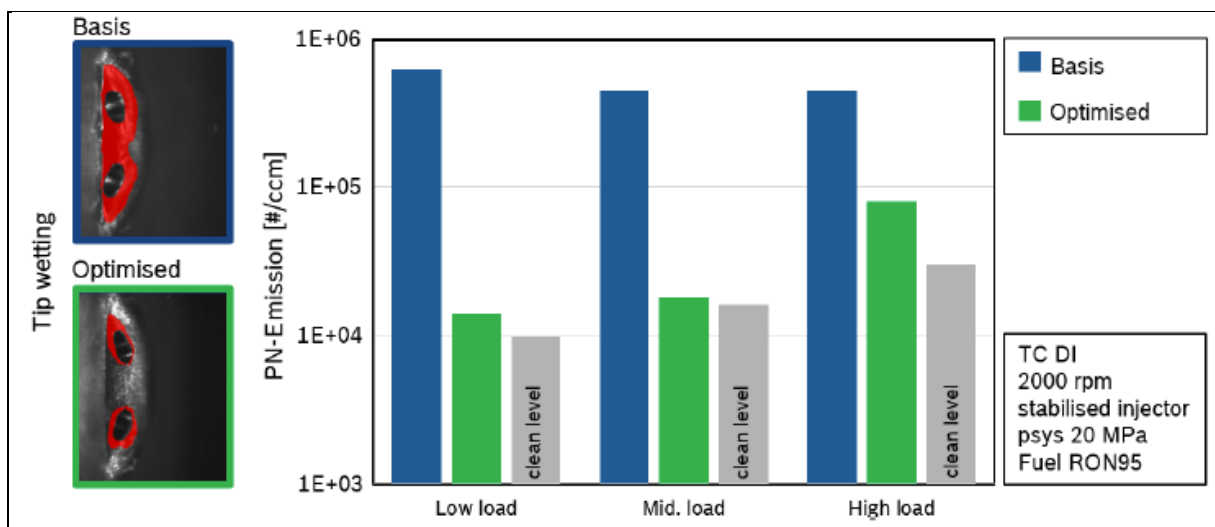


Figure 20: Improved injector design leads to particle reduction caused by tip sooting [8]

New innovative injector designs can also improve tip wetting leading to a small increase of PN emission from a clean to a stable injector [11].

Test with different fuel pressures and stable injectors in [7], [8] and [52] show improved tip sooting with increased pressure. Figure 21 compares the diffusion flame intensity for 3 different fuel pressures. Also multiple injections are investigated which increase

tip sooting compared to a single injection. This can be explained by the low flow velocity in the injector nozzle during opening and closing similar to low fuel pressure. More opening and closing events will therefore lead to more fuel stored in the deposits.

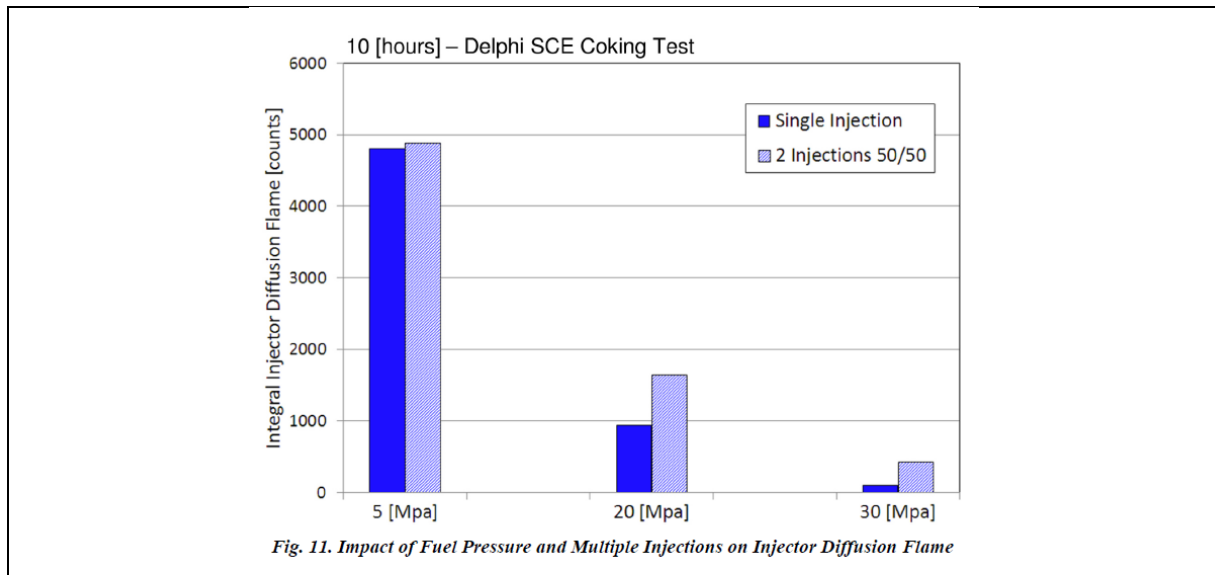


Figure 21: Injector Coking leading to diffusion flames depended on injection pressure and injection strategy [52]

Piock et al. [7] studied the influence of the cylinder charge air motion on the particle emissions due to diffusion flames. An increased air flow in the cylinder achieved by high tumble intake ports can reduce the sooting phenomenon. However, it is not clear from the study if the higher air flow around the injector tip reduced the tip wetting during injection or if the change is a result of improved evaporation and distribution of the wall film after injection. It is assumed that the improvement comes from the better evaporation as high air flow velocities across the fuel stream during injection cause radial fluctuation which normally worsens the tip wetting. The results for different operating points, fuel pressures and charge motions are shown in Figure 22

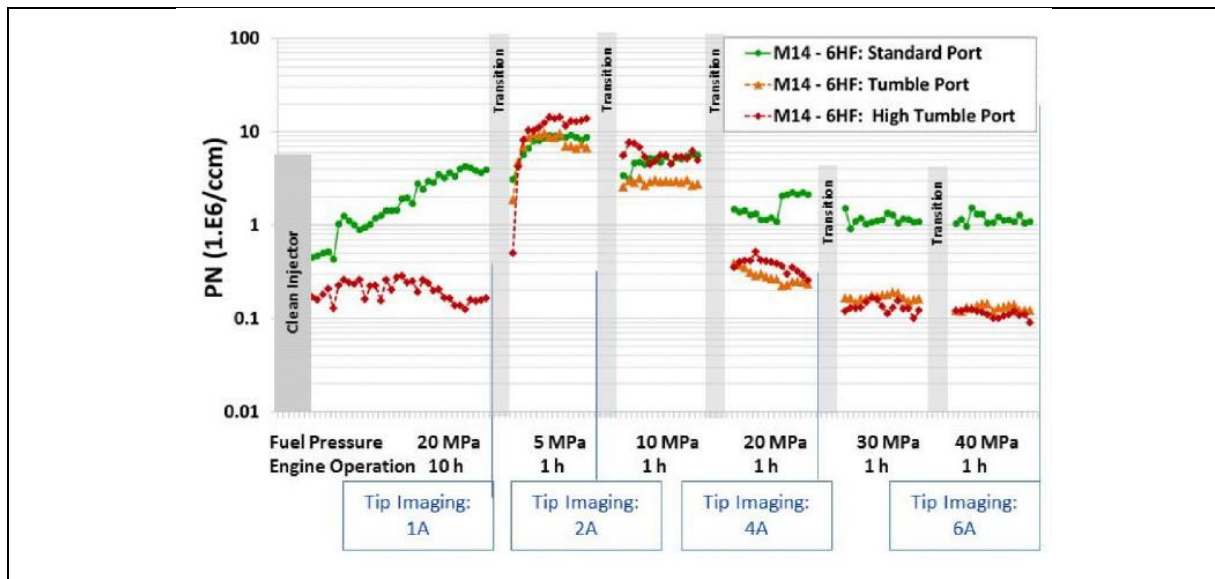


Figure 22: Influence of in Cylinder charge air motion and fuel pressure on tip sooting [7]

Currently there are no studies available investigating the influence of injector tip temperature, fuel temperature or fuel distillation curves on injector tip wetting and tip sooting. A study done by Brack et al. [53] however simulates the evaporation of a given wallfilm on the injector tip and in the counter-bores which improves with higher fuel and wall temperatures.

3 Engine Deposit Cycle

To investigate the influence of deposits on a next-gen TGDI engine several tests were conducted on a controlled engine testbed. The setup and results are described in this chapter.

3.1 Engine Description

The investigated engine is a 1.6l TGDI prototype which has been built for optimized fuel consumption. It is controlled by an AVL developed rapid prototype engine management system (RP-EMS) which allows full control of all functions. Some of the main features are:

- 1.6l Inline 4-cylinder TGDI engine
- 77mm Bore and 85.8mm stroke and a 11.5:1 compression ratio
- DVVT valvetrain with RFF and a Miller intake camshaft
- Cylinder head integrated cooled exhaust manifold
- Cooled forced HP EGR
- 12V Electric supercharger for increased low end torque and as EGR pump
- 104kW @ 4500 rpm and 250Nm @ 1200 to 4000 rpm
- Best point close to 200g/kWh BSFC with RON 98 fuel and extended sweetspot area below 240g/kWh

The AVL High Efficiency (HiEff) Engine was built in Austria and China and used for different demonstrator vehicles. Figure 23 shows the BSFC map of one of the engines in Austria normalized for a fuel calorific value of 42.57 MJ/kg from the year 2015. A Golf 7 equipped with this engine and improved functionalities like intelligent alternator control, start/stop and better aerodynamics could achieve 90g CO₂/km in the NEDC cycle. The micro hybrid functions all used 12V supplied by the main auxiliary battery.

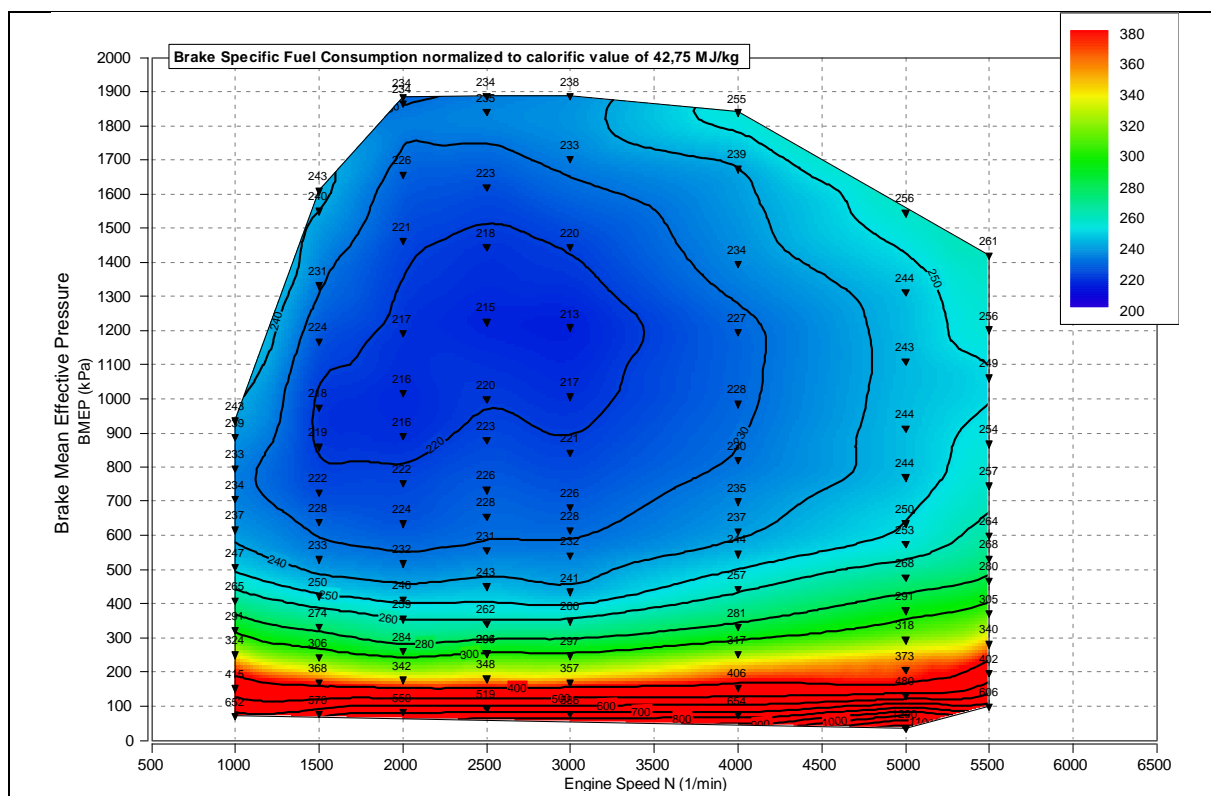


Figure 23: AVL HiEff Engine BSFC Map (2015) [54]

3.1.1 Layout

A simplified engine layout showing the air and high pressure EGR path can be seen in Figure 24. The air path from 1 to 11 is the same as a standard TGDI engine with a water-cooled intercooler (3) and an integrated exhaust manifold (8). Additionally exhaust gas before the turbocharger (HP-EGR) is taken from the main path (9) and cooled in a high temperature EGR cooler (12) which is connected to the engine cooling circuit. The exhaust gas flow is regulated with a high pressure EGR valve (13) and introduced to the main air path over an EGR rail (17). If the pressure difference between the exhaust side and intake side is not high enough to achieve the desired EGR rate the electric supercharger (15) is activated and acting as an EGR pump. To avoid further heat up of the exhaust gas both the supercharger and the low temperature EGR cooler (16) are cooled by the low temperature cooling circuit which is also used for the main intercooler (3). This setup allows to run EGR temperatures close to 30°C at the intake manifold. During transient operation at low engine speeds the air valve (18) in the secondary air path opens and the electric supercharger is used to further compress a part of the intake air resembling a two-stage charging concept. A one-way valve in front of the main throttle (5) inhibits back flow during this phase.

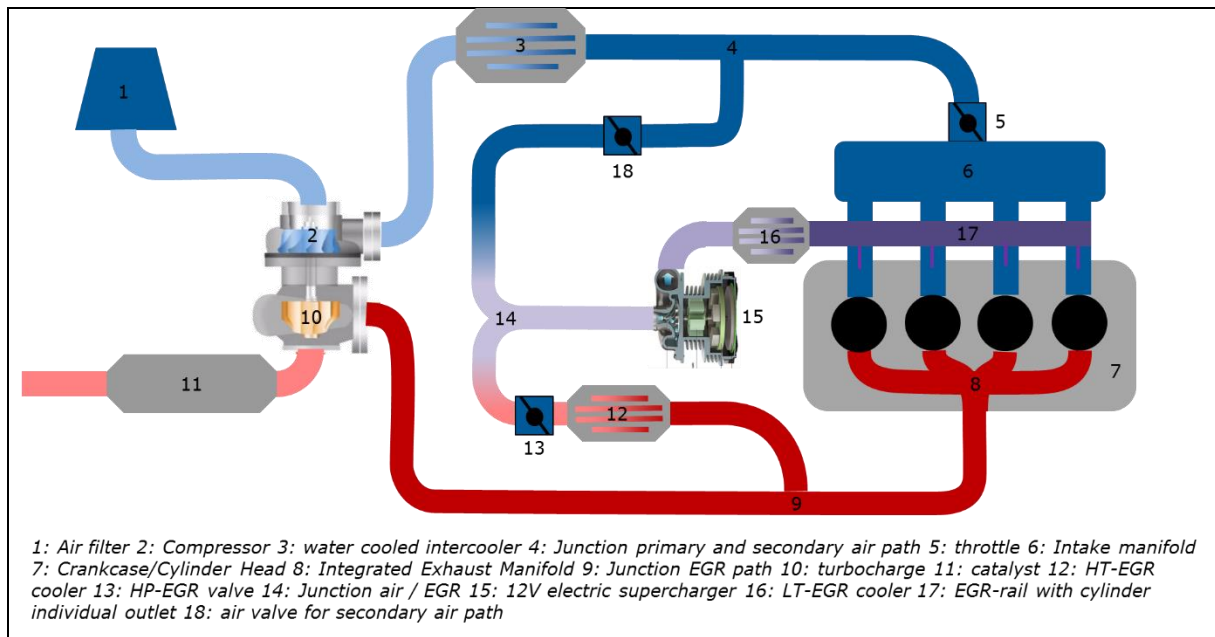


Figure 24: AVL HiEff Engine Layout

This setup in combination with dual VVTs and full control of all valves and the electric supercharger speed allows a calibration of internal and external EGR rates independent of engine speed and load. High EGR rates in combination with very early closing of the Miller intake camshaft lead to the shown low fuel consumption in a very large area.

3.1.2 Valve Lifts

The exhaust camshaft is a standard design with a 180° CrA opening duration and a maximum valve lift of 8.5mm. For the intake camshaft, the opening duration has been chosen with 140° CrA and a closing point (1mm lift) at 25° CrA before BDC to achieve a Miller effect. Despite the short opening duration, the camshaft still achieves a maximum valve lift of 7.2mm. Roller finger followers with hydraulic lift adjusters actuate the valves.

Both the intake and exhaust camshafts are equipped with a VVT with a 50° Crank Angle range. In the most advanced position the intake valves close 75° CrA before BDC which equals to a 42% longer expansion stroke. Figure 25 shows the valve lift curves for both camshafts in their advanced and retarded position with the full line representing the base position.

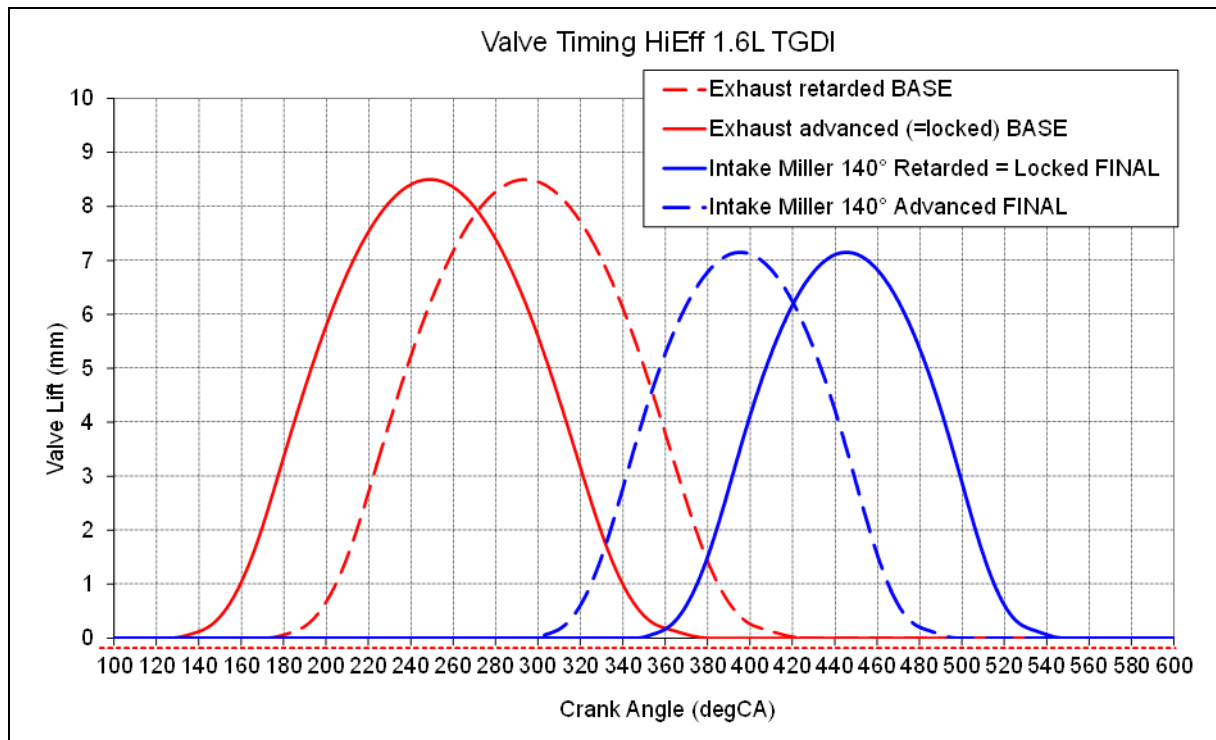


Figure 25: AVL HiEff Valve Timing

3.1.3 Injector

The HiEff engine is equipped with a 7-hole Bosch HDEV5 injector which is mounted in a side position on the intake side. It has a symmetrical spray pattern to the side and is targeted downwards to the piston. The nozzle design follows the Bosch standard with cylindrical holes and counter-bores. All 7 holes have a diameter of around 180µm and counter-bores with 360µm diameter. In the AVL HiEff engine the injector is operated with 50 to 200 bar fuel pressure but has been proven to be operational with 300 bar as well. Further details can be found in Figure 26.

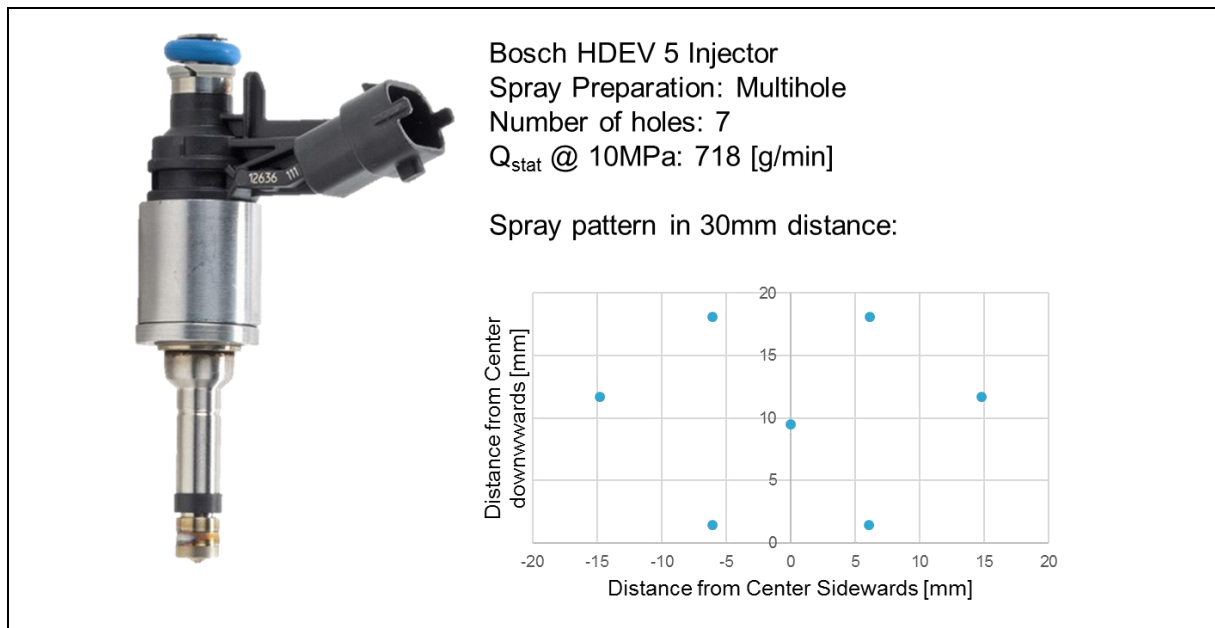


Figure 26: Injector configuration used in the test engine

3.1.4 Testbed Setup

To evaluate the possible effects of engine and injector deposits on the AVL HiEff engine it was installed on an engine testbed controlled by AVL puma at the AVL Shanghai Technical Center, China. Different from deposits test on the road or on a chassis dyno this setup allows an accurate control of all boundary conditions and repeatable tests but for increased costs.

The testbed is equipped with an active engine brake allowing also motoring of the engine. Additionally, conditioning units for engine coolant, engine oil and fuel are available. During the engine tests, most of the available engine signals are recorded together with over 80 additional sensors to ensure an accurate monitoring of all processes. Figure 27 shows the engine with all external sensors installed before connecting it to the brake in the engine test cell.

The focus was laid mainly on the EGR and secondary air path with temperature and pressure sensors after every part and junction. All coolers as well as the main engine cooling circuit were also equipped with flow meters to analyze the heat transfer. A full list of all recorded signals and installed sensors is listed in Appendix I – Engine Sensors and Parameters.

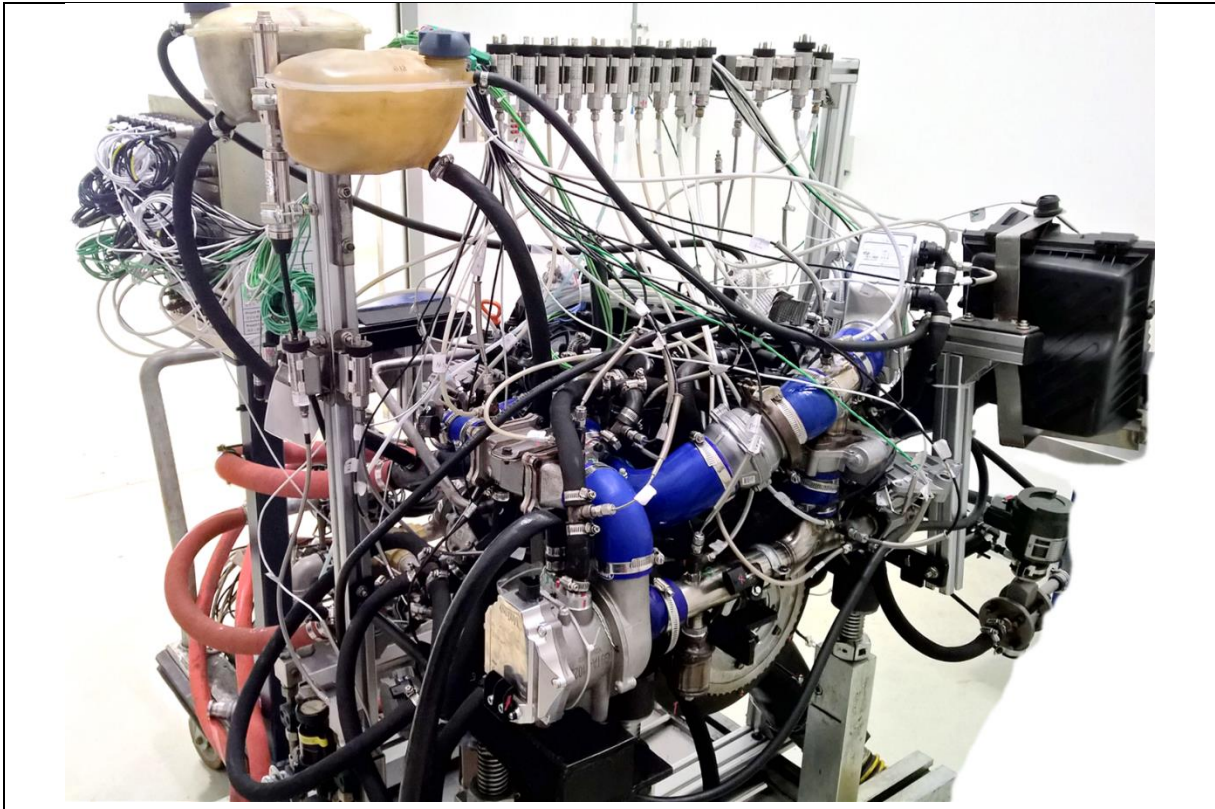


Figure 27: Engine Instrumentation before installation in the test cell

The installation of cylinder individual pressure indication (AVL Indicom) was used to monitor the engine operation for knocking and pre-ignition. It is also used to measure engine friction and combustion duration which can help detect spray altering internal deposits. As the engine uses a prototype EMS there is no knock control implemented. This function is replaced by AVL's Real Time Controller (RTC) in Cameo which uses the cylinder pressure signals to optimize the combustion time (MFB 50%) by adjusting the spark timing.

Engine out emission was recorded using an AVL AMA i60 while the particle number was analyzed with an AVL 489 particle counter.

3.2 Test Cycle Development

The target of the engine deposit test runs was to investigate the influence of different fuels on the engine behavior. To ensure repeatability and comparable results between different tests a specific test cycle had to be chosen or developed. While there are injector coking test cycles for diesel engines which are officially accepted to evaluate e.g. fuel influence on coking – like the CEC F-110-16 test [55] [56] – nearly every study investigating gasoline DI injector deposits uses their own cycle or operation strategy.

The cycles used for GDI engines depend on the focus of the respective study. Imoehl et al. [39] defined their test cycle based on the injector tip temperature while the study by Berndorfer et al. investigating the injector diffusion flames was only using one operating point [52]. Earlier tests were even done directly in the vehicle with a defined route [45] or with a specific vehicle speed cycle [46]. A detailed summary of the cycles used in GDI coking investigations in the last years can be found in [57].

Despite the variety of cycles for Diesel and Gasoline injector coking most of them share the following properties:

- All test cycles are a sequence of stationary points which are kept for a few minutes up to several hours.
- Test cycles done on an engine test bed use an alternating speed and/or load pattern – low engine speed and load followed by higher load at same or higher speed followed again by lower speed and load
- Vehicle tests with a fixed velocity cycle also show an alternating pattern of vehicle speed, however due to missing engine or transmission information the relation between vehicle speed and engine load point is not clear.
- The defined pattern of load points represents a sub-cycle which is then repeated multiple times until the request time (engine test bed) or mileage (vehicle tests) threshold is reached.
- Some tests also have a soaking period after one or several sub-cycles where the engine or vehicle is not operated

Based on the properties above and considering that the engine tests are performed in China and the engine uses advanced TGDI hardware the following test cycle requirements have been defined:

- One subcycle should consist of alternating speed/load points
- The total test duration should be 50h or longer
- After 10h there should be a soak duration of 4 hours
- One or more operating points should relate to a NEDC vehicle speed of a mid-sized passenger car in China
- One or more operating points should use a high engine load at low speed to represent the early upshift behavior observed in fleet tests performed in China
- At the beginning of a sub cycle the engine temperature should be low to simulate vehicle cold start conditions
- One operating point should use the maximum EGR rate of the test engine

As none of the available test cycles can meet the requirements a new cycle was developed. Table 1 lists the nine different operating points which are used in the new

cycle. The engine temperature is regulated by the set point for the coolant outlet (T_W_O). If the set point is lower than the current temperature cold water is used to reduce the level while for a set point exceeding it the test bed control system waits for the engine to warm up until the requested value is reached.

Table 1: AVL HiEff Test Cycle Operating Points

No.	Speed	Load	T_W_O	Time	Reason
#	rpm	bar BMEP	°C	min	
1	750	0	40	3	Cold idle as worst condition after vehicle start
2	2000	6	40	8	Acceleration with cold engine
3	1500	2	90	2	30-50kph NEDC point
4	1600	3	90	3	70 kph NEDC point
5	4000	12	90	8	High injector temperature point
6	3000	8	90	5	130 kpg NEDC point
7	2000	14	90	5	Acceleration after early upshift
8	3000	10	90	8	Maximum external EGR rate
9	1200	2	90-40	10	Slow engine cool down with 5°C/min to avoid deposit break off due to shearing forces

Operating point #3 was defined as reference point and will be set multiple times during a sub cycle to see possible changes caused by a specific operating point. Figure 28 shows the speed and load profile of a full sub-cycle which has a total duration of 1 hour. This sub-cycle will be repeated 10 times followed by a 4 hour soak period. The total injector coking test cycle ends after at least 5 of these 14 hour blocks to achieve a minimum of 50 hours engine run time.

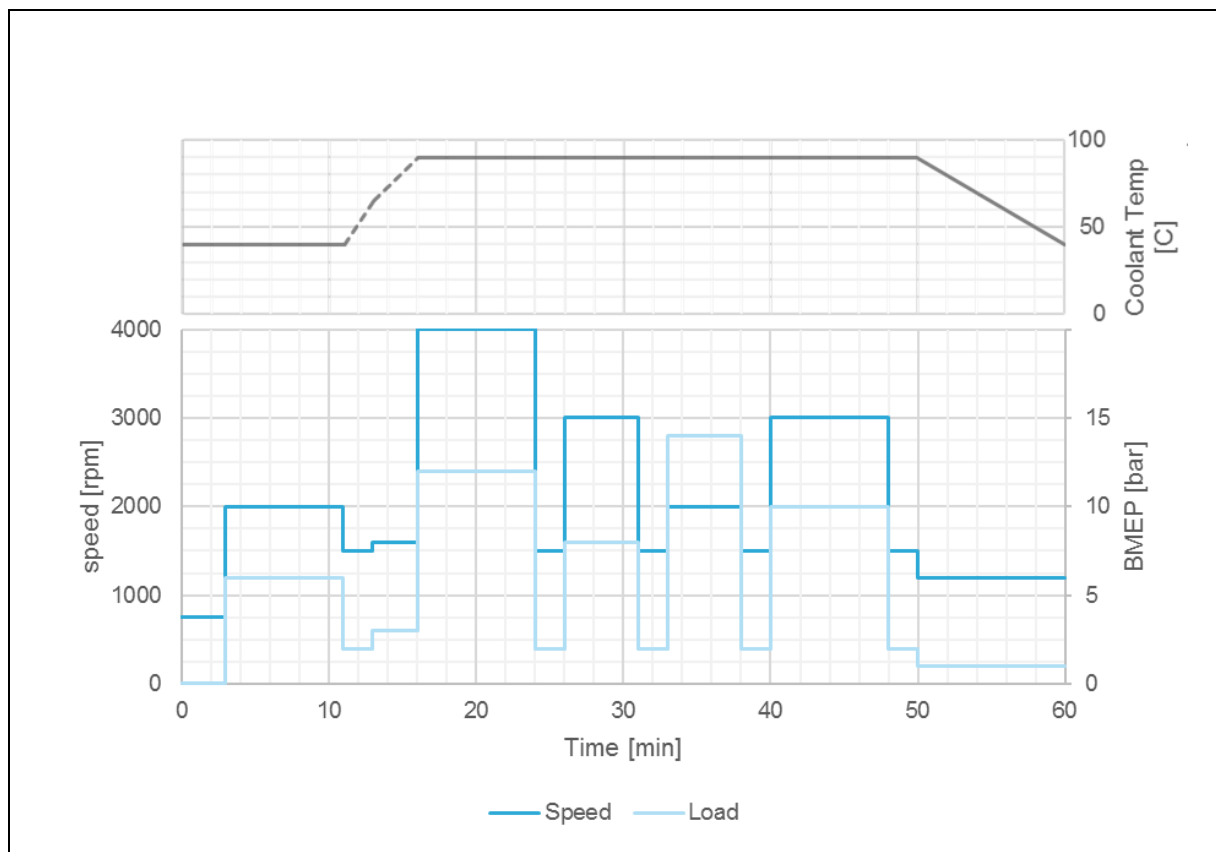


Figure 28: Speed, load, and coolant profile of the new developed test cycle

After the operating point #2 the T_{W_O} set point is raised to 90°C and the engine warms up while running the points #3 and #4. The warm up process is finished before reaching point #5 and the test bed conditioning unit is keeping the coolant temperature constant. At the end of the sub-cycle the engine is cooled down to the level of the next sub-cycle at a slow rate.

The engine is controlled by the test bed operating software Puma which automatically follows the cycle. The dynamometer fixes the engine speed and Puma sends a load request to the EMS to achieve the requested torque based on the BMEP. As mentioned in chapter 3.1.4 a real time controller is adjusting the spark timing continuously to keep the combustion in an optimized range. This will ensure that the engine is running with the best efficiency in each operating point.

When knocking occurs the RTC retards the spark for a few cycles which results in a small decrease of engine torque. The test bed software will try to compensate this decrease by increasing the load demand. In the standard configuration, a change of load demand will affect combustion and injection critical parameters such as camshaft position, fuel pressure and EGR valve position which is unwanted for this test cycle. Therefore, the values for the controls have been fixed for each operating point individually. The respective values are shown in Table 2.

Table 2: Fixed Injection pressure, intake VVT and EGR valve position for each test point

No.	Speed	Load	Fuel pressure	Intake VVT	EGR valve
#	rpm	bar BMEP	bar	°CrA adv.	opening %
1	800	0	50		0
2	2000	6	85	40	0
3	1500	2	68	30	0
4	1600	3	70	35	9
5	4000	12	150	25	0
6	3000	8	110	30	45
7	2000	14	100	30	0
8	3000	10	110	12	40
9	1200	2	60	18	0

Injector deposits will influence the engine behavior in several ways. Internal injector deposits which reduce the flow rate reduce the amount of fuel in the cylinder for a given injection duration and pressure. The cylinder will burn leaner and the closed loop lambda control is increasing the injection duration to achieve again lambda 1. This effect can also be monitored with the lambda correction factor.

A deposit caused change of the injector spray pattern could also lead to longer combustion durations as described in [6] [19]. Longer combustion durations lead to a lower combustion efficiency which decreases the engine torque. The control software will compensate this reduction by increasing the load demand which results also in a longer injection duration and higher intake manifold pressure.

External deposits causing tip sooting can be detected by an increase of particle mass and PN emission. However, combustion chamber deposits which disturb mixture processes and internal injector deposits which increase wall wetting and create rich air/fuel zones also effect these emissions. As no optical measurement tools were available during the test cycle which could identify diffusion flames a differential approach was chosen to identify particle emissions from external deposits. At the end of the test cycle the injectors were removed and optically investigated for external and internal deposits. Then they were cleaned in an ultrasonic bath and the engine was running another 1 hour sub-cycle. The drop of particle emissions can be directly accounted to the injector deposits as no other parts were modified. If the optical

investigation and the other parameters don't indicate internal deposits the change in particle emissions are caused by the external deposits.

The engine and sensor data was recorded and averaged over a 30 second measurement duration at the beginning and end of every operating point in the sub-cycle. After the test bed control sets the new operating point the system waits 30 seconds for the engine to stabilize. Then the first 30 second measurement is started. 30 seconds before the operating point is changed again the second measurement is triggered. This allows an investigation of parameter change during one operating point.

At the end of a full test cycle which included the additional sub-cycle after injector cleaning the cylinder head was removed and all combustion chamber parts were photographed. The piston crown, cylinder head, injectors and valves were cleaned and the oil and oil filter were renewed before starting the next cycle with a different fuel.

3.3 Test Fuels

Four different fuels have been selected to run in the test cycle. The target was to investigate the influence of different commonly used fuels in Asia on the engine behavior. To reflect realistic conditions no special blends have been used but fuel directly from several gas stations. All fuels fulfill the 2016 China 5 and Bharat Stage 4 fuel legislations however no ethanol blending is used for the Indian RON 91 fuel. The different fuel properties are listed in Table 3.

Table 3: Deposit Cycle Test Fuel Properties

Name	Shanghai RON92	China M15 (15% Methanol)	Indian RON 91	Shanghai RON95
RON	92.4	97.9	92.6	95.8
MON	84.7	84.6	81.6	84.5
IBP	32.8°C	31°C	35°C	29.8°C
T10	54.6°C	53.7°C	51.7°C	54.1°C
T50	104.5°C	92.5°C	94°C	108.2°C
T90	161.9°C	156.8°C	163°C	164.0°C
FBP	196.8	197	201.2°C	197.4°C
Benzene	0.54 %(v/v)	0.52 %(v/v)	0.7 %(v/v)	0.47 %(v/v)
Olefin	10.8 %(v/v)	29.8 %(v/v)	29.6 %(v/v)	7.9 %(v/v)
Aromatics	33.8 %(v/v)	8.1 %(v/v)	12.7 % (v/v)	39.1 %(v/v)
Unwashed gums	2 mg/100ml	n.a.	n.a.	2.5 mg/100ml
Washed gums	0.5 mg/100ml	1 mg/100ml	1 mg/100ml	1.0 mg/100ml
Sulfur	1.5 mg/kg	5.2 mg/kg	4.1 mg/kg	1.2 mg/kg
Manganese	<0.25mg/l	0.00025 mg/l	0.00025 mg/l	<0.25mg/l
Iron	<2mg/l	<0.002 mg/l	<0.002 mg/l	<2mg/l

The Shanghai RON92 fuel is the standard gasoline used in Shanghai for passenger cars. This batch has a high aromatic level and medium olefin level and very low levels of impurities like sulfur, manganese, or iron. The China M15 fuel is a standard gasoline fuel blended with 15% of Methanol which explains the high octane number. Different from the M15 fuel used for the fleet tests in chapter 1.2, this sample has the lowest T50 and T90 values of the four investigated. Both China M15 and Indian RON 91 have a high percentage of olefins and a low level of aromatics. They also both show higher sulfur levels compared to the two shanghai fuels. The Shanghai RON 95 was used to be comparable with the test to Europe but has very similar properties as the Shanghai RON 92 fuel.

3.4 Results

This chapter discusses a few of the numerous engine test results to show and explain trends. The focus of the charts is laid on the described indicators for deposit build-up explained above. The following diagrams always include the first 30 sec. measurement

at the beginning of the operating point within a sub-cycle and the second 30 sec. measurement at the end of an operating point.

3.4.1 Shanghai RON 92

The first test run was done with Shanghai RON 92 which was supplied from the AVL test center fuel distribution lines. During the total engine running time of 60 hours a continuous increase of particle emission was measured. Figure 29 shows the change for injection duration, lambda correction, spark timing, combustion duration and particle number for all 3000 rpm / 10 bar operating points. The injection time stays constant over the total test duration which would indicate an unchanged flow rate and no internal deposits.

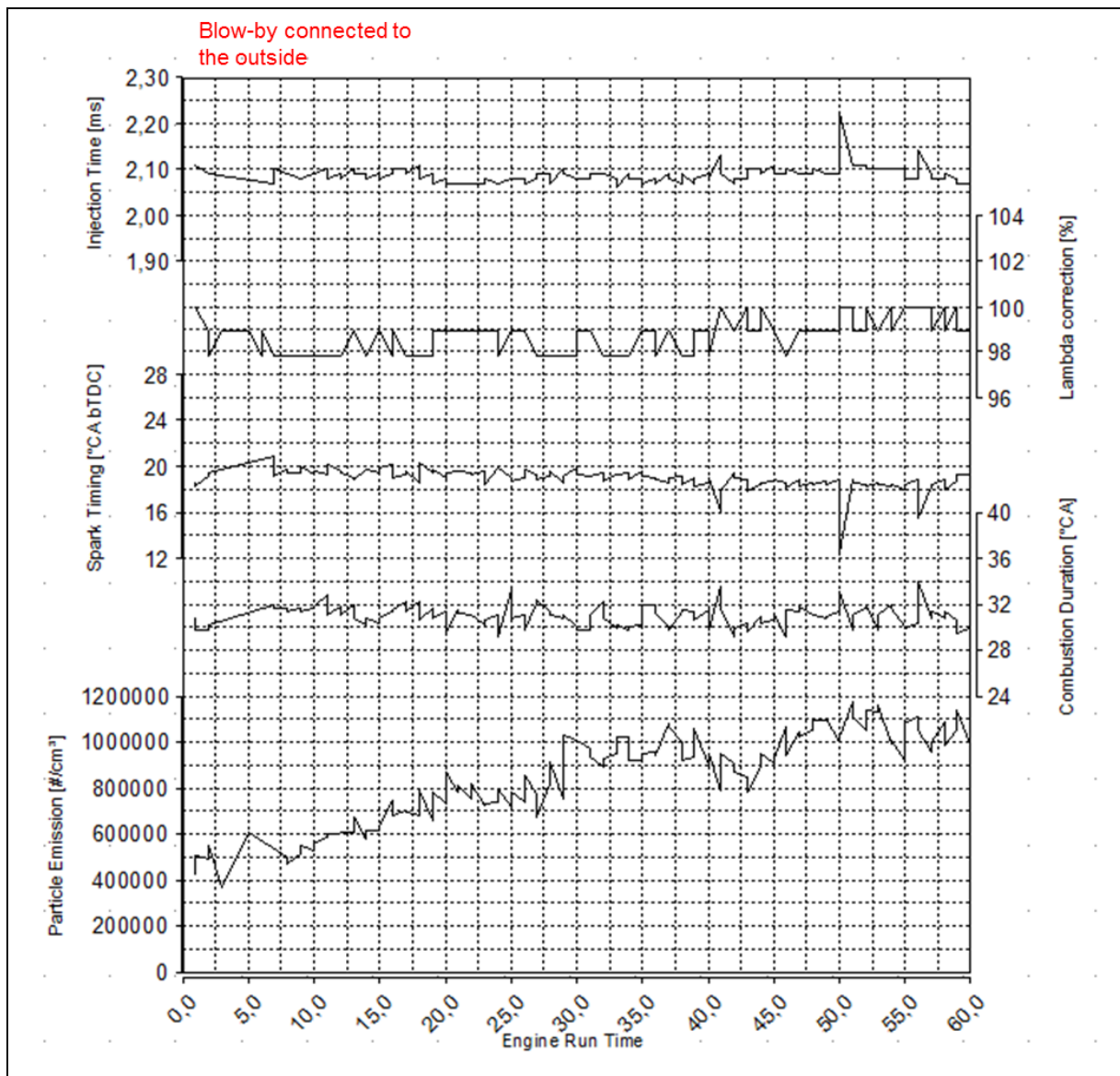


Figure 29: Shanghai RON 92 @ 3000 rpm / 10bar BMEP test result

At the end of the test cycle the spark timing is moving 1 to 2°CrA closer to the TDC indicating a slight increase of knocking events. While the combustion duration stays constant the MFB50% moves away from the optimum and the output torque would decrease. This is compensated by the test bed control which holds the load constant by opening the throttle leading to more air and a higher lambda correction.

Plotting all measurements at 2000 rpm / 14 bar in Figure 30 confirms the previous observations. While no results indicate a change of injector flow rate the particle numbers continuously increase over the total duration.

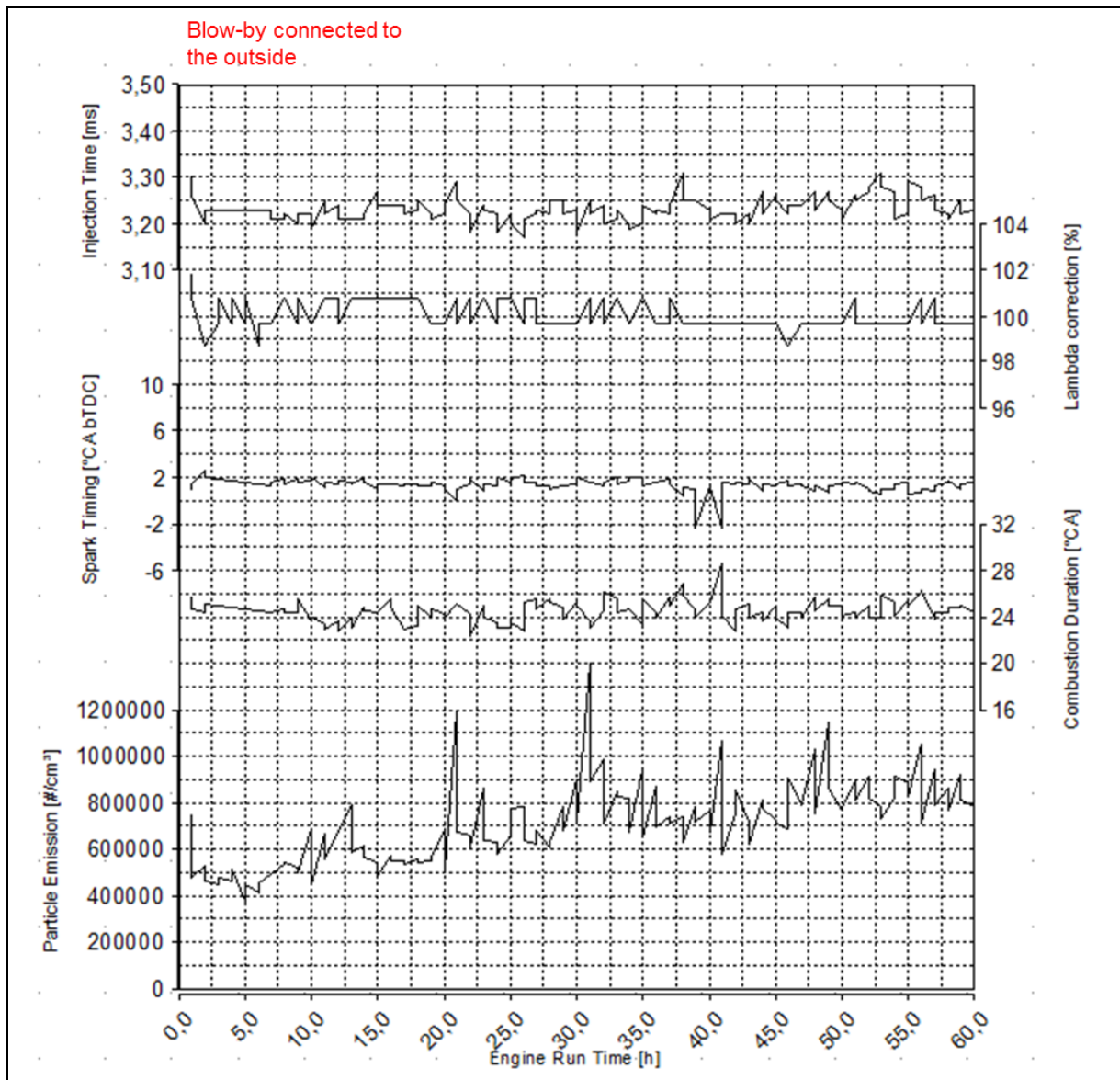


Figure 30: Shanghai RON 92 @ 2000 rpm / 14bar BMEP test result

During the whole test the blow by from the crankcase was routed over a blow-by meter and then over a filter to the outside. No blow-by gases were rerouted to the intake

manifold. Pictures showing deposits and the change of particle emission after injector cleaning are described in chapter 3.5 for all fuels.

3.4.2 China M15

The main difference between the 15% Methanol blend and the other fuels is the nearly 10% lower calorific value and the higher octane number. As all engine parameters remain the same for each operating point the EMS needs to inject more fuel to reach the same power output. Figure 31 shows the 3000rpm / 10 bar point with the M15 fuel and a 10% longer injection time than with the Shanghai RON 92

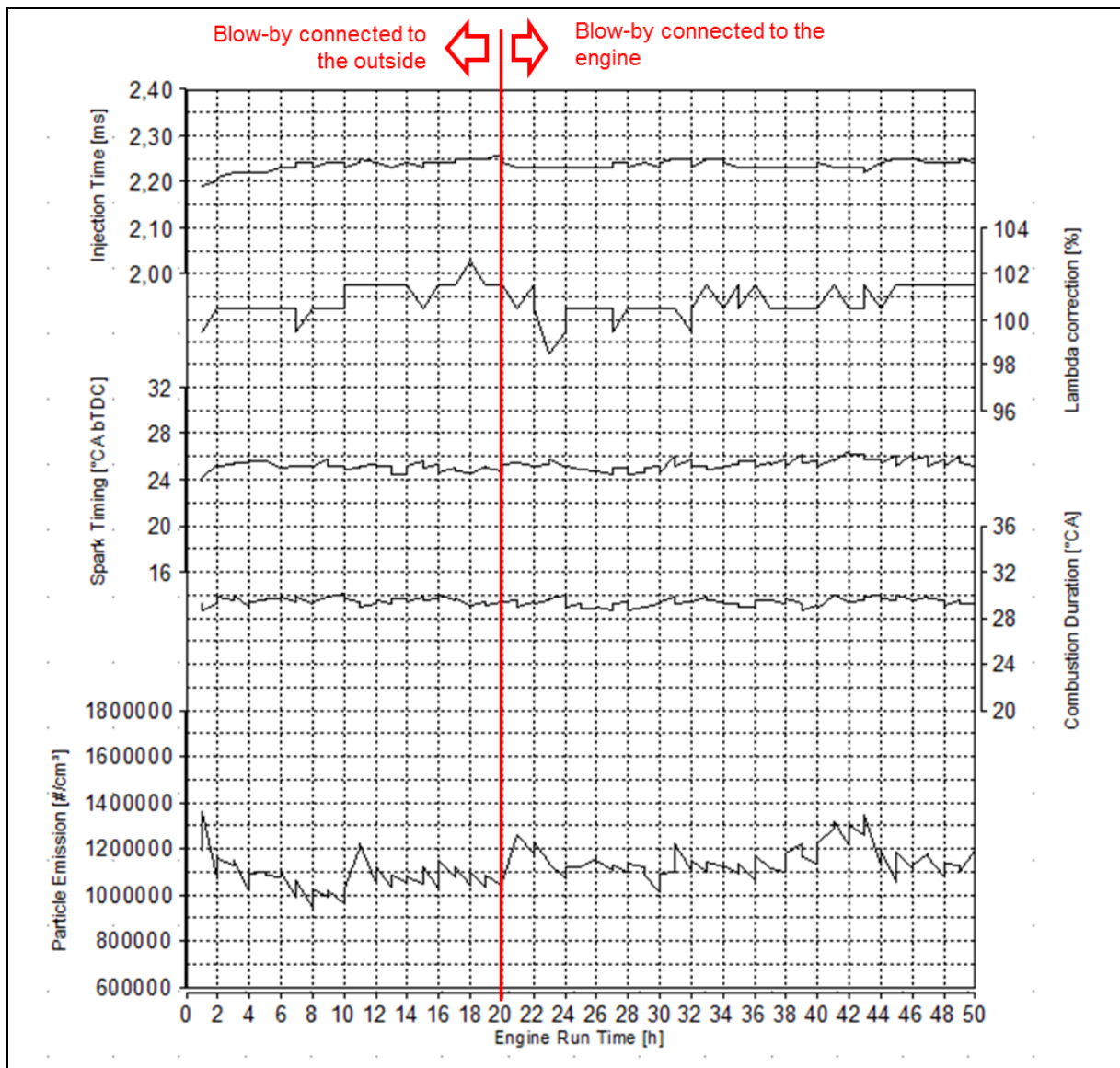


Figure 31: China M15 @ 3000 rpm / 10bar BMEP test result

For the first 20h of the engine test the blow-by system was routed to the outside and after that directly rerouted to the intake manifold. The blow-by configuration influences the air charge of the engine which explains the sudden drop of injection time and lambda correction.

During the test cycle the injection time and lambda correction increase about 2% in the first 20 hours. After the drop, due to the blow-by configuration change both values increase another 1% until the end of the cycle. As the spark timing is unchanged during the full 50 hours this change in injection time could indicate a change of injector flow rate and therefore internal deposits.

The PN emissions show no clear trend in any direction during the test cycle and stay at a very high level with values similar to the end of the test cycle with Shanghai RON 92 at the same operating point (compare with Figure 29). One possible explanation could be the lack of external deposits and diffusion flames at this operating point. Another explanation would be a very quick stabilization of the deposit process. Before a new test cycle is started the engine is running for around 1 to 2 hours to ensure no damage to the hardware during the engine cleaning. If the external deposits already built-up and stabilized during these first 2 hours, the test cycle would also show a constant PN emission.

The 2000 rpm / 14bar operating point confirms the observed trends (Figure 32). In the first 20 hours the injection time and lambda correction increase up to 3% and another 1% from hour 21 to hour 50. There is no clear explanation why the injection time continues to decrease after the change up to hour 26 before it increases again. This effect is not visible in the 3000 rpm / 10 bar BMEP point.

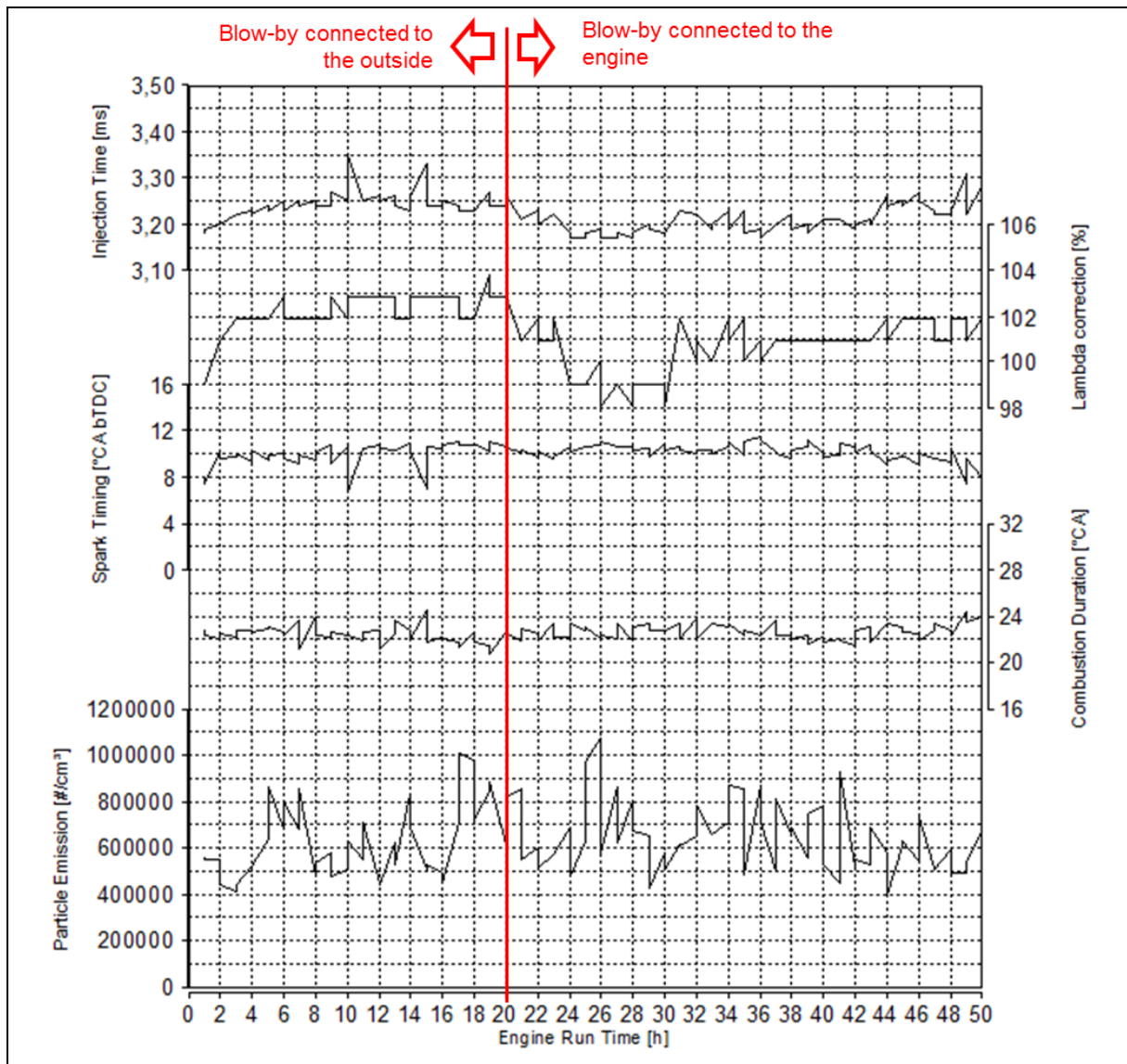


Figure 32: China M15 @ 2000 rpm / 14bar BMEP test result

The PN emission level at this operating point is lower than at the other operating point however it also doesn't show any clear trend indicating a stable injector or no external deposits.

3.4.3 Indian RON 91

The test cycle done with the Indian RON 91 fuel revealed a problem during cycle preparation. Both the M15 and the Indian RON 91 fuel were run out of barrels which were stored outside the test building. Long fuel pipes connected the barrels with the test cell and the engine and had to be filled prior to starting. After the M15 test the pipes have been flushed with 50l Indian RON 91 fuel. However, a check of the recorder data after the first 10 hours showed that there was still old fuel left in the system.

The injection time and spark timing during the first hour of the Indian RON 91 test (Figure 33) is identical with the end of the China M15 cycle (Figure 31) for 3000 rpm / 10 bar. With increasing test duration, the remaining old fuel is slowly replaced by the new Indian fuel and after 5 hours the values are stable. As the Indian fuel has a higher calorific value and a lower octane number the injection duration is decreasing and the spark is retarded until there is no M15 fuel left.

In line with the previous test the blow-by is routed to the outside for the first 20 hours and then connected to the engine afterwards. For the 3000 rpm / 10 bar point as shown in Figure 33 the injection time and lambda correction are stable with no trend in any direction. After the blow-by system change both values drop due to the change intake system boundaries. In the 4th 10 hour sub-cycle the intake manifold pressure sensor showed a too high value for no obvious reason. Thus, the calculated injection time increased despite the same amount of air in the cylinder. The lambda control compensated this by decreasing the lambda correction factor (orange circle) and the effective injection time staid the same. The sensor was cleaned after the 10-hour block and the lambda correction value raised back to the same level as before.

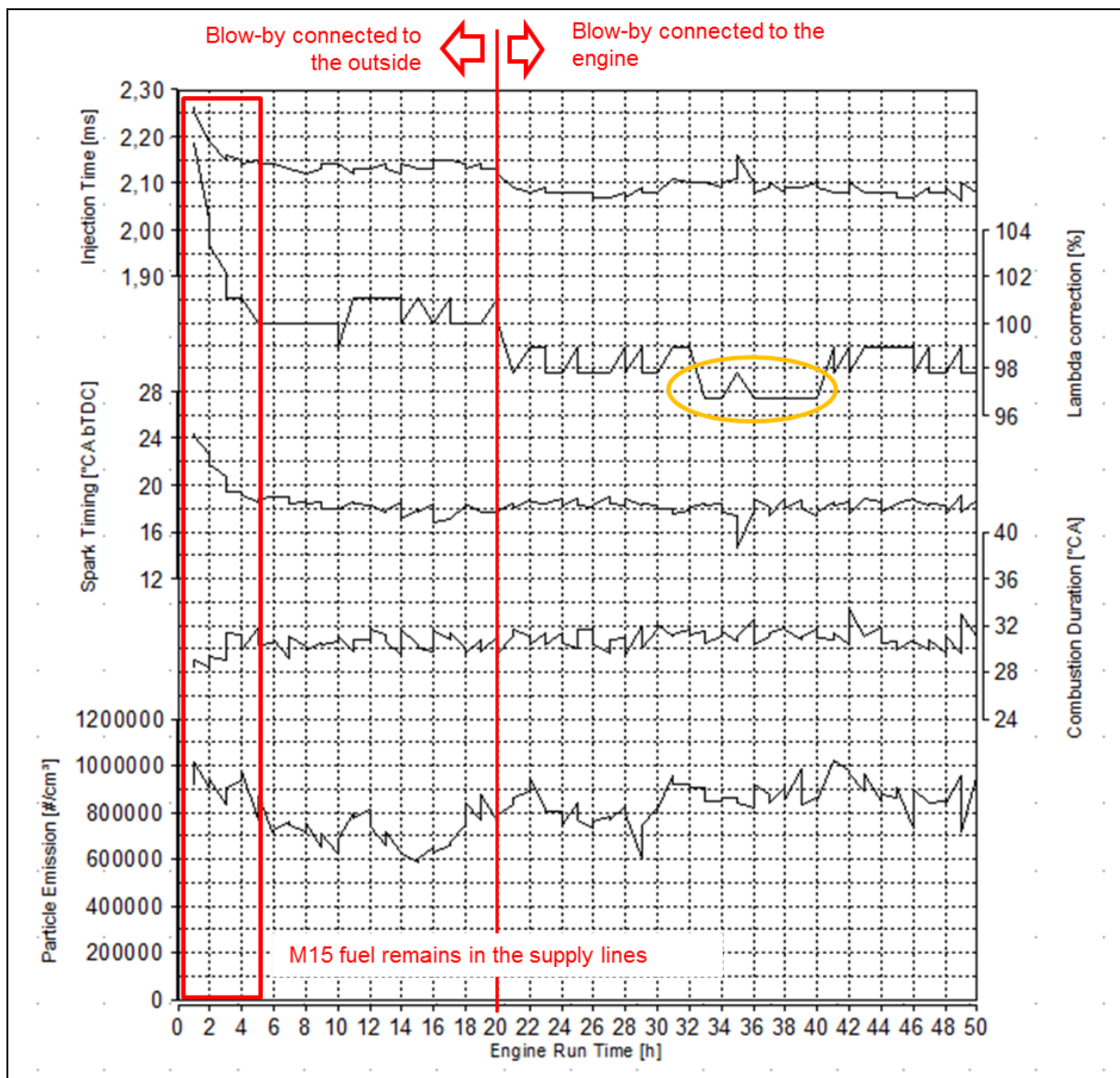


Figure 33: Indian RON 91 @ 3000 rpm / 10bar BMEP test result

The PN emission show a stable behavior during the first 20 hours. However, due to the wrong fuel at the beginning of the tests no conclusions can be made if there has been a stabilization process of external deposits and diffusion flames or the PN emissions are a result of other fuel related parameters. After the blow-by system change the particle number is slightly rising until the end of the test cycle.

The second operating point at 2000 rpm and 14 bar in Figure 34 behaves like the first one with stable injection time and lambda correction. The effect of the wrong intake manifold pressure sensor is also observed here (orange circle).

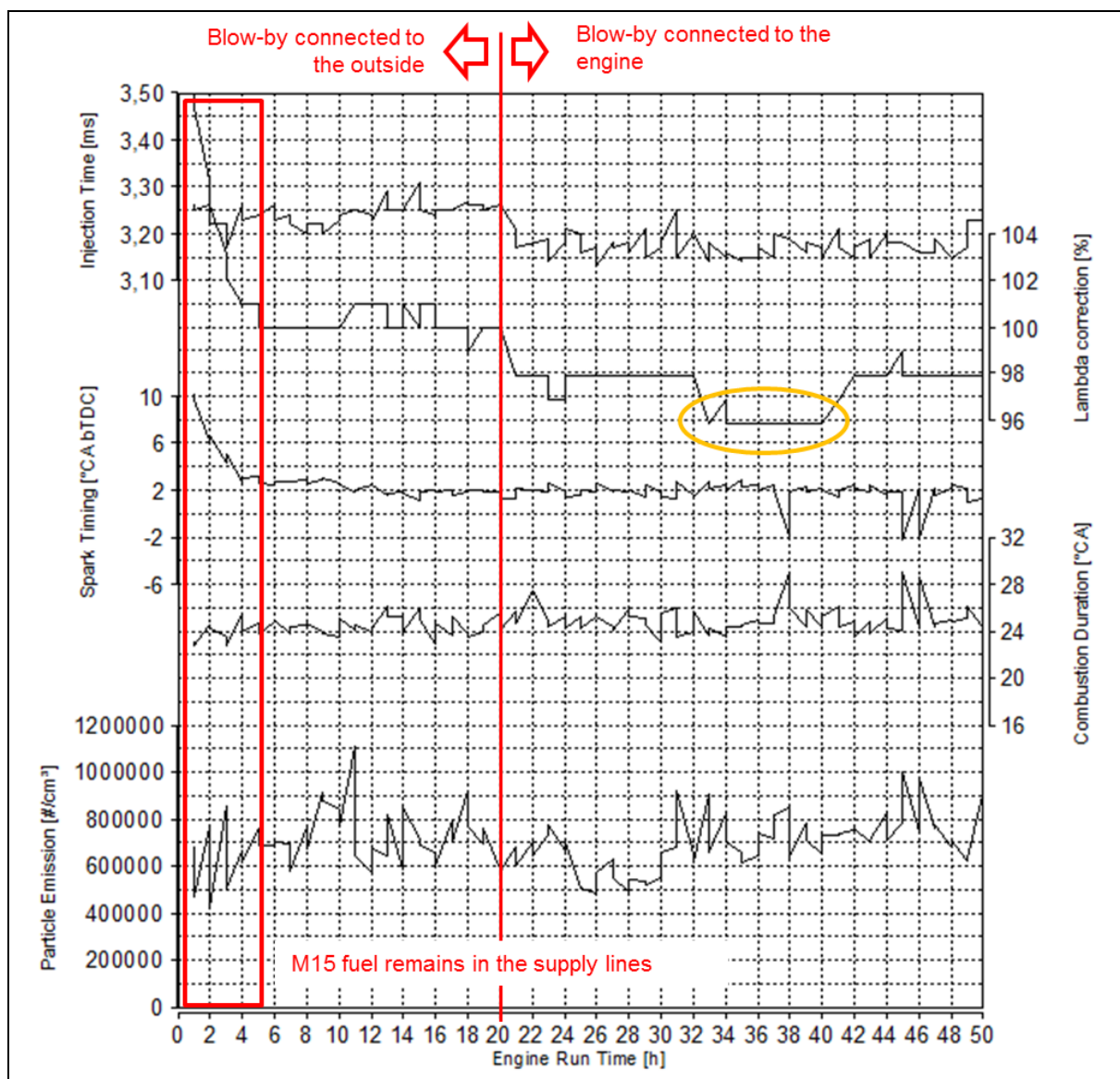


Figure 34: Indian RON 91 @ 2000 rpm / 14 bar BMEP test result

No measurement data is indicating any internal flow reducing or spray altering deposits. External deposits and their influence on PN emissions are evaluated in chapter 3.5 after running another sub-cycle with cleaned injectors.

3.4.4 Shanghai RON 95

The last test run was performed with Shanghai RON 95 fuel from the test bed supply lines. During the test cycle the engine showed an increased knocking behavior which leads to an unstable engine operation. The spark timing in Figure 35 shows a lot of fluctuations indicating knocking events. After severe knocking the spark timing is moved 1° CrA towards the TDC and after preignitions 2° CrA. Despite presenting 30 second average values some of the measurement points show a spark retard of 4 to 8 degree Crank Angle. Furthermore, the average spark timing should be earlier than

the measurements with Shanghai RON 92 (Figure 29) which is at 24°C_{rA} before TDC as this fuel has a higher RON.

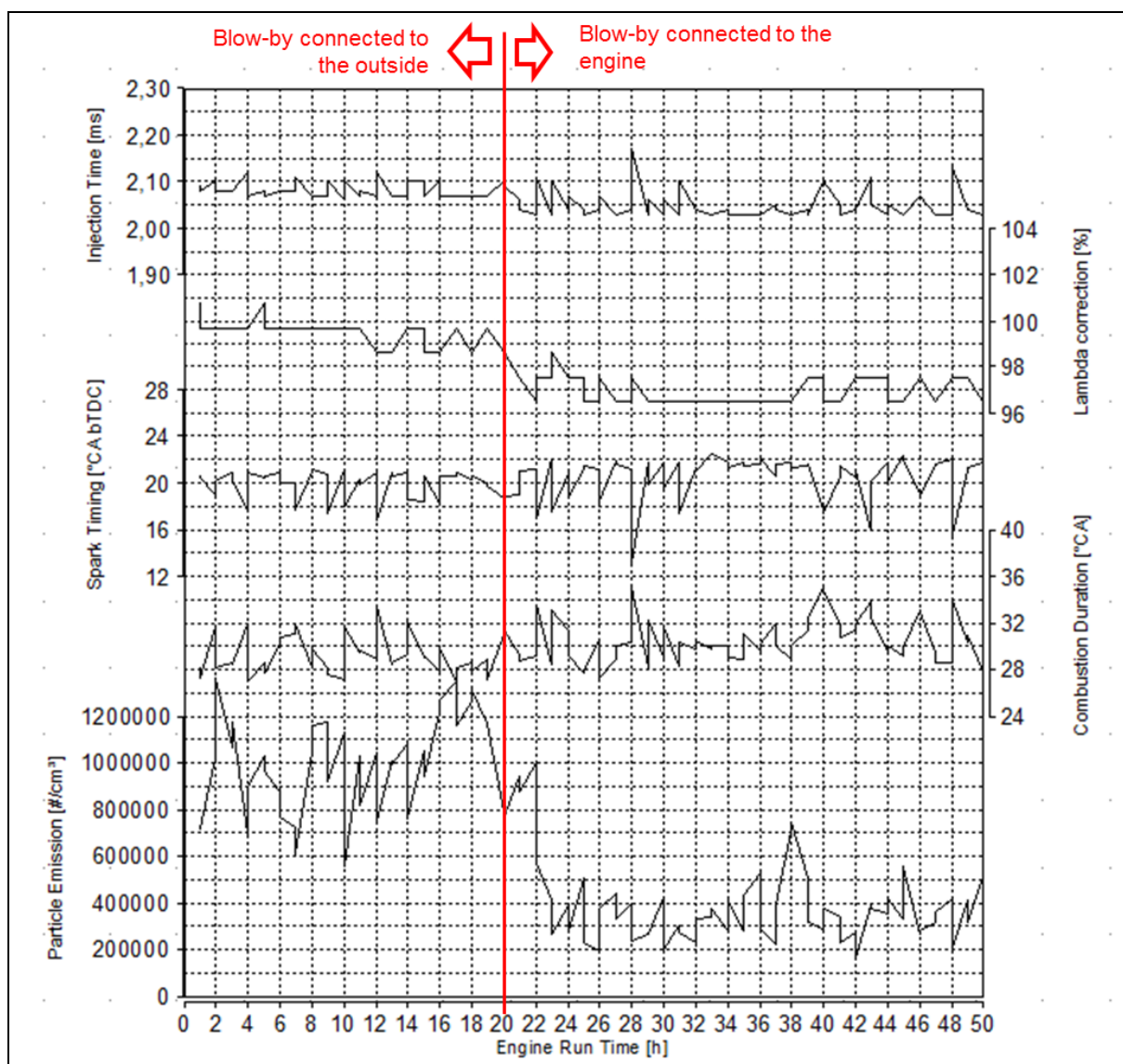


Figure 35: Shanghai RON 95 @ 3000 rpm / 10bar BMEP test result

Despite the heavy fluctuations, the injection time and lambda correction show a constant average value which leads to the conclusion that no internal deposits are present. The PN emissions show no clear trend and drop to the lowest level of all 4 investigated fuels at this operating point after changing the blow by system. If the particle emission is caused by diffusion flames on the injector tip the sudden drop of PN emission can only be explained if the new boundary conditions and the heavy knocking reduce or prevent tip wetting.

At this point the engine was already used for several test cycles, calibration studies and other experiments. The knocking behavior is probably indicating a hardware

problem which alters the test results. During the test several emergency stops were triggered by the knock detection. Due to the unreliability of the test it is not further used for investigation.

3.5 Injector Deposits as PN Source

At the end of the 60 hours test cycle for the Shanghai RON 92 fuel and the 50 hours test cycles for China M15 and Indian RON 91 fuel the injectors were disassembled and investigated. An ultra-sonic bath was used to remove all deposits before reassembling them to the engine. Then another 1 hour sub-cycle was started with the blow-by connection routed to the outside to ensure the same engine conditions as at the start of the test cycle. No other engine parts were modified which allows to link any change in particle emissions to the injector itself.

3.5.1 Shanghai RON 92

Figure 36 shows the injector tips for each cylinder after the 60h test cycle with Shanghai RON 92. All injectors show external deposits on the injector tip covering nearly the whole area. The deposits on injector 1, 2 & 4 are dry and mainly black indicating carbon as main component. Injector 3 has a wet tip which might be a result of an injector needle seat leakage or oil entrainment from a leaking intake valve stem sealing.

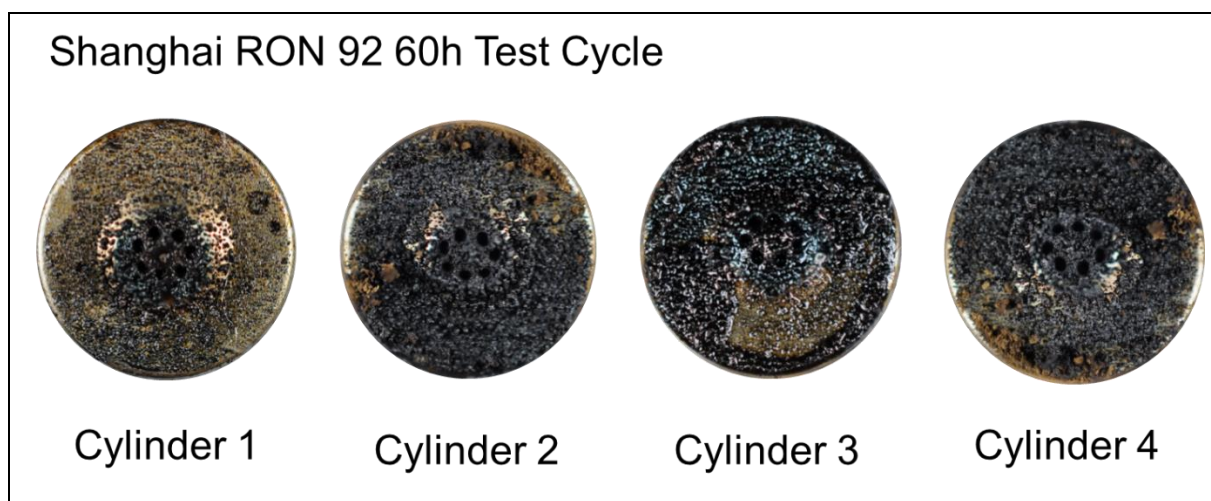


Figure 36: Deposits on Injector Tip after 60h Test Cycle with Shanghai RON 92

As mentioned in chapter 3.4.1 no signs are indicating internal injector deposits. Also, a visual check didn't reveal any suspicious structures inside the nozzle. After cleaning

the injectors, the PN emissions dropped nearly to the initial level of the complete clean engine while the lambda correction is the same as at the end of the cycle (Figure 37).

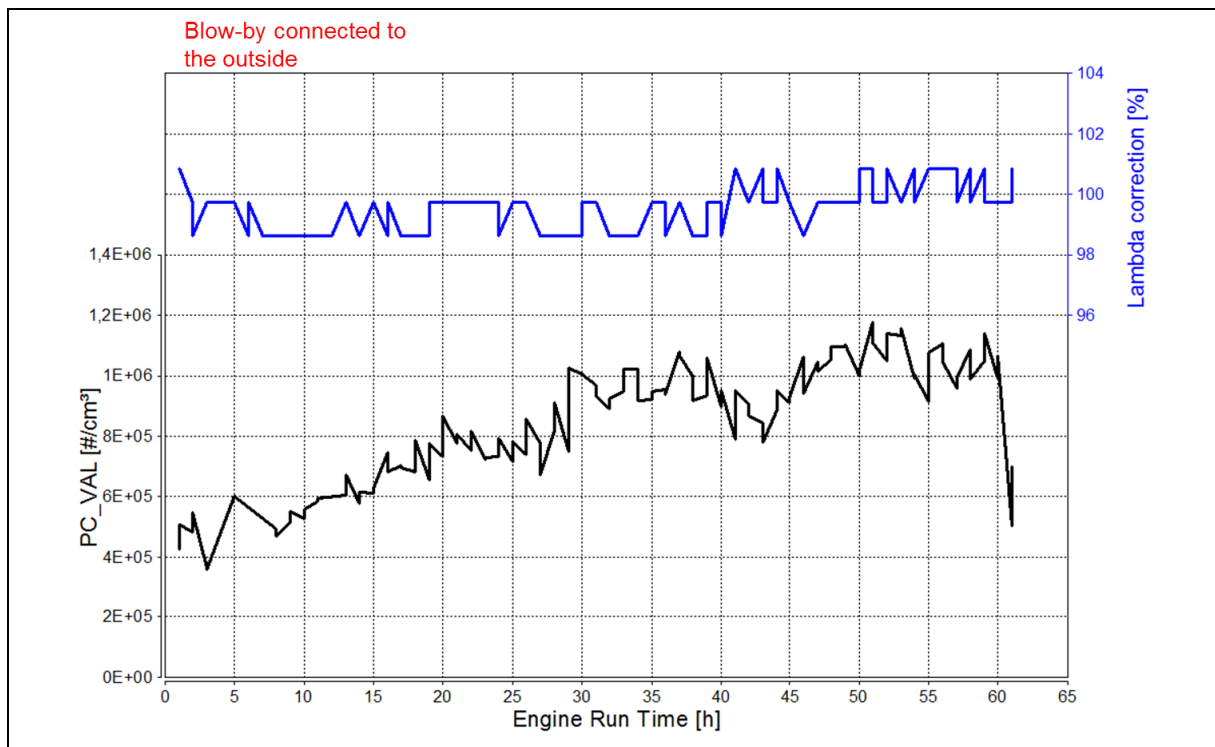


Figure 37: Shanghai RON 92 @ 3000 rpm / 10bar BMEP particle drop after injector

Several conclusions can be drawn from this engine test cycle:

- The coked injectors are the main reason for the nearly 3 times higher particle emissions at the end of the test cycle.
- As no signs indicate internal deposits and the lambda correction is unchanged after cleaning the injectors it can be assumed that there are no flow changing internal deposits present. The increase of particles can be accounted to diffusion flames (tip sooting) on the injector tip due to fuel on the tip and stored inside external deposits.
- The tip sooting is increasing over the test cycle time and seems to stabilize after around 50 hours. This indicates the self-amplifying effect described in [8] and [52].

3.5.2 China M15

The injectors of the 50h test cycle with China M15 were all covered with an oil like fluid which didn't disappear after a 24h drying period (Figure 38). As it is unlikely that all four injectors are leaking or were covered in oil from leaking valve stem sealings and

since the following test cycle with Indian RON 91 produced dry deposits again the oily film is probably made of high boiling components from the fuel itself.

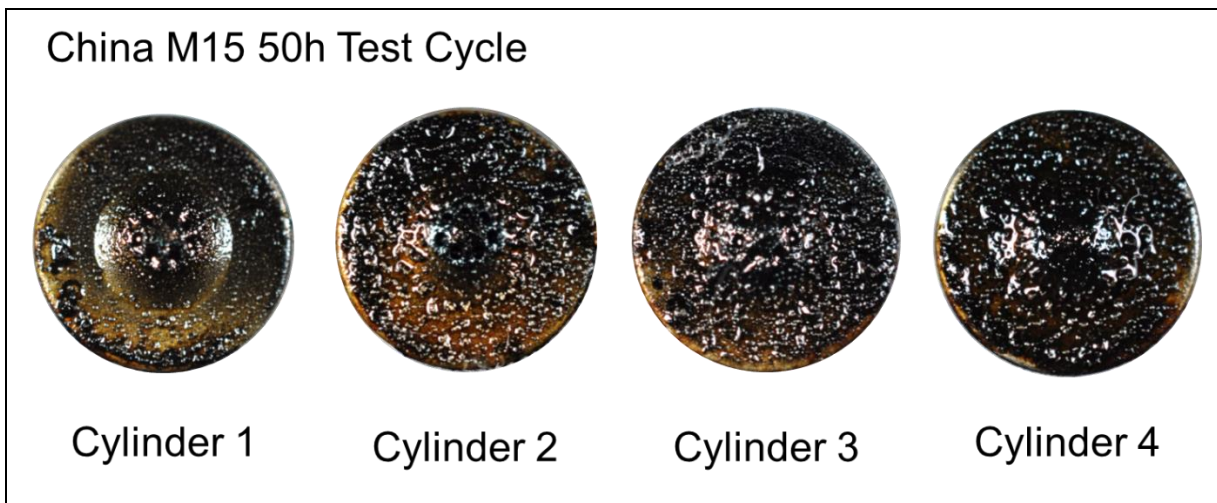


Figure 38: Deposits on Injector Tip after 50h Test Cycle with China M15

There are less solid deposits on the injector tip compared to the Shanghai RON 92 fuel but some of the deposits were growing inside the nozzle which matches with the observed increase of injection time and lambda compensation. The sub-cycle after cleaning the injectors shows a drop of the lambda correction back to the initial level as shown in Figure 39. The PN emissions also drop around 30% at the beginning of the 3000 rpm / 10 bar operating point (red dot). However, 7 minutes later at the end of the operating point the PN emission is back at the old high level.

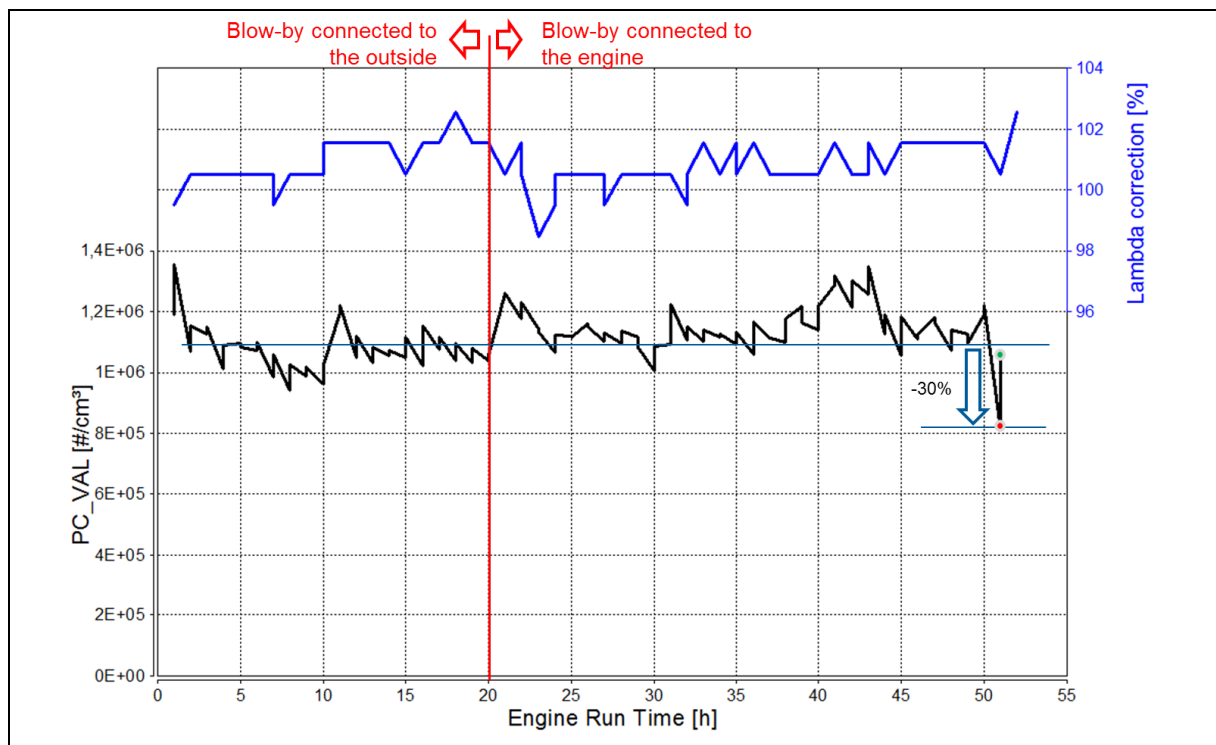


Figure 39: China M15 91 @ 3000 rpm / 10bar BMEP particle drop after injector cleaning

This behavior would indicate a very fast stabilization time as the engine was only operated for 40 minutes after cleaning the injectors which is significantly faster than the 50 hours in the previous test. On the other hand, the measurements done in [52] seem to be stabilized after only 15 minutes engine operation at a constant load point.

Following conclusions are drawn from this test:

- Injector deposits or tip wetting cause at least a 40% increase of PN emission in a very short time
- The change of injection time and lambda correction indicates internal deposits which could be responsible for a part of the PN increment
- Considering the condition of the injectors after disassembling them it is more likely that the high amount of wallfilm on the tip causes sooting flames which are responsible for the high PN emissions. Due to the amount of liquid fuel deposits have trouble to stick to the injector before the get washed away which would explain the reduced amount of solid deposits and the lack of or a very short self-amplifying effect.

3.5.3 Indian RON 91

The injectors from the Indian RON 91 50h test look similar to the test run with Shanghai RON 92. All four injectors are covered with mostly black carbon deposits on the injector

tip and partly in the counter-bores. The brown substance on injector 1 in Figure 40 are powder like residuals from the gap between cylinder head and injector and were pushed on the injector during disassembly. They can be removed easily with air or shaking and are therefore not counted to the injector deposits and have not been further investigated. The injector 2 and 4 from the Shanghai RON 92 test show traces of the same substance.

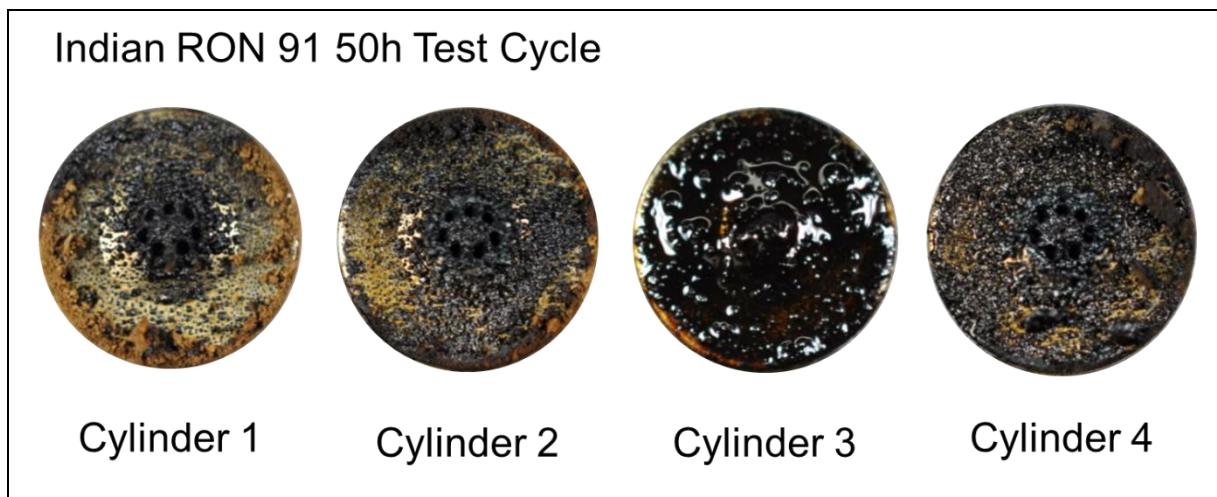


Figure 40: Deposits on Injector Tip after 50h Test Cycle with Indian RON 91

The injector from cylinder 3 also has a wet tip like the Shanghai RON 92 test. As the same injectors are installed for all test cycles in the same cylinder and the intake valve stem seals are replaced for every new cycle it can be assumed that indeed injector needle seat leakage is the reason for the increased wetting. The optical investigation showed no traces of internal deposits which is in line with injection time and lambda correction behavior during the test cycle.

Running the last sub-cycle with cleaned injectors resulted in an over 50% drop of PN emissions as shown in Figure 41. The lambda correction went back to the same initial values after the remaining M15 fuel was removed from the fuel supply lines. The orange circle marks the 10h cycle block which was run with a damaged intake manifold pressure sensor which only affected calculated injection time and lambda correction but not the real injection time (see chapter 3.4.3).

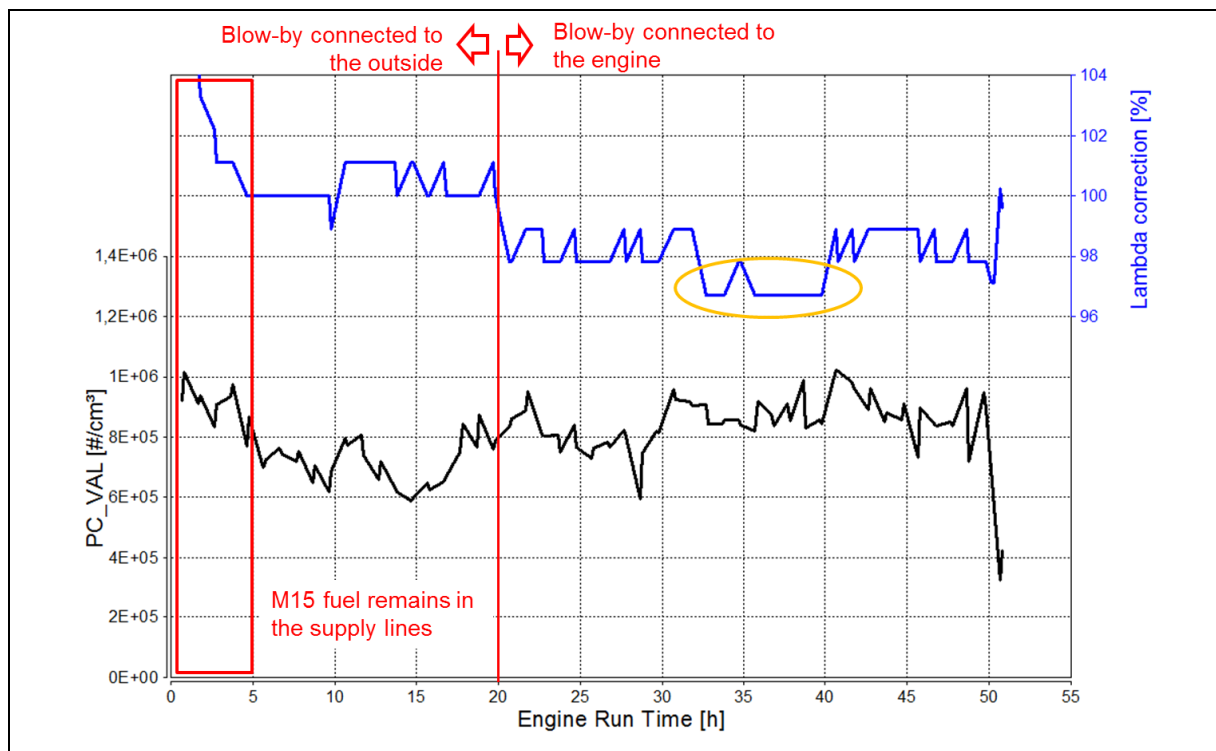


Figure 41: Indian RON 91 @ 3000 rpm / 10bar BMEP particle drop after injector cleaning

After the remaining M15 fuel was consumed the PN emissions staid at a constant level until the change of the blow-by system which indicates an already stable injector condition. The M15 fuel has probably accelerated the deposit build-up process. However, external deposits themselves don't increase the PN emission but the fuel stored inside them after every injection. The observed PN emission level after stabilization should be in the same range of a stable injector which was operated with the same fuel from the beginning. Based on the observations following conclusions are drawn:

- Injector deposits in combination with wall wetting caused an over 100% increase of particle emissions
- As no signs of internal deposits were found the increase can be accounted to the fuel wallfilm stored on the tip and inside the external deposits causing diffusion flames.
- The self-amplifying effect until stabilization couldn't be observed due to the M15 contamination. However, as the start and the end of the operating point after cleaning both show a low PN emission level it can be assumed that it would take at least several hours with just Indian RON 91 fuel.

4 Simulation Assumptions

The results from the engine test cycles showed that the injector is responsible for the major part of the increased particle emissions. The target of the following chapters is to accurately simulate the injector in AVL FIRE based on the engine hardware to understand and improve the coking and tip sooting conditions.

4.1 Deposits Model Assumption

While the injectors of the Shanghai RON 92 and Indian RON 91 tests had no flow rate altering (internal) deposits the M15 test resulted in around 3% longer injection duration after 50 hours. The reasons for the non-existing or only minor internal deposits are possible the high fuel pressure (see chapter 2.1.2) and optimized nozzle geometry which reduced the amount of fuel in the nozzle after an injection event. Additionally, improved fuel quality leads to less deposit precursors like metals or sulfur in the fuel which are required for deposit build-up in the nozzle according to the model by Kinoshita et al. [28]. It is assumed that for this engine internal injector deposits only play a minor role.

As described in chapter 2.2.2 fuel on the injector tip and in the counter-bores will lead to high sooting flames which increase the PN emission. During the Shanghai RON 92 and Indian RON 91 test external deposits built up which were able to store more fuel leading to high PN levels. The injectors of the M15 test showed such high amounts of fuel on the tip that no stabilization phase was observed and the PN emission exceeded the stabilized levels of the other two tests.

As mentioned before, the target must be to reduce the amount of fuel on the injector tip and counter-bores after injection and improve the evaporation of it before the flame reaches the injector during combustion. The fuel film which builds up on the injector during injection and evaporates afterwards will be simulated using the AVL FIRE Wallfilm module. Simulation variations will be performed to define counter-measures to minimize the wallfilm and optimize future engine developments.

4.2 Wallfilm Module

The AVL FIRE Wallfilm module was initially developed to simulate the liquid fuel film inside an intake manifold for port fuel injected gasoline engines. Today it is also used for Gasoline DI and Diesel engines to predict the fuel film on the piston and cylinder liners. However, up to now there are no report that it has been used to simulate the formation of fuel film on an injector during injection. Only a few cases are known where the model was used to evaluate the evaporation of a predefined single-component

wallfilm after end of injection (e.g. [53]). The main reasons are that until a few years back the injector area was of less interest in a cylinder simulation and the standard engine simulation only considers the injector as a point source for fuel without modeling the geometry. Additionally, the commonly used hexagon mesh has troubles to simulate very small areas like injector holes compared to the overall size of an engine cylinder.

According to the wallfilm model manual [58] the following fundamental assumptions and modeling approaches are used:

- Gas and wall film flow are treated as separate single phases. So this is not a complete two-phase model but rather two single phase models attached at the film surface. The coupling of the two phases is achieved by a modified set of boundary conditions based on semi-empirical relations.
- The film thickness is very small in relation to the mean diameter of the gas flow. Therefore, no adaptation of the volume grid to the film surface is necessary.
- The wavy surface of the film is not simulated in detail but modeled by a mean film thickness with a superimposed film roughness.
- The mean film surface is assumed to be parallel to the solid wall.
- The above assumptions lead to an implementation of the wall film model as 2D finite volume method on the wall boundaries of the air flow geometry.
- Due to thin film and its small velocity, wall friction and interfacial shear stress dominate the film behavior as compared to inertial forces and lateral shear. For these conditions, only a momentum equation can be dropped.
- Wall temperature is below Leidenfrost point.

During the simulation, the wallfilm is formed by impingement of spray droplets and reduced again by evaporation and entrainment. The standard physical model for wallfilm formation in gasoline engines is an advanced wallfilm interaction model by Kuhnke [59]. It uses a dimensionless temperature T^* which increases with wall temperature and a dimensionless droplet velocity K . T^* is defined as the Ratio between the wall temperature (T_w) and the saturation temperature (T_{sat}) of the droplet fluid:

$$T^* = \frac{T_w}{T_{sat}} \quad (4.1)$$

The K number combines both the dimensionless drop velocity, represented by the Capillary number (Ca) and the dimensionless drop size which is described by the Laplace number (La) in one dimensionless variable:

$$K = Ca^{5/4} La^{3/4} = \frac{(\rho d)^{3/4} * u^{5/4}}{\sigma^{1/2} * \mu^{1/4}} \quad (4.2)$$

with
$$Ca = \frac{u * \mu}{\sigma} \quad (4.3)$$

and
$$La = \frac{\rho * \sigma * d}{\mu^2} \quad (4.4)$$

K increases with the drop density (ρ), drop diameter (d) and drop velocity (u) while it decreases with higher drop surface tension (σ) and higher dynamic viscosity (μ). Figure 42 shows the four possible reactions of a spray droplet hitting a wall. High wall temperatures result in a rebound or thermal breakup effect without film formation. At lower temperatures, the fuel droplet is partially or completely converted into wallfilm.

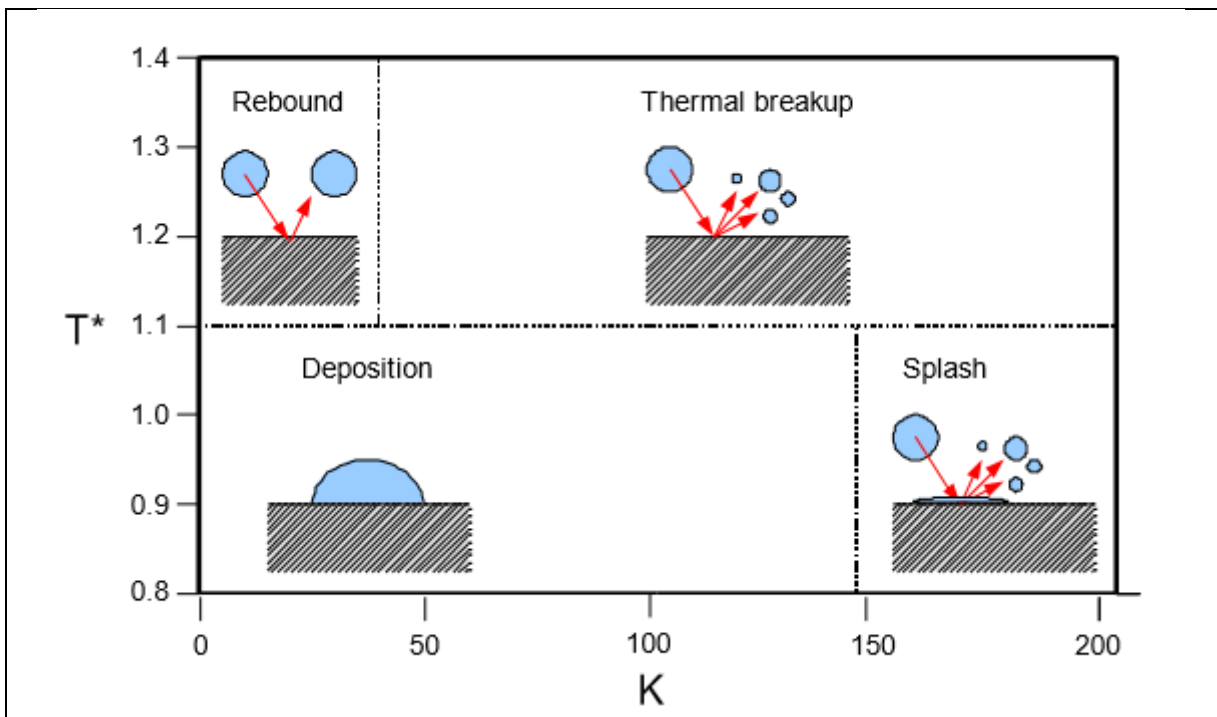


Figure 42: Spray/Wall Interaction based on dimensionless wall temperature (T^*) and droplet velocity (K) according to Kuhnke [59]

The evaporation rate of the wallfilm is calculated using the Sill [60]-Himmelsbach [61]-Model using the formula:

$$\dot{m} = -\rho_v u_{//} St_m \frac{c - c_l}{1 - c_l} \quad (4.5)$$

The formula includes the dimensionless Stanton number for mass transfer (St_m) which is used to model the mass transfer directly at the film surface which is normally not resolved by the computational grid:

$$St_m = \frac{\eta * c_f}{Sc_t * (1 + P_m * \sqrt{\eta * c_f})} \quad (4.6)$$

It is based on the dimensionless local friction factor c_f which is defined as:

$$c_f = \frac{\tau_w}{\rho * u_{//}^2} = \frac{u_\tau^2}{u_{//}^2} \text{ with } u_\tau = \sqrt{\frac{\tau_w}{\rho}} \quad (4.7)$$

where τ_w is the wall shear stress on the wallfilm surface caused by the gas flow over the wallfilm $u_{//}$ and u_τ the resulting shear velocity. The correction factor η is used to consider the wavy (rough) film surface [61] while the correction factor P_m simulates the influence of the laminar sublayer on the total mass transfer on rough surfaces [62]. The turbulent Schmidt number Sc_t is fixed to 0.9 for this model.

Based on equation (4.5) and (4.6) the evaporation rate \dot{m} is mainly depending on the gas velocity parallel to the wall ($u_{//}$) and the difference between the fuel concentration in the gas phase (c) and the fuel vapor concentration at the film surface (c_i). The vapor concentration at the film surface is depending on the saturation pressure which is a function of the fluid temperature.

Based on the concentration gradient in (4.5) the film can only evaporate if the concentration of fuel vapor at the film surface (c_i) is higher than in the gas around (c). A better charge air motion in the cylinder will transport the fuel vapor away from the injector niche and decreases the c which increases the evaporation rate. A higher wallfilm temperature increases c_i which improves the evaporation exponentially.

The velocity $u_{//}$ is the gas velocity parallel to the wall in the first internal cell in the mesh. This approach works well for standard cell sizes at the wall in engine simulations which are around 1mm high. However much smaller cells with only a few microns are needed to model the geometry of the injector and injector holes. As a result, the gas velocity at e.g. 10 μ m distance from the wall is used to calculate the evaporation and wall shear force even if the wallfilm is much thicker. As the flow velocity decreases with smaller distance to the wall due to the boundary layer the parallel gas velocity in the first small cell can be a lot smaller than the velocity at the film surface leading to a reduced evaporation rate.

AVL Fire switches to a diffusion model to simulate the evaporation if the velocities are small which calculates the evaporation independent from the gas velocity. While this works well at low Reynold number flows this model underestimates the evaporation at higher flow velocities. A combined model switches between the calculation methods based on the local velocity regimes. However, at in-cylinder conditions with high velocities but small cell sizes both models will underestimate the evaporation rate.

The second effect which reduces wallfilm is the entrainment due to high shear forces. The model calculates an entrainment mass flux first and then generates droplets out

of it which are reintroduced into the gas flow. During the following simulations, the Schadel-Hanratty Model is used which calculates a critical Weber number based on:

$$We_{cr,SH} = \frac{\rho_g u_{rel}^2 \delta}{\sigma} \quad (4.8)$$

AVL FIRE uses a threshold for the Weber number of $We_{cr} = 17$ after which the first droplets start to entrain. The entrainment rate therefore depends mainly on the relative velocity (u_{rel}), on the film thickness (δ) and surface tension (σ). The relative velocity is defined as the difference between the parallel gas velocity in the third cell layer from the wall and the film velocity. This simplification of defining the mean gas velocity works well for standard use cases however, similar to the evaporation rate it will underestimate the entrainment due to the smaller cell sizes. One reason is the low gas velocity even in the third cell from the wall when using 10 μ m cells compared to 1mm cells. The second reason is that wallfilm in the counter-bores won't be affected by the passing fuel stream if it is further away than 3 cells which is likely, considering a 360 μ m counter-bore diameter and cells of 10 μ m size or even smaller.

Based on the described wallfilm formation and reduction models it is expected that the formation rate can be simulated accurately while the reduction rate will be underestimated in the simulation. If all simulation variants use the same model parameters and meshes the reduction rate can still be used to evaluate trends. However, temperature variations might have a bigger effect on the evaporation rate in the simulation compared to gas velocity variations as wall temperature is independent from cell size.

4.3 Simulation Work Flow

The simulation work is split in three parts. First the injector will be simulated using a Euler Multiphase simulation to accurately assess the flow conditions inside the nozzle which have an influence on the tip wetting as described in chapter 2.2.2. The simulation helps to understand the influence of different fuel pressure and creates so called "nozzle-files" which are used as input for the following simulations. Flow rate measurements are used to verify this simulation.

The second step is a Lagrangian spray simulation coupled with the described wallfilm model using a spray box geometry. This simulation is used to visualize the spray development during injection as well as the wallfilm formation on the injector tip. Both results are compared to measurements to calibrate the spray break up model and verify the wallfilm model which hasn't been used for injector tip wetting before.

Additionally, a good relation between simulation and measurement also confirms the nozzle-files from the first simulation step.

In the last step one cylinder of the engine described in chapter 3 is simulated in one of the tested operating points for a full four-stroke cycle. During the simulation, the nozzle files from the first step are used together with the calibrated and verified spray and wallfilm models from the second step. The result of the simulation is the formation and reduction of a fuel wallfilm on the injector for different engine boundaries.

5 Injector Simulation

The following chapter describes the Euler Multiphase Injector Simulation. This simulation is used as base input for the spray and cylinder simulation. Results from this simulation include cavitation, distribution of fuel inside the nozzle and local velocity and turbulences.

5.1 Measurement Inputs

The available inputs for the simulation are described below.

5.1.1 X-Ray Images

The investigated HDEV5 Injector was available in hardware however no detailed 3D data could be obtained. Therefore, the injector has been scanned by a service provider using a Phoenix X-Ray machine by scanning planes in different depth and stacking them. An example of a measurement setup is shown in Figure 43. The result is a volume cloud which gets translated into STL format with an accuracy of $5\mu\text{m}$ (Figure 44). The advantage of this approach compared to mechanically opening the hardware and measuring the dimensions is the non-destructive imaging as well as having the geometry directly available in CAD for further use.

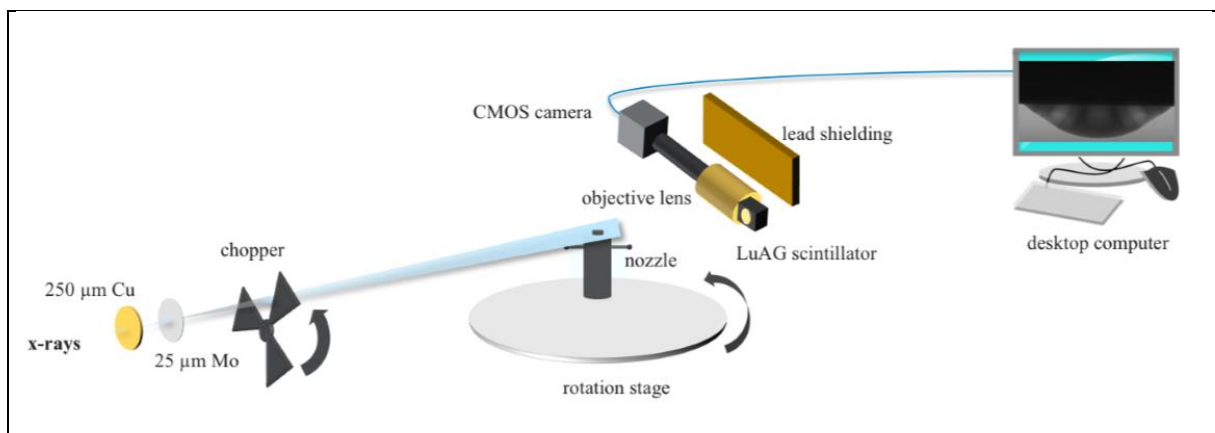


Figure 43: Schematic of the experimental setup used for nozzle tomography measurements [63]



Figure 44: Injector STL File converted from X-Ray

The resulting geometry is accurate enough to be used as input for the injector simulation as the resolution is much smaller than the hole diameter. To be used in the simulation the surface needs to be converted into the fluid volume with a separation between the needle and the injector body. The separation has been done using Catia V5 as CAD program. A cut through the STL file shows that due to the closed needle the X-Ray couldn't distinguish between seat and needle. Using the available needle head surface, the outline of the needle can be extrapolated and cut from the injector seat (Figure 45). However, the geometry of the nozzle hole entry (red circle) had to be assumed as it was not visible in the X-ray. For the first simulations, the entry has been designed with a sharp edge.

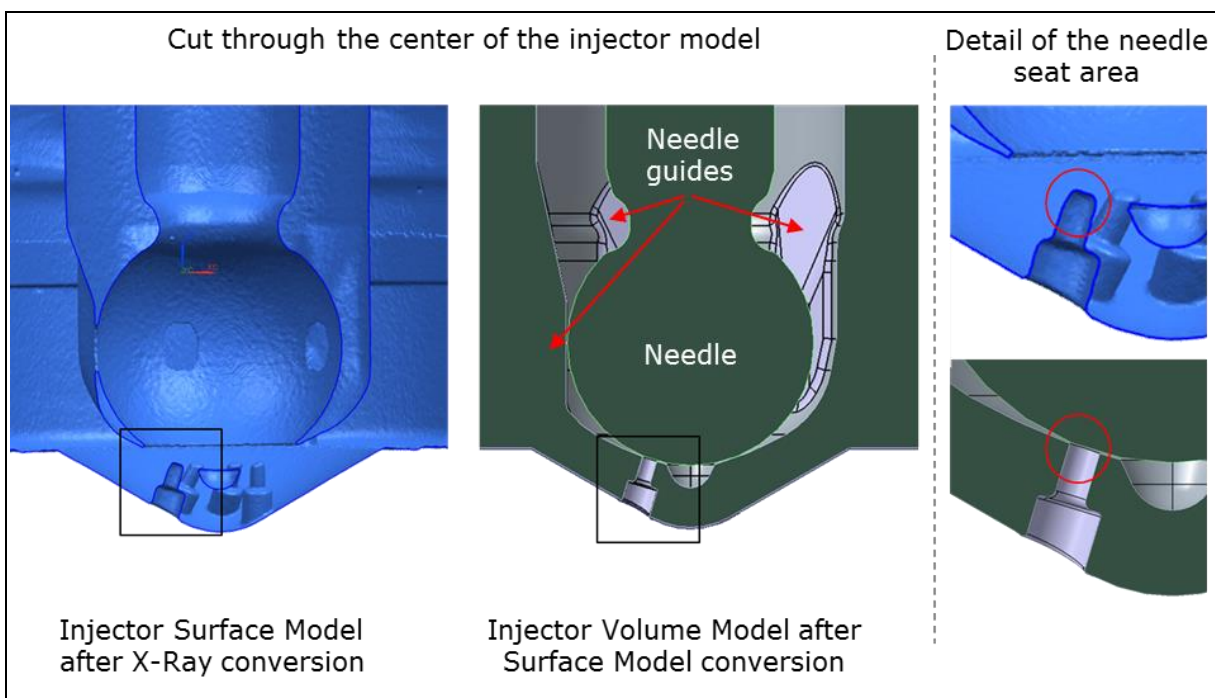


Figure 45: Cut through the injector geometry before (left) and after conversion in a CAD program

5.1.2 Cut Injector

After all measurements have been done with the selected injectors one unit has been cut open to investigate the exact hole geometry. Figure 46 shows the entry into the holes in detail after moving the needle a little. The upper hole entry (red circle) clearly shows a rounded edge while the lower hole entry is much sharper. It is assumed that the rounded edge is a result of the hole machining or happens during calibration of the requested massflow with abrasive particles.

As the cut was only available at a later phase in the project both variants, sharp and round entry are simulated and compared in the following simulation.

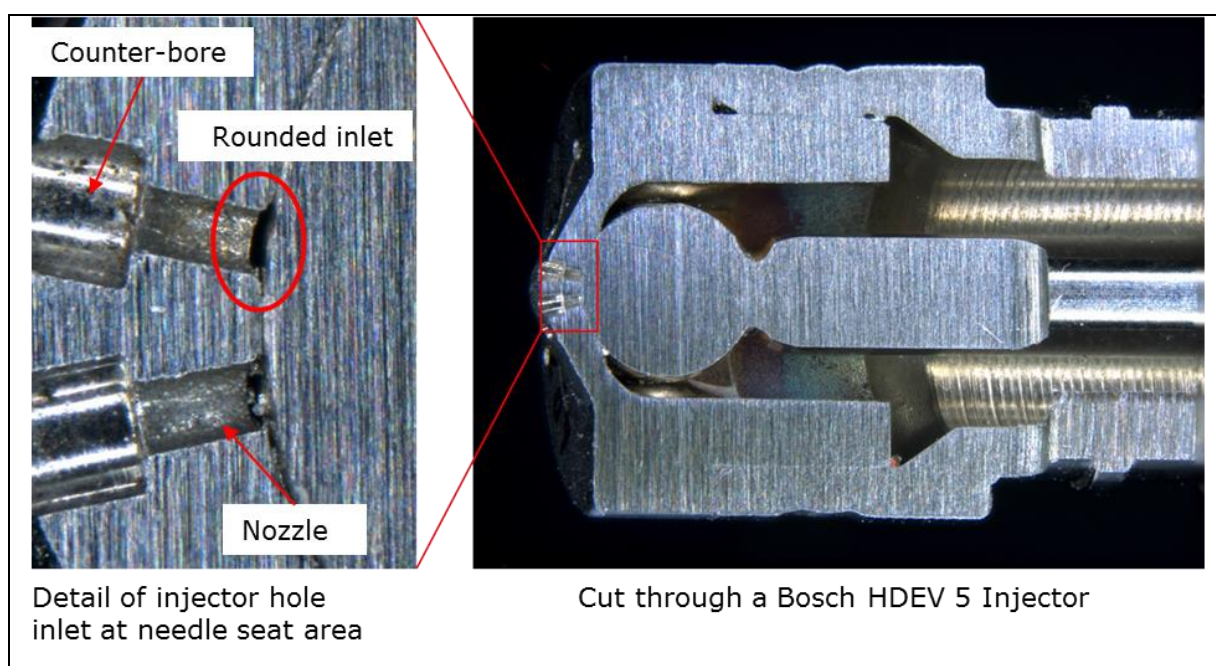


Figure 46: Injector cut along needle

5.1.3 Massflow Measurement

During the engine test cycle, several injection related parameters have been recorded like injection start, injection signal duration and fuel pressure. Additionally, the total fuel mass injected is needed for the correct combustion simulation. Several fuel pressures and injection times have been measured on the AVL injector flow bench () while recording actuation current and massflow rate. N-Heptane has been used as fuel for the injections listed in Table 4.

Table 4: Injector massflow measurement variations

Number #	Fuel Pressure [bar]	Signal Duration [ms]	Injected Mass [mg]
1	50	1	8.01
2	70	1	9.53
3	100	3.2	38.00
4	110	2.1	26.20
5	150	2.1	30.56
6	200	2.0	33.03

An example of the resulting measurement curves can be seen in Figure 47. Integrating the injection rate leads to the requested total injected mass. In addition, the delay between signal start and injection start as well as the closing duration after signal end can be found in the diagram. The opening delay is around 0.3ms while the closing takes 0.4ms. The measured injection rate can also be used to calibrate the needle lift curve described in chapter 5.1.4.

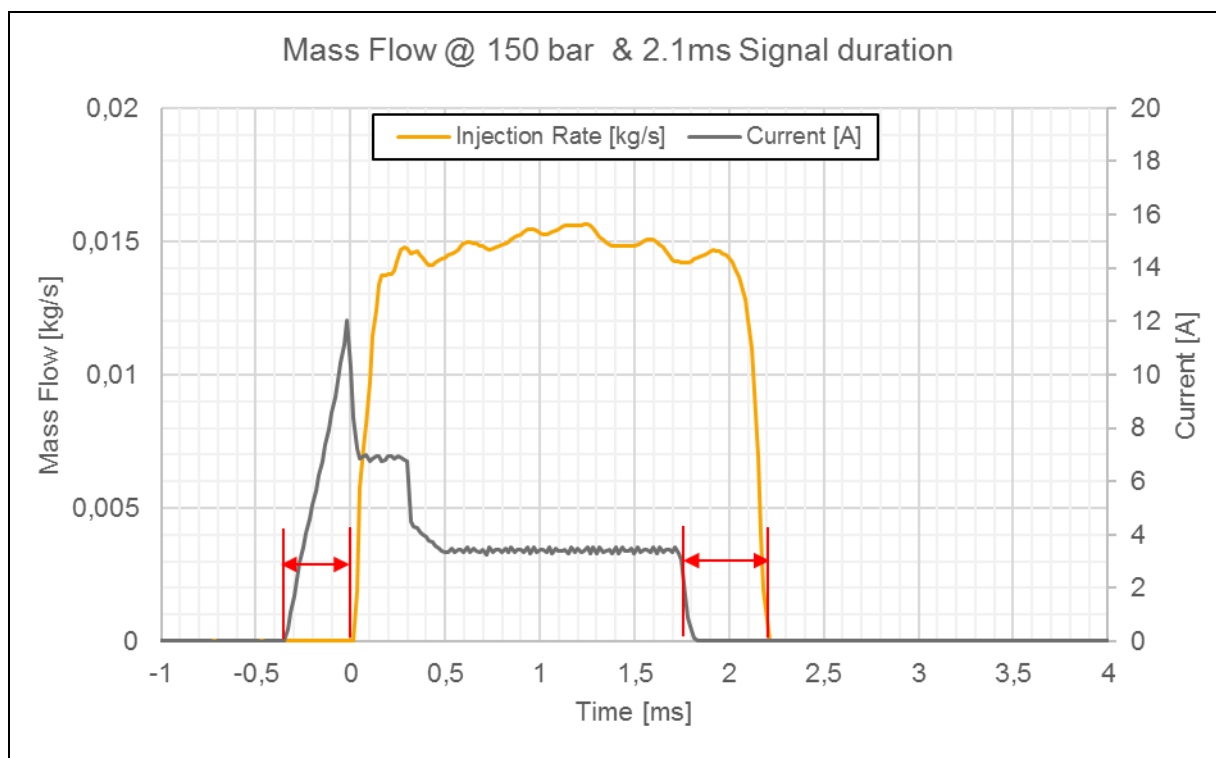


Figure 47: Measured injection rate and signal current for 2.1ms signal duration @ 150bar

5.1.4 Needle Lift

To accurately simulate the injection rate and velocities in the injector it is necessary to define an injector needle lift which matches closely to the real hardware. There are several ways to define the lift curve such as measuring the needle movement under X-Ray, receiving the curve from the injector supplier or estimating it based on the measured mass flow.

Receiving a curve from the supplier would be the fastest and most accurate way however this is not possible in most cases due to IP issues. Measuring the curve under X-Ray as shown in [64] is complex and was not possible in this project. The X-Ray supplier was not able to actuate the injector under X-Ray.

For the following simulations, a combined approach has been used by calibrating an existing needle lift curve from the supplier (Figure 48) with the measured mass flow.

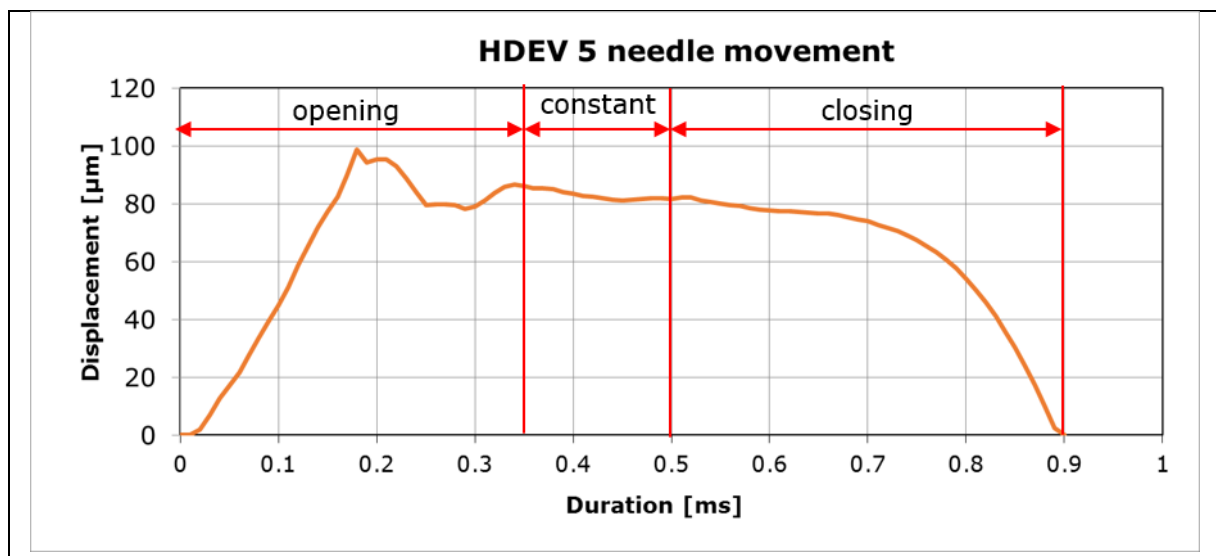


Figure 48: example of a Bosch HDEV5 needle lift curve

The shape of the curve will be kept while the displacement and duration will be scaled according to mass flow and signal duration. The overshoot during opening can also be observed in [64] which uses a very similar injector with lower needle lift.

Based on the massflow measurements from chapter 5.1.3 the curve is split into 4 parts – opening delay, opening, constant and closing phase. After the injection signal starts there is a delay of 0.3ms followed by 0.35ms opening phase. The constant part will be stretched until end of the signal duration followed by the 0.4ms closing phase. By multiplying the displacement with a factor, the lift curve can be scaled to match the measured mass flow rate.

Figure 49 shows an example for a stretched lift curve with 2.1ms signal duration and a scale factor of 0.6.

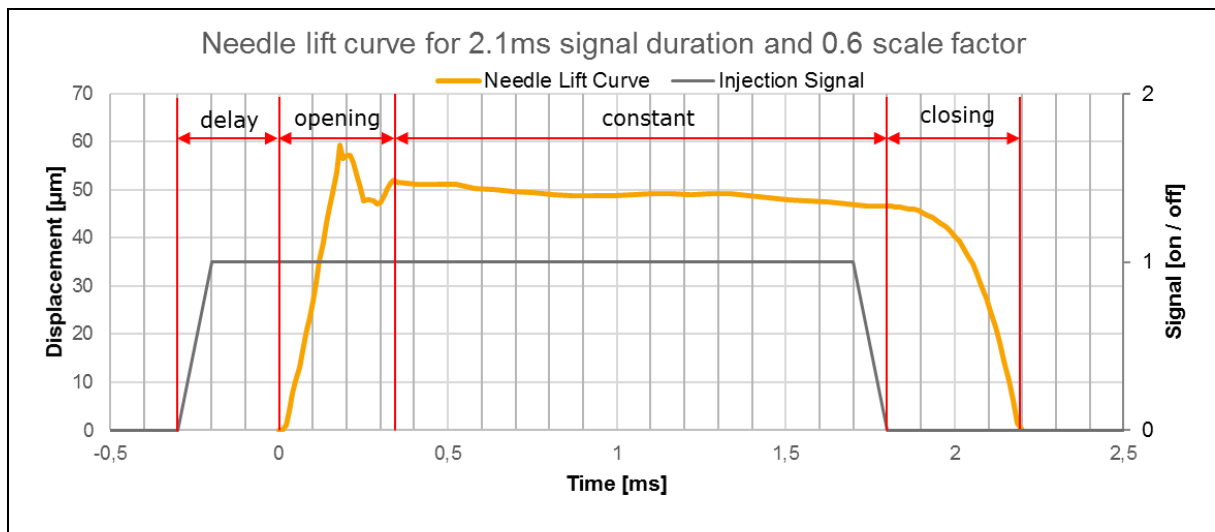


Figure 49: Scaled and stretched needle lift curve for 2.1ms signal duration

5.2 Model description and boundaries

The injector has been meshed using AVL FIRE M's Interactive Mesher while the multiphase simulation has been run in FIRE 2014.2. Further details about the simulation models and properties can be found in [65].

5.2.1 Mesh Setup

Before meshing, the 3D model was inverted to reflect the fluid area inside the injector. The 5 needle guides have been removed to improve the mesh quality as the small area between guides and needle would create distorted cells. The mesh itself was created in Fire M as a structured hexagonal mesh where the cells are aligned in nozzle direction for better convergence. A cut through nozzle #2 can be seen in Figure 50 in detail. As the transition from seat to the nozzle is critical for the flow inside the nozzle this area has been modeled with a very high resolution.

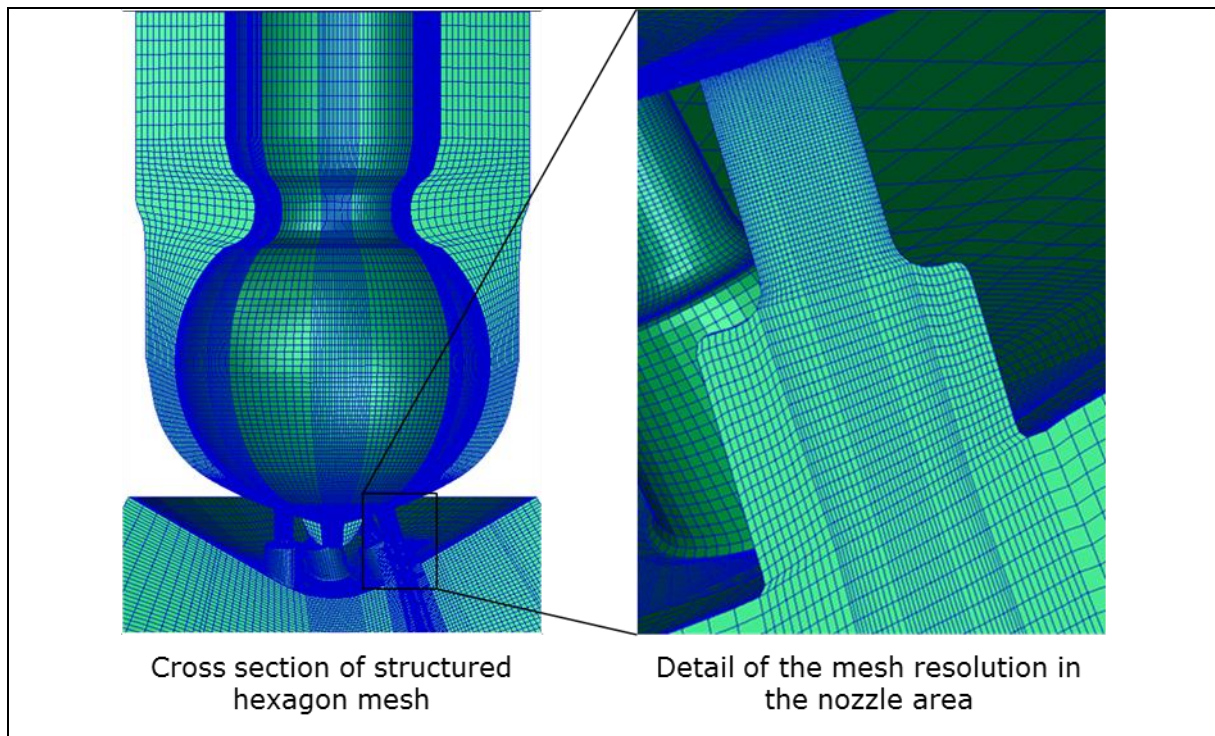


Figure 50: Structural Hexagon Injector Mesh

Every simulation consists of a full injection cycle starting from needle opening and finishing after needle closing. The number of cells stays the same during injection and the needle movement is realized by moving the needle surface upwards following the define lift curves while stretching the cells in the seat area. Outside the injector, a discharge volume is designed. Further details can be found in Table 5.

Table 5: Injector Mesh Data

Number of cells	3.24 Mio Cells (sharp edge),
Min / max cell size	~1 μ m to 0.5mm
Simulation steps	0.0001 to 1°CrA (360°CrA for closed to closed)
Simulation results	Cavitation, Local fuel distribution in the nozzle, velocities vectors in measurement plane, massflow

5.2.1.1 Sharp edge

Based on the 3D input after X-Ray conversion the step from the injector seat to the nozzle has been designed as a sharp edge in first simulation runs. Figure 51 shows the edge in detail with small cells in the seat area and nozzle. It is expected that the

fluid will separate from the wall while entering the nozzle – the small cells help simulating the stream accurately.

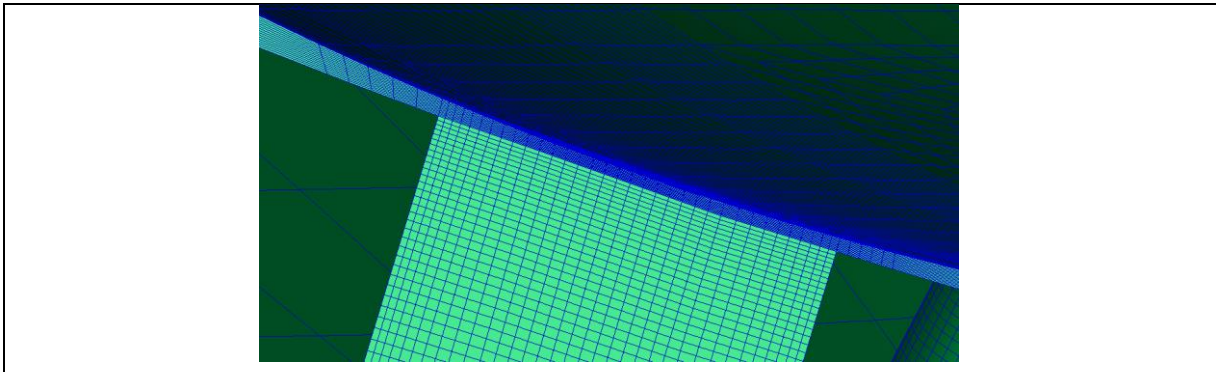


Figure 51: Sharp edge between injector seat and nozzle

5.2.1.2 Round edge

As described in chapter 5.1.2 the injector shows a rounded edge in the seat area after opening it. To investigate the influence of the edge design on fuel distribution and velocity the mesh has been adapted to reflect this geometry by adding a radius of $20\mu\text{m}$. The number of cells in the nozzle have been kept the same by stretching the outside layers to follow the curvature. In the seat area around the nozzle the cells have been made smaller to allow the stream to follow the wall in the simulation.

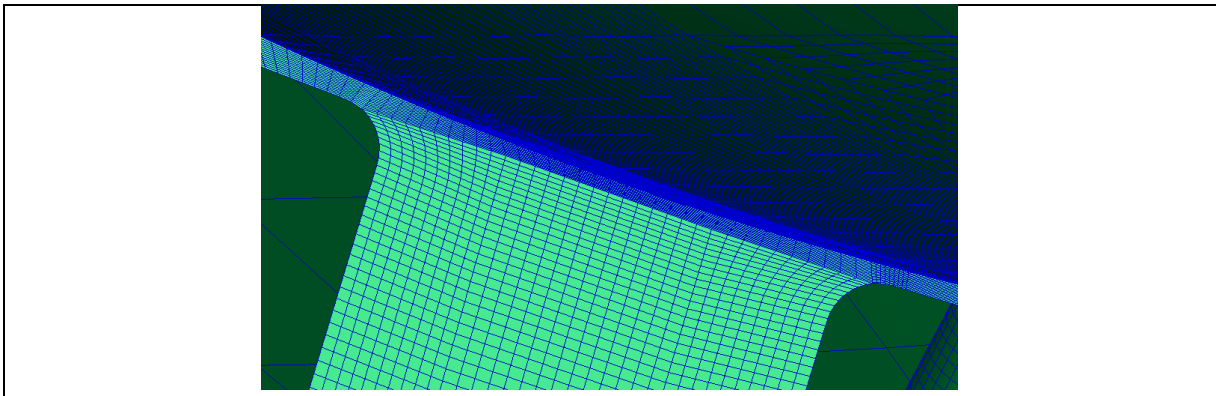


Figure 52: Rounded edge ($r=20\ \mu\text{m}$) between injector seat and nozzle

5.2.2 Boundaries and Simulation Setup

The injector simulation is a Euler multiphase simulation consisting of at least 3 different phases. In case of a single component fuel like n-Heptane or Iso-Octane the first phase is the liquid fuel, the second phase represents the vapor and the third phase is the air in the discharge volume. To simulate a fuel consisting of 3 different components the simulation is set up with 7 phases – 3 liquid, 3 corresponding vapor and 1 air phase.

Two different sets of simulations have been performed:

- Simulation with n-Heptane at 20°C system temperature to compare massflow and spray with the flow bench measurements and to calibrate the break up model
- Simulation with Iso-Octane and Multi-Component fuel at real engine environment conditions as input for the wallfilm and cylinder simulation

For the first set all wall temperatures and the phase temperatures are set to 20°C which represents the conditions at the flow bench during spray measurements. For the second set the initial wall temperatures can be found in Figure 53 for the standard engine setup which are estimated based on fuel temperature (50°C), engine coolant temperature and a typical injector tip temperature (150°C). The inlet pressure is set up according to the rail pressure of each variant according to Table 6 and Table 7.

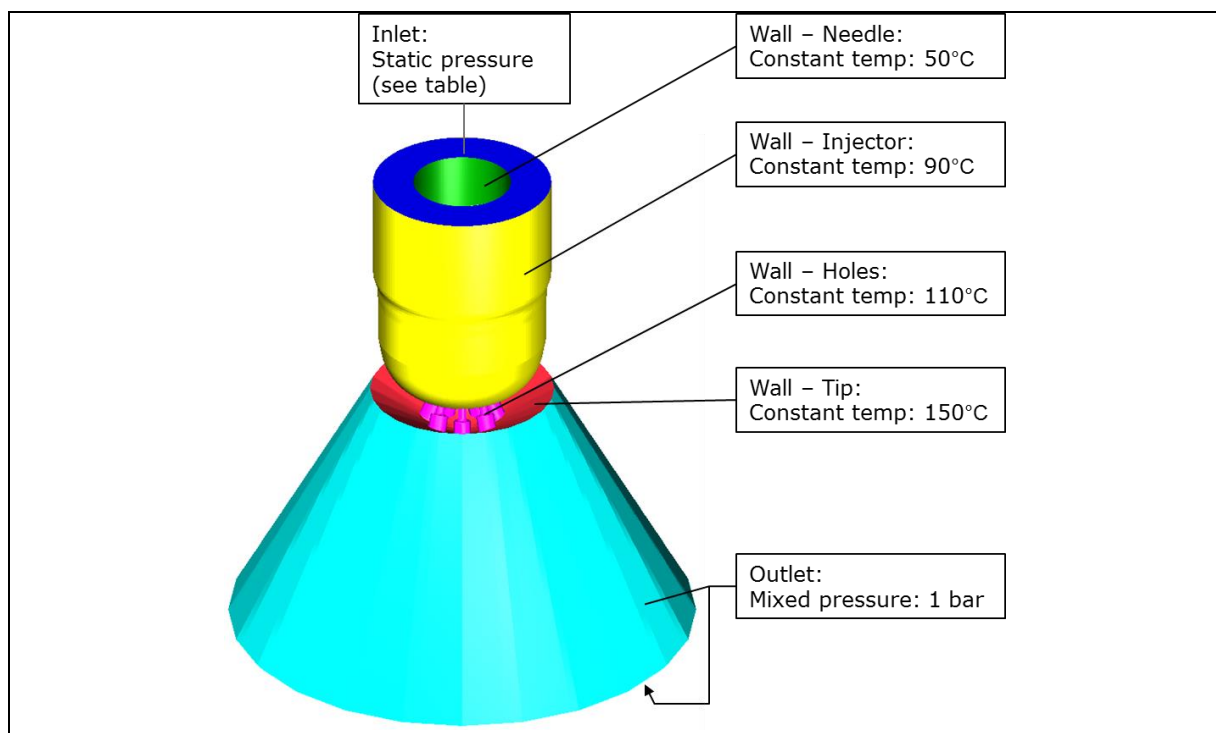


Figure 53: Injector Simulation Boundaries

To use the results of this simulation as input for the spray and cylinder simulation it was necessary to define measurement areas in each injector nozzle. At the end of the small nozzle before opening to the counter bore all spray relevant data is recorded and saved in a so called 'Nozzle-file' (.nzf). This file includes data for each time step about the local phase distribution in the measurement area with velocity vectors and density.

Further simulation details can be found in Appendix II - Injector Simulation.

5.3 Variations

During the project, several simulation loops were necessary to calibrate the correct massflow by modifying the signal duration and lift scale factor. Each new lift curve required a new mesh setup. Only calibrated cases are described in this chapter except case #3 which was chosen to highlight the difference between the sharp and round edge in terms of massflow and velocity.

5.3.1 Single Component Fuel

Single component fuel simulations consist of the mentioned 3 phases liquid, vapor and air. Case #1 to #4 in Table 6 have been used to compare the simulation with the measurement results for massflow and later to calibrate the break up model in the spray simulation.

Case #6 to #10 are used as input in the cylinder simulation with Iso-Octane. Case #7 is a variant of Case #6 with a round edge while Case #8 to #10 are needed for cylinder simulation variants with different fuel or injector tip temperatures.

Table 6: Simulation variants single component fuel

Case	Fuel Temp	Tip Temp	Pressure	Signal	Lift Scale	Edge	Fuel
#	°C	°C	bar	ms	-	-	-
1	20	20	50	1	1	sharp	n-Heptane
2	20	20	150	2.1	1	sharp	n-Heptane
3	20	20	150	2.1	1	round	n-Heptane
4	20	20	150	2.1	0.5	round	n-Heptane
5	20	20	110	2.1	0.5	round	n-Heptane
6	50	150	110	2.1	1	sharp	Iso-Octane
7	50	150	110	2.1	0.5	round	Iso-Octane
8	80	150	110	2.1	0.5	round	Iso-Octane
9	50	180	110	2.1	0.5	round	Iso-Octane
10	50	210	110	2.1	0.5	round	Iso-Octane

5.3.2 Multi Component Fuel

In this work the difference of single and multi-component fuels in terms of wallfilm evaporation has been investigated. Current research shows simulation influence of fuel composition on spray ([66]) and wallfilm ([67], [68]) even if the single component and multi component evaporation curves are identical. The evaporation of each component is influenced by its mass fraction in the blend and the evaporation of the other components. It is expected that an injector tip wallfilm simulation with multi component fuel shows higher amount of wallfilm on the injector tip compared to a single component fuel like Iso-Octane.

To investigate the influence of different fuel compositions surrogates with 3 to 4 components are created. Case #11 in Table 7 shows similar evaporation behavior as a European RON 95 standard gasoline. Case #12 should reflect a more volatile fuel with lower high boiling components which is expected to represent countries with a high share of Diesel vehicles and therefore a focus on Diesel fuel in refinery processes leaving Gasoline fuel with short CH-chains. The components have been adjusted to match a volatile European RON 92 winter fuel.

Countries like china with a very high share of Gasoline vehicles will shift the refinery process towards Gasoline leading to longer CH-chains and high boiling components within the fuel – Case #13 uses N-Dodecane as a 4th component to represent the low volatile components in the Chinese M15 fuel which was also used in the fleet tests mentioned in chapter 1.2.; this is a different M15 fuel than the one used on the engine test bed.

Table 7: Simulation variants multi component fuel

Case	Fuel Temp	Tip Temp	Pressure	Signal	Iso-Pentane	Iso-Octane	Mesitylene	Dodecane
#	°C	°C	bar	ms	%	%	%	%
11	50	140	150	2.1	37	39	24	0
12	50	140	150	2.1	30	58	12	0
13	50	140	150	2.1	38	34	22	6

The results of the multiphase multicomponent injector simulations are not further discussed in this chapter as they are only required to create the nozzle files for the cylinder simulation in chapter 7.4.4.2 where the influence of fuel composition on the injector wallfilm is investigated.

5.4 Results

The following results are based on the nozzle numbers shown in Figure 54. The injector is symmetrical around Nozzle #2 which is the main cut for the results in this chapter.

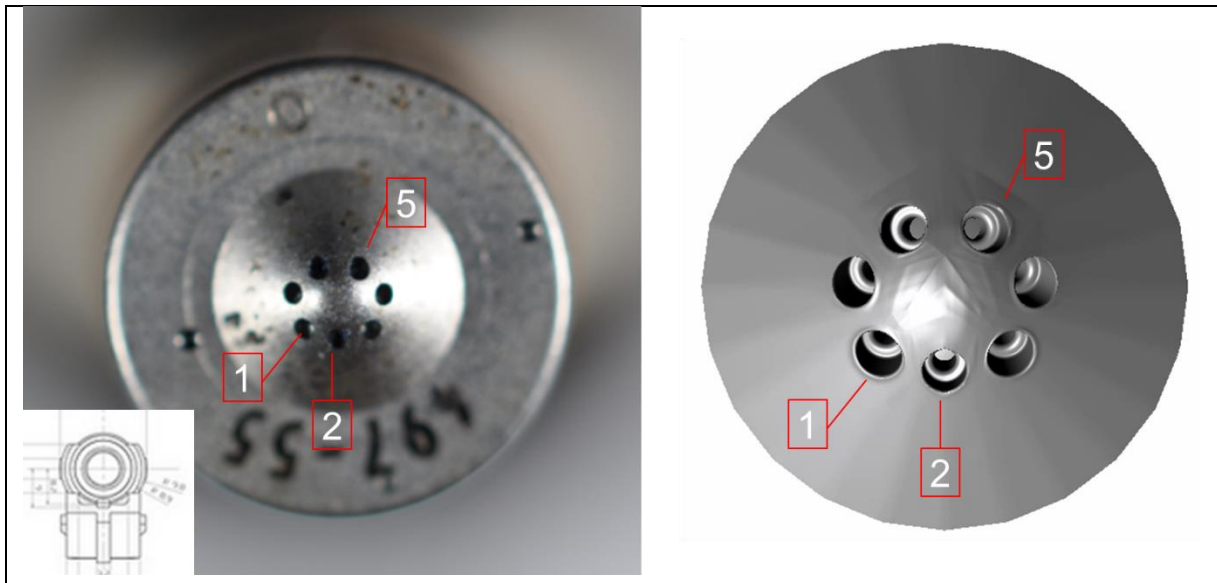


Figure 54: Injector Nozzle Numbers

5.4.1 Massflow Results

As the geometry of the injector is fixed by using the X-ray model, only the needle lift curve can be modified to match the measured mass flow at a given rail pressure and signal duration. The conversion from signal time to injection duration is already shown in chapter 5.1.4. During the project the massflow from the simulation was compared to the measurement and the needle lift scale factor was adjusted if necessary.

Figure 55 shows the massflow comparison for Case #1 and #2 with a lift factor of 1, indicating that the original available needle lift curve has been used and only stretched to match the signal time. Simulation and measurement show a very good correlation with only a total deviation of $\sim 1.5\%$ for Case #2 – 150 bar. Both cases use the injector mesh with sharp edge in the seat area.

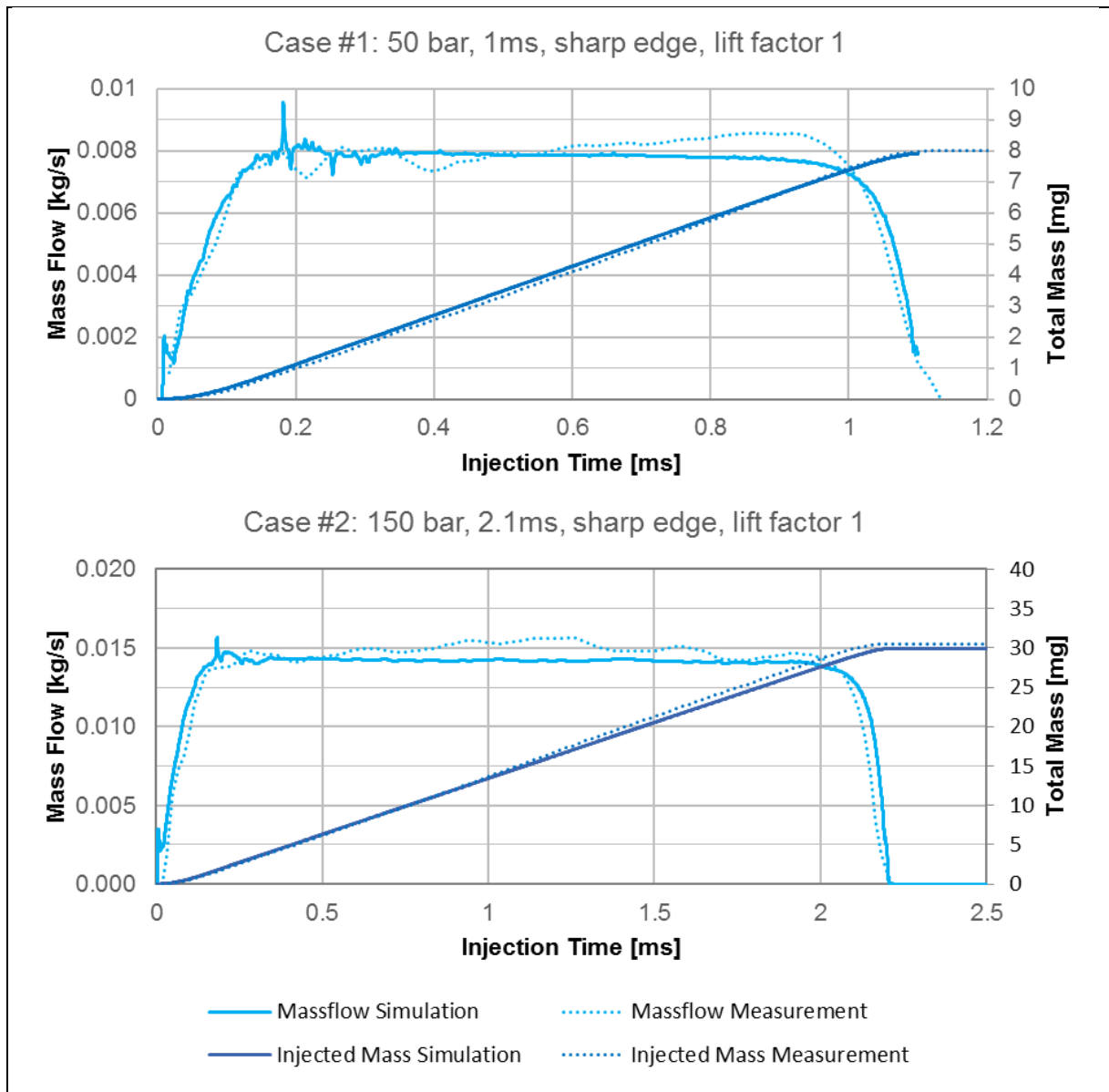


Figure 55: Injector Massflow @ 50 / 150 bar – Simulation vs. Measurement

Case #3 is simulated under the same conditions as Case #2 with 150 bar rail pressure, a signal duration of 2.1ms and lift factor 1. However, Case #3 uses the mesh with the rounded edges at the seat area. The results show a 34% higher mass flow due to better flow conditions at the nozzle entry area. The fuel can follow the wall which leads to better nozzle filling – further details are shown in chapter 5.4.3. To achieve the same massflow as the measurement the lift scale factor has been reduced to 0.5 resulting in half of the original needle lift.

Case #4 is simulated with this new lift factor while keeping the same boundaries as Case #2. The simulated massflow rate and total mass flow match the measurement perfectly as shown in Figure 56.

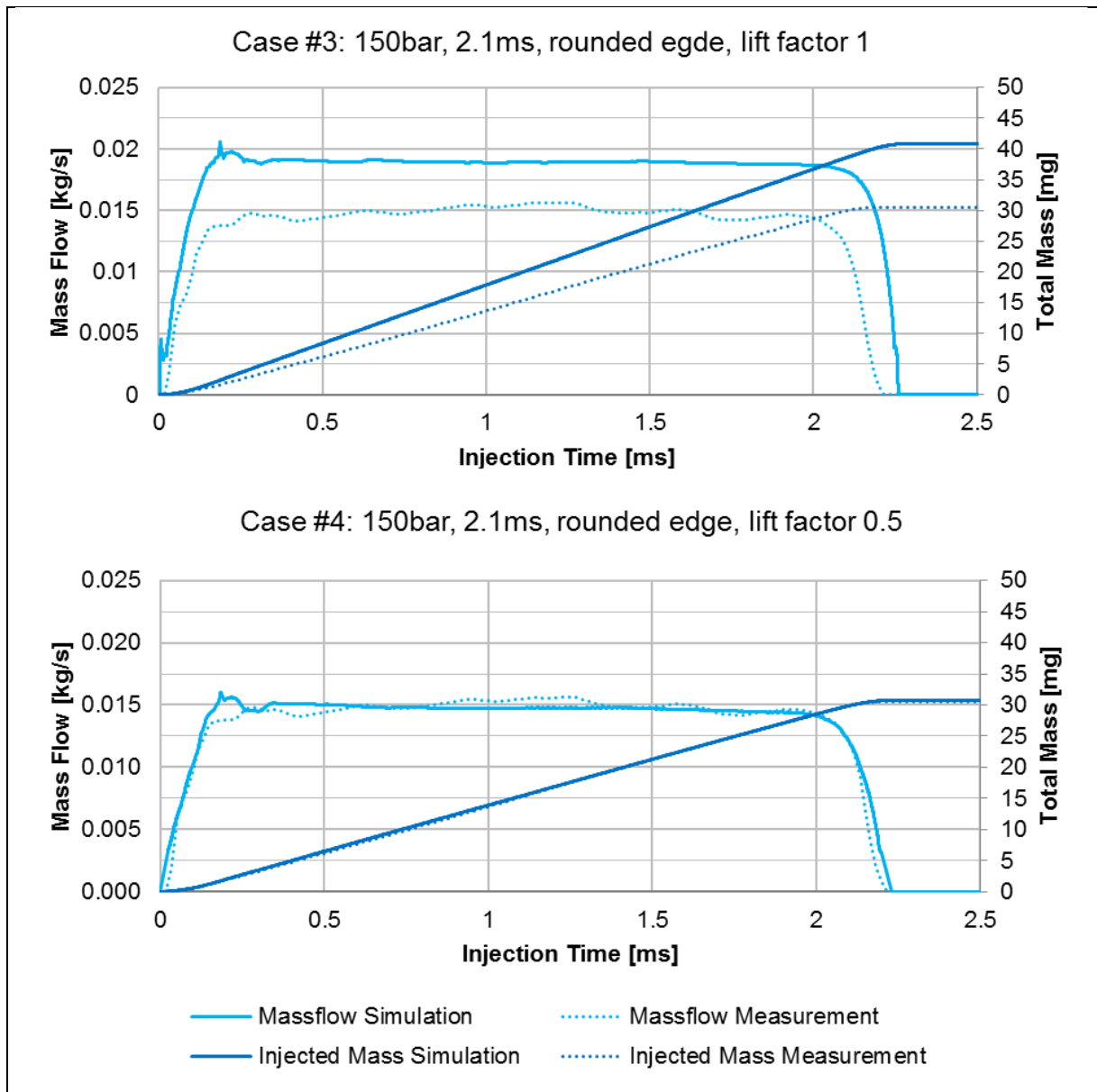


Figure 56: Injector Massflow @ 150 bar lift factor 1 / 0.5 – Simulation vs. Measurement

5.4.2 Fuel Distribution and Velocity

In this chapter, only the calibrated Cases (#1, #2 and #4) are discussed. Figure 57 shows a section through the symmetry plane and Nozzle #2 at 0.2ms after opening, during the constant needle lift phase and during closing. Red areas represent 100% liquid fuel while blue means 0% fuel (can be air and/or vapor). All 3 cases show similar effect in the needle seat area. In Case #1 and #2 the fuel is separated from the wall at the sharp edge. In Case #4 the fuel also can't follow the wall due to the small gap between needle and seat resulting in high velocities.

In Case #1 the liquid stream follows better the nozzle direction while in Case #2 and Case #4 due to the higher pressure the stream can't follow the sharp angle. Both cases show a stream more directed to the center of the injector.

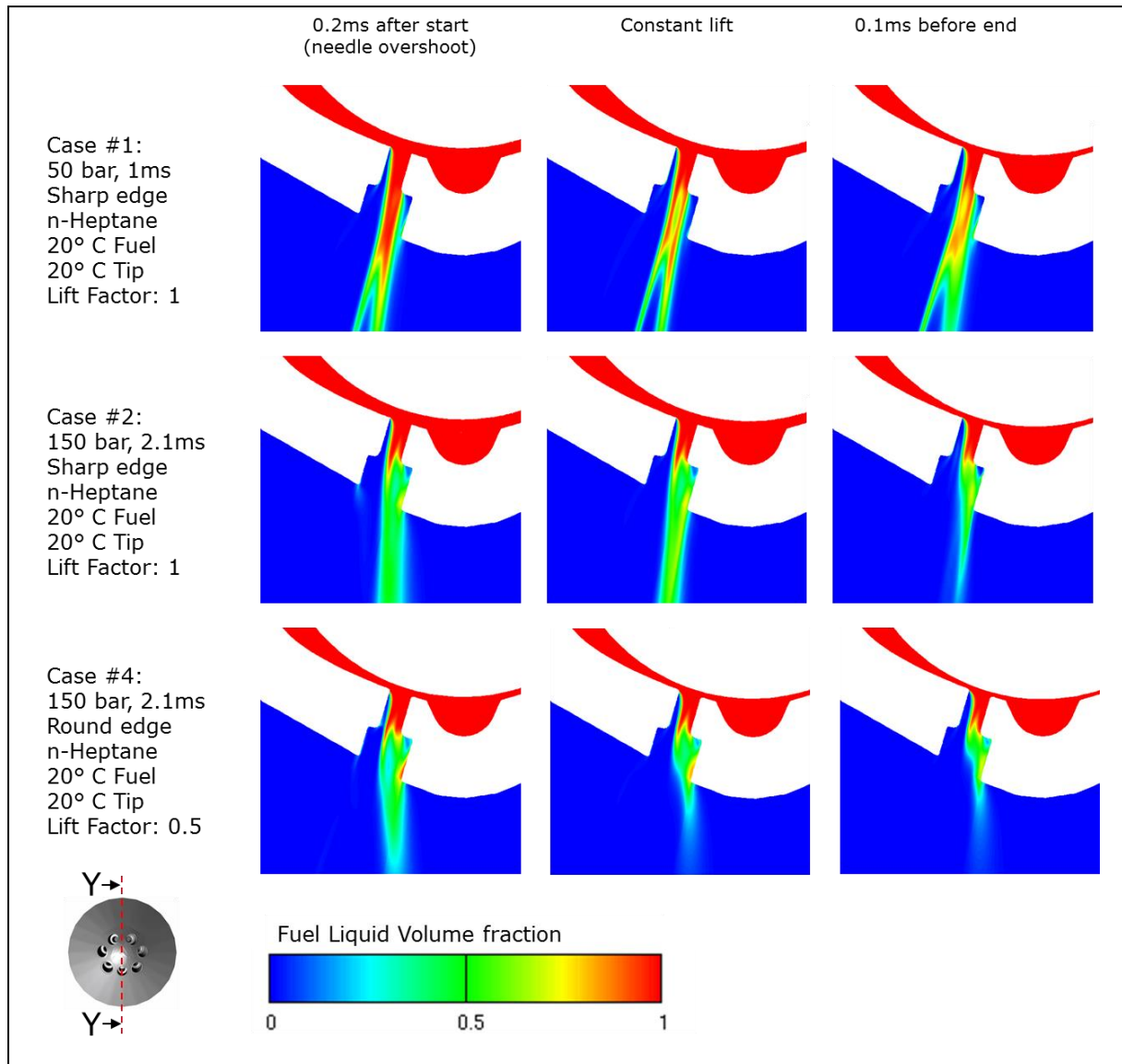


Figure 57: Y-Cut Liquid Phase Volume Fraction for Case #1, #2, #4

The apparently shorter penetration length in Case #4 is a result of the section plane as the main stream continues in front and behind the section plane. Figure 58 shows the velocity in the same cut plane ranging from 0 to 120 m/s for Case #1 (50 bar) and 0 to 180 m/s for Case #2 and #4 (150bar).

Case #4 – constant lift shows the mentioned increased velocity in the needle – seat – gap leading to a separation of fuel from the wall. Case #2 and #4 show similar velocity levels in the nozzle file area. Case #2 has air recirculation areas with high velocities

close to the nozzle entry indicated by a small red area surrounded by a blue area (in this area the flow direction inverts leading to a low velocity).

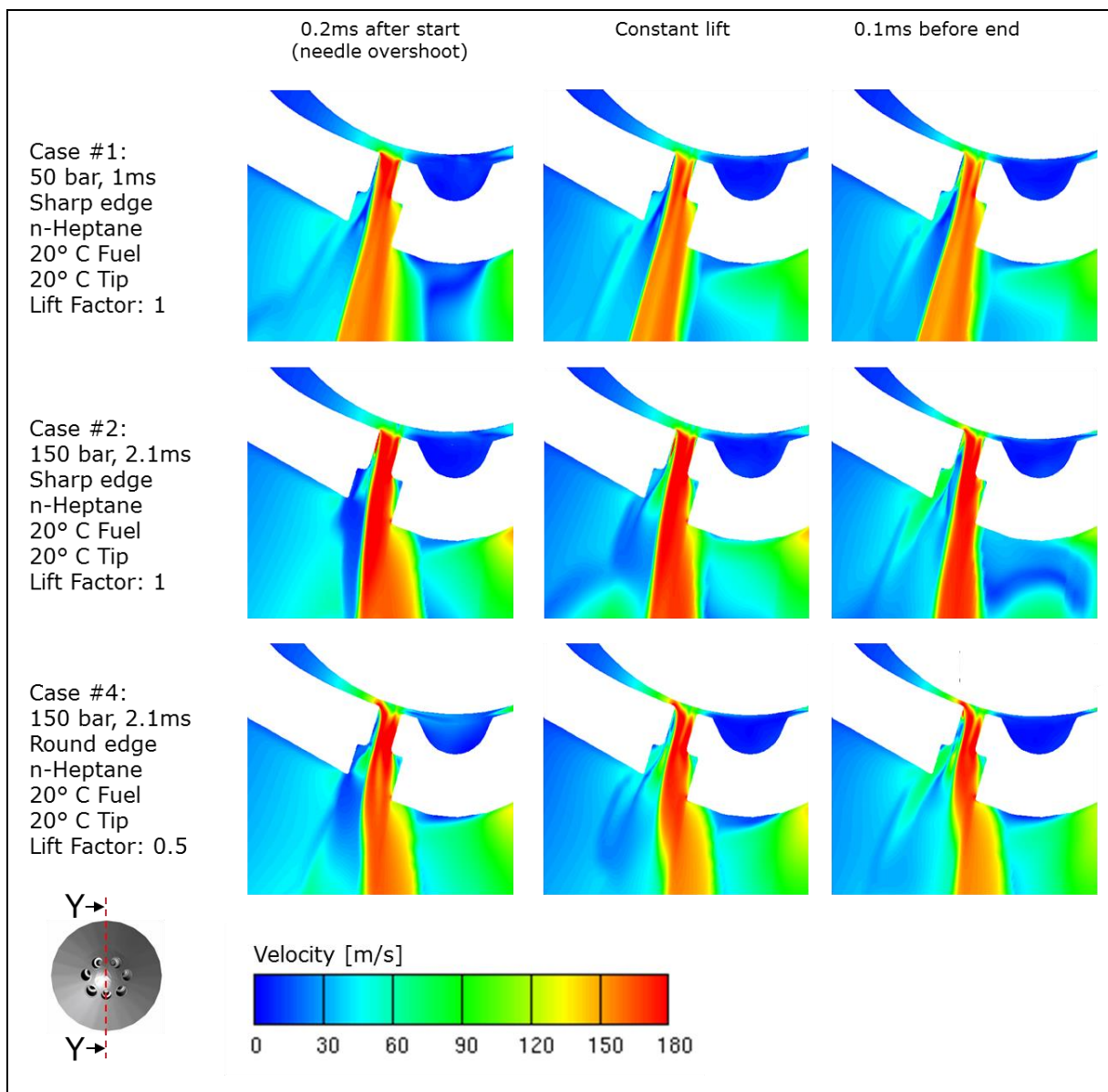


Figure 58: Y-Cut Liquid Phase Velocity for Case #1, #2, #4

The air recirculation is also visible in Figure 59 which displays the vapor and air volume fraction in the nozzle. Vapor is only created if cavitation happens in the nozzle. Due to the air circulation in Case #2 only small cavitation around the edge can be observed. On the right side a high air volume fraction close to the seat area is visible.

In Case #4 the liquid fuel tries to follow the wall around the rounded edge but is separated due to high velocities. This creates a low pressure in the edge area leading to cavitation in the nozzle and only little air recirculation.

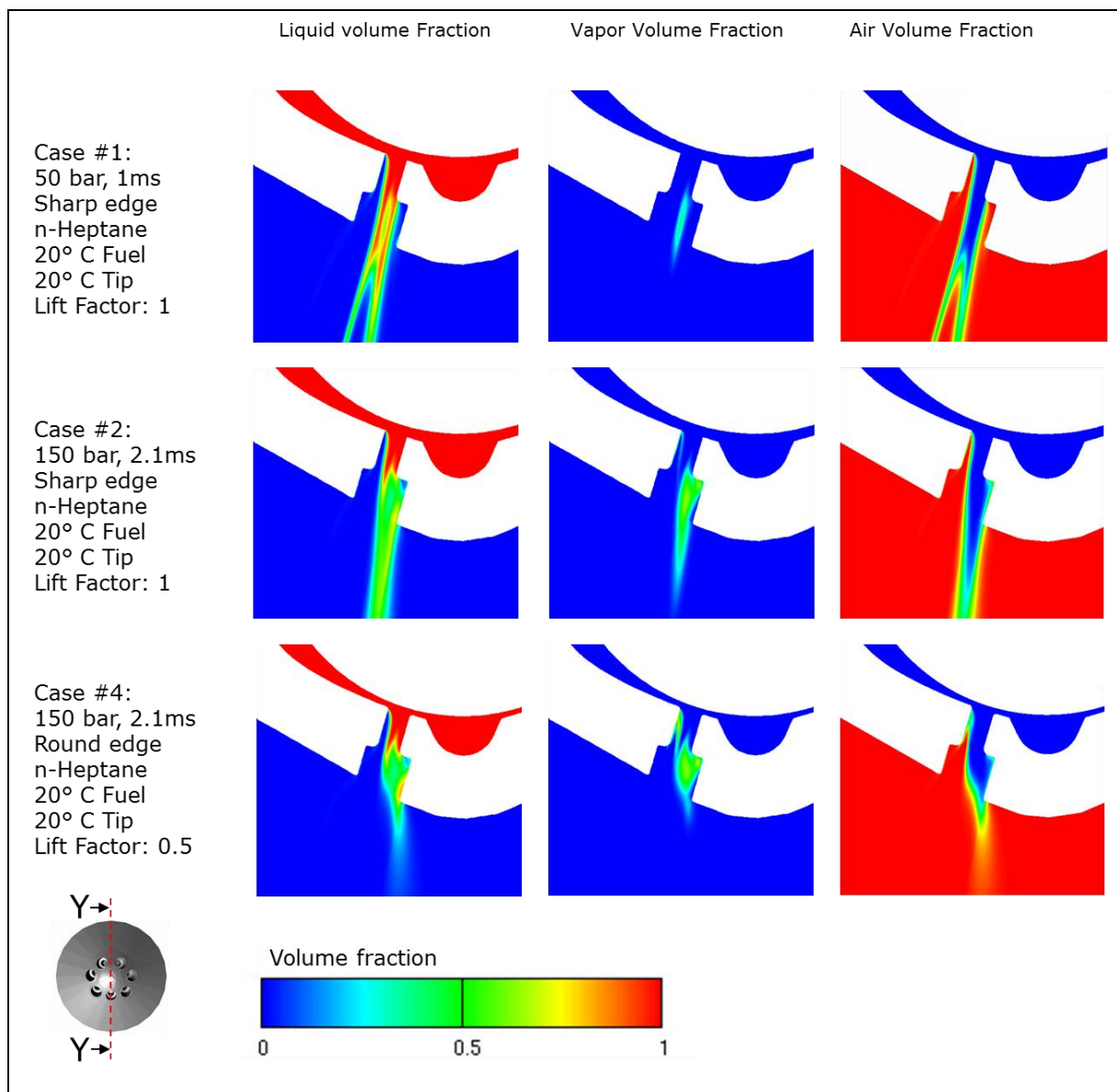


Figure 59: Y-Cut Liquid, Vapor and Air Phase for Case #1, #2, #4

In Figure 60 an isometric surface is shown for a liquid volume fraction of 10%. The surface is colored according to the current velocity in this area. The velocity range is the same as above with max. 120 m/s for 50 bar and 180 m/s for 150 bar. The front view for Case #4 explains why the penetration length seems shorter in the Y-Cut as the stream splits after leaving the counter bore.

Another phenomenon can be observed in case #2: due to air recirculation in the nozzle the area with 10% liquid volume fraction is wider than in case #4 (wide vs. small streams). The further away the isometric surface is from the stream core the lower

velocities levels are displayed on the surface. However, the sections in Figure 58 show same or even a higher velocity than in Case #4.

Also, the deviation between nozzle direction and stream at higher fuel pressures is clearly visible when comparing case #1 with #2 and #4 in the side view.

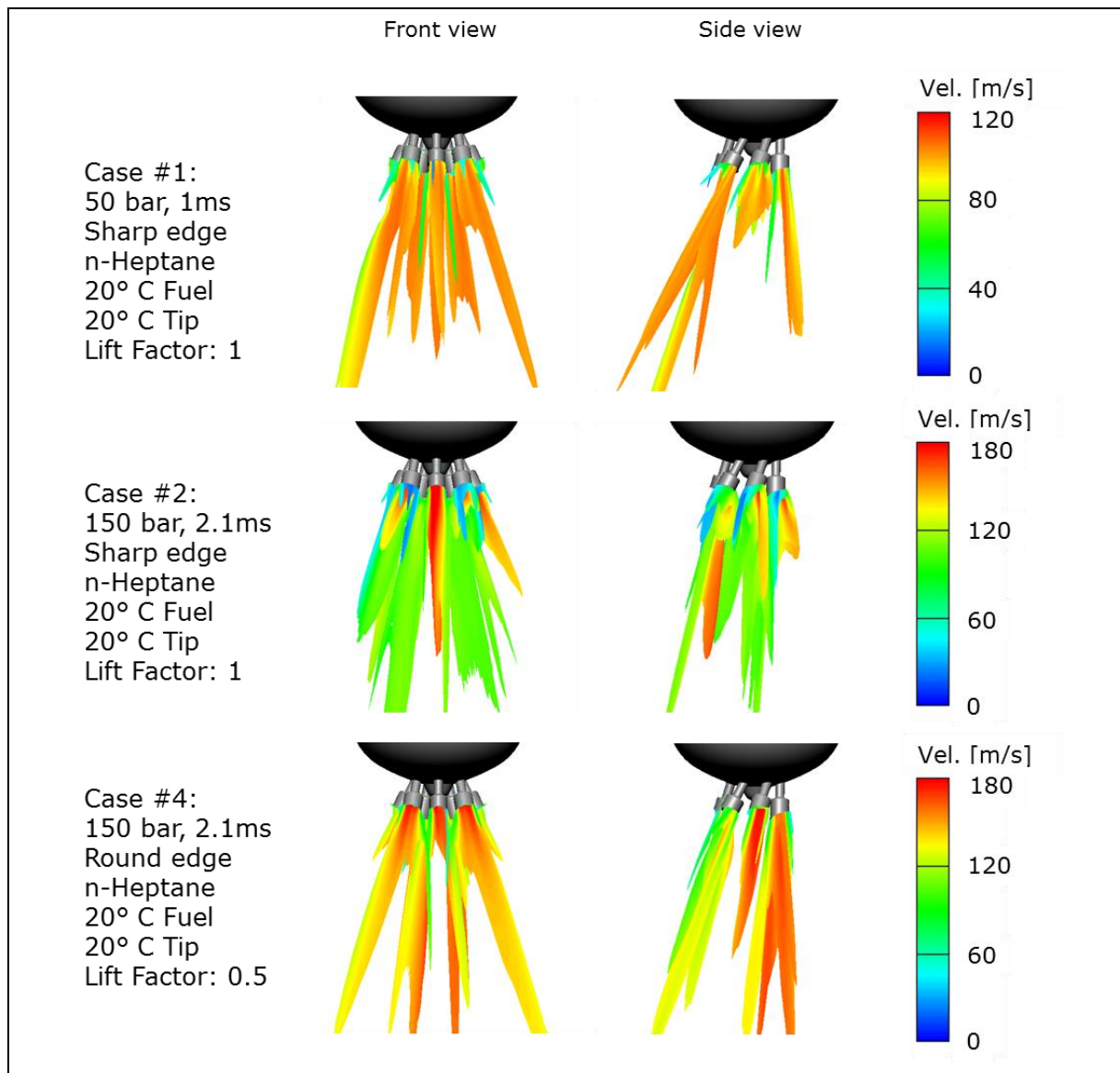


Figure 60: Isometric surface (liquid volume fraction = 0.1) colored with velocity at constant needle lift for Case #1, #2, #4

As mentioned in a previous chapter the spray and cylinder simulations use the data recorded in the nozzle file measurement area shown in Figure 61. Differences in these areas will lead to different spray and wallfilm behavior. A wider fuel volume fraction area in the nozzle file cross-section will lead to lower velocity and shorter penetration compared to a smaller liquid area at the same mass flow. Liquid fuel close to the edge

in the counter-bore section will increase wallfilm build-up in the counter-bore and on the tip.

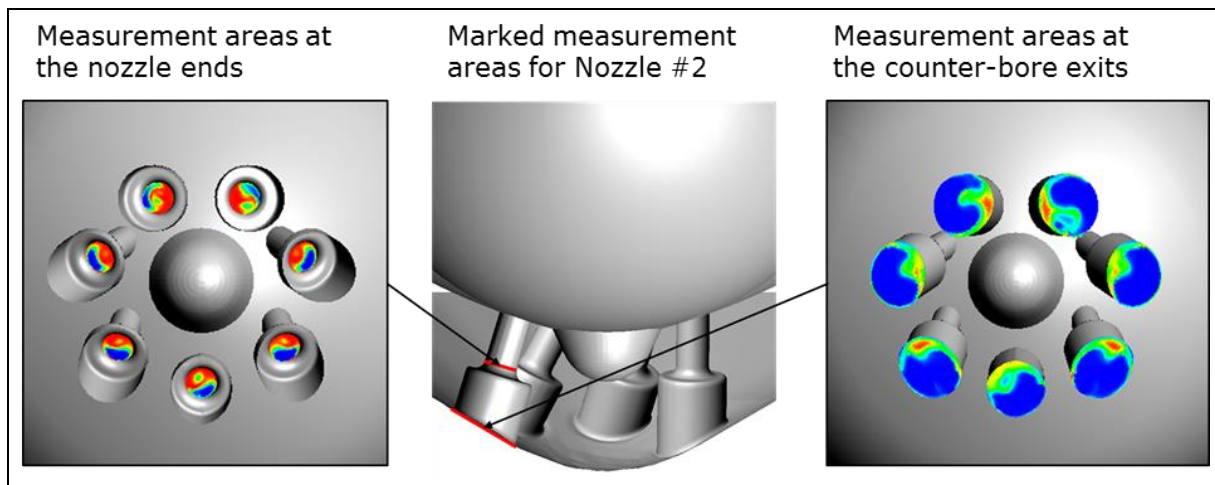


Figure 61: Measurement area for nozzle file (left picture) and counter-bore exit at injector tip (right picture)

Comparing Case #1 (50 bar) and Case #2 (150 bar) in Figure 62 shows a very similar distribution of the liquid volume fraction in the nozzle measurement area. In the counter-bore however Case #2 shows more liquid close to the edge due to the higher deviation between stream and nozzle direction mentioned before. It is expected that Case #1 shows less wallfilm on the injector tip than Case #2.

Case #2 and Case #4 show only little differences for the liquid volume fraction in the nozzle section. As both cases have been calibrated to the same massflow velocities in the same section will be similar as well. The influence of the air recirculation in Case #2 is visible in the counter-bore section: While the liquid in Case #4 is more concentrated in the area close to the injector center, Case #2 builds up a liquid ring around the edge (e.g. Nozzle #1 and #3).

The velocities in the nozzle section and counter-bore can be seen in Figure 63 at the same time step as the liquid volume fraction. As expected the velocity values between Case #2 and #4 are similar while the area of maximum velocity is different due to the turbulences in the nozzles for Case #2.

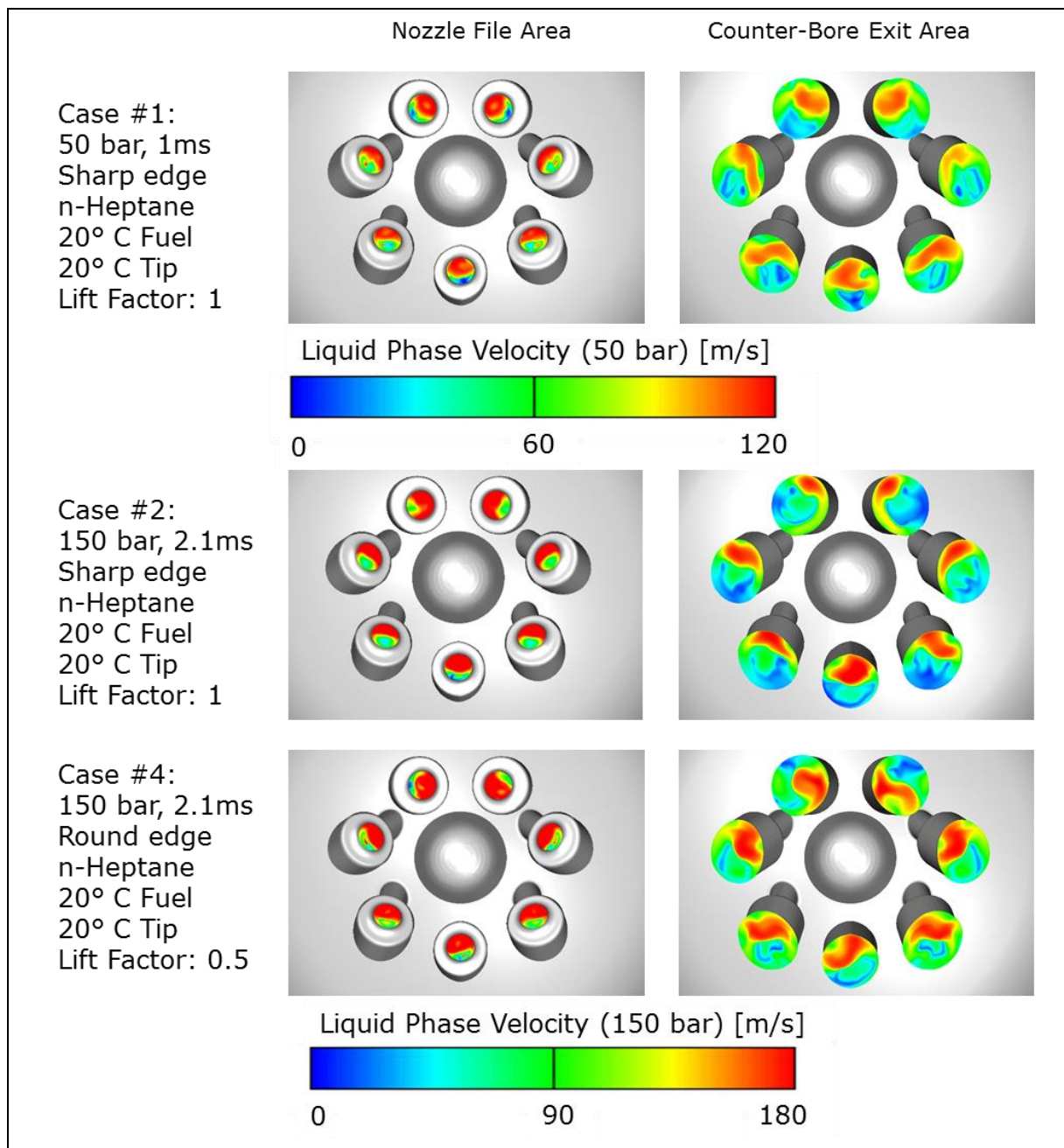


Figure 63: Liquid Phase Velocity in the Nozzle measurement area and counter-bore outlet for Case #1, #2, #4

5.4.3 Comparison sharp to rounded Edge with same Needle Lift

The following results focus on the difference between a sharp and rounded edge with the same needle lift (Case #2 and #3) leading to a 34% increase in mass flow (see chapter 5.4.1).

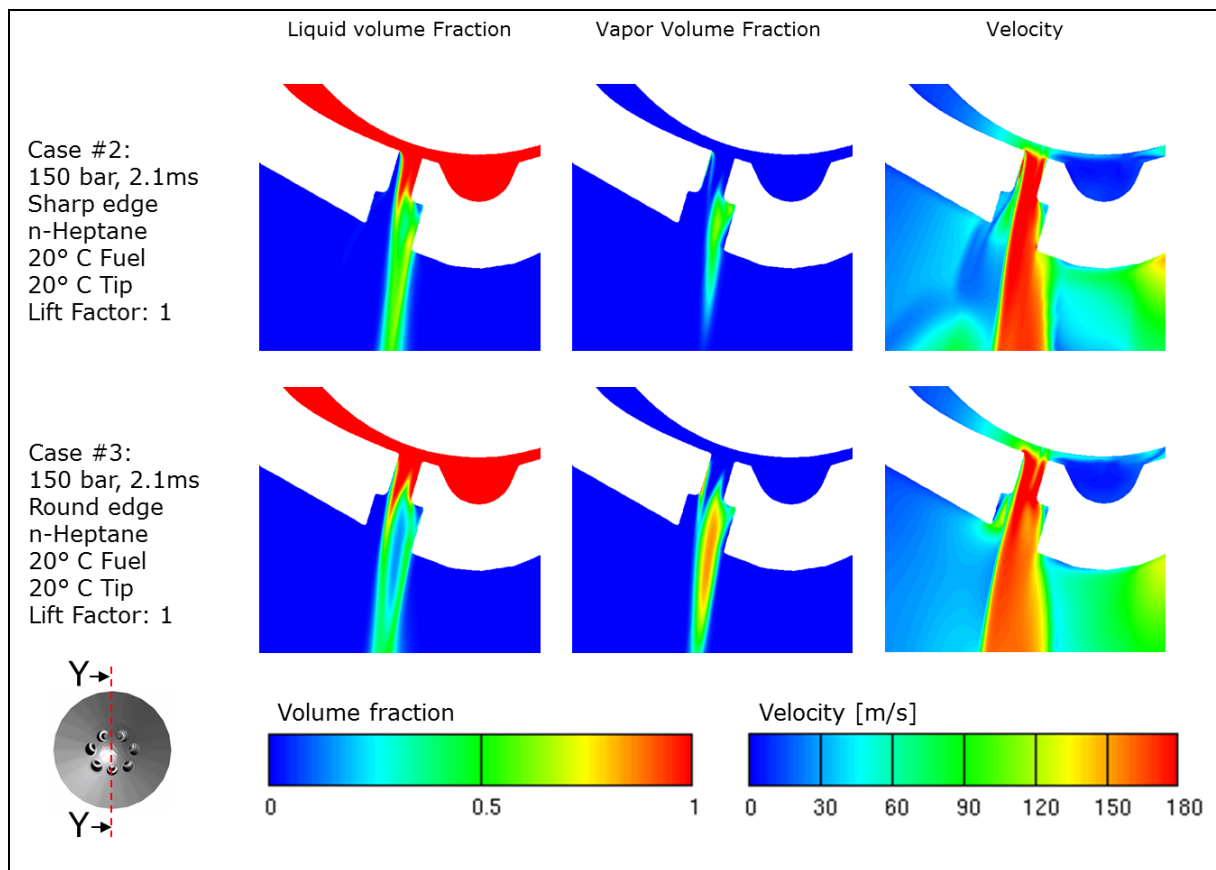


Figure 64: Y-Cut Liquid, Vapor Volume Fraction and Velocity for Case #2, #3

Comparing the liquid volume fraction and velocity in the Y-cut (Figure 64) makes the difference of the edge visible. The liquid phase can follow the rounded edge much better leading to a nearly completely filled nozzle. The improved flow conditions also result in a decreased deviation between nozzle direction and stream.

While the maximum velocity remains similar the massflow increases in Case #3 due to the better filled nozzle. A filled nozzle however prohibits air to recirculate leading to much higher cavitation.

Figure 65 shows the increased area of the liquid phase in the nozzle section and counter-bore as suggested by the Y-cut above. In line with Case #4, Case #3 experiences a fuel concentration in the counter-bore section mainly towards the injector center and not showing a liquid ring like Case #2.

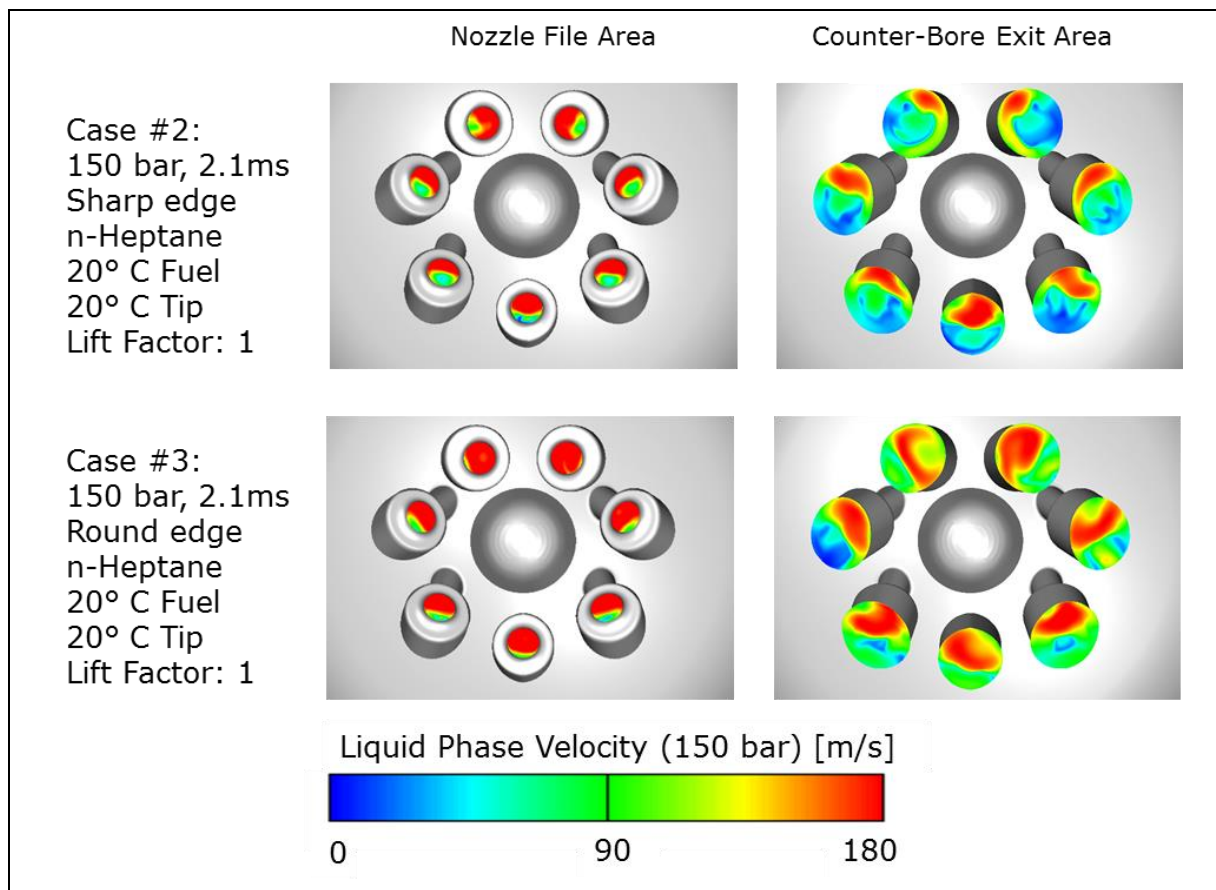


Figure 65: Liquid Volume Fraction in the Nozzle measurement area and counter-bore outlet for Case #2, #3

5.4.4 Conclusion from Results

Several tendencies can be concluded from the presented results:

- The deviation between nozzle direction and stream increases with higher pressure for the injector with sharp edges. A bigger deviation leads to more contact of the stream with the counter-bore and edge at injector tip.
- Comparing a sharp and rounded edge with same massflow at same pressure (Case #2 and #4) shows very similar liquid phase distribution and velocities. Due to the reduced needle lift for a rounded edge the fuel gets separated from the wall similar to the sharp edge.
- The simulations with a sharp edge show increased air recirculation in the nozzle which reduces cavitation and leads to wider streams after leaving the nozzle.
- The local distribution of the liquid phase at the counter-bore exit suggest that wallfilm will built up in the tip center first.
- A rounded edge increases the massflow in the nozzle by around 30% while using the same needle lift as a sharp edge injector. The liquid phase can follow the wall better also decreasing angle deviation between nozzle and stream.

Recirculation of gas from the discharge volume and deviation between nozzle direction and spray have also been observed in [64] & [69].

6 Spray Simulation

The following chapter describes the Lagrangian spray simulation coupled with the wallfilm model described in chapter 4.2 which is a new step in simulating deposit critical areas on the injector tip.

6.1 Measurement Inputs

A Lagrangian Spray simulation is a standard task in injection simulation which is calibrated using injection measurements to align spray shape and penetration. Additionally, new measurement methods had to be developed to verify the available wallfilm model in this new use case.

6.1.1 Spray Shape and Droplet SMD

The investigated injector is installed in a spray test rig consisting of a n-Heptane fuel tank, a high-pressure fuel pump up to 500bar and a discharge box with glass walls. The spray shape is captured using an image-capturing system shown in Figure 66. The injector is actuated multiple times in a row using the requested fuel pressure and injection time. During each injection one picture is taken at a defined time step which moves further after every injection. The result is a video from injection start to end showing the spray development but also fluctuations between each injection.

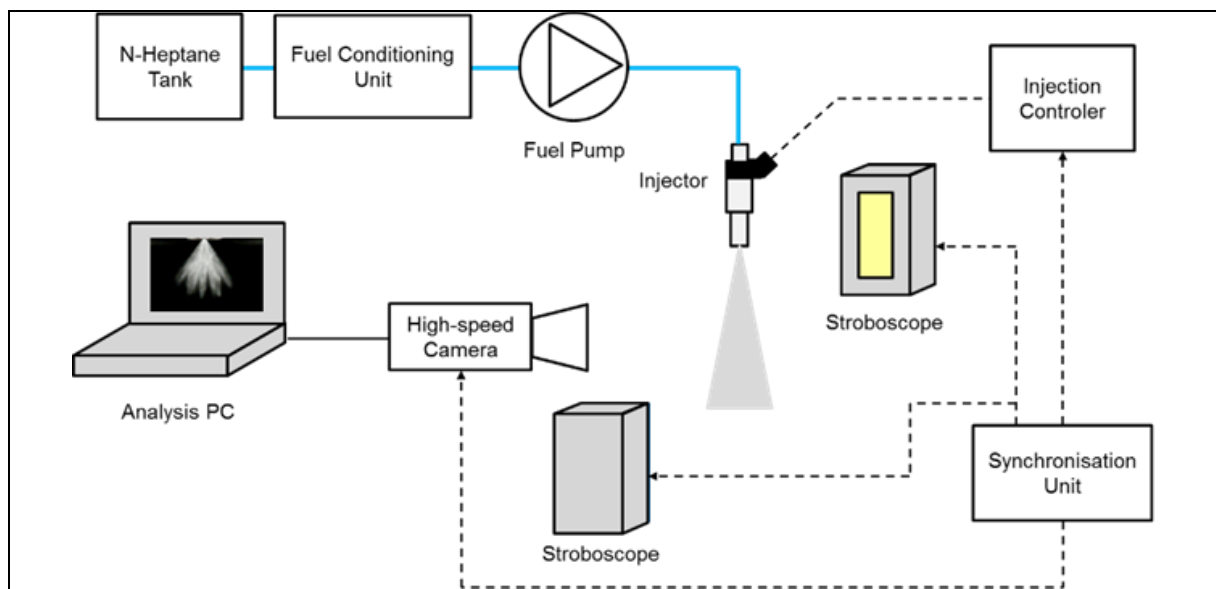


Figure 66: Injector Spray Imaging Capturing system

The simulation results are scaled to the same dimensions as the measurement using referent pictures from the test rig and simulation setup to compare spray angle and

penetration depth. Based on the comparison the simulation break-up models can be calibrated.

Additional to the spray shape and development the droplet sauter mean diameters (SMD) have been measured in a plane 50mm from the Injector tip using the Malvern method. The SMD is defined as the diameter of a sphere that has the same volume to surface area ratio as the investigated particle [70].

6.1.2 Wallfilm on Injector Tip

The FIRE wallfilm model is used in combustion simulation to investigate the wall and piston wetting. However, in this work the model is applied to the injector holes and tip during injection for the first time currently known. As no reference data is available the results have to be verified with measurements to ensure correctness of the model.

A new measurement method was developed together with an AVL measurement engineer consisting of a high-speed camera coupled with a powerful macro lens to capture the buildup of wallfilm on the injector tip. Although recent papers use similar measurement setups the purpose is different from the presented one. In [64] microscopic pictures of the injector tip during injection are used to verify the spray behavior of a multiphase simulation at the nozzle outlet. [53] on the other hand, also focuses on wallfilm but uses the pictures as input to define the wallfilm area after end of injection. In both cases it seems the cameras only captured one picture per injection similar to the spray shape measurement while the presented method below is able to record one full injection from needle opening to closing.

Figure 67 shows the test rig which is based on the setup from chapter 6.1.1. The standard camera and light source have been removed as well as the glass walls from the discharge box.

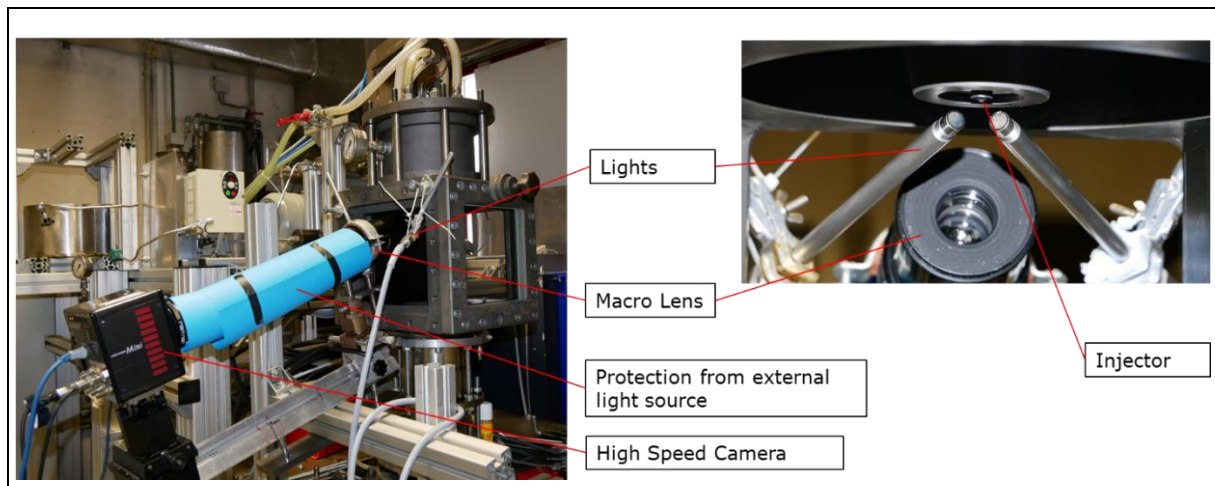


Figure 67: Test rig setup for high speed injector tip measurements during injection

The new installed high speed camera is able to capture images with up to 35.000 fps with exposure times below 1/200.000s. By setting the distance between the camera and the macro lens the magnification level can be adjusted; a simple paper tube is used to block external light between the two components. To ensure sufficient light with such short exposure times two dot light sources with flexible mounting have been used. As the focus length of the macro lens was shorter than the distance between injector tip and the glass walls of the discharge volume the walls have been removed.

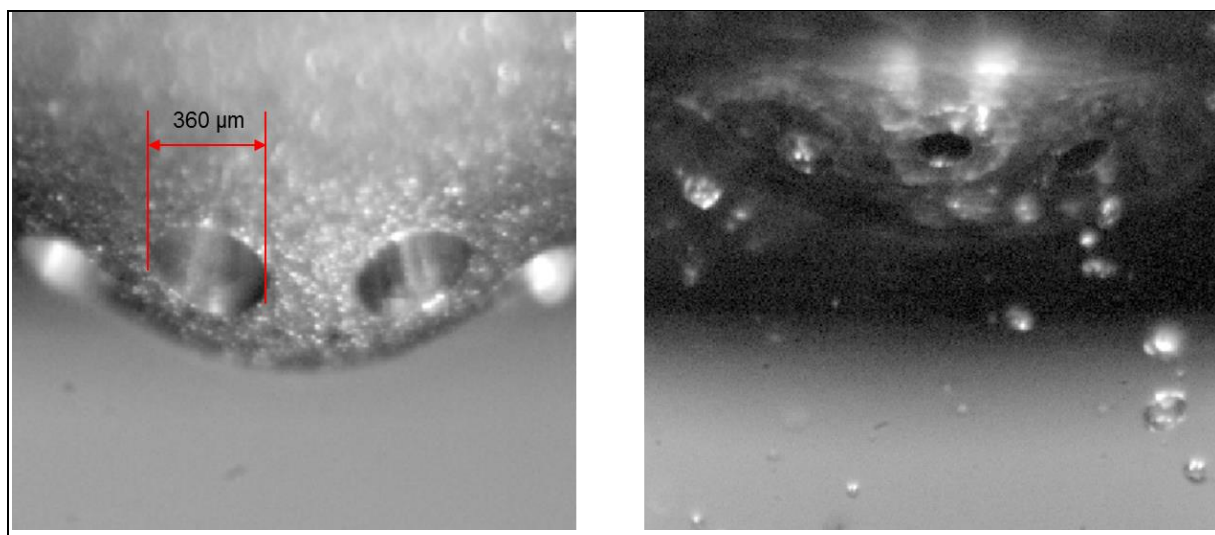


Figure 68: Microscopic pictures of injector tip for two different injectors.

Example pictures from the setup can be seen in Figure 68 for two different injectors. The left picture is the HDEV 5 injector used in the simulations while the right picture shows an injector from another supplier with a different zoom level. Another difference is the surface roughness of the tip.

While the wallfilm border is clearly visible for injectors with a polished tip the rough surface made it difficult during measurements to identify the wallfilm area. The injector tip had to be prepared beforehand by applying a thin soot layer with a flame on the tip. During injection, the occurring wallfilm washed the soot away leaving a clean area.

Further test rig details can be found in Table 8.

Table 8: Test Rig properties

High speed camera	Photron Fastcam Mini AX100 type 540K-M-8GB
Macro Lens	UV-Nikkor f=105mm, 1:4.5
Min. Exposure time	1.05 μ s independent from frame rate
Max frame rate	540.000 fps at 128 x 16 pixels

6.2 Model Description and Boundaries

The presented mesh for the spray investigations has been created in AVL FIRE M using the automatic meshing tool while running the simulations in FIRE 2014.2 using the Lagrangian Multiphase (Spray) Module [71] and the Wallfilm Module [58].

6.2.1 Mesh Setup

For the spray simulation, a cube with 100mm side length has been used as base for the mesh. Unlike a standard spray simulation, the injector tip, counter-bore and nozzles were added in the center of the top increasing the complexity of the setup and requirements for break-up calibration. The mesh itself is a polygon mesh with several refinements along spray direction to capture spray shape and development. Refinements around the injector tip and inside the nozzles ensure a high resolution of the simulated wallfilm area. In Figure 69 a cross section through the mesh is shown with details of the injector tip.

The main reason for using a polyhedral instead of a hexagon mesh in this case is the ratio between biggest and smallest cell of the mesh. To decrease simulation time large cells several mm in size are used on the outside of the box while cells down to 5 μ m can be found inside the nozzle.

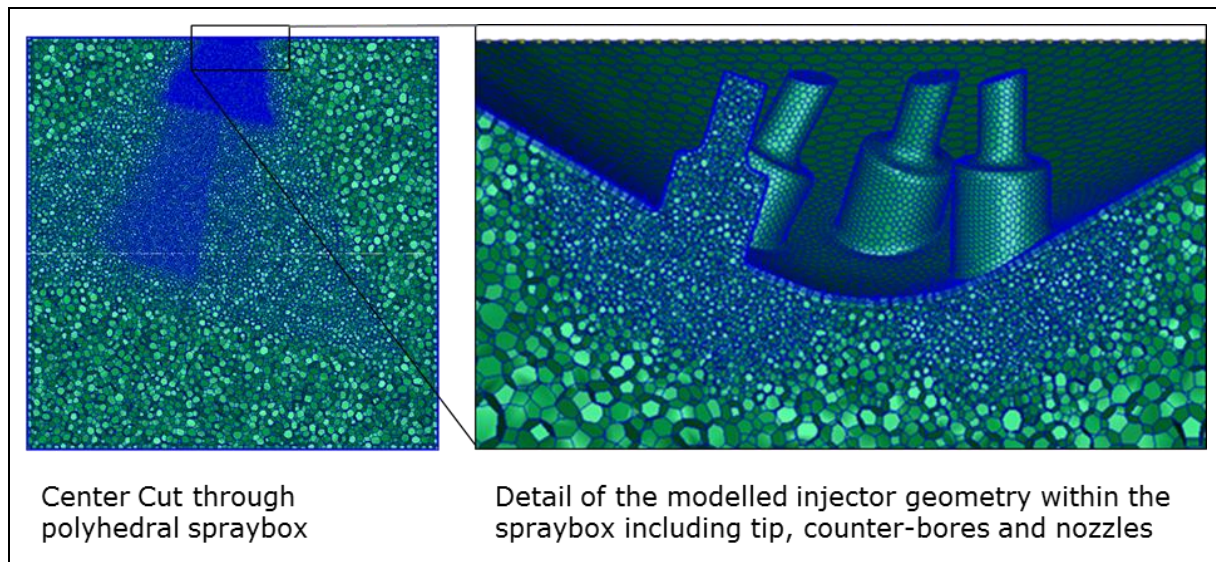


Figure 69: Polyhedral Spraybox mesh with refinements in spray direction and modelled injector nozzles

The same mesh is used for all operating conditions to ensure comparable results. Further details are described in Table 9.

Table 9: Spray Box mesh properties

Number of cells	0.95 Mio Cells
Min / max cell size	3.5 μ m / 3mm
Simulation steps	0.01 ms
Simulation results	Spray shape and development (break-up models), Wallfilm distribution around injector tip, verify nozzle files from injector simulation

6.2.2 Boundaries and Simulation Setup

The simulation is a Lagrangian spray simulation which uses inputs from the injector simulation and primary and secondary break-up models to predict spray shape and development. All walls of the mesh are also defined as walls in the simulation with 20°C wall temperature. There is no inlet or outlet boundary to simulate a closed case.

The complete volume is initialized with air at 20°C and ambient pressure, the same conditions as in the spray chamber from the test rig.

In this simulation, the nozzle files from the injector simulation are used as input. Every simulation step, droplets are introduced in the defined cross section at the area where a liquid phase is present with the same velocity. The primary breakup is modeled by

the Blob injection model which is the standard approach in FIRE when nozzle files are available. It can fully capture the time resolved injector flow as the nozzle files provide local fuel velocity, turbulence intensity and fuel vapor mass fraction. In this model, the initial jet is formed by randomly introduced droplets in the orifice where liquid fuel is present. The initial diameter of the droplets in the nozzle has been set up with $60\mu\text{m}$ and will be subsequently reduced according to the mass detachment rate calculated by the breakup model. To avoid too much influence from small turbulences caused by air recirculation in the nozzle area which would result in mist, droplets are only introduced in areas with 0.97 liquid volume fraction or higher. Together with the chosen droplet diameter it is possible to cover the fuel areas in the nozzles from chapter 5.4.2 without interfering with the air recirculation area (see Figure 70).

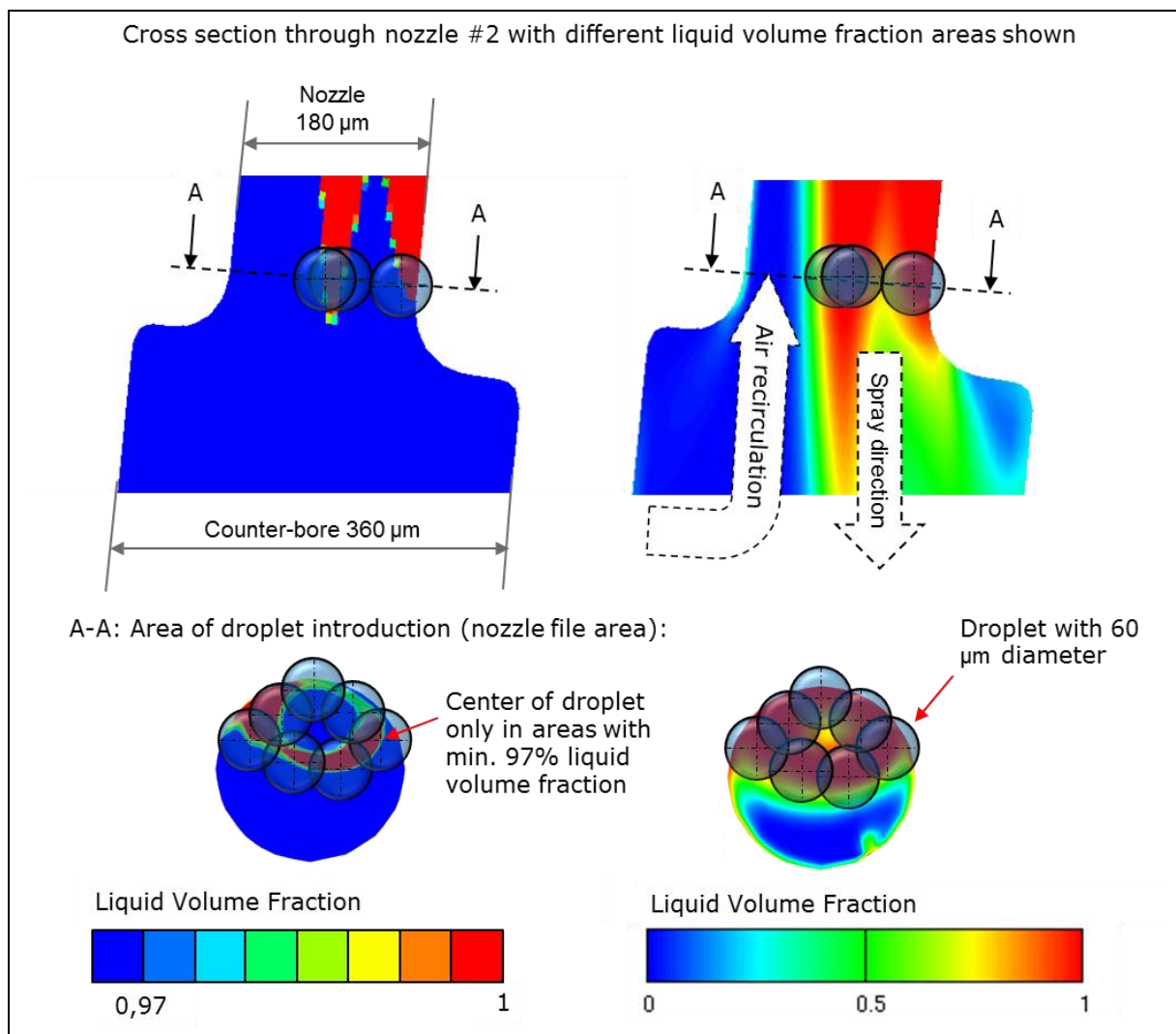


Figure 70: Case #2, Nozzle #2 Liquid Volume Fraction. Area with min. 0.97 volume fraction for droplet introduction (left) and total liquid volume fraction

This approach - using a fixed droplet size in the nozzle area - doesn't consider different droplet sizes in the opening and closing phase of the needle due to lower velocities which should be investigated in future studies.

As secondary break-up model, the TAB approach was used which showed good results for gasoline direct injections in past projects. The calibrated values for both break up models are listed in Table 10. For the Blob break-up, AVL experience based values have been used while the TAB model values have been adjusted towards shorter penetration and smaller droplet size. Further information regarding break-up models and the link between nozzle file and Lagrangian Spray simulation can be found in [71].

Table 10: Primary and Secondary Break-up Model Constants

Blob Primary Break-up Model											
C1	C2	C3	C4	C5	C6	C7	C8	C9	C10	C11	C12
0.61	12	2	10	1	0.3	0.03	1E+12	0.188	1	1	0

Tab Secondary Break-up model								
C1	C2	C3	C4	C5	C6	C7	C8	C9
1	1	0	8	2.4	0.4	10	0.1	1

Further simulation details can be found in Appendix III - Spray Simulation.

6.3 Results

All following results have been simulated with the presented break-up constants and n-Heptane at 20°C according to Table 6.

6.3.1 Spray Shape and Penetration

Simulation with 50 and 150 bar and sharp nozzle entry edge (Case #1 and #2) have been used to define the model parameters. Case #4 with 150 bar and rounded edge was used to verify the settings. Spray shape and penetration won't have much effect on the wallfilm build-up as primary and secondary breakup happen after the fuel leaves the nozzle. However, the comparison allows a verification of the used nozzle files in terms of velocity and fuel distribution in the nozzle. The massflow of the nozzle files already has been verified. Furthermore, a correct spray improves the cylinder simulation with combustion in chapter 7.

Figure 71 and Figure 72 compare the spray measurement with the simulation using the same break-up constants for case #1 and #2. Both front and side view are

compared for 0.6ms and 1ms after injection start. The TAB break-up model produces visible spray cones for the individual nozzles which matches the measurement. The overlay of simulation (colored yellow for better visibility) and measurement shows no to little deviation between the directions of the spray plumes confirming the simulated flow direction inside the nozzle.

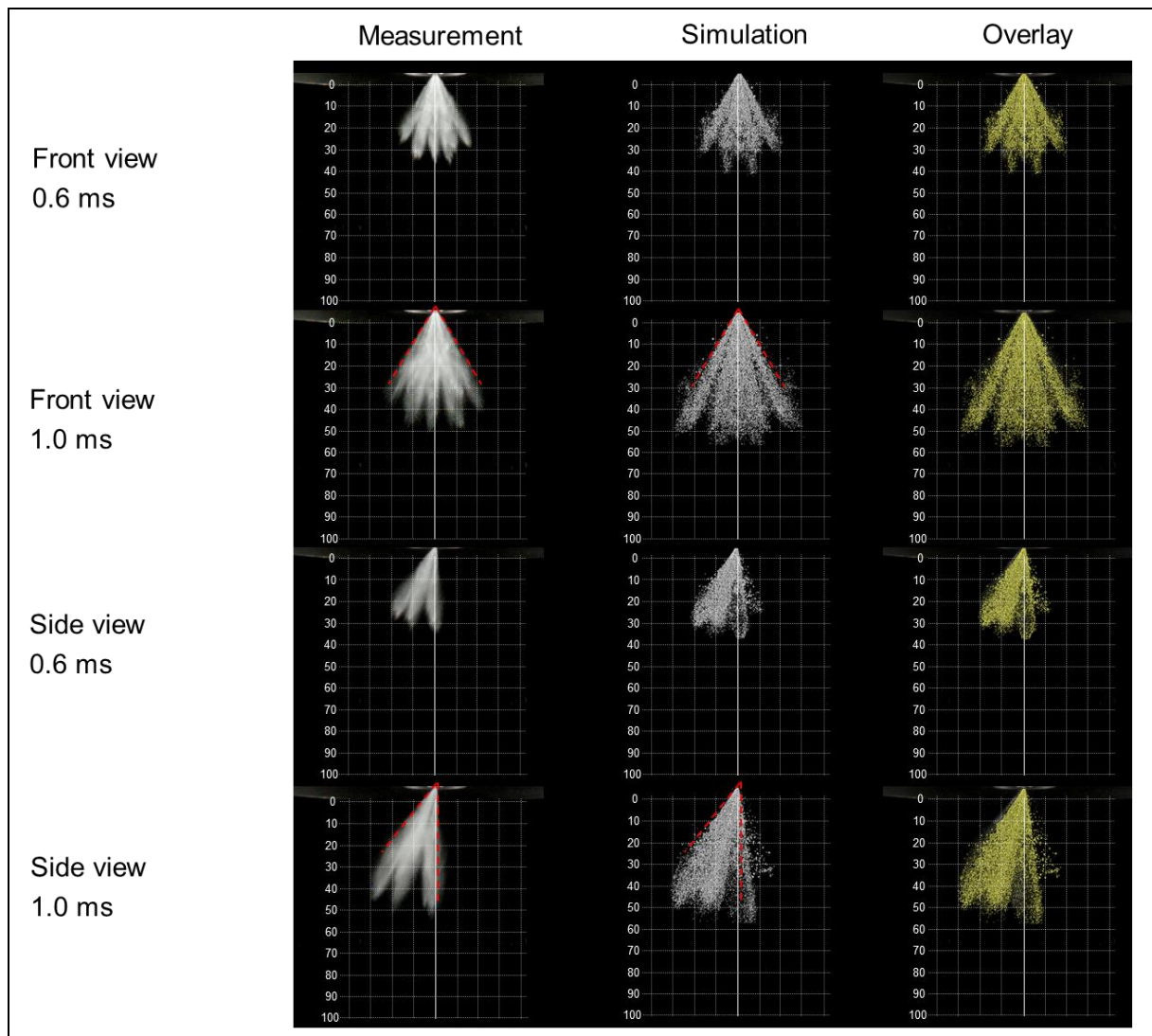


Figure 71: Spray Development and Shape for 50 bar, 1ms and sharp edge (Case #1)

For Case #1 (Figure 71) several checks can be performed to confirm the nozzle file input and break up calibration. The spray cone angles in Front view and side view at 1ms show a good correlation as well as the general shape of the spray. For 0.6ms the individual sprays match nearly perfectly with the measurements while at 1ms the spray from nozzle 2 has a slightly higher penetration. It should be considered however that the measurement pictures are taken from different spray events with fluctuations between the sprays.

The validation of the velocity from the nozzle files can be done by comparing the spray development at 0.6ms and 1ms. Both measurement and simulation show very similar penetration depths at these time steps indicating similar spray velocities.

Figure 72 shows the result of the spray simulation for Case #2 with 150 bar using the same settings as Case #1.

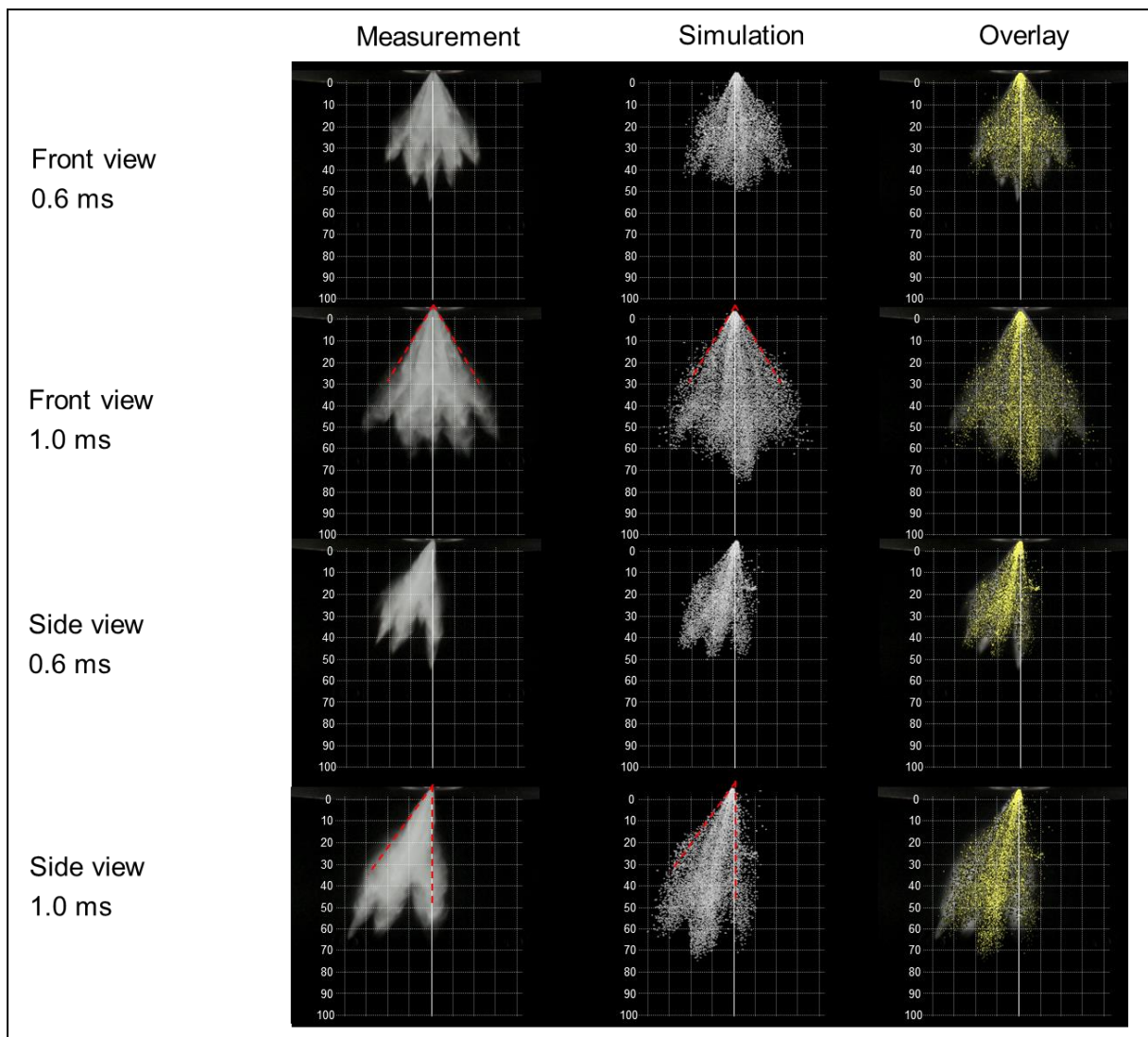


Figure 72: Spray Development and Shape for 150 bar, 2.1ms and sharp edge (Case #2)

Simulation and Measurement show similar correlations as Case #1 confirming the correct setup of the break-up parameters and valid nozzle file inputs independent from the rail pressure.

Applying the calibrated spray settings for Case #4 with rounded edge at nozzle entry shows small differences to Case #2 (Figure 73). Spray cone angle and spray velocity

correlate well with the measurements however the shape of individual sprays is not as clear as Case #1 and #2. This can be explained by the increased cavitation in the nozzle.

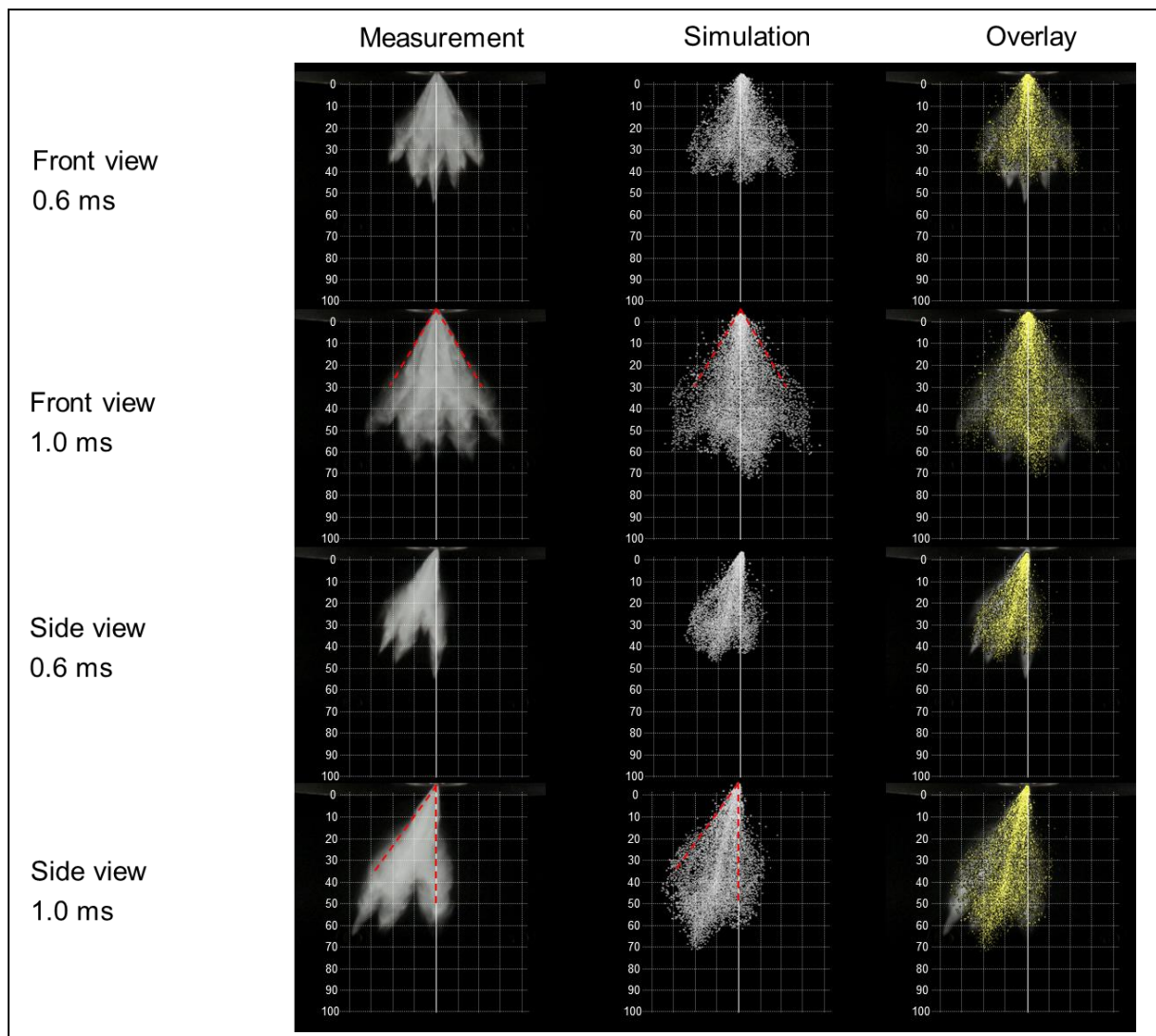


Figure 73: Spray Development and Shape for 150 bar, 2.1ms and rounded edge (Case #4)

Another way to verify the calibrated models is to compare the particle sauter mean diameters in a certain distance from the injector tip. Figure 74 and Figure 75 compare the measured particle diameters averaged from 100 injections 50mm from the injector tip with the simulated droplets at the same distance. Case #2 and #4 show similar distributions as the measurement with slightly bigger droplets for Case #4. The results confirm the chosen approach for using 60 μ m as initial diameter (see chapter 6.2.2).

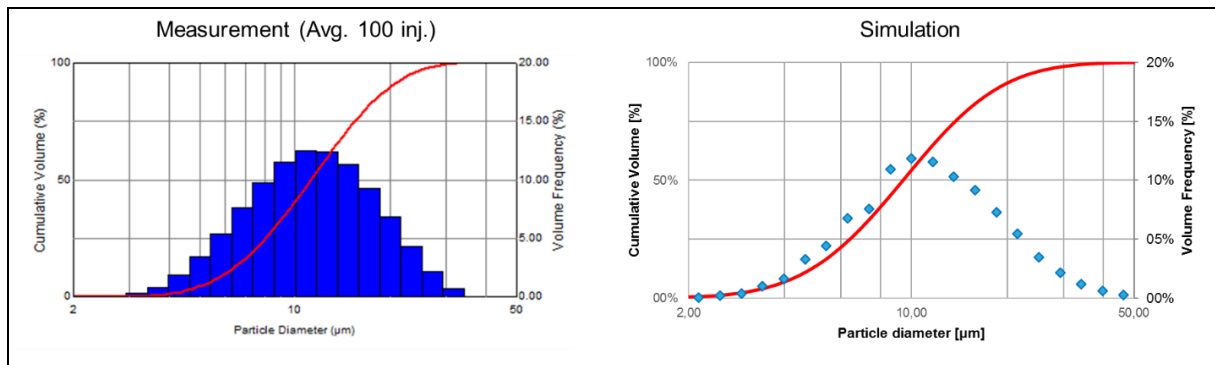


Figure 74: Particle Diameter Distribution Measurement vs. Simulation for 150bar, 2.1ms and sharp edge (Case #2)

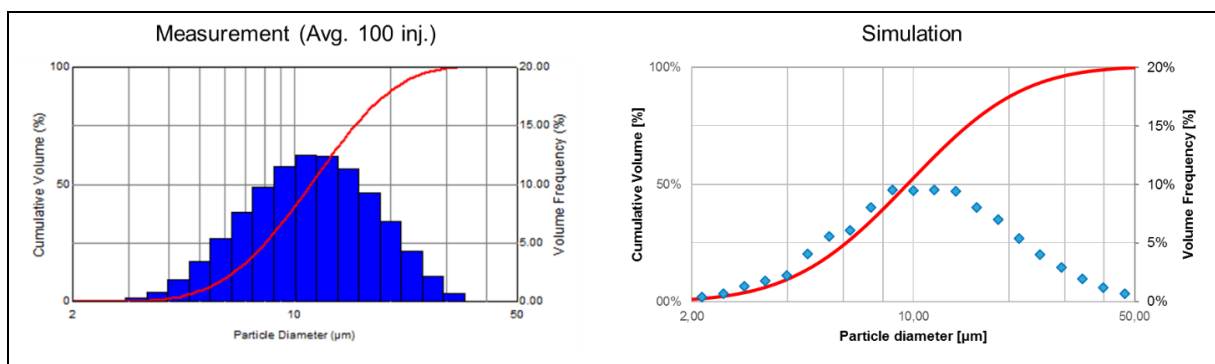


Figure 75: Particle Diameter Distribution Measurement vs. Simulation for 150bar, 2.1ms and rounded edge (Case #4)

As Case #1 (50 bar) shows similar fuel distribution in the nozzle as Case #2 & #4 also 60 μm initial droplet diameter has been chosen. Slower velocities in the nozzle leads to bigger droplets compared to injections at higher pressure. Figure 76 compares the Malvern measurement for 50 bar with the simulation results. In line with the results for 150 bar, the 50 bar simulation comes close to the measurement in terms of droplet diameters at the reference plane.

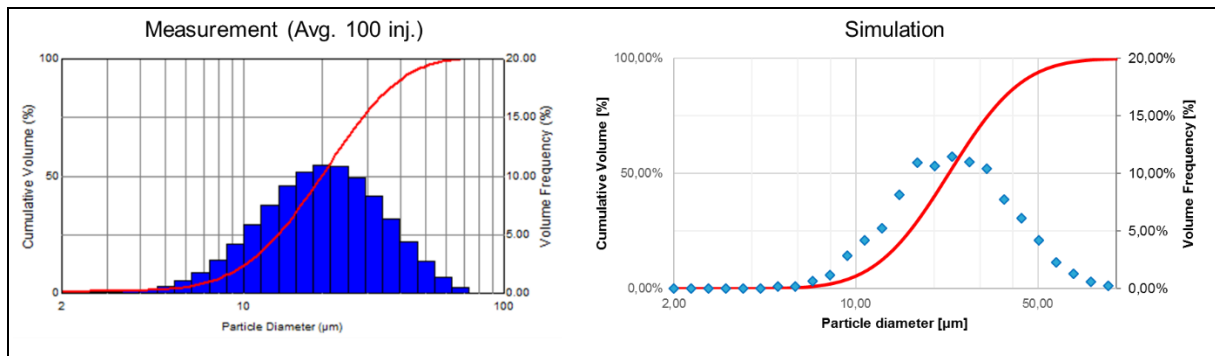


Figure 76: Particle Diameter Distribution Measurement vs. Simulation for 50bar, 1ms and sharp edge (Case #1)

Considering the good overall correlation between measurement and simulation for different fuel pressures despite including the nozzle geometry in the mesh and using nozzle files from meshes with different edge geometry the break-up parameters are sufficient calibrated for further investigations.

6.3.2 Wallfilm on Injector Tip

After calibration of the break-up models the focus was shifted to the wallfilm development during injection and correlation between simulation and measurement. As mentioned in chapter 6.1.2 the investigated HDEV5 injector showed no visible wallfilm boarder due to a rough tip surface. A thin soot layer was applied to the tip to make wallfilm areas visible – the liquid is washing the soot away leaving a non-sooted area where the film is supposed to be.

Figure 77 puts the measurement and simulation side by side from start of injection until the end. Wallfilm areas in the simulation have been colored white for easier comparison. During the injection (0.8ms and 1.6ms) the injector tip is hidden due to the bright stream of liquid but around the counter-bores a wash up of the soot can be observed. In the simulation, the wallfilm also starts to build up between the injector holes and even more on the tip. Comparing the 0.8ms step with the 1.6ms step the film starts to evaporate on the outside reducing the area above the counter-bores.

At the end of injection, the cleaned area in the measurement matches the wallfim area of the simulation. The red dotted line follows the border between sooted and cleaned injector tip from the measurement and is overlaid onto the simulation for better comparison.

The pictures from the simulation have been taken from Case #4 (150 bar, 2.1ms, rounded edge). In this case the wallfilm model delivers an accurate prediction of the expected film area.

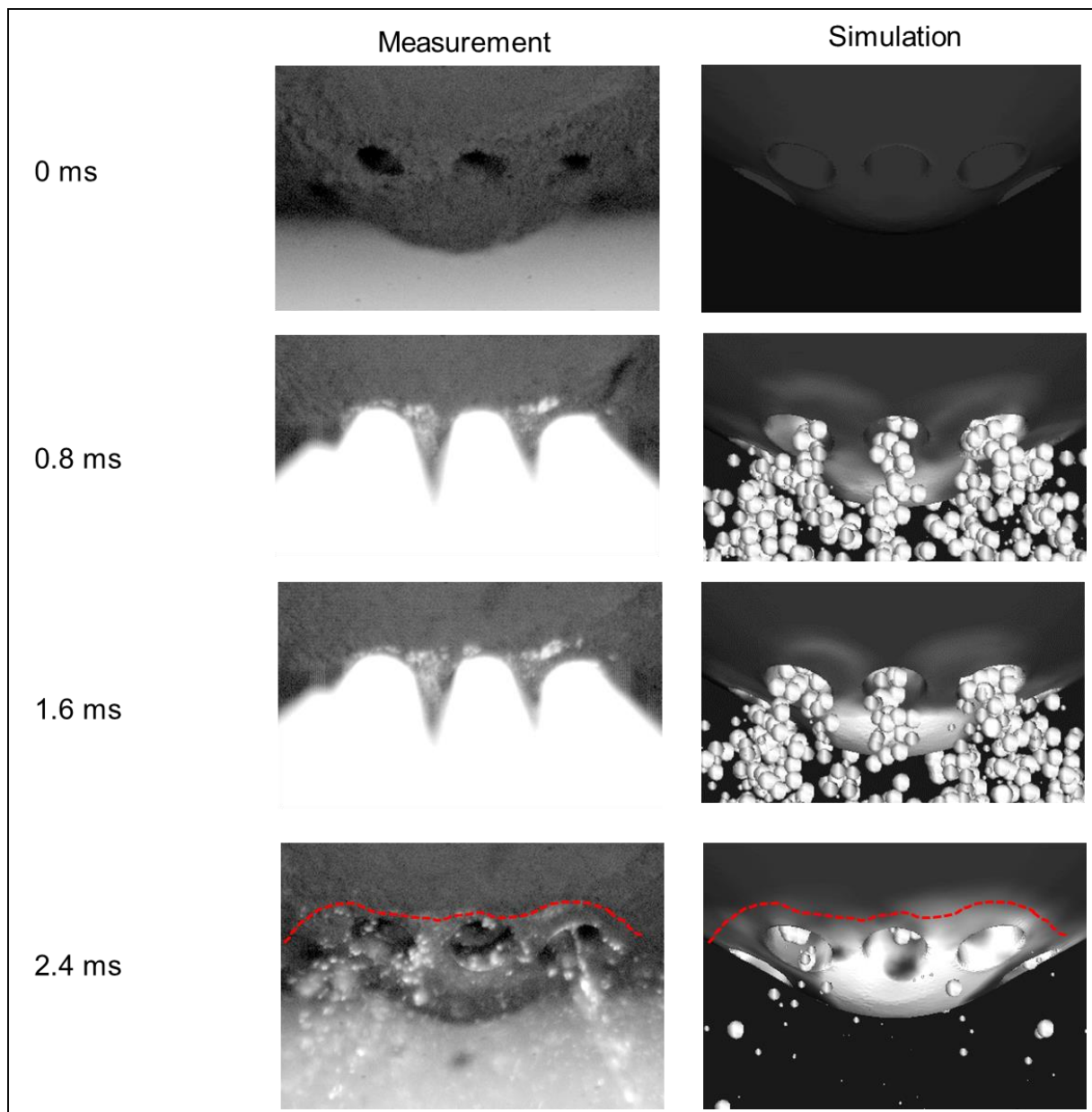


Figure 77: Wallfilm Measurement and simulation (Case #4, rounded edge) on injector tip at 150 bar, 2.1ms injection. Sooted tip to increase visibility

Comparing the results from Case #2 with the measurement which has also been simulated at 150 bar shows a different result (Figure 78). While the result at 2.4ms looks similar to Case #4 and the measurement the intermediate steps are different. During the injection, no film can be seen between the holes and only a little in the center on the tip. Furthermore, the simulation shows no symmetry for hole #1 and #3 with #1 having a lot more wallfilm than #3.

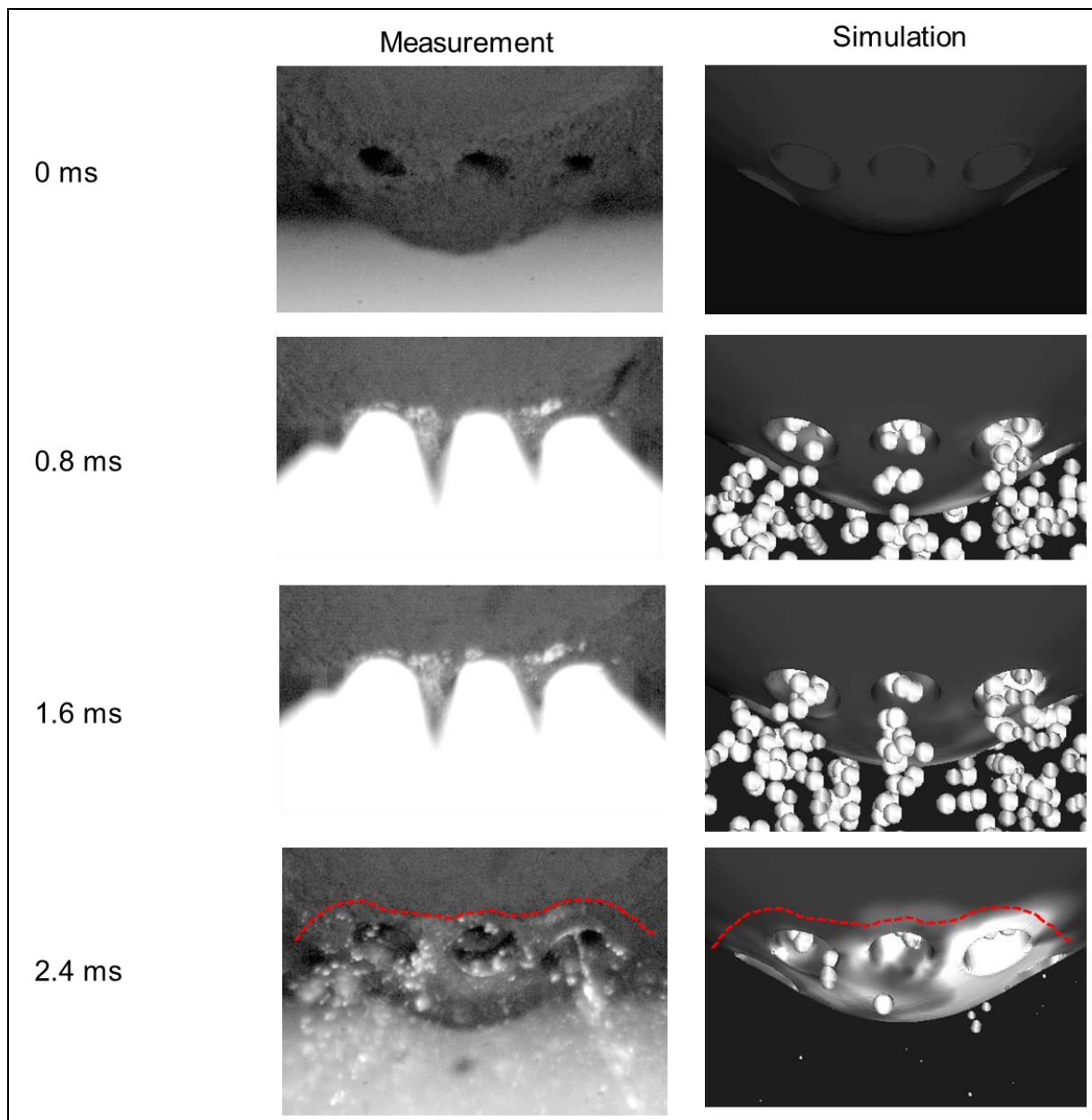


Figure 78: Wallfilm Measurement and simulation (Case #2, sharp edge) on injector tip at 150 bar, 2.1ms injection. Sooted tip to increase visibility

Based on this observation Case #4 with rounded nozzle entry seem to represent the wallfilm area better and is therefore chosen for further investigations.

Investigating the development of the wallfilm in Figure 79 shows the Injector holes #4 & #7 as source for early wetting. At the beginning of the injection the wallfilm in the center of the tip is mainly fed by these holes later joined by hole #1 and #3. After 1ms there is a film visible in all seven counter-bores and the film thickness in the wet area is increasing. At the end of injection (needle is closed at 2.2ms) the film inside the nozzle and counter-bores is feeding the film on the tip leading to the shape at 2.4ms which can be compared to the measurement where the tip becomes visible again (see

above). This development continues after 2.4ms until there is only a little film left in the nozzles.

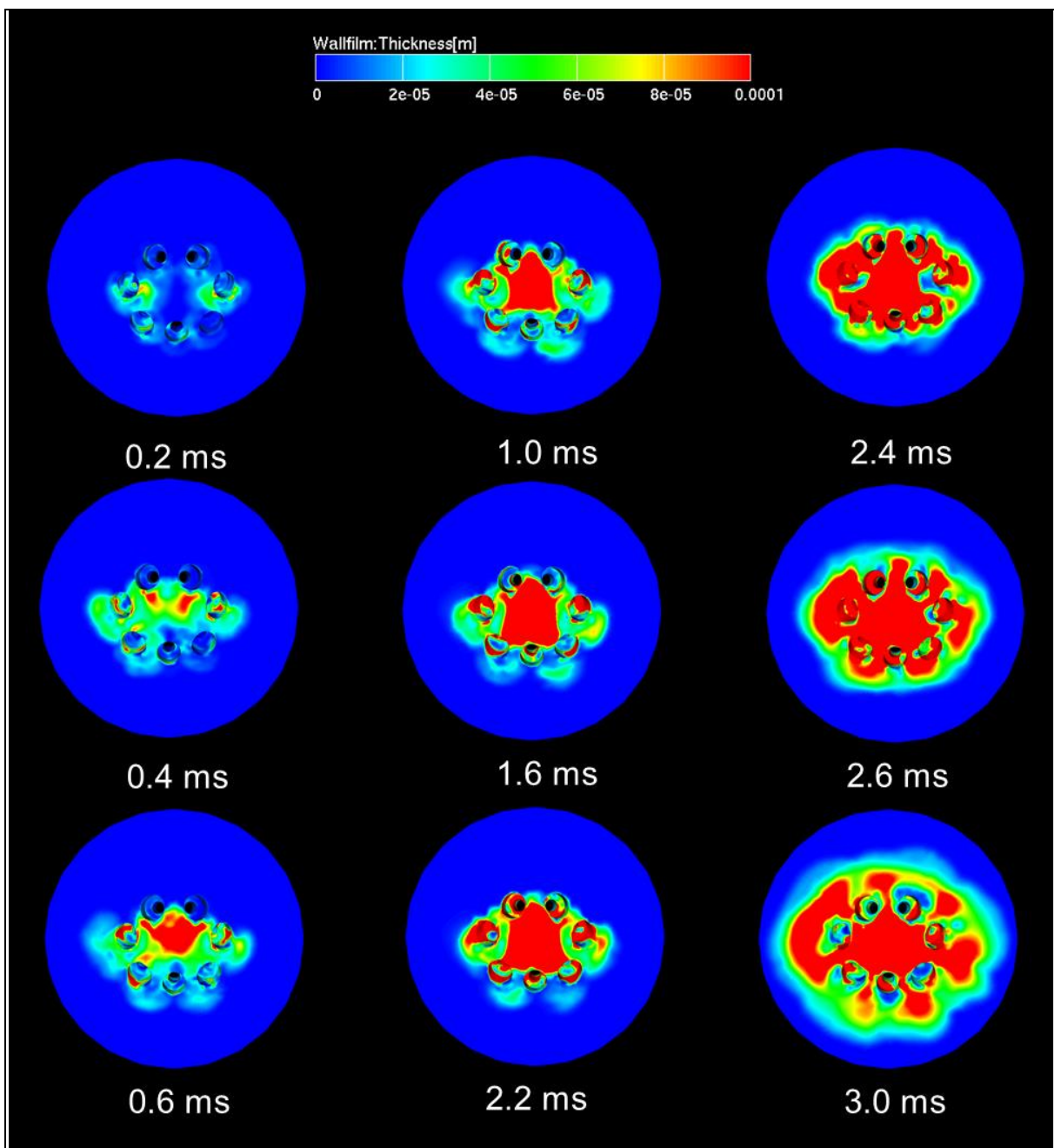


Figure 79: Wallfilm development on injector tip and in holes during injection for Case #4 (Needle is closed at 2.2 ms)

The observations above are also visible in Figure 80 which gives an overview over the wallfilm mass in the injector holes (small holes and counter-bore combined) and on the tip. After the needle closed at 2.2ms the wallfilm in the holes is decreasing and feeding the film on the tip.

The total film mass reaches its peak when the needle is closed and is then slowly decreasing due to limited evaporation at 20°C chamber temperature.

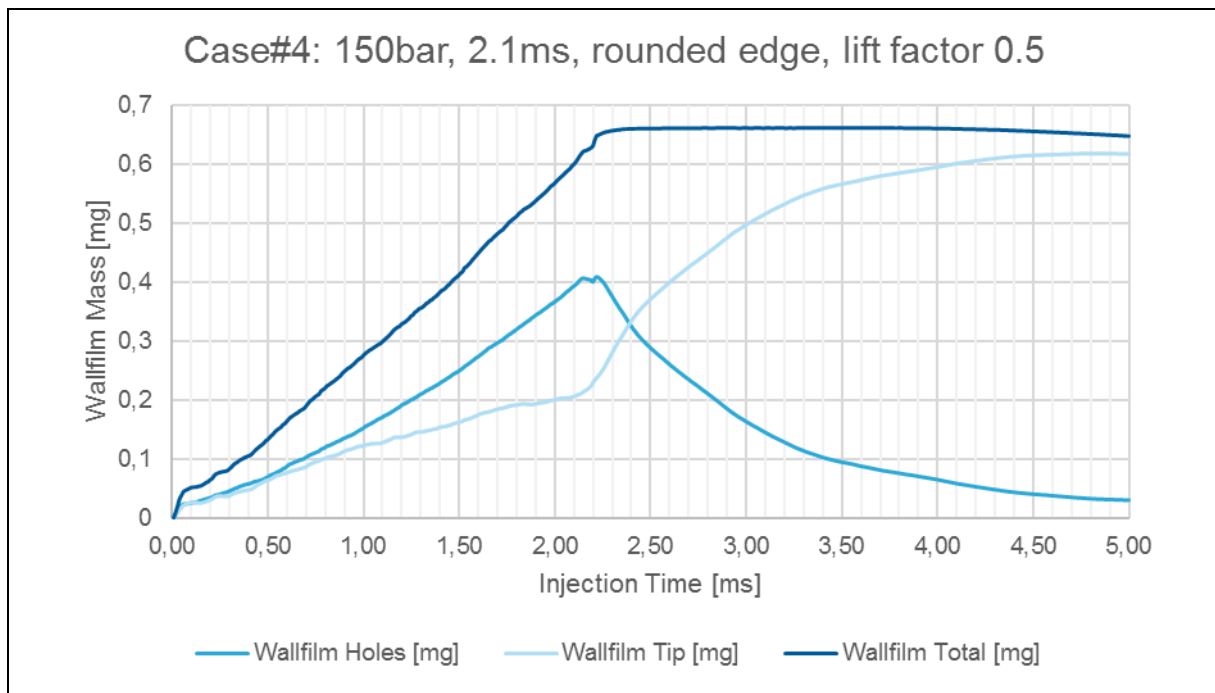


Figure 80: Wallfilm mass during and after injection for Case #4 in holes and on the tip

Based on the wallfilm assumptions described in 4.2 the presented simulations will overestimate the total film mass and thickness while using small cells. Currently there is no workaround possible as bigger cells in the tip area (e.g. 0.5mm) would lead to simulation divergence (cell size steps to big between counter-bore and tip) and decrease the available resolution of the film area.

The influence of a reduced entrainment and evaporation rate at cells further away from the nozzle is the same for all simulations using the same mesh meaning that trends still can be observed due to different system boundaries like higher tip temperatures, fuel temperature and so on. To compare the results with the coked hardware from chapter 3.5 the trade-off has been made in favor of an accurate film area.

Figure 81 compares the simulation of case 4 at the end of injection with the measurement. The simulation shows a film area with 200µm at the tip. The measurement was taken without applying soot first, leading to a non-visible wallfilm area however, a wallfilm with this level of thickness would be visible as droplet in the red marked area. The absence of the droplet confirms the overestimation of wallfilm mass due to reduced film entrainment.

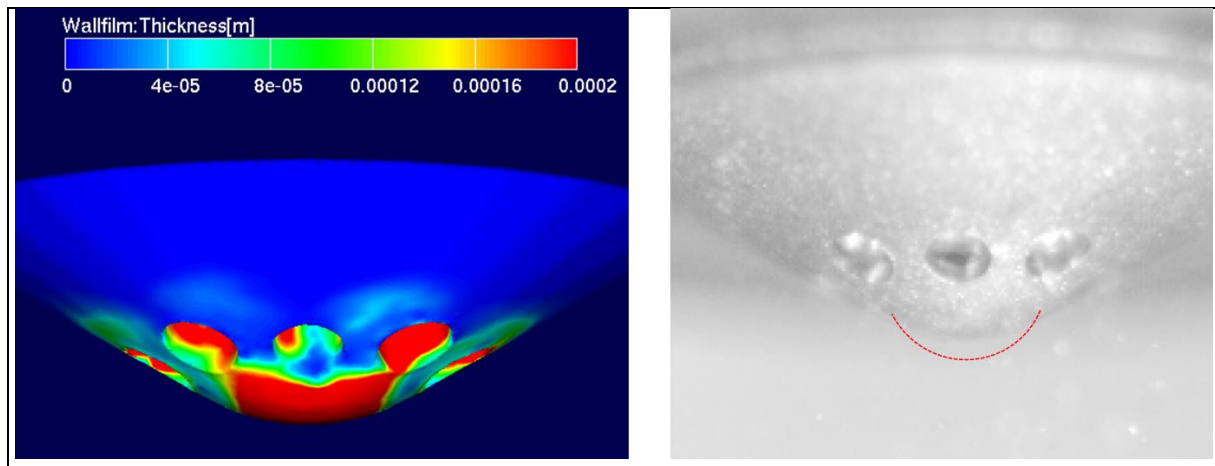


Figure 81: Overestimation of wallfilm thickness in simulation

When comparing the total film mass on the injector in relation to the injected mass for the investigated cases a clear trend can be observed. As seen in Figure 82 an increase of injection pressure from 50 bar (Case #1) to 150 bar (Case #2) with the same geometry significantly reduced the relative wallfilm mass. This is also valid for the simulations with the rounded nozzle entry when increasing fuel pressure from 110 bar (Case #5) to 150 bar (Case #4). A further increase to 300bar brings the wallfilm level down to the same level as the sharp edge geometry. This could be explained by the increased velocity of the fuel droplets with higher pressure which increases shear forces on the film.

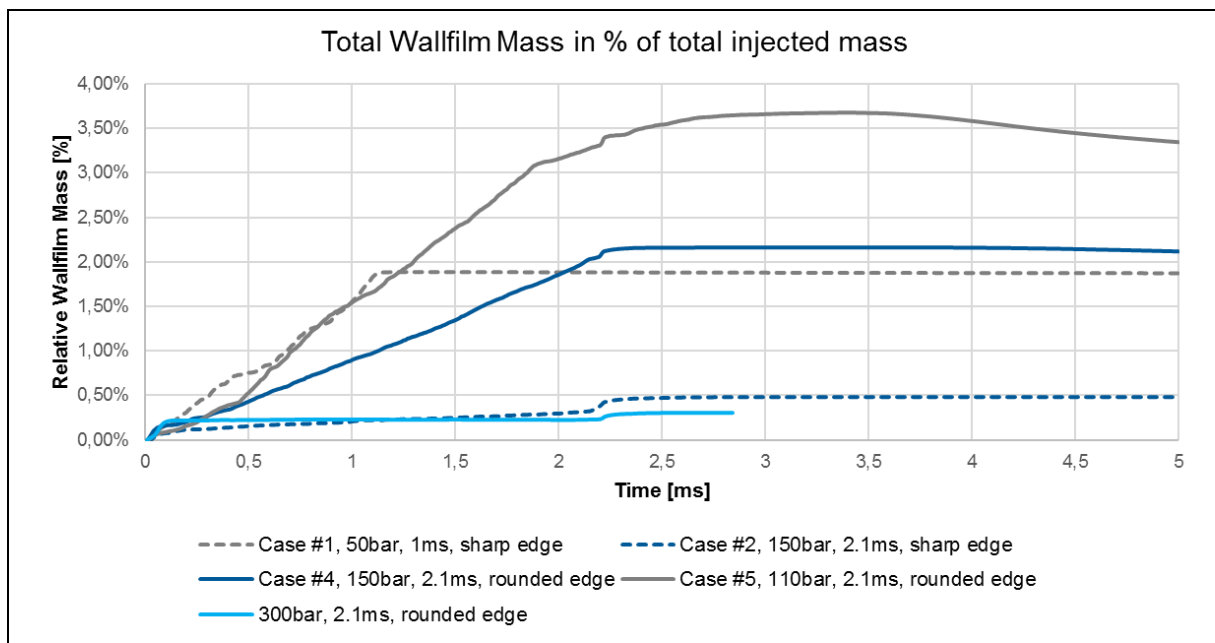


Figure 82: Relative Wallfilm Mass for Case #1, #2, #4 & #5 and 300 bar.

Comparing Case #2 and Case #4 with the same fuel pressure and injected mass shows a up to 4 times higher film mass for the injector with rounded edges. One possible explanation for this behavior is the stream development in the nozzle in Figure 57 which shows more fuel (increased volume fraction) hitting the edge of the counter-bore in Nozzle #2 for Case #4.

6.3.3 Conclusion from Results

Following conclusion can be drawn from the presented results:

- The available nozzle files from the injector simulation are a valid input for the spray simulation
- Break-up model parameters are calibrated to match spray shape, penetration and droplet distribution for different fuel pressures
- Wallfilm on the injector can be simulated and matches the measured area which was made visible using a thin soot layer
- Total wallfilm mass is overestimated due to too small cell size around the injector tip but can still be used to compare trends. In the following simulations, the wallfilm mass will be used as a relative value.
- Higher injection pressure leads to a reduced wallfilm; a rounded edge at the nozzle entry in the seat area increases the film mass.

7 Engine Simulation

This final simulation chapter describes the setup and result of the engine simulation based on the previous chapters

7.1 Measurement Inputs

The following chapter describes the available inputs for the cylinder simulation.

7.1.1 Operating Point from Test Cycle

Based on the test cycle measurement results from chapter 3 the 3000 rpm / 10bar BMEP operating point has been chosen for the simulation. This operating point showed a continuously increase of PN emission over the test duration with a significant drop close to the base level after cleaning the injectors. Additionally, the observable increase of PN levels from start to end of the single 8-minute phase indicated quick deposit build up suggesting a critical operating point.

Table 11 list some of the over 200 different recorded measurement results for the chosen operating point at the beginning of the 60-hour test cycle. The fuel injection is timed quite early but showed good BSFC values during base calibration. There is no exact EGR rate measurement as calibration has been done based on EGR valve opening position. However, earlier investigations in a different project with the same engine indicate around 20% EGR rate at this operating point.

Table 11: Engine boundaries at 3000 rpm / 10 bar for simulation input

Engine Speed	3000 rpm	Lambda	1
Engine Load	10 bar BMEP	Intake Air Temp	35°C
Fuel Pressure	110 bar	Intake Pressure	1.25 bar abs
Injection Time	2.1 ms	Exhaust Pressure	1.35 bar abs
Injection Start	306°CrA BTDC	Oil Temperature	107°C
Ignition	18°CrA BTDC	Coolant Temp	93°C
MFB 2%	3°CrA BTDC	EGR	40% valve opening
MFB 10%	1.8°CrA ATDC	boosted EGR temp	34°C
MFB 50%	13.5°CrA ATDC	Max Cyl. Pressure	55 bar
MFB 90%	32.5°CrA ATDC	Fuel	China RON 92

7.1.2 Crank Angle based Inlet and Outlet Boundaries

During the deposit cycle tests, only the cylinder pressure curves were monitored in crank angle resolution to avoid engine damage due to knocking and to run the tests with the AVL real time controller for combustion optimization. All other values are averaged over the 30 seconds' measurement period.

For an accurate cylinder simulation, it is necessary to use crank angle based inlet and outlet boundaries like air massflow on the intake side instead of static averaged pressure. As this data is not available from the tested engine due to a too complex sensor setup inputs from a geometrically similar engine have been used.

This reference engine is a 2.0l TGDl engine using the same 140° Miller intake camshaft as the 1.6l test engine (HiEff) from this project; intake port size and shape are similar (Figure 83). To use the available data for the simulation the results must be adapted to the different swept volume and valve timing. The volume based intake massflow curve will be scaled by the factor S according to (7.1). This approach has been used successfully in previous projects for Miller engines in AVL.

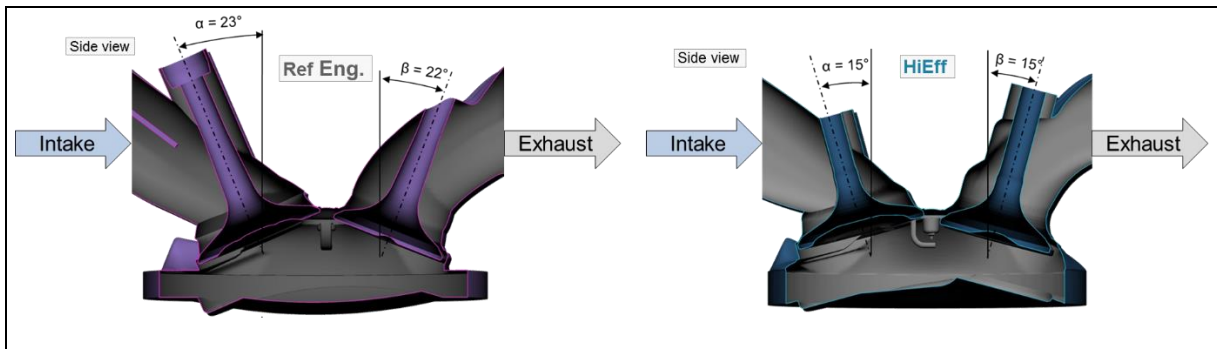


Figure 83: Cut through the valves for the reference and HiEff engine

$$S = \frac{V_h(Hieff)}{V_h(Reference)} \quad \text{with} \quad V_h = \frac{Bore^2 \pi}{4} * Stroke \quad (7.1)$$

In total 3 crank angle based inputs are required: intake air mass flow rate, intake air temperature and exhaust backpressure. Out of these 3 curves only the intake mass flow rate needs to be scaled using the described factor. The scaled mass flow curve, the temperature curve and the exhaust backpressure curve then need to be shifted to match the different valve timing. In Figure 84 the valve lift curves for the reference engine and the HiEff engine from the deposit tests are shown.

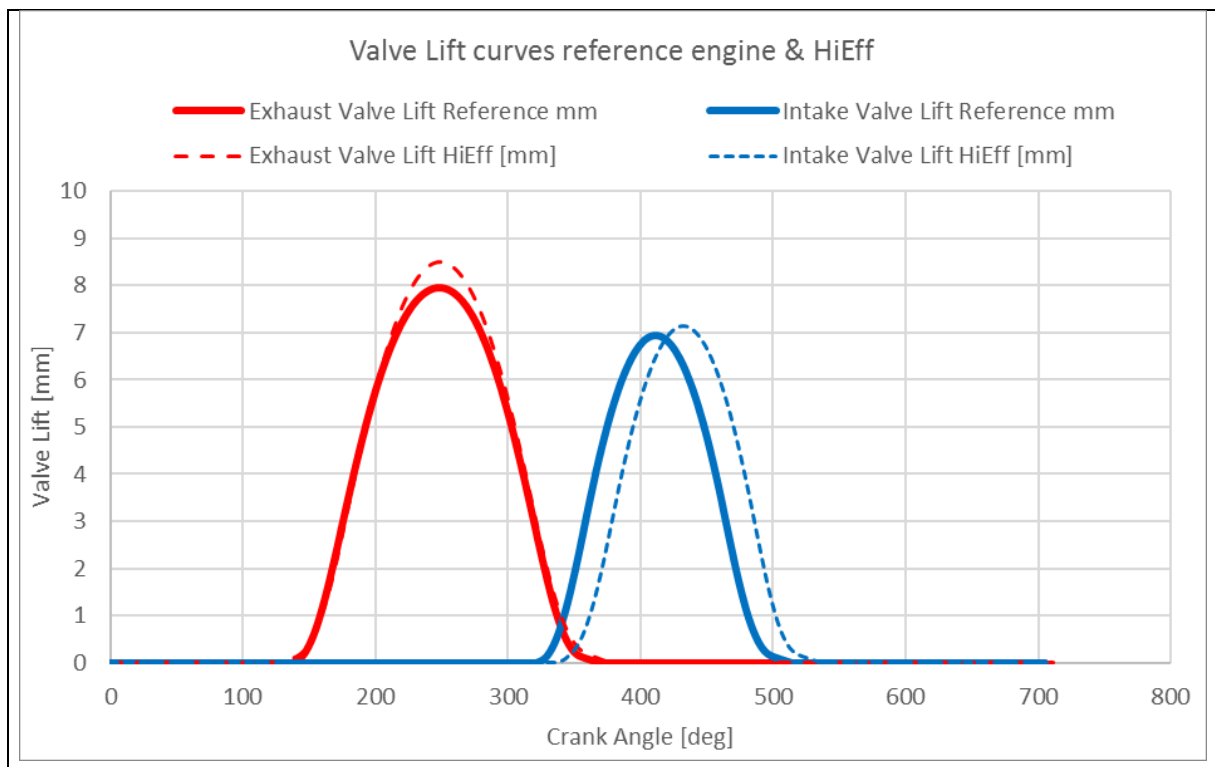


Figure 84: Intake and Exhaust Valve Timing for the HiEff and reference engine at 3000 rpm / 10 bar BMEP

The exhaust valve curves match in terms of timing, therefore no shifting is required for the exhaust back pressure input. Regarding the intake valve timing the investigated HiEff engine opens 18° Crank Angle after the reference engine. As a result, the scaled intake mass flow curve and the intake temperature curve are shifted towards firing TDC. The used mass flow curve for the simulation can be seen in Figure 85.

It has to be considered that the intake mass flow and temperature curves from the reference engine don't include EGR. As the power output is kept constant the intake massflow rate will be increased for simulations including EGR to keep the same air mass in the cylinder. For a 20% EGR rate the mass flow needs to be increased by more than 20% to compensate the flow losses in the valve seats. The correct rate is chosen iteratively during simulation.

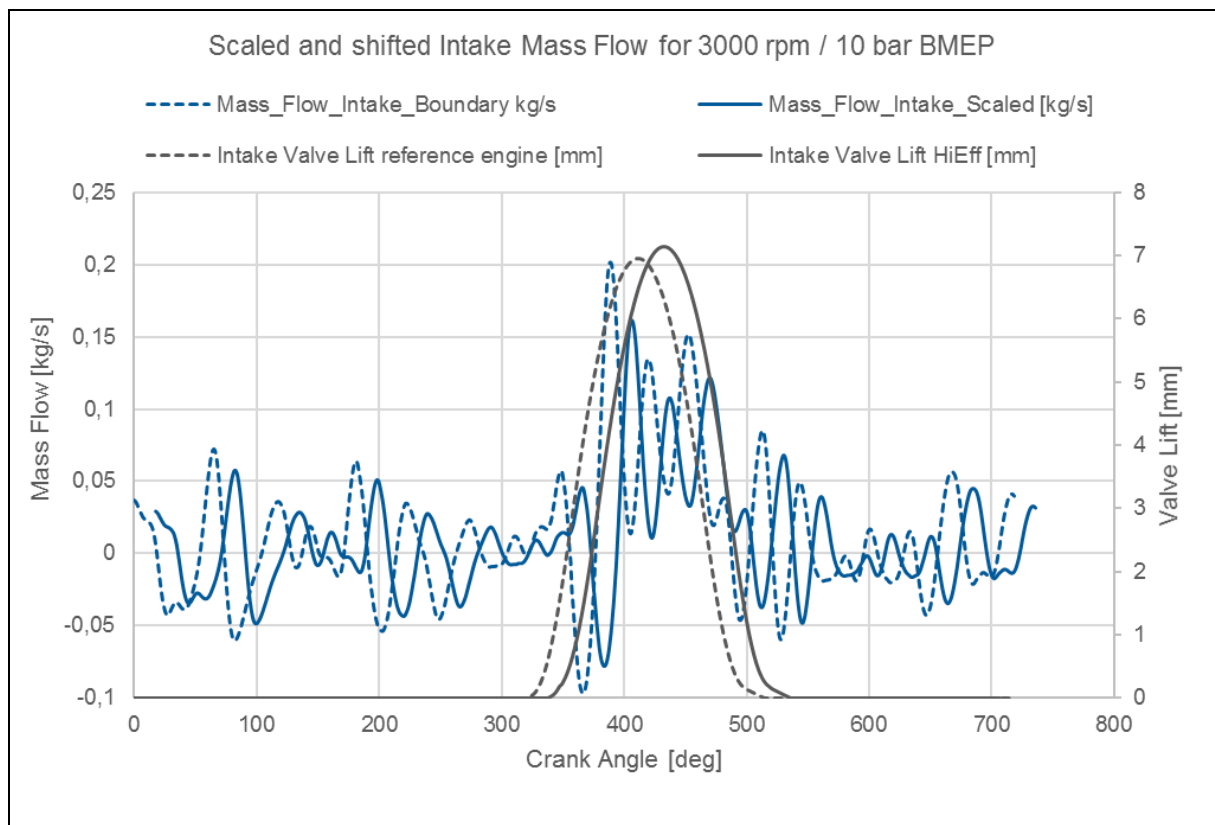


Figure 85: Scaled and shifted intake mass flow over crank angle as simulation input @ 3000 rpm / 10 bar BMEP

7.1.3 Deposit Pictures

The deposit pictures taken during and after the engine tests in chapter 3 can be used to validate the wallfilm simulation by comparing the coked area in the injector tip with the remaining fuel in the simulation. As the engine test run consist of several operating points the wallfilm area in the simulation doesn't need to fill the complete coked injector area to be plausible. It is possible that other operating points fill the remaining area. To fully compare the coked hardware with the simulation it would be necessary to run the coking test only in one operating point or to simulate all tested points. Both options can be considered for further studies but are not part of this work.

On the other hand, a simulated wallfilm area which exceeds the coked area can also be plausible as wallfilm is a requirement for coking but doesn't necessarily lead to it. However, the main wallfilm area should be within the coked area on the injector tip shown in Figure 86. Injector from cylinder 2 shows more deposits compared to cylinder 1 indicating variations between the cylinders.



Figure 86: Coked injectors from China 92 deposit test runs from cylinder 1 (left) and 2 (right).

7.1.4 Nozzle Files

Another input for the engine simulation are the nozzle files which are used to simulate the fuel injection. The creation and verification of the nozzle files has been already done in the previous two chapters for 50 and 150 bar and different edge geometry in the injector nozzle seat area.

However, for the current operating point the fuel pressure is set with 110 bar therefore all nozzle files for the engine simulation are created with this pressure. It is assumed that the earlier presented calibration values which are valid for 50 and 150 bar will also match for 110 bar. A quick confirmation can be done by comparing the simulated fuel mass rate for n-Heptane at 110 bar (Case #5) with the measurement as shown in Figure 87.

The nozzle files have been created using the mesh with rounded nozzle entries at the seat area as the corresponding simulation at 150bar showed the best correlation with the wallfilm measurements.

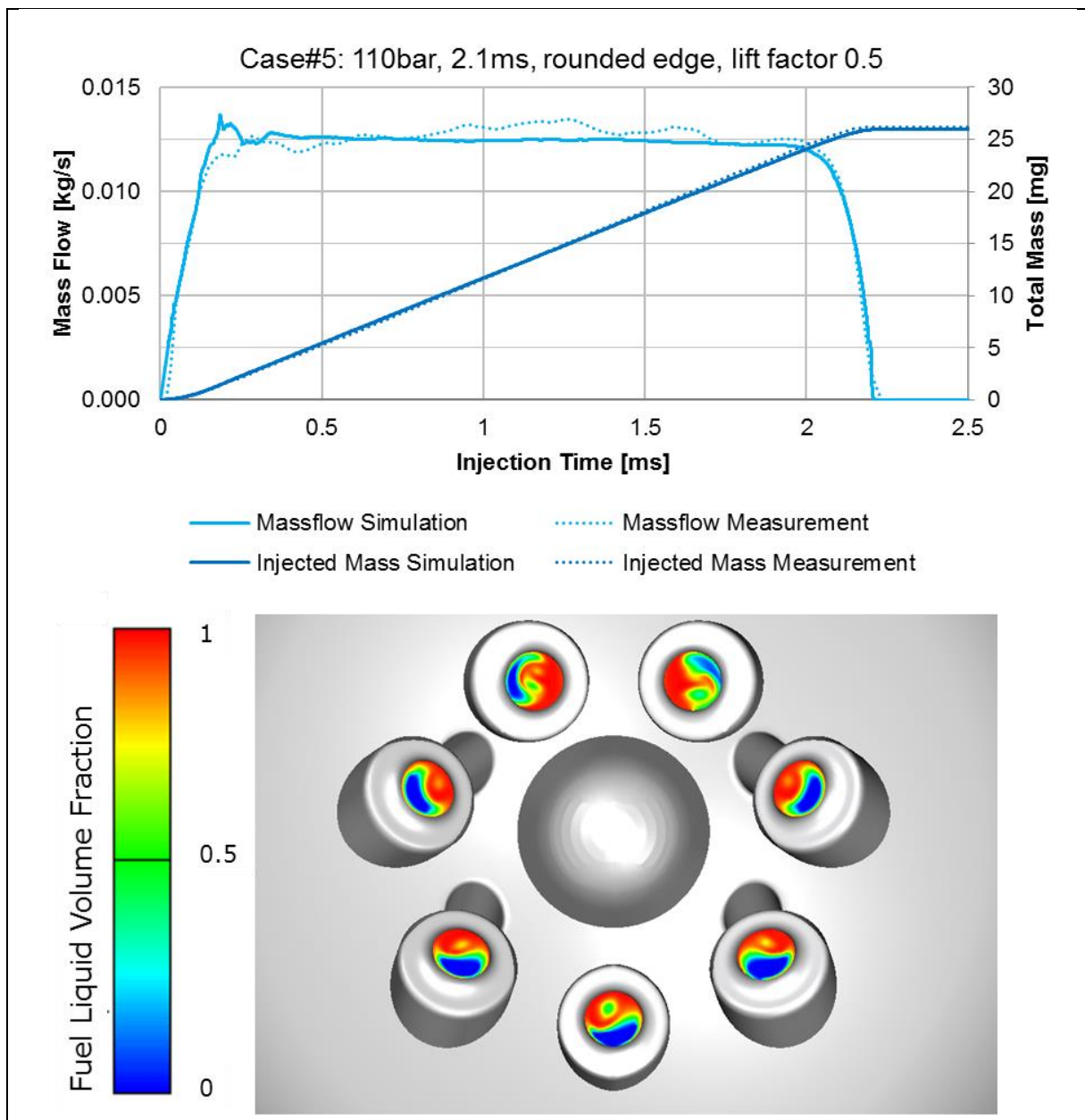


Figure 87: Fuel Mass Flow and fuel volume fraction for 110 bar and n-heptane (Case #5)

7.2 Model Description and Boundaries

The mesh has been created using AVL FIRE’s Fame Engine Plus for polyhedral meshes while the simulation was run in FIRE v2017 and v2017.1 using a combination of the Lagrangian Multiphase (Spray) Module [71], Combustion Module [72] and Wallfilm Module [58].

7.2.1 Mesh Setup

As input for the mesh an inverted 3D model of the HiEff has been used which represents the air volume. The model included intake port, intake valves, cylinder with combustion chamber, piston and liner, spark plug, injector nozzle, exhaust valves and exhaust port. The movement of the mesh is based on a geometric function and on the provided valve lift curves. The Fame Engine Plus tool moves the piston and valves according to the input data at a certain crank angle and creates a new poly mesh. This mesh is then stretched for a few crank angles and matched with the mesh from the next step.

A polyhedral mesh has been used for the same reason as the spray box simulation – it allows high cell size ratios which is important if the injector nozzle geometry should be included in the mesh. Cell size ranges from 4mm down to 5 μ m in the injector orifice area. A full 720-degree cycle was modeled starting with exhaust valve opening and also finishing at EVO. Figure 88 shows a cut through the valves at start position (0.2mm valve opening) and through the spark plug during intake phase.

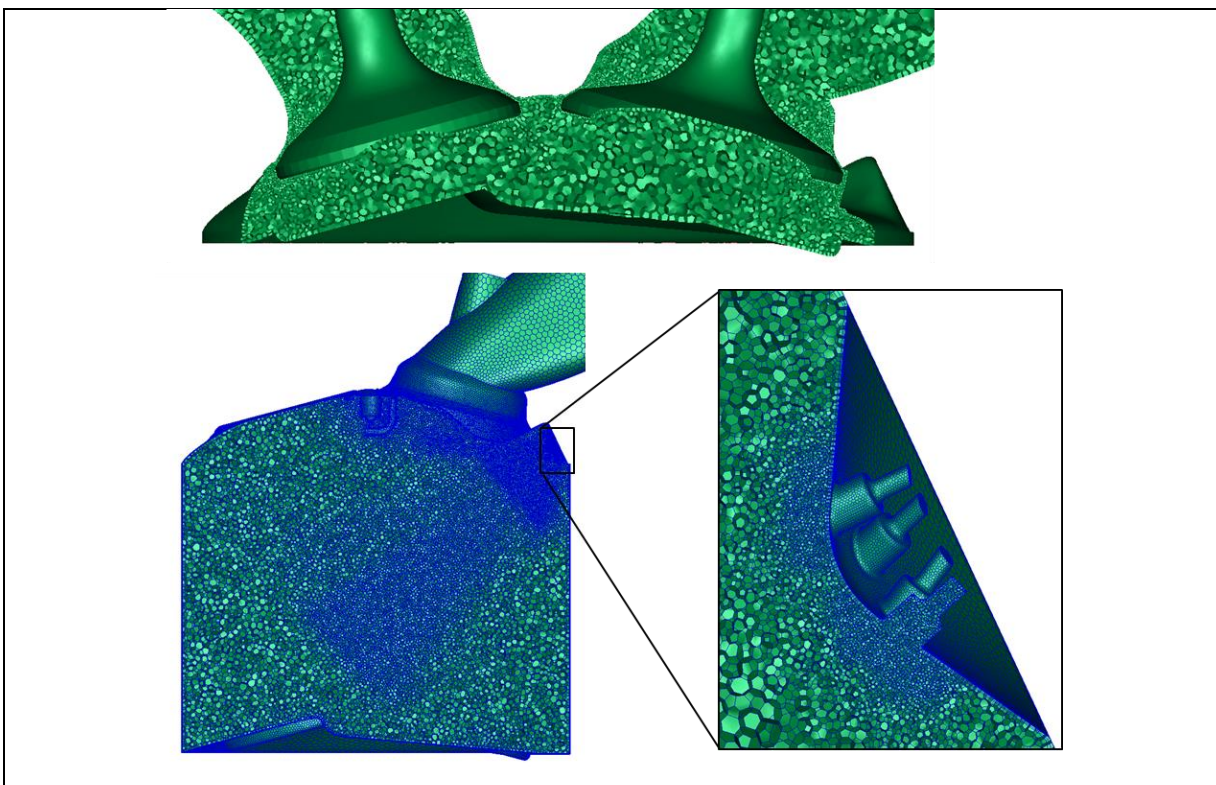


Figure 88: FIRE FEP mesh with detail in the injector area

The different cell sizes are clearly visible as well as the fine resolution of the injector tip area including the nozzles. During injection, there is also a cone refinement in the

spray direction for better simulation of the mixture process. Further details can be found in Table 12.

Table 12: Engine Cylinder mesh properties

Number of cells	0.6 Mio (Firing TDC) to 4.7 Mio (Overlap phase)
Min / max cell size	5 μ m / 4mm
Simulation steps	0.1° - 0.5° Crank Angle
Simulation results	Air charge movement in Cylinder, Spray behavior, Wallfilm build-up during injection, Wallfilm evaporation after injection, combustion

7.2.2 Boundaries and Simulation Setup

The simulation is a combination of a Lagrangian spray simulation with a ECFM-3Z combustion simulation. This Extended Coherent Flamelet Model (ECFM) considers 6 different zones in each cell from air and exhaust gas to fuel, mixture, flame and burnt gases. It's the standard model used in AVL for gasoline combustion. The same spray break-up and wallfilm settings as in the spray box simulation are used as they have been verified by measurements.

As the wallfilm development and evaporation on the injector tip are the main focus of this simulation standard Miller engine values have been used for the non-injector wall temperature boundaries. The values in Figure 89 are experience based and are not further investigated. Injector Tip and Hole Temperature is varied for different simulations. Inlet and Outlet boundary conditions are taken from the reference engine as described in 7.1.2.

Table 13: Simulation variants engine simulation

Engine Case	Fuel Temp	Tip Temp	Hole Temp	EGR Rate	Intake Temp	Fuel	Nozzle File Case
#	°C	°C	°C	%	°C	-	-
E1	-	150	110	0	30	No injection	
E2	50	150	110	0	30	Iso-Octane	#7
E3	50	150	110	20	30	Iso-Octane	#7
E4	50	150	110	20	50	Iso-Octane	#7
E5	80	150	110	0	30	Iso-Octane	#8
E6	50	180	160	0	30	Iso-Octane	#9
E7	50	210	180	0	30	Iso-Octane	#10
E8	50	150	110	0	30	Multi-Comp	#11
E9	50	150	110	0	30	Multi-Comp	#12
E10	50	150	110	0	30	Multi-Comp	#13

All simulations are performed for the same operating point at 3000rpm / 10 bar BMEP with 110bar injection pressure and 2.1ms injection time. Engine Case #E1 is the reference case for air charge motion and tumble measurement without injection and ignition. Engine case #E2 to #E7 was simulated with Fire v2017 as only a single component fuel is used. For case #E8 to #E10 the simulations were performed in Fire v2017.1 which supports a multi-component wallfilm model. This model considers individual components in the film with different evaporation behaviors.

7.4 Results

The following chapter discusses the results obtained from the engine simulation variants.

7.4.1 Air Charge Motion from #E1

The simulation without injection and ignition is used to investigate the air flow around the injector tip and the charge air motion during a full cycle. Figure 90 shows the velocity vectors during the intake valve opening phase in a cut through the intake valve.

The air flow in the intake port is pulsating visible through the change of velocity in the valve seat area from one step to another. A swirl motion is created especially through the high velocity along the cylinder walls at 120°CrA after TDC. This motion continues then until it breaks up close to firing TDC visible in Figure 91.

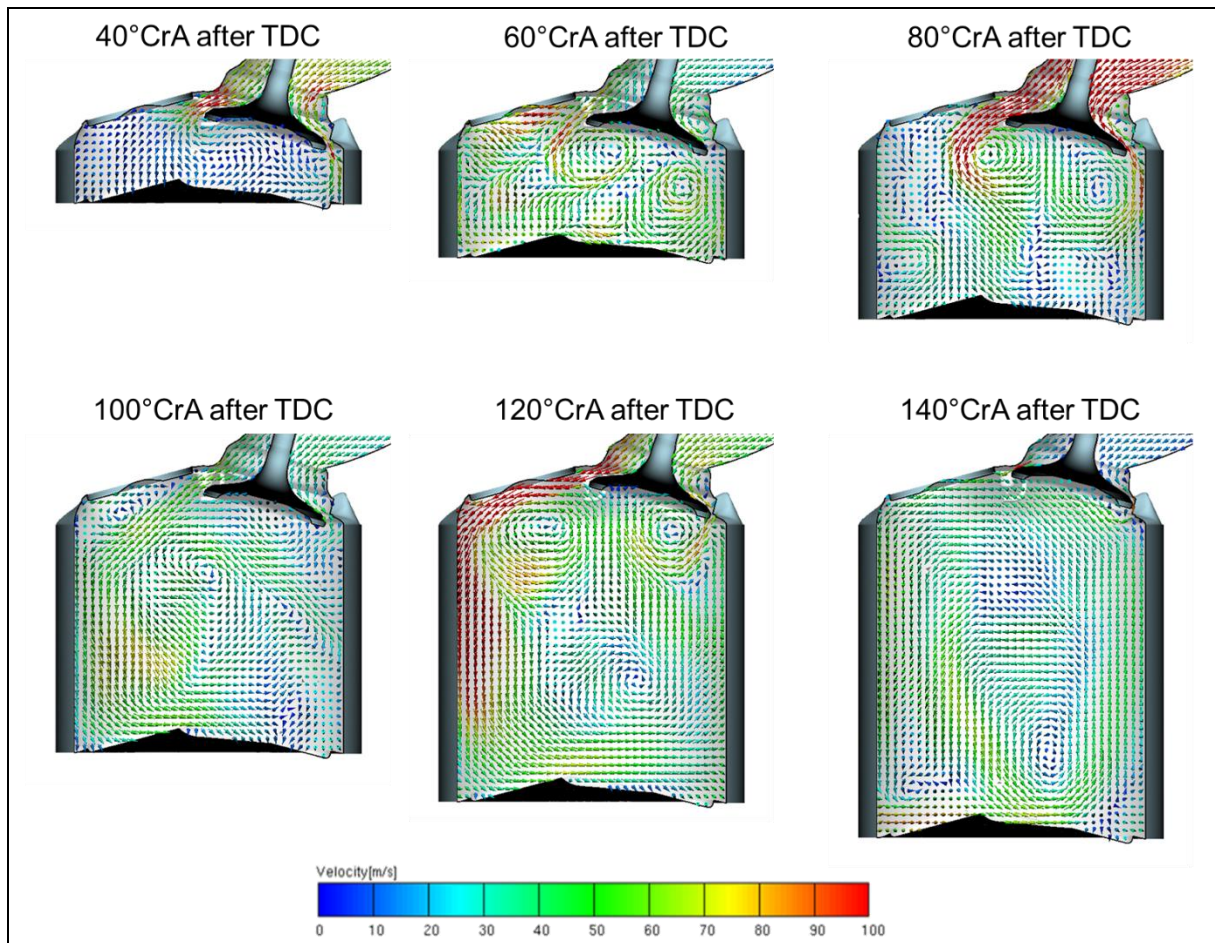


Figure 90: Air charge motion development during intake valve opening – cross section through intake valve (Case #E1)

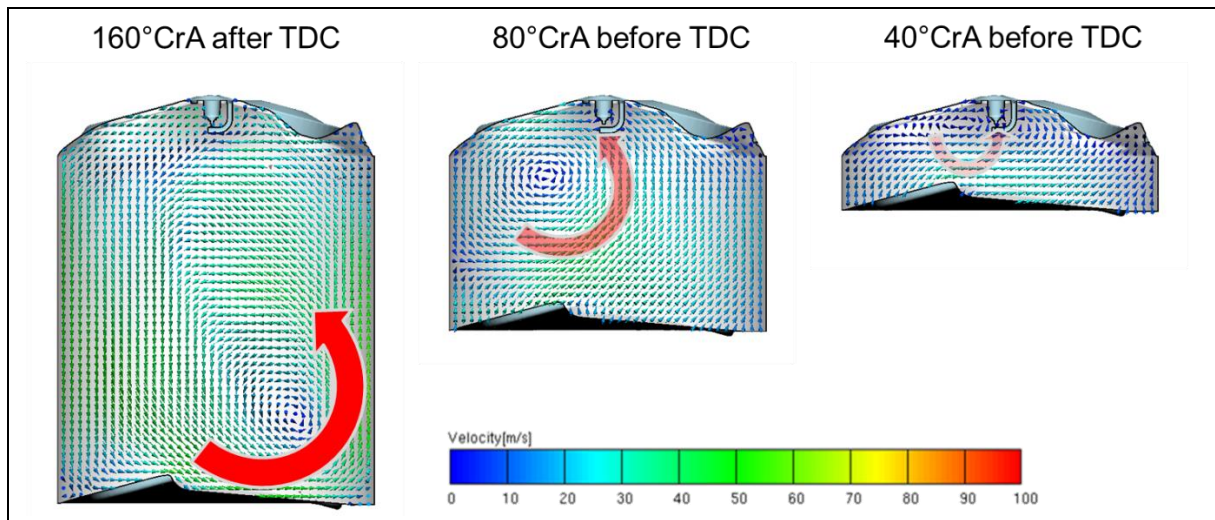


Figure 91: Swirl break-up towards firing TDC – cross section through the center

As shown in chapter 4.2 wallfilm evaporation on the injector tip mainly depends on the flow velocity parallel to the wall, concentration of fuel in the gas and film temperature which is a function of fuel temperature, injector tip temperature and gas temperature. Fuel and injector temperature are fixed boundary conditions in the different cases while gas temperature depends mainly on the inlet temperature boundary. Fuel concentration in the gas depends on the fuel air mixture during injection which is not active for case #E1.

Wall parallel gas velocity mainly depends on the intake massflow and combustion chamber geometry which has been proven to have a big influence on diffusion flames coming from fuel on the injector tip; see [7]. In this project the combustion chamber geometry is fixed while the intake mass flow is only increased for Case #E6 and #E7 keep the air mass constant while adding EGR.

Figure 92 represents the base boundaries around the injector tip from end of injection to start of ignition. While the gas temperature stays for a long duration below 200°C the gas velocity decreases towards TDC and stays around 10m/s. These conditions will probably lead to slow wallfilm evaporation.

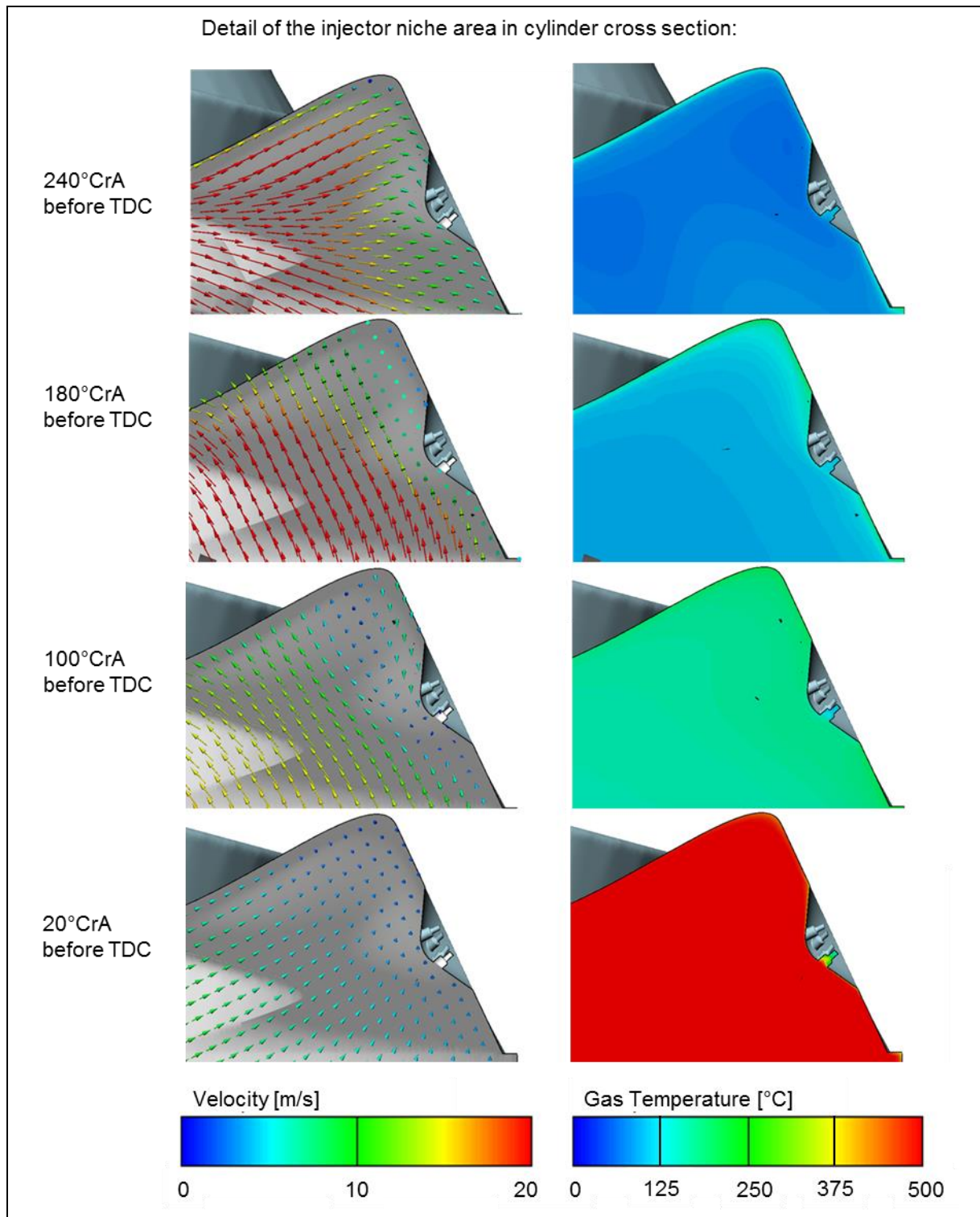


Figure 92: Velocity and Temperature at the injector tip from end of injection to ignition timing (Case #E1)

The gas velocities parallel to the injector tip in the niche show the same trend as above (Figure 93). After 240°CrA before TDC which is shortly after end of injection for the other cases the velocity decreases down to 10m/s around the injector tip. The

observed unsymmetrical flow field is possibly caused by small fluctuations during the exhaust stroke due to the non-symmetrical exhaust port.

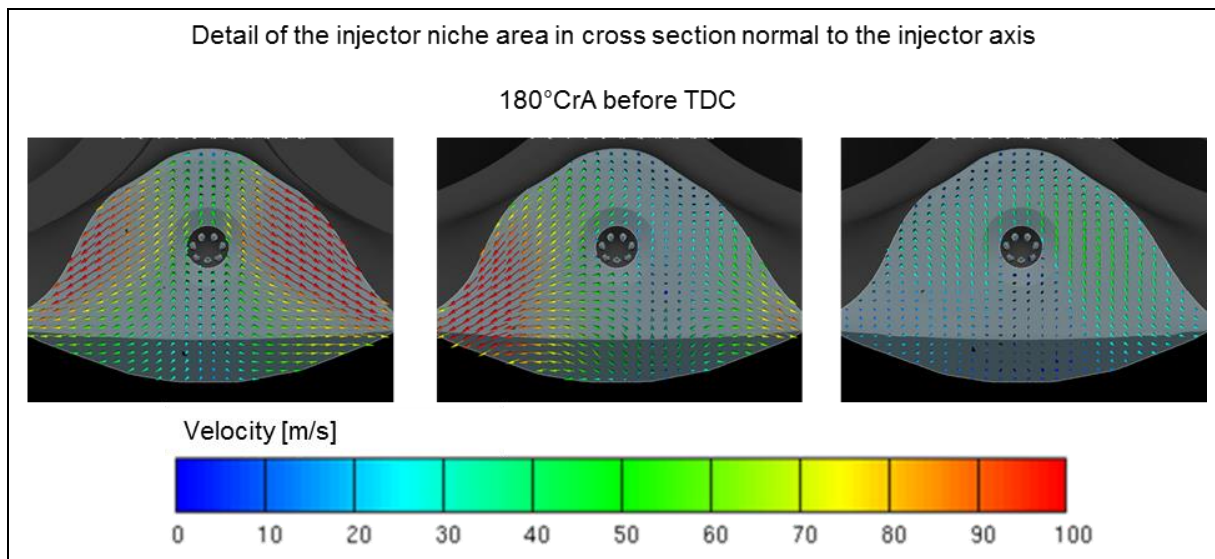


Figure 93: Gas Velocity Field development after end of injection (Case #E1)

7.4.2 Base Engine Result #E2

Although Engine Case #E3 would correspond better to the investigated operating point using cooled EGR, Case #E2 has been selected as base engine result as most variants don't consider EGR. Furthermore, this case can be used to verify the boundaries from the reference engine which didn't include EGR by comparing the air to fuel ratio.

As the test engine is operated at Lambda 1 and the injected fuel mass has been verified by measurement the simulation should also show similar lambda values if the air mass is correct. Figure 94 displays the unburnt average equivalence ratio in the cylinder volume (excluding intake port) over a full 720° Crank Angle Cycle. Before spark ignition the unburnt equivalence ratio corresponds to the standard equivalence ratio.

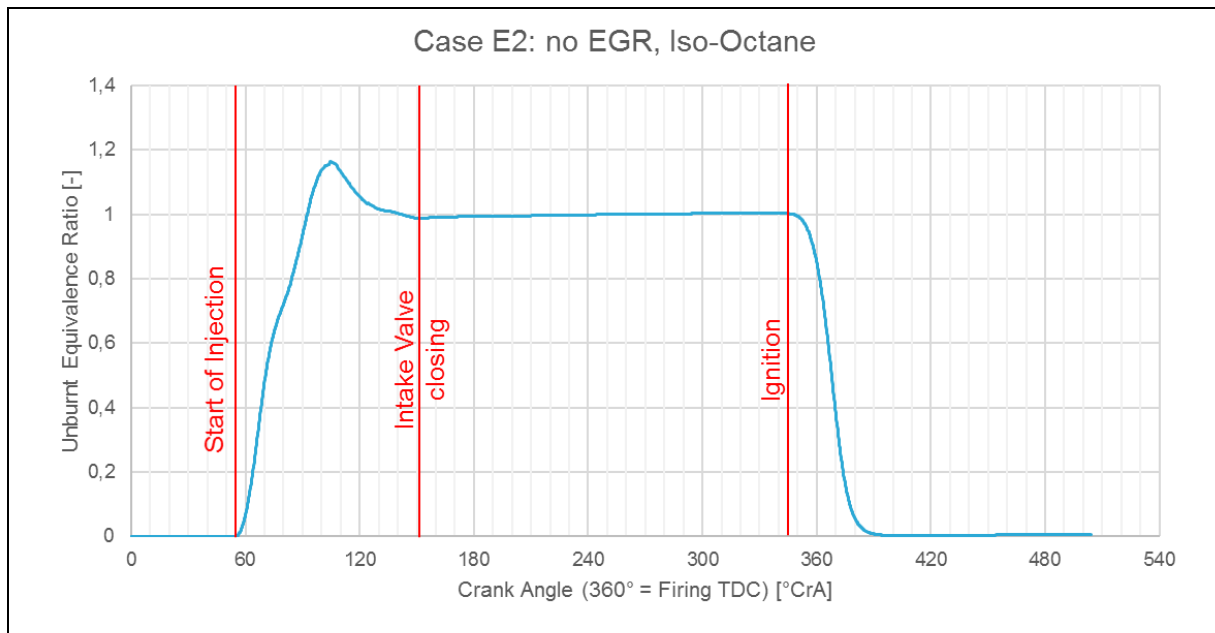


Figure 94: Unburnt Equivalence Ratio for simulated Engine Case #E2

After the injection start at 54° after TDC the equivalence ratio increases up to the end of injection. As the intake valve is still open it then decreases until intake valve closing where it stays constant at 1.0 until the spark ignition confirming the reference engine boundaries as valid for this simulation.

At the selected load point the injection signal duration is 2.1ms which relates to 2.2ms total opening duration of the injector. This equals to roughly 40° crank angle at 3000 rpm. Figure 95 shows an isometric surface for $\lambda=1$ colored in the local gas velocity during injection. Due to the early injection timing, the spray hits the piston which is visible in the middle picture. The right picture is taken at the end of injection where the fuel already fills a big part of the cylinder indicating a good homogenization. Furthermore, the injection accelerates the gas which explains the high velocity area in the middle picture.

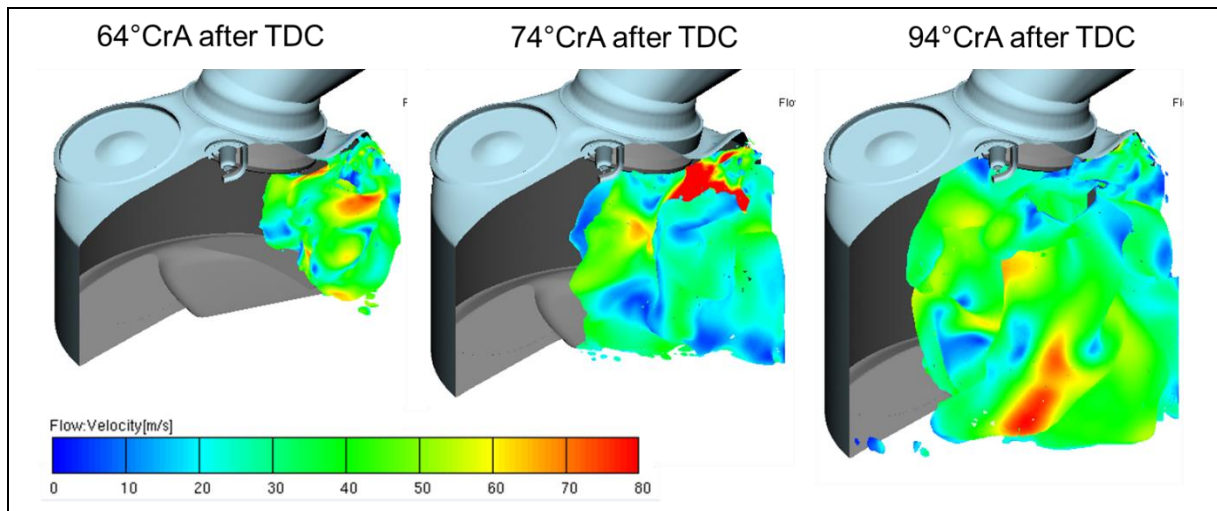


Figure 95: Isometric Surface for Lambda=1 overlaid with gas velocity during injection (Case #E2)

Due to the direction of the gas flow during injection the fuel cloud also fills the injector niche which increases the local fuel concentration and therefore limits evaporation rates. High flow velocities in this area would help to reduce fuel concentration and accelerate wallfilm evaporation. Figure 96 shows the equivalence ratio in the injector niche after end of injection until start of ignition. A more than 5 times higher fuel concentration than in the rest of the cylinder can be observed.

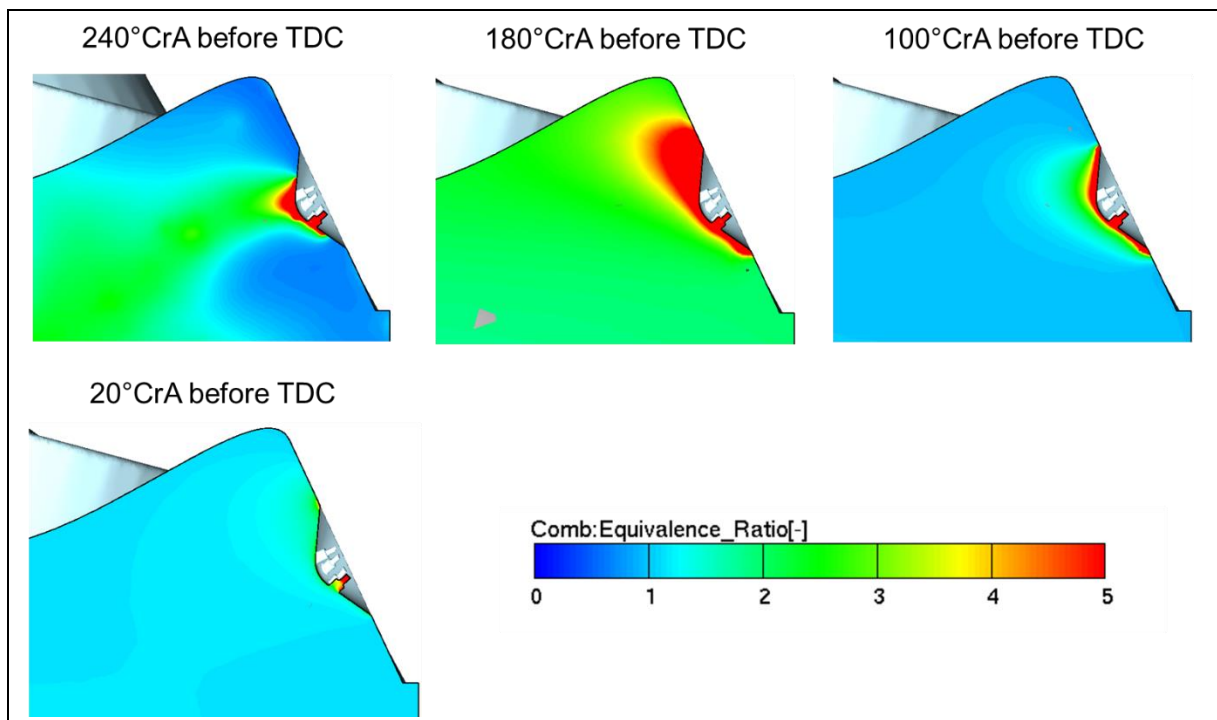


Figure 96: Equivalence ratio in the injector niche from end of injection until start of ignition for case #E2

The wallfilm model was set up with the same configuration as in chapter 6 which could replicate the wallfilm area from the measurement. The area development and total wallfilm mass will differ from the spraybox investigations due to different gas and wall temperatures and flow velocities.

Comparing the wallfilm build-up during injection in the cylinder in Figure 97 with the results from the spray box investigations from Figure 79 shows similar behavior. The wallfilm starts to build up from injector holes #4 and #7 first followed by #1 and #3. Most of the mass accumulates at the center on the injector tip while a small fuel amount is pushed towards hole #5 close to the end of injection.

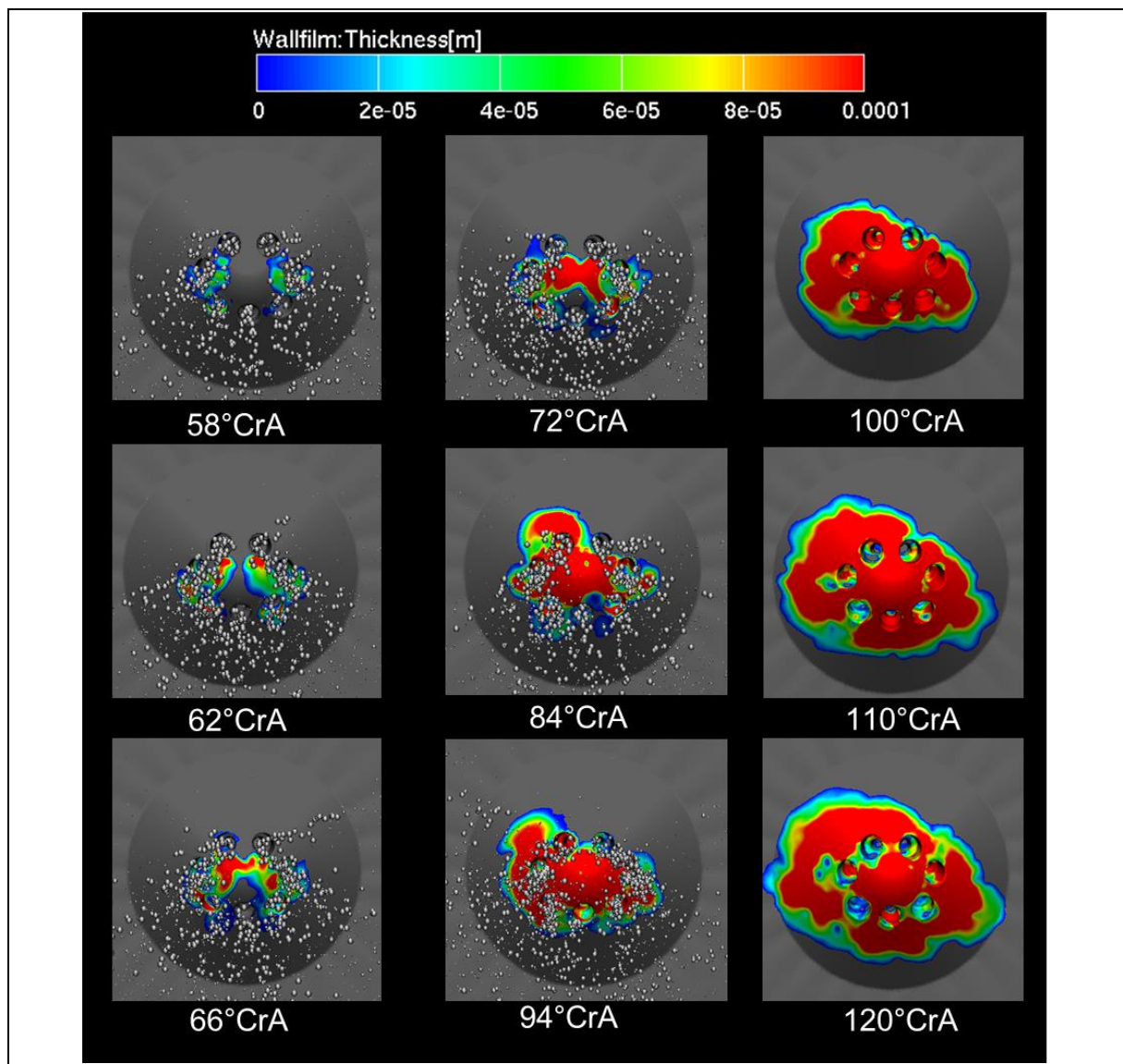


Figure 97: Wallfilm development on injector tip and in holes during injection for Case #E2 (Needle is closed at 94°CrA after TDC)

When plotting the wallfilm mass on the tip and in the holes over crank angle (Figure 98) the behavior is as expected from the initial tests. During injection, the film in the holes, mainly in the counter-bores increases faster than on the tip up to end of injection. At needle closing the total film mass reached its maximum while the mass on the tip is further increasing fed by the fuel which is running out of the nozzles.

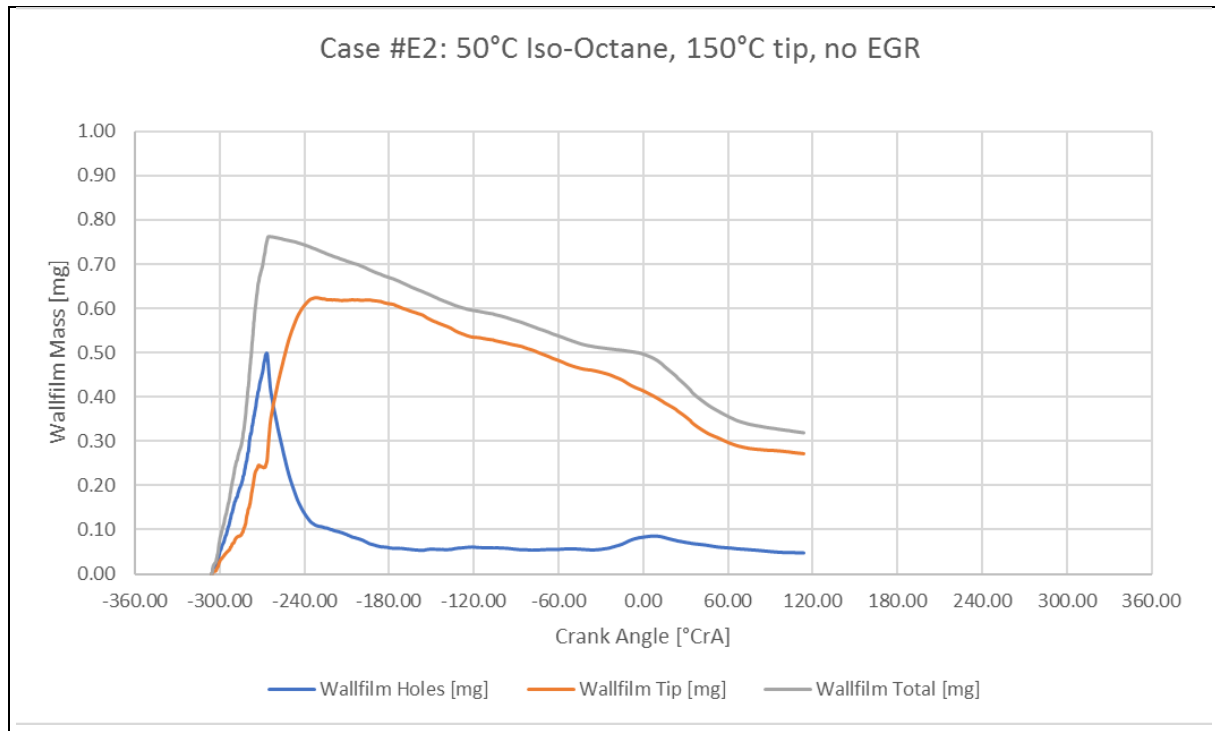


Figure 98: Wallfilm mass on injector tip and holes for Case #E2 as reference for the following variants

For Case #E2 total wallfilm mass reaches $\sim 0.76\text{mg}$ which would correspond to 2.9% of the total injected fuel mass. However as stated in chapter 6.3.2 the wallfilm model is overestimating the absolute mass therefore the 0.76mg is understood as reference for the simulation variants representing 100% wallfilm.

After injection, the total film mass is slowly but constantly decreasing up to around TDC where the flame front reaches the injector. Before burning less than 50% of the initial mass on the tip is evaporated providing a liquid layer for particles to accumulate (Figure 99). When the flame front reaches the injector tip, the evaporation rate increases due to much higher gas temperatures and turbulence. As a result, the total film mass decreases with a faster rate. However, even after the flame goes extinct as it is lacking oxygen there is around 40% liquid film left.

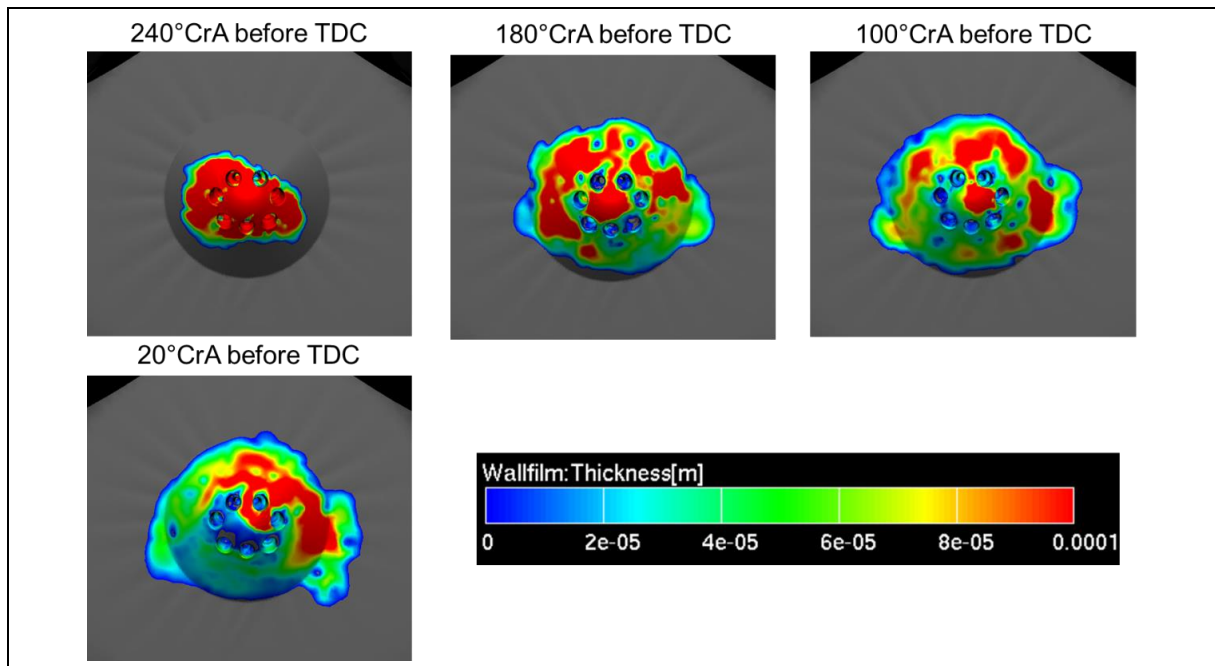


Figure 99: Wallfilm on injector from end of injection to start of ignition for case #E2

An isometric surface for a combustion reaction rate of 5J/s was used to visualize the flame front in the cylinder during combustion. This value is a part of the ECFM-3Z combustion model describing the current reaction rate in each cell. The pictures in Figure 100 show the development of the flame during combustion together with the wallfilm on the injector tip.

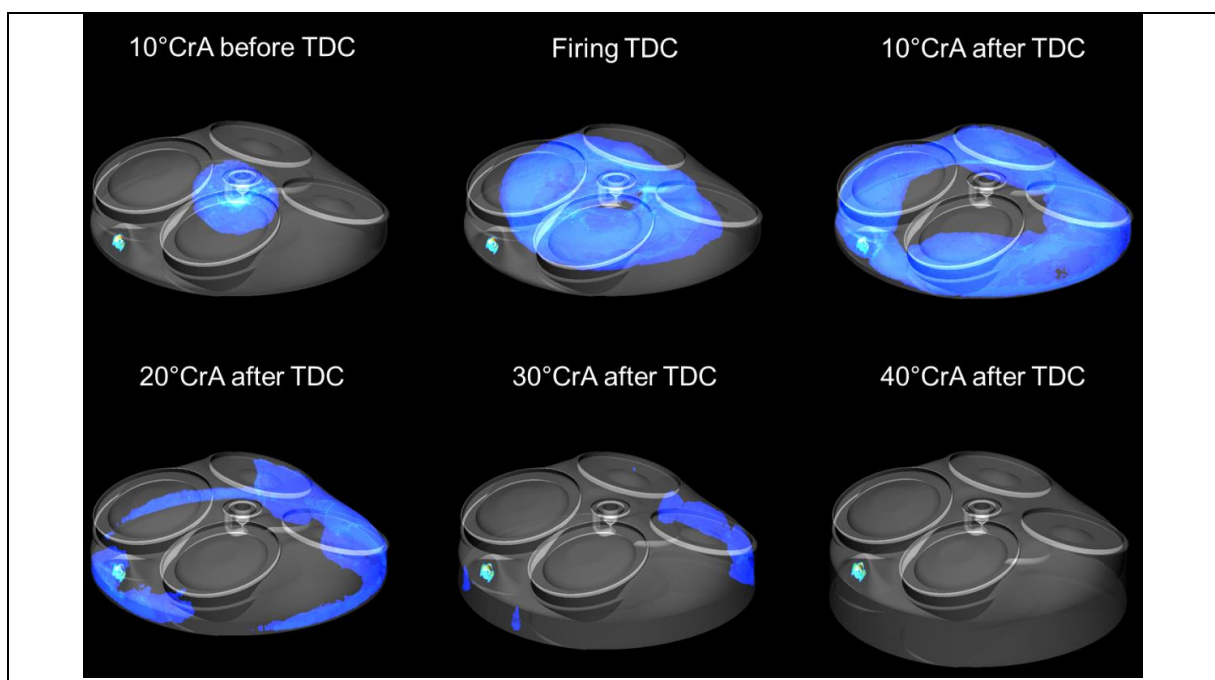


Figure 100: Flame front during combustion with wallfilm thickness on the injector for Case #E2

After the flame front passes the injector there is still liquid fuel present on the tip which continues to slowly burn. At one point the local fuel to air ratio reaches levels outside combustible areas decreasing the reaction rate below the set limit. Displaying the unburnt equivalent ratio after ignition shows a similar picture (Figure 101) – the green area marks a mixture within normal combustion areas from 0.8 (equals to $\lambda = 1.2$) to 1.2 (equals to $\lambda = 0.83$). The blue area has no fuel left while the red areas show mixture levels outside burning conditions ($\lambda < 0.5$). The increasing red area at the end of injection is evaporated fuel from the tip mixing with burnt gas.

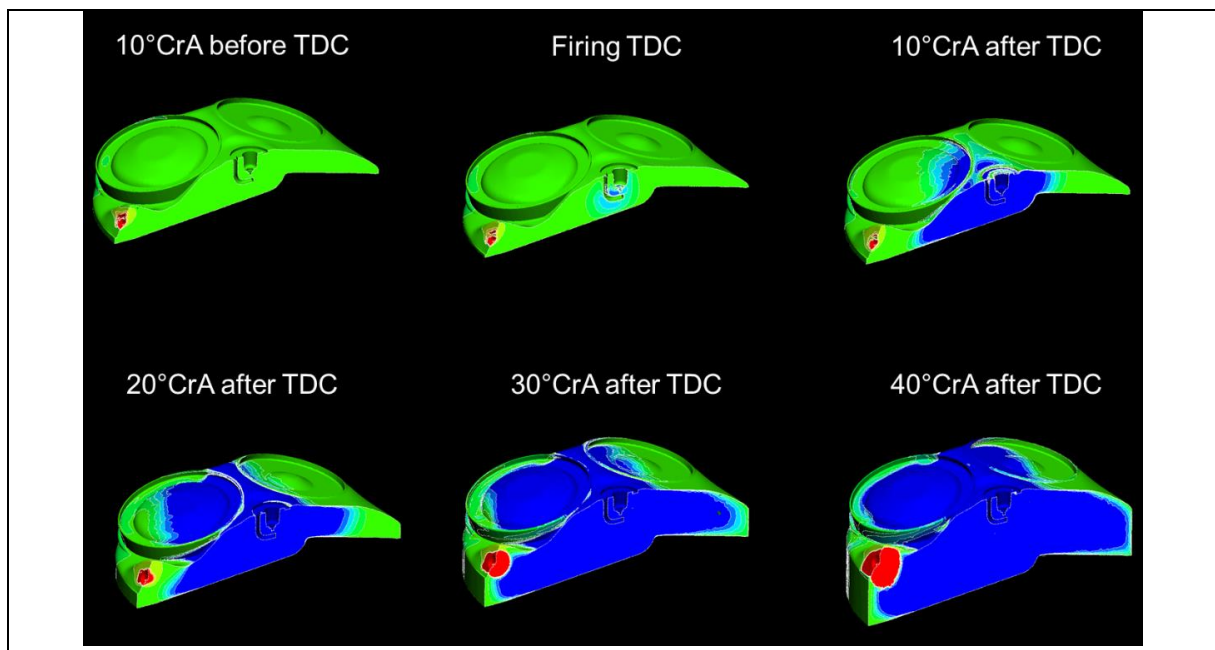


Figure 101: Unburnt Equivalent Ratio for Case #E2

Another output of the combustion model is the heat release rate and the total heat release over crank angle from which the mass fraction burnt (MFB%) values can be derived. The combustion model has been calibrated using case #E3 which uses similar amounts of EGR as the measurement (see chapter 7.4.3). In case #E2 no EGR is considered which leads to a faster combustion and therefore heat release rate compared to the real engine operating point. Figure 102 shows the heat release over crank angle and compares it to the measurement results. As expected the MFB10%, 50% and 90% are met earlier than the engine measurement.

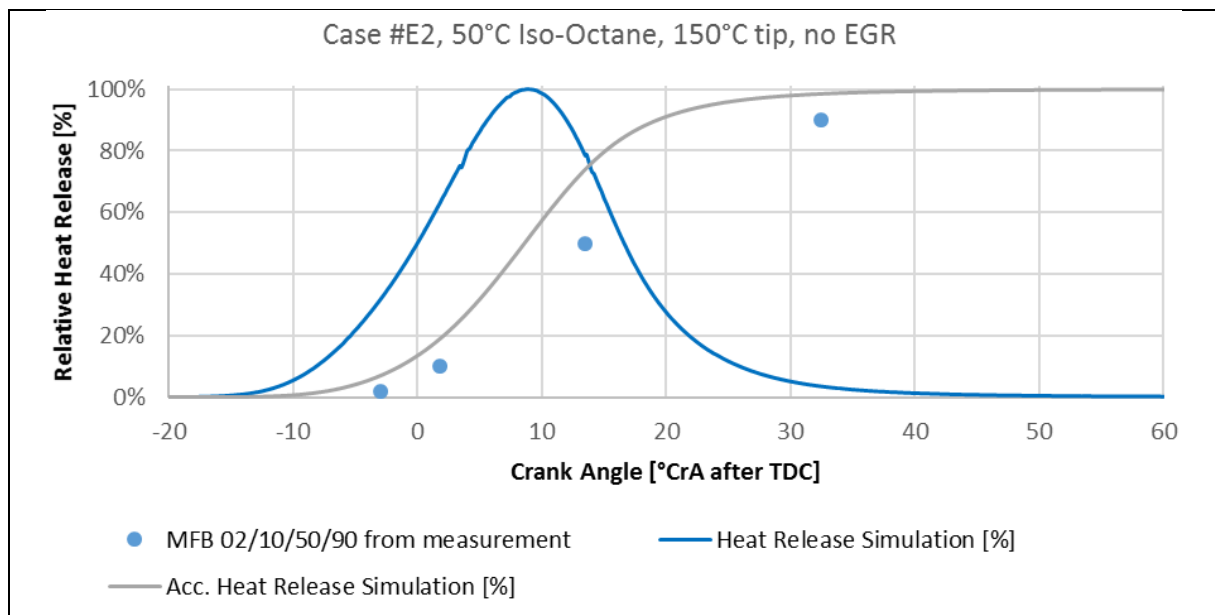


Figure 102: Heat Release rate and total heat release for case #E2

7.4.3 Combustion Model Calibration using Case #E3

To represent combustion conditions close to the engine measurement the ECFM-3Z combustion model was calibrated using case #E3 with 20% cooled EGR which is the estimated rate for the investigated operating point. The model has been calibrated to match the simulated combustion speed with the real one by aligning the simulated heat release curve with the MFB points from the measurement. Starting with experience based values the combustion delay and combustion speed were adjusted to match the simulation with the four available MFB points from the measurement.

The resulting combustion parameters are used for all investigated variants which leads to different peak firing pressures and power output for the cases without EGR. As the focus of this work is on accurately simulating the wallfilm on the injector tip under different conditions the power output plays a smaller role and is therefore not further investigated.

Cases without EGR will burn faster using the same parameters as cases with EGR. As a result, the wallfilm mass curves in chapter 7.4.4 show different gradients after ignition. The final parameters for the combustion model are listed in Table 14.

Table 14: ECFM-3Z combustion model parameters

ECFM-3Z combustion				
Initial flame surface density	Stretch Factor	Consumption Factor	Spark Ignition Model	Auto-Ignition Model
1000 1/m	0.8	1	Spherical	No
ECFM-3Z ignition				
Spark Timing	Flame Kernel Size	Ignition duration		
18.2°CrA b TDC	0.001 m	0.0003 s		

Comparing the accumulated heat release of case #E3 with the measurement shows an acceptable correlation of the burnt mass fraction points with the simulation curve. Figure 103 also shows the heat release rate for this case.

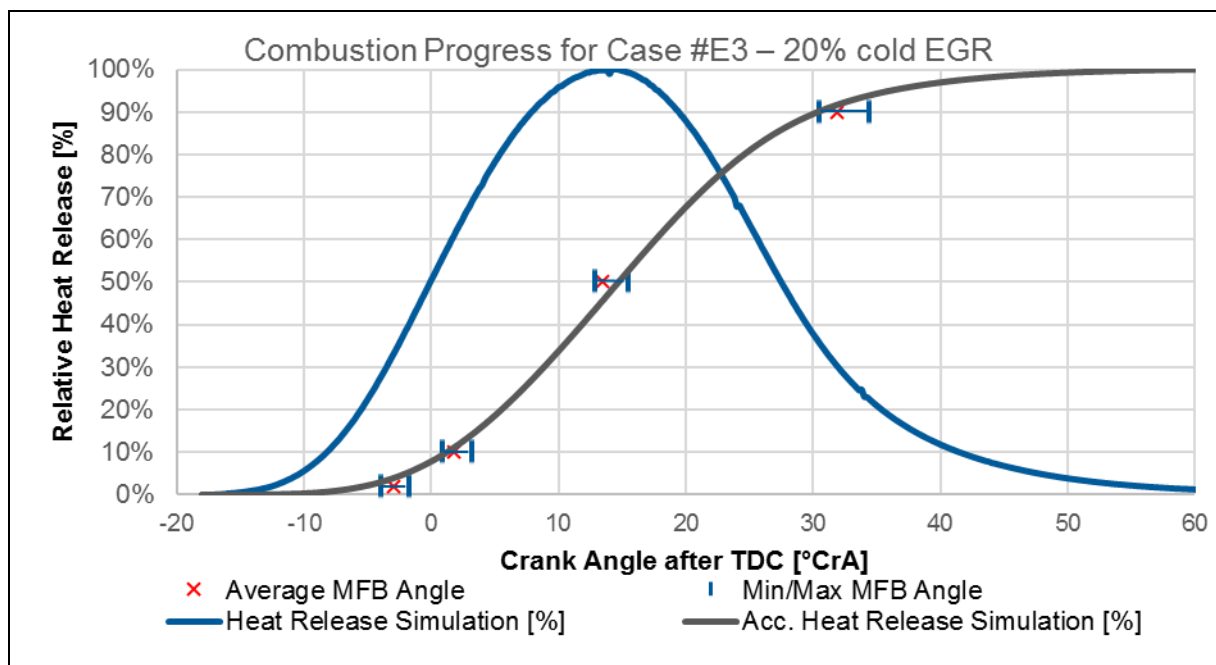


Figure 103: Heat release rate and accumulated heat release for case #E3 compared with the measurement MFB% points

7.4.4 Variations Results

This chapter compares the results of all simulation variants from Table 13 on page 108. First the single component cases #E2 to #E7 are compared followed by the multi component cases #E8 to #E10.

7.4.4.1 Single component fuel

When comparing the different variants for the cylinder simulation the wallfilm development can be split in three phases:

- Wallfilm build up during injection (306°CrA to 266°CrA before TDC)
- Wallfilm evaporation after injection until ignition (266°CrA to 701.8°CrA before TDC)
- Wallfilm evaporation during combustion (701.8°CrA to 780°CrA)

The first phase will define the relative amount of fuel on the injector tip while the second phase is responsible for the evaporation speed. The best variation would show low mass after injection followed by a high evaporation rate. The third phase during combustion is of lower interest as the combustion model is simplified and the absolute mass on the injector tip is too high compared to the measurement. However, it can be used to show trends in the evaporation rate for cases with and without EGR.

Comparing the wallfilm area and thickness at the end of phase 1 after injection in Figure 104 shows big differences between the cases. While for the base case #E2 most of the tip is covered with fuel there is nearly no wallfilm present for case #E5.

All cases except for Case #E5 show a concentration of the film around the injector tip. Case #E3 and #E4 with EGR experience different gas flow conditions due to the increased intake mass flow. As a result, the shape develops differently from the base. The increase of tip temperature in Case #6 and #7 decreases the size of the film area compared to case #E2 but keeps a similar ratio.

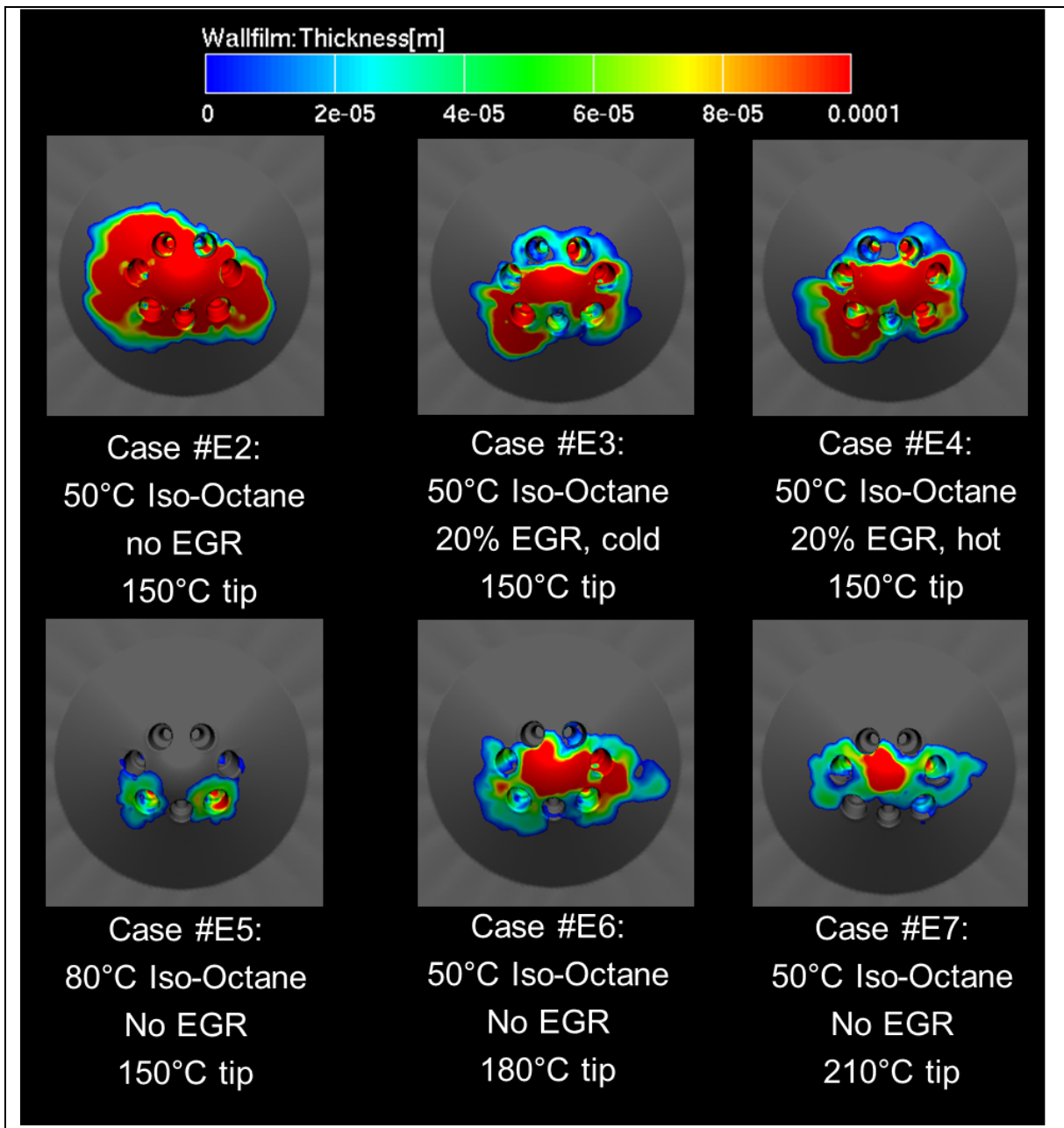


Figure 104: Wallfilm area and thickness after injection (260°Cra before TDC) for Case #E2 to #E7

Figure 105 compares the total film mass on the injector after the injection with the base case #E2. As expected from the distribution and thickness above Case #E5 produces the least amount of film with only 10% of the base. Investigation of the wallfilm build-up for Case #E5 during injection shows that the fuel is also spreading from the counterbores towards the center but evaporates before accumulating at the tip.

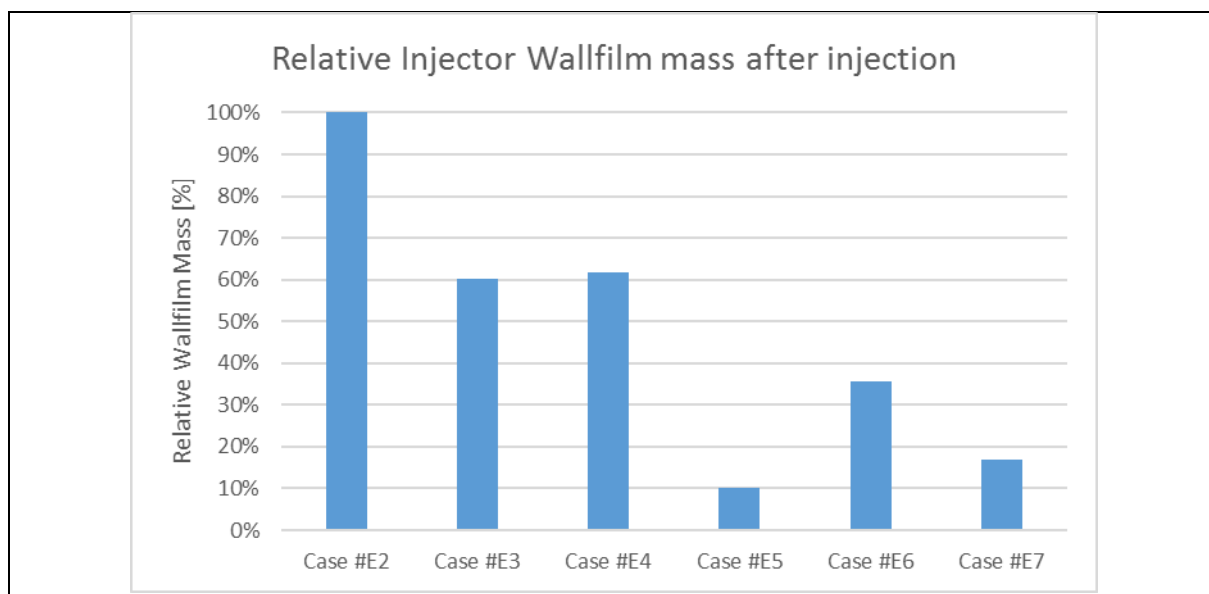


Figure 105: Relative wallfilm mass on injector tip after injection (260°C_{CrA} before TDC) for case #E2 to #E7

The difference between case #E2 and #E3 is only the increased intake mass flow while keeping the same inlet gas temperature. The decrease of 40% is a direct result of higher flow velocities around the injector during injection. Case #E4 is based on Case #E3 with a higher inlet temperature and slightly increased intake mass flow to compensate the different gas density. The 20°C higher inlet temperature shows no reduction of the initial wallfilm as the gas temperature is still low compared to fuel and injector tip temperature. The total mass is even slightly higher than Case #E3 possible due to the higher cylinder pressure reducing the evaporation.

As mentioned before Case #E5 shows a reduction of over 90% compared to the base case by increasing the fuel temperature from 50°C to 80°C. However, a higher fuel temperature can lead to several fuel related disadvantages like higher knock probability and influences on the fuel delivery path due to a different viscosity. An increase of the fuel temperature therefore must be verified carefully by considering all possible side effects.

Increasing the injector tip temperature by 30°C (from 150°C to 180°C) while keeping the fuel temperature at 50°C like in case #E6 however reduces the wallfilm by nearly 70% without the disadvantages of a higher fuel temperature. Further increasing the temperature on the tip to 210°C (Case #E7) leads to a total of 85% reduction which is close to the result from Case #E5. High injector temperatures put higher stress on the hardware and may affect lifetime and functionality. Optimization in this area should be done in cooperation with the injector supplier.

The second phase of the wallfilm development is the time after injection until ignition which is defined by the evaporation rate of the film. However, as the initial mass on the injector tip is different for each case a direct comparison of the evaporation rate is not suitable to evaluate the different boundaries. A bigger wallfilm area will lead to an increased evaporation rate favoring cases like #E2 over #E5. Investigations regarding the influence of different boundary conditions on the evaporation rate of wallfilm on the injector tip for the same initial mass and area can be found in [53].

Figure 106 shows the reduction of the wallfilm between end of injection and ignition relative to each initial mass. Case #E2 to #E4 experience a similar reduction of around 30% due to low gas velocity in the injector niche after injection as shown in Figure 92 and Figure 93.

As expected higher fuel and injector temperatures lead to higher evaporation for case #E5 to #E7. Again case #E5 shows the best wallfilm behavior closely followed by case #E7. Both cases have nearly no wallfilm left at the time of ignition. Case #E6 is in the middle between the worst and best result with a reduction of 46%.

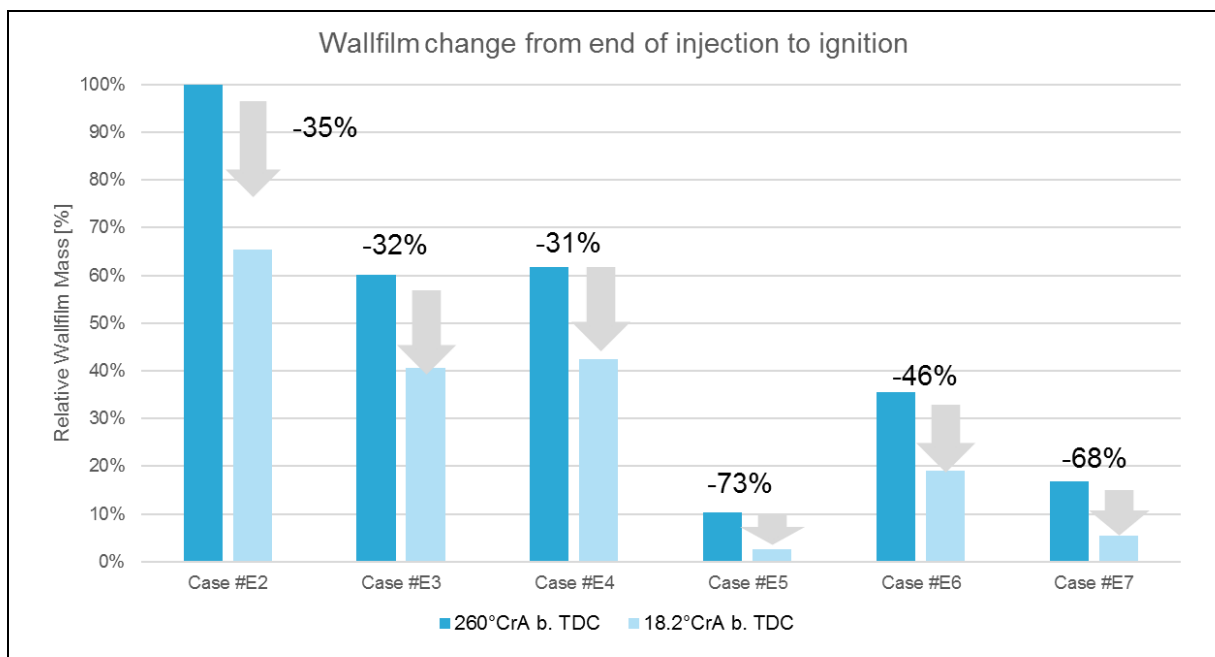


Figure 106: Wallfilm from end of injection to ignition for case #E2 to #E7

In Figure 107 the development of the total wallfilm mass over a full cycle for all single component simulations is displayed. All cases have their peak at the end of injection followed by the evaporation phase. At around TDC the flames reach the injector and the evaporation rates increases.

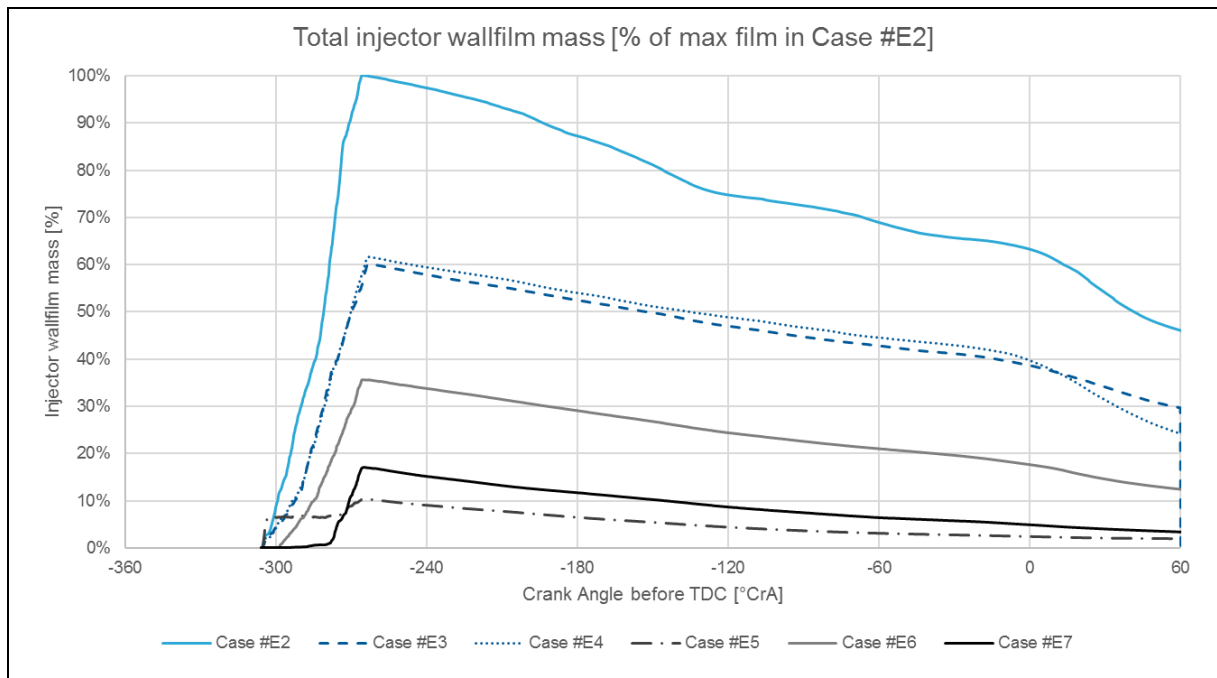


Figure 107: Total injector wallfilm over full cycle for single component fuel variants.

To compare the simulation with the measurement Figure 108 shows the coked injector from cylinder 1 after 60h with RON 92 fuel next to the remaining wallfilm in Case #E3 at spark timing. Case #E3 is the closest setting of the simulated operating point as it uses cooled EGR. The injector and the simulation show similar trends in deposit and wallfilm distribution making the simulation plausible. However, it has to be considered that the simulation only models one operating point while the injector was running a 60h test cycle with 9 different operating points.

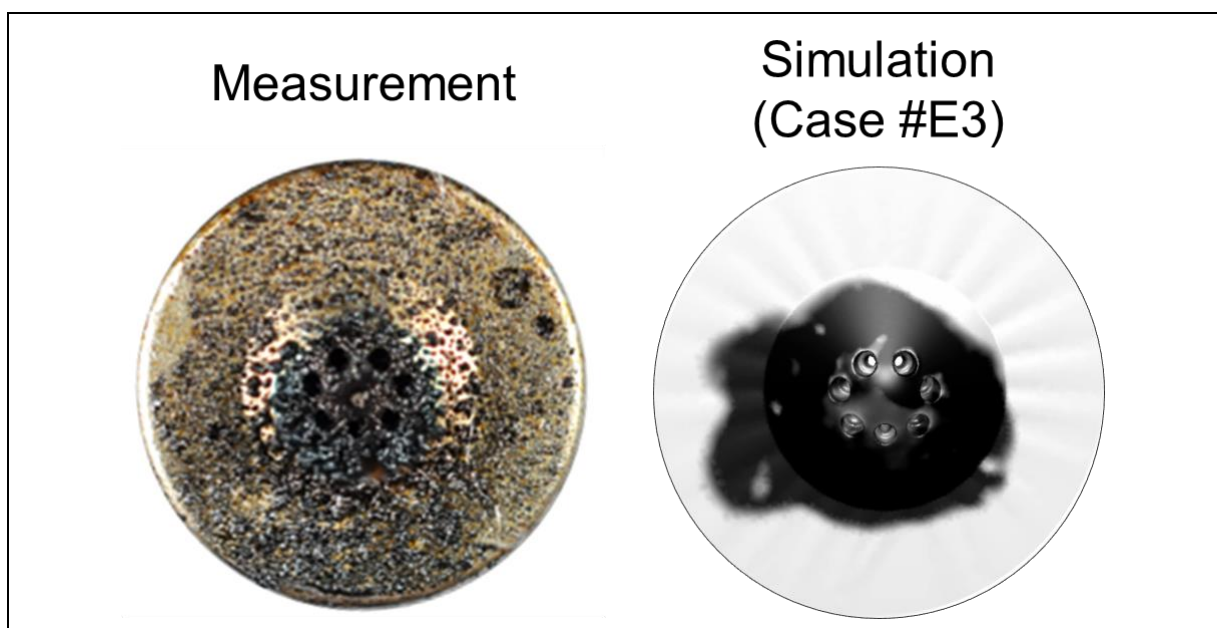


Figure 108: Comparison of coked injector with wallfilm simulation at spark timing

7.4.4.2 Multi component fuel

The multi-component cases have been simulated using a pre-release version of Fire 2017.1 which was not officially released at the time of investigation. When simulating a multi-component wallfilm in Fire 2017.0 or earlier versions the mass fractions of all components is frozen when droplets hit the wall and film is created. The wallfilm module then simulates the evaporation with the diffusion coefficient of the component with the highest mass fraction. As a result, all components evaporate with the same rate not distinguishing between high and low volatile components.

In the new version, the wallfilm model considers the individual diffusion coefficients of single components in a multi-component film if multi-component evaporation is selected. Every component has its own evaporation rate in the film leading to high volatile components evaporating first while low volatile components remain in the film leading to a more realistic simulation.

Figure 109 shows the simulated distillation curves for the 3 investigated gasoline surrogates comparing them to a commercial European RON 95 fuel, a volatile RON 92 Winter fuel and a low quality Chinese M15 fuel which was used in the fleet tests described in chapter 1.2. The engine simulation #E8 uses the European RON 95 surrogate, case #E9 the Winter RON 92 surrogate and case #E10 the Chinese M15 surrogate.

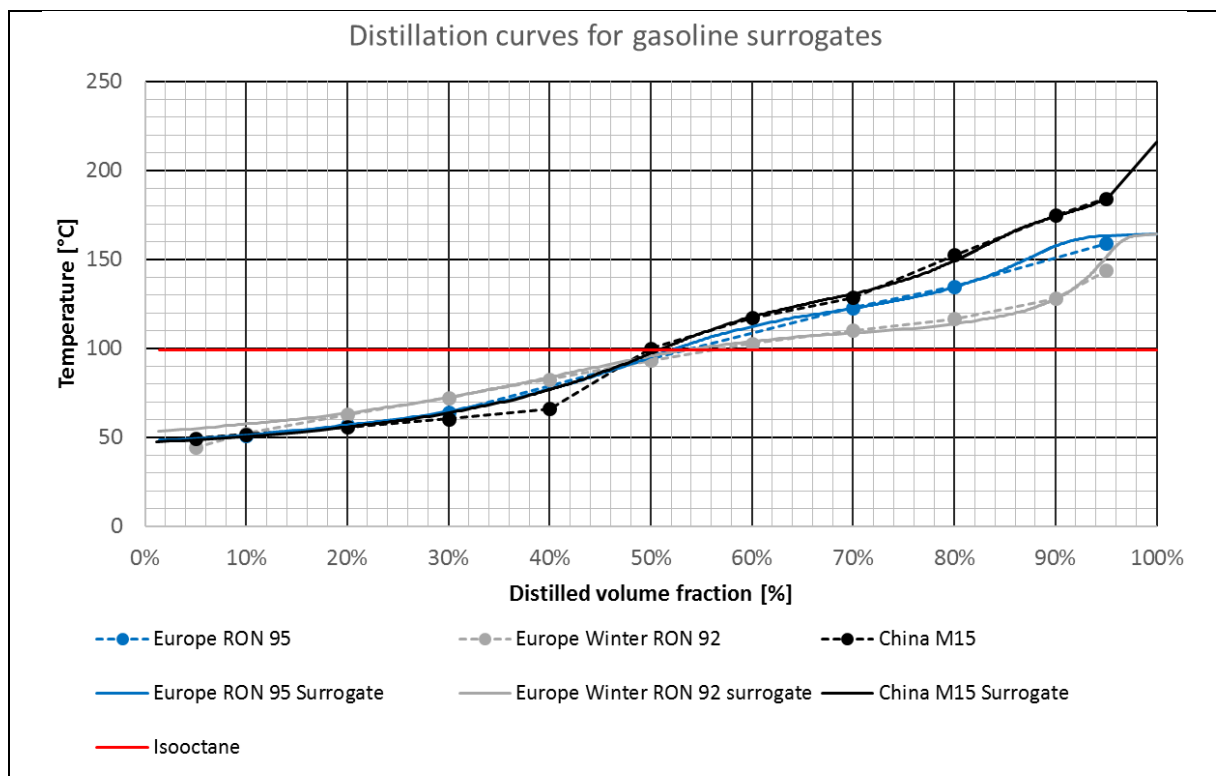


Figure 109: Distillation curves for gasoline surrogates

The distillation curves have been simulated with the new multi-component wallfilm evaporation model. However, during the engine simulation the evaporation model showed an unstable behavior which could not be solved by changing simulation parameters.

Due to this problem, the following simulations used the same wallfilm evaporation model as the single component simulations which is described in chapter 4.2. As mentioned above the diffusion coefficient is now taken from the component with the highest mass fraction in the film. Despite the simplification of this evaporation model the evaporation rates for the 3 gasoline surrogates will still be different based on their composition. Additionally, the multi-component spray evaporation model can simulate the early evaporation of the volatile components before the impingement process on the wall. Therefore, the results are still valuable to identify trends and the influence of different fuel compositions.

To compare the different FIRE versions Engine Case #E2 (50°C Iso-Octane) has been simulated again with the pre-release of Fire 2017.1 (referred to as #E2b) using the same settings as in Fire 2017.0. While the amount of wallfilm after the injection is very similar the evaporation rate differs between the 2 Fire versions. The Iso-Octane Film in Case #E2b in Fire 2017.1 evaporates faster than in Fire 2017.0 leading to a different result at ignition time. The multi-component cases have therefore to be compared to Case #E2b to evaluate trends.

Figure 110 displays the wallfilm mass of Case #E8 to #E10 (Fire 2017.1) with the different gasoline surrogates compares to the results from Case #E2 (Fire 2017.0) and Case #E2b (Fire 2017.1). As mentioned before both Fire versions simulate a similar amount and trend of wallfilm formation during injection but around 140°CrA before TDC the evaporation in Fire 2017.1 is faster.

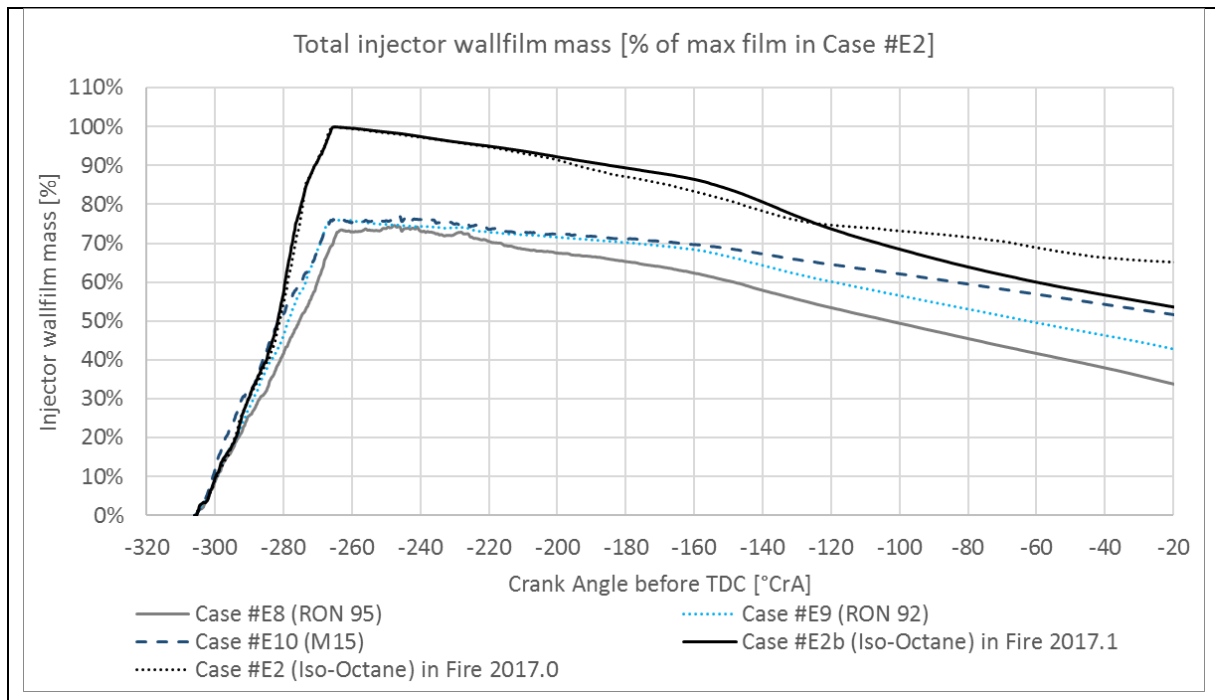


Figure 110: Multi-Component Wallfilm on Injector tip from start of injection to ignition

The difference between the wallfilm area is visible in Figure 111 which shows the total area from injection to ignition as well as the local distribution at 160°CrA before TDC. Additional to the larger film area which increases the evaporation rate the area around the protruded tip has a higher temperature than the tip due to boundary conditions. As Case #E2b has more fuel around the protruded tip than Case #E2 the film will heat up faster. The reason for the different wallfilm expansion should be investigated in future studies.

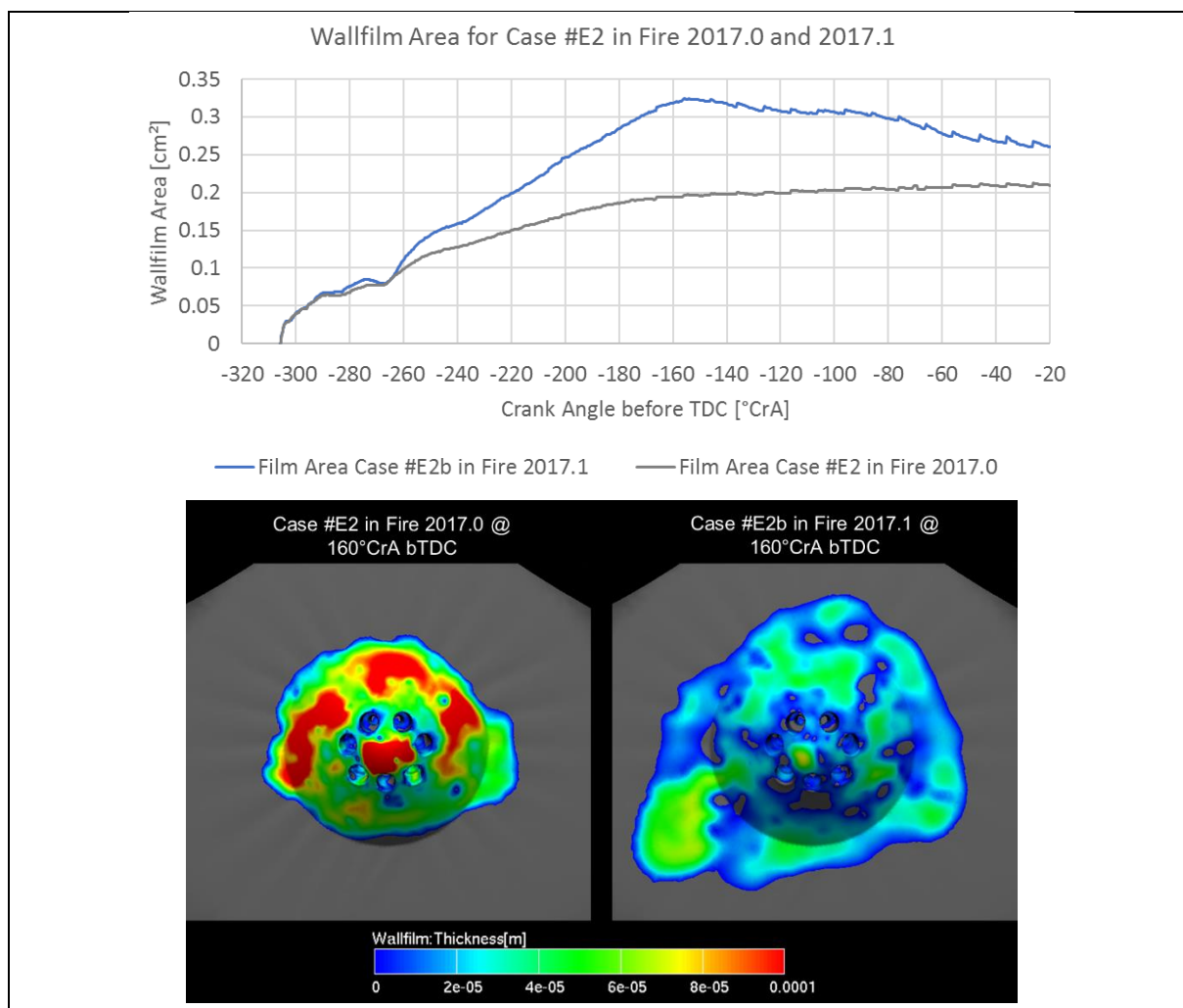


Figure 111: Wallfilm Area for Case #E2 (Fire 2017.0) and #E2b (Fire 2017.1)

As all cases in Fire 2017.1 show the same increased film distribution the multi-component simulations can be compared to Case #E2b in Figure 110. During injection, the volatile Iso-Pentane from the gasoline surrogates evaporate partly before forming a wallfilm which explains the lower mass after injection compared to Iso-Octane. This can be also seen in the distillation curves where 50% of the gasoline surrogate volume fractions has a lower boiling point than Iso-Octane. After injection, the multi-component wallfilm evaporates slower than Iso-Octane due to the higher boiling points of the remaining components. As expected the M15 surrogate has the lowest evaporation rate. However, compared to the single-component cases the influence of different distillation curves is not as obvious as fuel or wall temperature changes. At ignition, the wallfilm in Case #E10 (M15) has the same mass as Case #E2b despite lower initial mass and is around 10% higher than Case #E8 and #E9. This shows that with the current simplified wallfilm evaporation model Iso-Octane is a good substitute for gasoline.

7.5 Conclusion from Results

The following conclusions can be drawn from the single and multi-component engine simulations:

- The engine simulation at 3000 rpm / 10 bar BMEP shows a good correlation with the engine measurement results in terms of equivalence ratio and combustion course. The used crank angle based inlet and outlet boundary conditions taken from a Miller reference engine were successfully adapted to the HiEff engine
- The base simulation (Case #E2) as well as the simulation reflecting the real engine conditions (Case #E3 – cooled EGR) show a significant amount of fuel on the injector tip at the time of ignition which will result in high particle emission when the flame front reaches the injector. The particles will partly stick to the injector creating the observed external deposits and leading to the measured tip sooting.
- The simulations showed an increased fuel temperature as the most effective way to reduce the wallfilm formation and increase evaporation with a given injector geometry. However, a higher fuel temperature can also lead to disadvantages such as knocking and needs to be evaluated carefully.
- The second most effective way to reduce formation and increase evaporation was a high injector temperature. As this might influence the injector lifetime or function it needs to be evaluated with the injector supplier.
- First multi-component simulations showed the influence of different distillation curves based on a simplified evaporation model. The surrogates have a lower initial wallfilm mass but evaporate slower. Future investigations with the advanced wallfilm evaporation model and different boundary conditions will help to get more detailed tip wetting results.

8 Overall Conclusion and Outlook

8.1 Conclusion

In the beginning of the study a new engine coking test cycle was developed to investigate the influence of engine deposits on a next generation TGDI engine. The tests resulted in an increase of PN emissions which could be linked to injector tip sooting. Based on current research injector tip wetting was identified as predecessor of the tip sooting phenomenon.

In further steps, a methodology and tool chain was developed to simulate the tip wetting process which allows an early optimization of the engine-injector system and a reduction of engine testbed hours. The first step in the toolchain was the investigation of the available injector hardware which allowed to setup an accurate injector flow simulation. The results from this simulation were used as input for a spray simulation coupled with a wallfilm model. In a last step, a full engine cylinder was modelled to show the influence of different engine boundaries. The simulations were verified with existing and new measurement methods and showed possible counter-measures to reduce the wallfilm mass. Additionally, first multi-component simulations were conducted which are currently of great interest in the industry as they can reflect market relevant fuel effects. Following conclusions can be drawn from the study:

- An innovative high efficient GDI engine has been intensively tested in a new developed test cycle to evaluate the long-term emission behavior. Increased PN emissions due to tip sooting were identified as main problem. No deposits inside the nozzle which influence the injector flow rate were found.
- Current research suggests that tip sooting can be directly linked to fuel remains on the injector tip after injection. Measurements with a highspeed microscopic camera made the film on the tip visible. The key to reduce tip sooting is therefore to reduce the wallfilm formation on the injector tip and to optimize the evaporation of the fuel before the main combustion reaches the injector.
- If it is possible to accurately simulate the wallfilm formation on the tip, engine developers can evaluate different injector types in an early development phase and optimize engine boundaries without the need of cost intensive engine test.
- To simulate an accurate wallfilm formation detailed injector information is required. It was possible to build a model with great accuracy by combining different measurement methods without data from the injector supplier
- It was shown that small differences in injector geometry like the shape of the nozzle inlet at the needle seat area in combination with a different needle lift

have a great influence on the flow inside the nozzle and therefore on the wallfilm formation.

- The existing AVL FIRE wallfilm model was able to predict the wallfilm formation for an injection with n-Heptane at room temperature in a spray box which was verified with a highspeed video of the injector tip during injection. This allowed more complex simulations in a cylinder of the investigated engine.
- Engine simulation of one of the operating points from the new test cycle with different variants showed potential counter-measures to improve wallfilm formation or film evaporation before combustion. These findings can be used to further optimize future engine developments in an early concept phase.
- The flexibility of the simulation setup allows to investigate different operating conditions in the future. By changing wall and flow temperatures in the engine simulation, warmup or cool-down phases can be simulated. The model can also be modified to consider multiple-injections.

8.2 Outlook

In the next steps, the multi-component simulation should be repeated with the advanced wallfilm evaporation model to investigate market related different evaporation curves and their influence on the injector tip wetting.

Further engine and injector measurements can be conducted to validate the findings from the simulation. The spray chamber which was used for the highspeed videos could be modified to heat up the injector or fuel allowing a verification of the wallfilm model also in hot conditions. Pressurizing the chamber offers another possibility to optimize the simulation model. Regarding the spray simulation, additional tests should be considered to investigate the influence of different droplet sizes in the nozzle area on the wallfilm formation especially during injector opening and closing phases.

The engine simulation could be verified with measurements from a transparent research engine which could also considering different operating conditions like stationary, transient, warm-up or cool-down to optimize the simulation models. A Laser-Interferometer (LIF) measurement to verify the simulated wallfilm thickness should also be considered.

In future FIRE versions, a deposit model could be implemented which combines the wallfilm module with a particle model estimating the deposit growth per cycle. A next step would be the simulation of this accumulated deposit layer as porous material and the fuel stored inside leading to the characteristic diffusion flame.

9 Appendix

The appendix lists the recorded engine signals and used simulation settings for future reference and documentation.

9.1 Appendix I – Engine Sensors and Parameters

The engine testbed setup includes a set of standard testbed sensors as well as additional sensors to cover the new air path configuration. The standard sensors are listed in table Table 15 with the location shown in Figure 112. The engine layout in this figure shows an example setup.

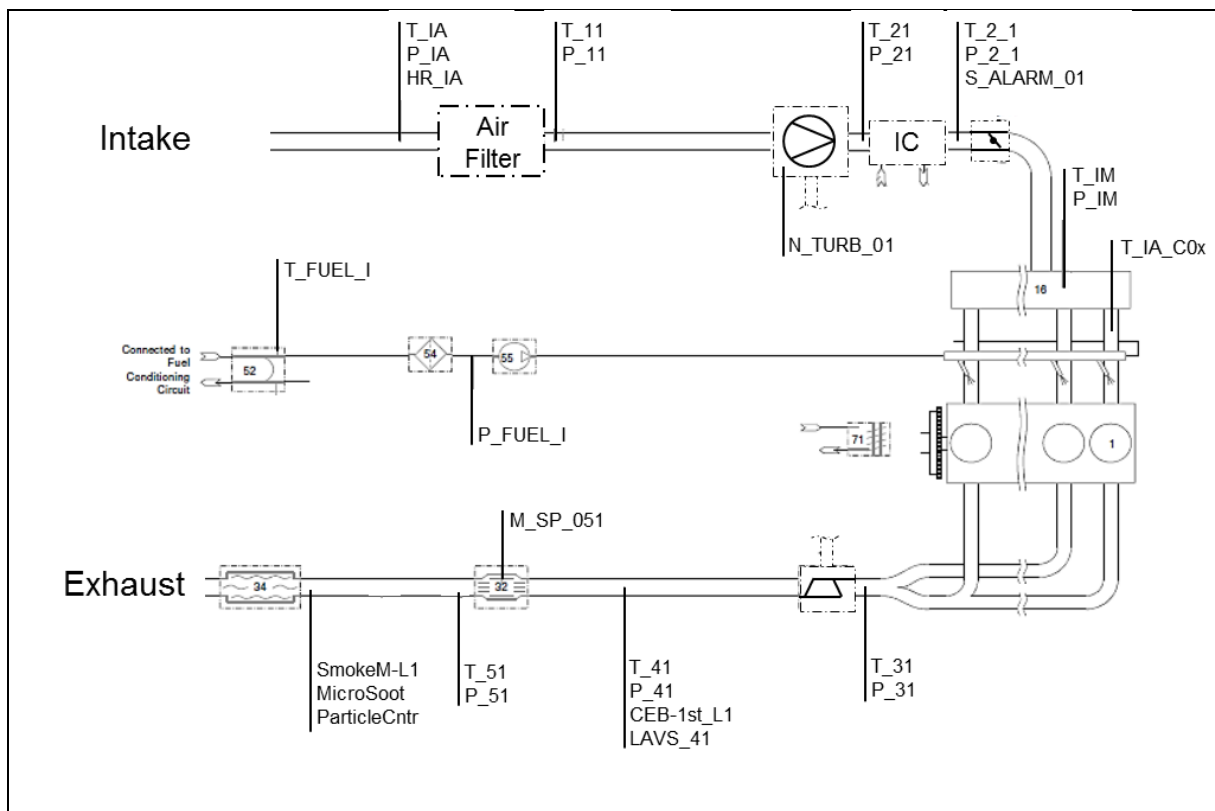


Figure 112: Standard sensor location (example)

Table 15: Standard engine testbed sensors

Standard engine sensors		
Normname	Position	Comment
T_IA	6	Intake Air Temperature before Air filter
P_IA	6	Intake Air Pressure before Air filter
HR_IA	6	Intake Air Humidity
T_11	8	Intake Air Temperature after air filter
P_11	8	Intake Air Pressure after air filter

T_21	12	Intake Air Temperature after Compressor
P_21	12	Intake Air Pressure after Compressor
T_2_1		Intake Air Pressure after air filter
T_2_1		Intake Air Temperature after Intercooler
T_IM	15	Intake Air Temperature in intake manifold
P_IM	15	Intake Air Pressure in intake manifold
T_IA_C0x	16	Intake Air Temperature for Cyl 1-4 in port
T_W_I	60	Engine Coolant Temperature In
T_W_O	61	Engine Coolant Temperature Out
P_W_I	0	Engine Coolant Pressure In
P_W_O	0	Engine Coolant Pressure Out
T_OIL	64	Oiltemperature
P_OIL	64	Oilpressure
VF_W	109	Engine Coolant Volume Flow
T_FUEL_I	50	Fuel Temperature of supply line
P_FUEL_I	51	fuel pressure of supply line
T_31	27	Exhaust Temperature before Turbine
P_31	27	Exhaust Pressure before Turbine
T_41	30	Exhaust Temperature after Turbine
P_41	30	Exhaust Pressure after Turbine
T_OILPAN	111	Oiltemperature in Oilpan
S_ALARM_01	103	Water Sensor after Water-Air Intercooler
N_TURB_01	90	Turbine speed
LAVS_41	30	Lambda Sensor
P_CRANKC	98	Crankcase Pressure
VF_BBY	0	Blowby Volume Flow
M_SP_051	104	Brick Temp Closed Coupled Catalyst
T_51	31	Exhaust Temperature after Catalyst
P_51	31	Exhaust Pressure after Catalyst
PCYLFIX1-4	81	Cylinder Pressure Sensor
CEB-1st_L1	30	Emission Bench
SmokeM-L1	33	Smoke Meter
MicroSoot	33	Micro Soot Sensor
ParticleCntr	33	Particle Counter

Additional to the standard sensor installations several EGR and ESC system related sensors were installed. Figure 113 shows the location of the new sensors related to the description in Table 16.

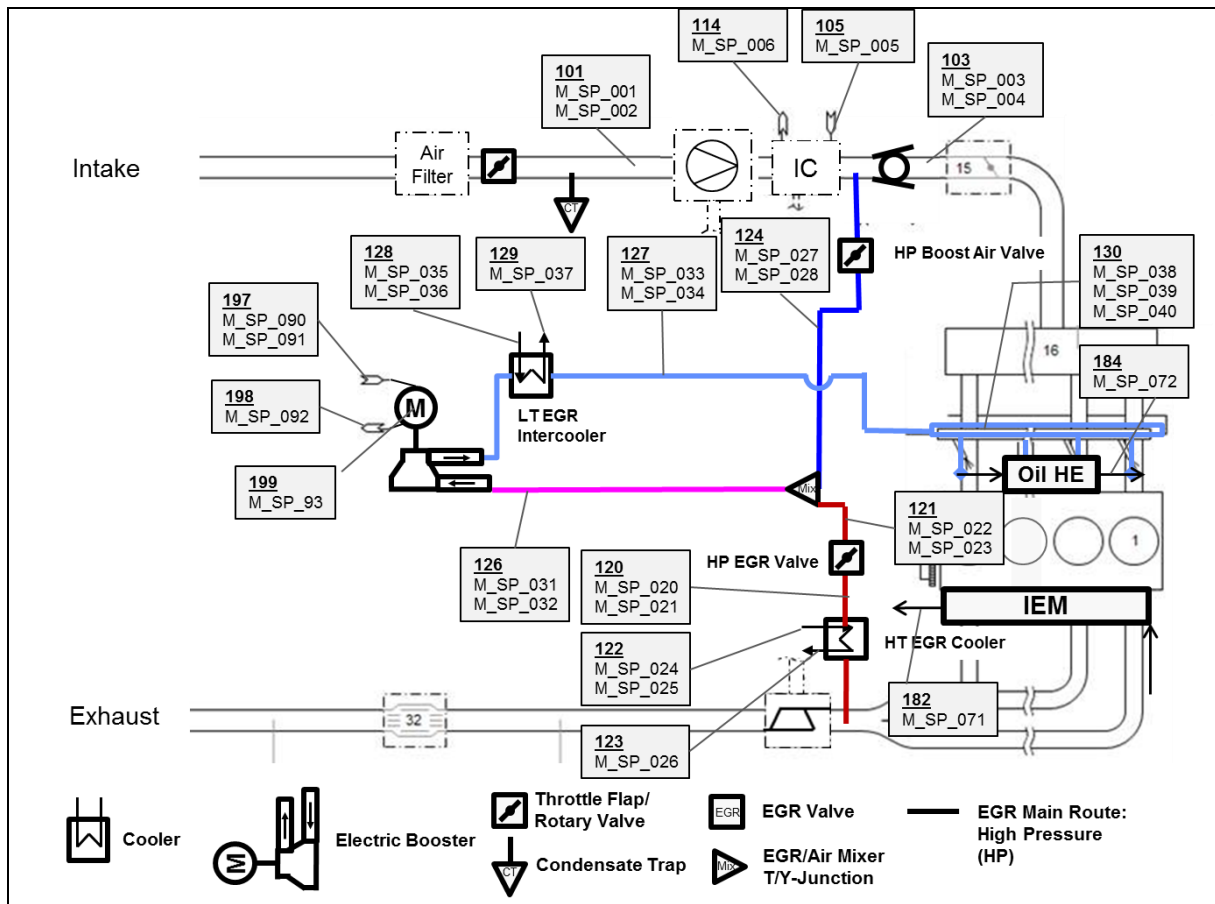


Figure 113: EGR and ESC system sensor positions.

Table 16: Additional EGR and ESC related sensors

China Stage 4 Demo Engine Sensors		
Normname	Position	Comment
M_SP_001	101	Intake Air Temp before Compressor
M_SP_002	101	Intake Air Pressure before Compressor
M_SP_003	103	Between Bypass Valve and Throttle
M_SP_004	103	Between Bypass Valve and Throttle
M_SP_005	105	Coolant Flow Intercooler
M_SP_006	114	Coolant Temp Low Temperature Intercooler Out
M_SP_020	120	EGR Temp between HT EGR Cooler and HP EGR Valve
M_SP_021	120	EGR Pressure between HT EGR Cooler and HP EGR Valve
M_SP_022	121	EGR Temp after HP EGR Valve
M_SP_023	121	EGR Pressure after HP EGR Valve
M_SP_024	122	Coolant Temp High Temperature EGR Cooler In
M_SP_025	122	Coolant Flow High Temperature EGR Cooler In
M_SP_026	123	Coolant Temp High Temperature EGR Cooler Out
M_SP_027	124	Temp Boost Air between fresh Air throttle and EGR/Air Mixer
M_SP_028	124	Pressure Boost Air between fresh Air throttle and EGR/Air Mixer
M_SP_029	125	Temp before electric Supercharger

M_SP_030	125	Pressure before electric Supercharger
M_SP_031	126	Temp after electric Supercharger
M_SP_032	126	Pressure after electric Supercharger
M_SP_033	127	EGR Temp after Low Temp EGR Cooler
M_SP_034	127	EGR Press after Low Temp EGR Cooler
M_SP_035	128	Coolant Temp Low Temperature EGR Cooler In
M_SP_036	128	Coolant Flow Low Temperature EGR Cooler In
M_SP_037	129	Coolant Temp Low Temperature EGR Cooler Out
M_SP_038	130	Temp in HP EGR Rail under Intake Manifold
M_SP_039	130	Pressure in HP EGR Rail under Intake Manifold
M_SP_071	182	Temp after Integrated Exhaust Manifold Out
M_SP_072	184	Temp after Oil Cooler out
M_SP_090	197	Coolant Temp ESC In
M_SP_091	197	Coolant Temp ESC Flow
M_SP_092	198	Coolant Temp ESC Out
M_SP_093	199	Voltage of ESC Supply
M_SP_094	199	Current of ESC Supply

During the engine test runs the data from the sensors was recorded as well as signals from the engine management system and the testbed operating system. These signals are listed in Table 17. The description can be found in the AVL RP-EMS manual.

Table 17: Testbed and EMS signals

Testbed Signals			
N	[1/min]	Testbed Brake Speed	
PWR	[kW]	Testbed Brake Power	
MD	[Nm]	Torque	
BMEP	[kPa]	Brake Mean Effective Pressure	
BSFC	[g/kWh]	Fuel Consumption	
IMEP	[kPa]	Indicated Mean Eff. Pressure	
ISFC	[g/kWh]	Indicated Fuel Consumption	
LAVS_EO	[-]	Testbed Lambda Signal	
PED	[%]	Pedal Position	
IMEPC	[%]	Variance of IMEP	
FMEP	[kpa]	Friction Mean Eff. Pressure	
MF_FUEL	[kg/h]	Fuel Mass Flow	
MF_IA	[kg/h]	Air Mass flow	
EMS Signals			
ECU_001	EngineSpeed	ECU_100	eoi33
ECU_002	EngineLoad	ECU_101	trqbase
ECU_003	saout	ECU_103	C_idle
ECU_004	aped1	ECU_104	C_catheat

ECU_005	tpsdem	ECU_105	C_camrel0
ECU_006	tpsact1	ECU_106	C_sa2map
ECU_007	camdem_0	ECU_107	C_lsu1ready
ECU_008	diffcam_0	ECU_108	C_hom
ECU_009	camdem_1	ECU_111	C_antipump
ECU_010	diffcam_1	ECU_113	tpsdem_1
ECU_013	egrctrl_pwm_0	ECU_114	lamprot
ECU_014	EGRValvePosition	ECU_115	lambdadiff1_4
ECU_015	praildem	ECU_117	boostpwmout
ECU_016	prail	ECU_118	dwelltime
ECU_017	pboostdem	ECU_119	C_vtec0state
ECU_018	pboost	ECU_121	saeff
ECU_019	pintakedem	ECU_122	lameff
ECU_020	pintake	ECU_123	dsalam
ECU_021	lambdadem	ECU_124	msvopen
ECU_022	lambda1	ECU_125	msvclose
ECU_023	mairhfm	ECU_126	egrvalve_dem
ECU_024	pwm2_dutycycle	ECU_127	egrvalve_act
ECU_026	tsrm_w	ECU_128	tengoil
ECU_027	tambient	ECU_129	t_EgrCoolerOut
ECU_028	pambient	ECU_130	pwm3_dutycycle
ECU_029	teng	ECU_131	oilpump_pwm
ECU_030	ub	ECU_132	mapthermpwm
ECU_031	soi_1	ECU_133	WaPuEGR_PWM
ECU_032	tinjraw1	ECU_134	VTESSpeedDem
ECU_033	ti_1	ECU_135	VTESSpeed
ECU_034	rf	ECU_150	EngineLoadMax
ECU_035	fr1_4	ECU_151	boostchrgmx2
ECU_037	sabase0	ECU_152	boostchrgmx3
ECU_038	mairmod	ECU_153	boostchrgmx4
ECU_040	periodin0mean_corr	ECU_154	trqopt
ECU_042	tengoil	ECU_155	trqairdem
ECU_043	evtmod	ECU_156	trqopl1
ECU_044	tair	ECU_157	trqdrivbl
ECU_050	gpintrc_0	ECU_158	trqmx
ECU_051	piegr_0	ECU_159	trqmin
ECU_053	rc	ECU_160	saeffdem
ECU_055	rcpressure	ECU_161	dsadem
ECU_056	rchfm	ECU_162	sadem
ECU_057	EngineLoadDem	ECU_163	C_wotrq
ECU_058	trqact	ECU_164	C_pintpboostcrit
ECU_059	trqloss	ECU_165	dtpscor
ECU_060	saopt	ECU_166	mflwnthrcordem
ECU_062	eoi22	ECU_167	quotpintpboost

ECU_064	ti_2	ECU_168	tpsdemulim
ECU_067	rc_32	ECU_169	trqdrivf
ECU_068	pintm	ECU_170	trqdem
ECU_080	camgravfac	ECU_172	t_esc_cooler_out
ECU_081	camoverlapwo	ECU_173	p_esc_cooler_out
ECU_082	dsvpwm	ECU_174	dsak
ECU_083	EngineLoadRaw	ECU_175	dsaegr
ECU_084	faccamoverlap0	ECU_176	dsaegr1
ECU_085	ftbr	ECU_177	trqdrivs
ECU_086	gpintrc_1	ECU_178	C_lctrlon
ECU_087	pexhexvalv	ECU_179	B_Eboost
ECU_088	piegr_1	ECU_180	B_EBoost_Steady
ECU_091	wgpos1	ECU_181	c_EGRAcv
ECU_092	boostpwmout		
ECU_095	C_vtec0		

9.2 Appendix II - Injector Simulation

The Euler Multiphase Injector Simulation parameters are described in Table 18

Table 18: Euler Multiphase Simulation parameters

<u>Version</u>	Fire 2014.2			
<u>Run Mode:</u>	Run Mode:	Crank-Angle		
	Delta Alpha	crank-angle	crank-angle	
		upto	0.0001	0.0001
		upto	0.5	0.001
		upto	5	0.01
		upto	10	0.02
		upto	15	0.05
		upto	340	0.2
		upto	358	0.05
		upto	360	0.01
		upto	365	0.05
upto	720	1		
<u>Module Activation:</u>	Multiphase, User-functions			
Solver Control				
<u>Discretization:</u>	Calculation of Derivatives:	Least Sq. Fit		
	Variable Limits:	yes		
	Cell quality check	no		
	Cell face adjustment - equation:	yes		
	Cell face adjustment - geometry:	no		
	Realizability Constraints:	yes		
	Decoupled Domains:	yes		
Mode:	Simple			
<u>Active equations:</u>	Momentum & Continuity:	yes		
	Volume Fraction:	yes		

	Turbulence:	k-zeta-f
	Energy	yes
		static enthalpy
	Viscous heating	yes
	Pressure work	yes
	Scalar	no
	Compressibility	Incompressible
	Wall Treatment	Hybrid Wall Treatment
	Heat Transfer Wall Model	Standard Wall Function
<u>Underrelaxation Factors</u>	Momentum	0.3
	Pressure	0.15
	Turb. Kin. Energy	0.125
	Turb. Diss. Rate	0.125
	Energy	0.6
	Mass source	1
	Viscosity	1
	Scalar	0.8
	Volume Fraction:	0.8
<u>Differencing scheme:</u>	Momentum	Upwind
	Continuity	Central Differencing (1)
<u>Linear Solver:</u>	Momentum	GSTB (0 / 50 / 0.1)
	Continuity	GSTB (0 / 500 / 0.005)
<u>Convergence Criteria</u>	Min. Iterations	15
	Max. Iterations	80
Multiphase		
<u>Mass Interfacial exchange:</u>	Fuel - Fuel Vapor	Linear Cavitation Model
<u>Momentum Interfacial exchange</u>	Fuel - Fuel	Homogeneous
	Fuel - Fuel Vapor	Two-Fluid (Cavitation Drag)
	Air - Fuel	Two-Fluid (Gas-Liquid 3)
	Air - Fuel Vapor	Homogeneous
	Fuel Vapor - Fuel	Two-Fluid (Gas-Liquid 3)
<u>Enthalpy Interfacial Exchange</u>	Fuel - Fuel	Homogeneous
	Fuel Vapor - Fuel Vapor	Homogeneous
	Fuel - Fuel Vapor	Two-Fluid (Ranz-Marshall 2)
	Air - Fuel	Two-Fluid (Ranz-Marshall 2)
	Air - Fuel Vapor	Homogeneous
<u>Turbulence Interfacial Exchange</u>	Fuel - Fuel	Homogeneous
	Fuel Vapor - Fuel Vapor	Homogeneous
	Air - Fuel	Homogeneous

9.3 Appendix III - Spray Simulation

The Lagrangian Spray Simulation parameters are described in Table 19

Table 19: Lagrangian Spray Simulation parameters

<u>Version</u>	Fire 2014.2			
<u>Run Mode:</u>	Run Mode:	Timestep		
	Delta t	0.01 ms		
<u>Module Activation:</u>	Species Transport, Spray, Wallfilm			
Solver Control				
<u>Discretization:</u>	Calculation of Derivatives:	Least Sq. Fit		
	Variable Limits:	no		
	Cell quality check	no		
	Cell face adjustment - equation:	no		
	Cell face adjustment - geometry:	no		
	Realizability Constraints:	yes		
	Decoupled Domains:	no		
	Mode:	Simple/Piso		
<u>Active equations:</u>	Momentum & Continuity:	yes		
	Turbulence:	k-zeta-f		
	Energy	yes		
		Total enthalpy		
	Viscous heating	yes		
	Pressure work	yes		
	Scalar	no		
	Compressibility	Compressible		
	Wall Treatment	Hybrid Wall Treatment		
	Heat Transfer Wall Model	Standard Wall Function		
<u>Underrelaxation Factors</u>	Momentum		ms	Momentum
		upto	0.3	0.25
		upto	5	0.4
	Pressure		ms	Pressure
		upto	0.3	0.15
		upto	5	0.2
	Turb. Kin. Energy		ms	TKE
		upto	0.1	0.125
		upto	5	0.15
	Turb. Diss. Rate		ms	Turb. Diss.
		upto	0.1	0.125
		upto	5	0.15
	Energy	0.8		
	Mass source	1		
	Viscosity	1		
	Scalar	0.8		
	Species transport equations:	0.8		
	<u>Differencing scheme:</u>	Momentum	MINMOD Relaxed (1)	
		Continuity	Central Differencing (1)	
	<u>Linear Solver:</u>	Momentum	GSTB (0 / 50 / 0.1)	

	Continuity	AMG (0 / 100 / 0.005)
<u>Convergence Criteria</u>	Min. Iterations	25
	Max. Iterations	150
<u>Spray</u>		
<u>Submodels</u>	Drag Law model	Schiller Neumann
	Turbulent dispersion model	Enable
	Particle interaction model	Disabled
	Evaporation model	Dukowicz
	Breakup model	Tab
<u>Nozzles</u>	Primary Breakup	Blob Injection
	Particle Size	0.06 mm
	Nozzle File	Active
	Parcels per time step	60
	Liquid volume fraction	0.97
<u>Wallfilm</u>		
<u>Solver</u>	Minimum film thickness	1.00E-06
	Solution flags:	Wall shear, TKE, Heat transfer, Temperature, Evaporation, Entrainment, Balancing, Splashing, Momentum Equation
<u>Submodels</u>	Evaporation submodel	combined
	Entrainment submodel	Schadel-Hanratty
	Entrainment droplet size model	Kataoka
	Entrainment droplet per parcel	3
	Splashing submodel	Kuhnke
<u>Expert</u>	Reyks update iterations	13
	Max. number of subcycles	1000
	Film velocity limit	100 m/s
	Evaporation rate limiter	40 kg/(m ² *s]

9.4 Appendix IV - Engine Simulation

The Lagrangian Spray Simulation parameters are described in Table 20.

Table 20: Engine Simulation parameters

<u>Version</u>	Fire 2017.0 (single component), Fire 2017.1 (multi-component)	
<u>Run Mode:</u>	Run Mode:	Crank-Angle
	Delta alpha	
<u>Module Activation:</u>	Species Transport, Combustion, Emission, Spray, Wallfilm	
<u>Solver Control</u>		
<u>Discretization:</u>	Calculation of Derivatives:	Least Sq. Fit
	Variable Limits:	yes

	Cell quality check		°CrA	-
		upto	EVO10	yes
		upto	EVO720	no
	Cell face adjustment - equation:	no		
	Cell face adjustment - geometry:	no		
	Realizability Constraints:		°CrA	-
		upto	EVO10	yes
	upto	SOI	no	
	upto	SOI2	yes	
	upto	EVO720	no	
	Decoupled Domains:	no		
	Mode:	Simple/Piso		
<u>Active equations:</u>	Momentum & Continuity:	yes		
	Turbulence:	k-zeta-f		
	Energy	yes		
		Total enthalpy		
	Viscous heating	yes		
	Pressure work	yes		
	Scalar	no		
	Compressibility	Compressible		
	Wall Treatment	Hybrid Wall Treatment		
	Heat Transfer Wall Model	Standard Wall Function		
<u>Underrelaxation Factors</u>	Momentum		°CrA	Momentum
		upto	EVO2	0.2
		upto	EVO10	0.3
		upto	IVO10	0.6
		upto	EVO720	0.5
	Pressure		°CrA	Pressure
		upto	EVO10	0.1
		upto	IVO	0.2
		upto	IVO10	0.1
		upto	SOI	0.2
		upto	Spark	0.3
		upto	EVO720	0.4
	Turb. Kin. Energy	0.15		
	Turb. Diss. Rate	0.15		
	Energy		°CrA	Energy
		upto	EVO10	0.6
		upto	IVO	0.9
		upto	IVO10	0.6
	Mass source	1		
	Viscosity	1		
Scalar	0.8			
Species transport equations:	0.8			
<u>Differencing scheme:</u>	Momentum	MINMOD Relaxed (1)		
	Continuity	Central Differencing (1)		

<u>Linear Solver:</u>	Momentum	GSTB (3 / 50 / 0.1)
	Continuity	AMG (3 / 100 / 0.005)
<u>Convergence Criteria</u>	Min. Iterations	10
	Max. Iterations	
<u>Combustion</u>		
<u>Combustion Model</u>	Combustion models	ECFM-3Z
	Initial Flame surface density	1000 1/m
	Stretch factor	0.8
	Spark ignition model	Spherical
<u>Emission</u>		
<u>NO models</u>	NO models	Not used
<u>Soot Models</u>	Soot Models	Not used
<u>Spray</u>		
<u>Submodels</u>	Drag Law model	Schiller Neumann
	Turbulent dispersion model	Enable
	Particle interaction model	Disabled
	Evaporation model	Dukowicz / Multi-component
	Breakup model	Tab
<u>Nozzles</u>	Primary Breakup	Blob Injection
	Particle Size	0.06 mm
	Nozzle File	Active
	Parcels per time step	60
	Liquid volume fraction	0.97
<u>Wallfilm</u>		
<u>Solver</u>	Minimum film thickness	1.00E-09
	Solution flags:	Wall shear, TKE, Heat transfer, Temperature, Evaporation, Entrainment, Balancing, Splashing, Momentum Equation
<u>Submodels</u>	Evaporation submodel	combined (single and multi component)
	Entrainment submodel	Schadel-Hanratty
	Entrainment droplet size model	Kataoka
	Entrainment droplet per parcel	3
	Splashing submodel	Kuhnke
<u>Expert</u>	Reyks update iterations	13
	Max. number of subcycles	1000
	Film velocity limit	40 m/s
	Evaporation rate limiter	20 kg/(m ² *s)

10 Bibliography

- [1] J. Dulac, "Global Transport Outlook to 2050," International Energy Agency, 2012.
- [2] K. Straif, A. Cohen and J. Samet, "Air Pollution and Cancer," WHO Press, Lyon, 2013.
- [3] A. Mamakos, "Feasibility of Introducing Particulate Filters on Gasoline Direct Injection Vehicles," Publications Office of the European Union, Luxembourg, 2011. DOI: 10.2788/23375.
- [4] The European Commission, "Commission Regulation (EU) No 459/2012 of 29 May 2012 amending Regulation (EC) No 715/2007 of the European Parliament and of the Council," Official Journal of the European Union, 2012.
- [5] C. Lambert, T. Chanko, D. Dobson, X. Liu and J. Pakko, "Gasoline Particle Filter Development," *Emiss. Control Sci. Technol.*, vol. 3, pp. 105-111, 2017. DOI: 10.1007/s40825-016-0055-x.
- [6] C. Wang, H. Xu, J. M. Herreros, J. Wang and R. Cracknell, "Impact of fuel and injection system on particle emissions from a GDI engine," *Applied Energy*, vol. 132, pp. 178-191, 2014. DOI: 10.1016/j.apenergy.2014.06.012.
- [7] W. F. Piock, B. Befrui, A. Berndorfer and G. Hoffmann, "Fuel Pressure and Charge Motion Effects on GDI Engine Particulate Emissions," *SAE Int. J. Engines*, vol. 8, no. 2, pp. 464-473, 2015. DOI: 10.4271/2015-01-0746.
- [8] T. Pauer, H. Yilmaz and J. Zumbärgel, "The New Generation Bosch Gasoline Direct Injection Systems," in *38th international vienna motor symposium*, Vienna, 2017. ISBN: 9783183802128.
- [9] R. Wurms, R. Budack and M. Grigo, "The new Audi 2.0l Engine with innovative Rightsizing - a further Milestone in the TFSI Technology," in *36th international vienna motor symposium*, Vienna, 2015. ISBN: 9783183738120.
- [10] D. OudeNijeweme, P. Freeland, M. Behringer and P. Aleiferis, "Developing Low Gasoline Particulate Emission Engines Through Improved Fuel Delivery," SAE Technical Paper , 2014. DOI: 10.4271/2014-01-2843.
- [11] J. Kazour, B. Befrui, H. Husted, M. Raney and D. Varble, *Innovative Sprays and Particulate Reduction with GDI Injectors*, SAE Technical Paper, 2014. DOI: 10.4271/2014-01-1441.

- [12] G. Lepperhoff and M. Houben, "Mechanisms of Deposit Formation in Internal Combustion Engines and Heat Exchangers," in *SAE International Congress and Exposition*, Detroit, Michigan, 1993. DOI: 10.4271/931032.
- [13] J. Schommers, *Ursachen der Ablagerungsbildung auf den Einlaßventilen von Verbrennungsmotoren*, Aachen: RWTH Publications, 1986. RWTH-CONV-132046.
- [14] O. Weber, *Ursachen der Ablagerungsbildung in Abgaswärmeübertragern von Verbrennungsmotoren*, Aachen: RWTH Publications, 1990. RWTH-CONV-135129.
- [15] G. Hörnig and P. Völk, Verschmutzung von AGR Kühlern I, Frankfurt am Main: FVV Nr. 929, 2011.
- [16] K. Noma, T. Noda, T. Ashida, R. Kamioka, K. Hosono, T. Nishida, A. Kameoka, K. Koseki, M. Watanabe, K. Takahashi, S. Koide, T. Suzuki, H. Fukui, M. Hirose, S. Ohta and Y. Notsuki, "A Study of Injector Deposits, Combustion Chamber Deposits (CCD) and Intake Valve Deposits (IVD) in Direct Injection Spark Ignition (DISI) Engines," SAE Technical Paper, 2002. DOI: 10.4271/2003-01-3162.
- [17] J. Tang, *Belagbildung in Einspritzdüsen direkteinspritzender Dieselmotoren*, Aachen: RWTH Publications, 2010. RWTH-CONV-125298.
- [18] Y. Bravo, C. Larrosa, C. Arnal and V. Gargiulo, "Untersuchung der Ablagerungsbildung bei AGR-Kühlern," *MTZ*, pp. 36-41, 05 2015.
- [19] A. Joedicke, J. Krueger-Venus, P. Bohr, R. Cracknell and D. Doyle, "Understanding the Effect of DISI Injector Deposits on Vehicle Performance," SAE Technical Paper, 2012. DOI: 10.4271/2012-01-0391.
- [20] A. G. Amelin, "Theory of Fog Condensation. 2nd Edition augmented and revised, edited by Derygagin, B.V.," 1967.
- [21] D. E. Rosner and K. Seshadri, "Experimental and theoretical studies of the laws governing condensate deposition from combustion gases," in *18th symposium on combustion*, Waterloo, Canada, 1990.
- [22] S. Reichel, *Beeinflussung der Partikeln im Dieselabgas bei Abkühlung und Vermischung mit Umgebungsluft*, Aachen: RWTH Publications, 1983. RWTH-CONV-130455.

- [23] V. Rüdinger, "Ein Modell der Ablagerungsbildung am Dieselmotorkolben," *Erdöl und Kohle*, vol. 27, pp. 353-358, 1974.
- [24] P. S. Meyers, O. A. Uyehara and R. DeYoung, "Fuel Composition and Vaporization Effects on Combustion Chamber Deposits," U.S. Dept. of Energy, 1981.
- [25] J. Davis, "A New Theory of Aerosol Deposition From Turbulent Fluids," *Chemical Engineering Science*, vol. 38, no. 1, pp. 135-139, 1983. DOI: 10.1016/0009-2509(83)80143-2.
- [26] G. Lepperhoff, "Deposit Formation on Inlet Valves: The Influence of Mixture Formation as well as the Interaction between Oil, Fuel and Exhaust Gas," in *10th European Automotive Symposium*, Lyon, 1990.
- [27] J. Fabri, "Ventilverkokung, Teil 2, Ursachen der Koksbildung an Einlassventilen von Verbrennungsmotoren," FVV Nr. 365, 1987.
- [28] M. Kinoshita, A. Saito, S. Matsushita and H. Shibata, *A Method for Suppressing Formation of Deposits on Fuel Injector for Direct Injection Gasoline Engine*, SAE Technical paper, 1999. DOI: 10.4271/1999-01-3656.
- [29] S.-w. S. Cheng, "The Impacts of Engine Operating Conditions and Fuel Compositions on the Formation of Combustion Chamber Deposits," SAE International, 2000. DOI: 10.4271/2000-01-2025.
- [30] D. R. Tree and J. E. Dec, "Extinction Measurements of In-Cylinder Soot Deposition in a Heavy-Duty DI Diesel Engine," SAE Technical Paper, 2001. DOI: 10.4271/2001-01-1296.
- [31] Z. Ye, Q. Meng, H. P. Mohamadian, J. T. Wang, L. Chen and L. Zhu, "Investigation of Deposit Formation Mechanisms for Engine In-cylinder Combustion and Exhaust Systems Using Quantitative Analysis and Sustainability Study," *International Journal Thermophys*, vol. 28, pp. 1056-1066, 2007. DOI: 10.1007/s10765-007-0228-5.
- [32] H. Sandquist, I. Denbratt, F. Owrang and J. Olsson, "Influence of Fuel Parameters on Deposit Formation and Emissions in a Direct Injection Stratified Charge SI Engine," SAE Technical Paper, 2001. DOI: 10.4271/2001-01-2028.
- [33] K. Noma, T. Noda, H. Isomura, T. Ashida, R. Kamioka, T. Isoda, T. Nishida, H. Goto and A. Kameoka, "A Study of Injector Deposits, Combustion Chamber Deposits (CCD) and Intake Valve Deposits (IVD) in Direct Injection Spark Ignition

- (DISI) Engines II," in *Powertrain & Fluid Systems Conference & Exhibition*, Pittsburgh, Pennsylvania USA, 2003.
- [34] Y. Ra, R. D. Reitz, M. W. Jarrett and T. P. Shyu, "Effects of Piston Crevice Flows and Lubricant Oil Vaporization on Diesel Engine Deposits," SAE Technical Paper, 2006. DOI: 10.4271/2006-01-1149.
- [35] F. M. Isa and M. Z. Haji-Sulaiman, "An investigation of the relationship between used engine oil properties and simulated intake valve deposits," *Proceedings of the Institution of Mechanical Engineers*, vol. 211, no. D, pp. 325-336, 1 May 1997. DOI: 10.1243/0954407971526470.
- [36] J. Rossetti, O. Buhaug and A. Longva, "A Comparative Study of the Use of Fuel Additives for the Reduction of: Environmentally Harmful Emissions, Combustion Chamber Deposits and Specific fuel and oil consumption," in *International Council of combustion engines*, Hamburg, 2001.
- [37] F. Zhao, M.-C. Lai and D. L. Harrington, "Automotive spark-ignited direct-injection gasoline engines," *Progress in Energy and Combustion Science*, vol. 25, no. 5, pp. 437-562, October 1999. DOI: 10.1016/S0360-1285(99)00004-0.
- [38] B. P. S. V., S. J.K., G.-F. J. M. and M. C. J., *Engine test for accelerated fuel deposit formation on injectors used in gasoline direct injection engines*, SAE Technical Paper, 2009. DOI: 10.4271/2009-01-1495.
- [39] W. Imoehl, L. Gestri, M. Maragliulo, L. Del-Frate, M. Klepatsch and R. Wildeson, "A DOE Approach to Engine Deposit Testing used to Optimize the Design of a Gasoline Direct Injector Seat and Orifice," *SAE Int. J. Fuels Lubr.*, pp. 1078-1095, 2012. DOI: 10.4271/2012-01-1642.
- [40] A. A. Aradi, W. J. Colucci, H. M. S. Jr. and M. J. Openshaw, "A Study of Fuel Additives for Direct Injection Gasoline (DIG) Injector Deposit Control," SAE Technical Paper, 2000. DOI: 10.4271/2000-01-2020.
- [41] A. Aradi, B. Imoehl, N. Avery and P. Wells, *The Effect of Fuel Composition and Engine Operating Parameters on Injector Deposits in a High-Pressure Direct Injection Gasoline (DIG) Research Engine*, SAE Technical Paper, 1999. DOI: 10.4271/1999-01-3690.
- [42] B. Argueyrolles, S. Dehoux, P. Gastaldi, L. Grosjean, F. Levy, A. Michel and D. Passerel, *Influence of injector nozzle design and cavitation on coking phenomenon*, SAE Technical Paper, 2007. DOI: 10.4271/2007-01-1896.

- [43] P. Bacho, J. Sofianek, J. Galante-Fox and C. McMahon, *Engine Test for Accelerated Fuel Deposit Formation on Injectors Used in Gasoline Direct Injection Engines*, Sae Technical Paper, 2009. DOI: 10.4271/2009-01-1495.
- [44] T. Ashida, Y. Takei and H. Hosi, "Effects of Fuel Properties on SIDI Fuel Injector Deposit," SAE Technical Paper, 2001. DOI: 10.4271/2001-01-3694.
- [45] A. A. Aradi, J. Evans, K. Miller and A. Hotchkiss, "Direct Injection Gasoline (DIG) Injector Deposit Control with Additives," SAE Technical Paper, 2003. DOI: 10.4271/2003-01-2024.
- [46] R. J. DuMont, J. A. Evans, D. P. Feist, W. M. Studzinski and T. J. Cushing, *Test and Control of Fuel Injector Deposits in Direct Injected Spark Ignition Vehicles*, SAE Technical Paper, 2009. DOI: 10.4271/2009-01-2641.
- [47] S. S. Smith and W. Imoehl, *Measurement and Control of Fuel Injector Deposits in Direct Injection Gasoline Vehicles*, SAE Technical Paper, 2013. DOI: 10.4271/2013-01-2616.
- [48] K. Dearn, J. Xu, H. Ding, H. Xu, A. Weall, P. Kirkby, B. Cooper, I. Edington and J. Krueger-Venus, "An Investigation into the Characteristics of DISI Injector Deposits Using Advanced Analytical Methods," *SAE International Journal Fuels & Lubrication*, vol. 7, no. 3, pp. 771-782, 2014. DOI: 10.4271/2014-01-2722.
- [49] H. Song, J. Xiao, Y. Chen and Z. Huang, "The effects of deposits on spray behaviors of a gasoline direct injector," *Fuel*, vol. 180, pp. 506-518, 2016. DOI: 10.1016/j.fuel.2016.04.067.
- [50] R. Lindgren, M. Skogsberg, H. Sandquist and I. Denbratt, "The Influence of Injector Deposits on Mixture Formation in a DISC SI Engine," SAE Technical Paper, 2003. DOI: 10.4271/2003-01-1771.
- [51] B. Wang, T. Badawy, Y. Jiang, H. Xu, A. Ghafourian and X. Zhang, "Investigation of deposit effect on multi-hole injector spray characteristics and air/fuel mixing process," *Fuel*, vol. 191, pp. 10-24, 2017. DOI: 10.1016/j.fuel.2016.11.055.
- [52] A. Berndorfer, S. Breuer, W. Piock and P. V. Bacho, "Diffusion Combustion Phenomena in GDi Engines caused by Injection Process," SAE Technical Paper, 2013. DOI: 10.4271/2013-01-0261.
- [53] W. Brack, M. Banholzer, F. Schwarzmüller and E. Brußies, "Potential of 3D-CFD for the Analysis of Particulate Emissions using the Example of Optimized Injector

- Tip Flows," in *AVL Advanced Simulation Technologies Conference Germany*, 2016.
- [54] G. Fraidl, P. Kapus and M. Neubauer, "Gasoline Engine 2020: 200 kW/l and 200 g/kWh?," in *SIA Powertrain*, Versailles, 2015.
- [55] A. Panesar, A. Martens, L. Jansen, S. Lai, D. Ray and M. Twilley, "Development of a New Peugeot XUD9 10 hour Cyclic Test to Evaluate the Nozzle Coking Propensity of Diesel Fuels," SAE Technical Paper, 2000. DOI: 10.4271/2000-01-1921.
- [56] R. Quigley, R. Barbour, A. Panesar and D. V. Arters, "A Review of Fuel and Additive Performance in the New CEC F-98-09 DW10 Injector Fouling Test.," in *International Colloquium "Fuels 2009"*, Esslingen, 2009.
- [57] H. Xu, C. W. X. Ma, A. K. Sarangi, A. W. and J. Krueger-Venus, "Fuel injector deposits in direct-injection spark-ignition engines," *Progress in Energy and Combustion Science*, vol. 50, pp. 63-80, 2015. DOI: 10.1016/j.pecs.2015.02.002.
- [58] AVL List GmbH, *FIRE v2014.2 - Wallfilm Module Manual*, Graz, 2016.
- [59] D. Kuhnke, "Spray Wall Interaction Modeling by dimensionless Data Analysis," PhD Thesis, Darmstadt, 2004.
- [60] K. Sill, "Wärme- und Stoffübergang in turbulenten Strömungsgrenz-schichten längs verdunstender welliger Wasserfilme," PhD-Thesis, Karlsruhe, 1982.
- [61] J. Himmelsbach, "Zweiphasenströmung mit schubspannungsgetriebenen, welligen Flüssigkeitsfilmen in turbulenter Heißluftströmung – Meßtechnische Erfassung und numerische Beschreibung," PhD-Thesis, Karlsruhe, 1992.
- [62] C. Jayatilleke, "The Influence of Prandtl Number and Surface Roughness on the Resistance of the Laminar Sub-Layer to Momentum and Heat Transfer," *Progress in Heat and Mass Transfer*, no. 1, 1969.
- [63] K. Matusik, D. Duke, A. Swantek, C. Powell and A. Kastengren, "High Resolution X-Ray Tomography of Injection Nozzles," *ILASS Americas 28th Annual Conference on Liquid Atomization and Spray Systems*, 2016.
- [64] E. T. Baldwin, R. O. Grover Jr., S. E. Parrish, D. J. Duke, K. E. Matusik and C. F. Powell, "String flash-boiling in gasoline direct injection simulations with transient needle motion," *International Journal of Multiphase Flow*, vol. 87, pp. 90-101, Dezember 2016. DOI: 10.1016/j.ijmultiphaseflow.2016.09.004.

- [65] AVL List GmbH, *FIRE v2014.2 - Eulerian Multiphase Manual*, Graz, 2016.
- [66] L. Araneo and R. Donde, "Flash boiling in a multihole G-DI injector – Effects of the fuel distillation curve," *Fuel*, vol. 191, pp. 500-510, 2017. DOI: 10.1016/j.fuel.2016.11.104.
- [67] L. Itani, G. B. A. D. Lella and C. Schulz, "Two-tracer LIF imaging of preferential evaporation of multi-component gasoline fuel sprays under engine conditions," in *Proceedings of the Combustion Institute*, 2015. DOI: 10.1016/j.proci.2014.06.108.
- [68] N. Giovannoni, S. Breda, S. Paltrinieri, A. D'Adamo, S. Fontanesi and F. Pulvirenti, "CFD Analysis of the Effects of Fuel Composition and Injection Strategy on Mixture Preparation and Fuel Deposit Formation in a GDI Engine," SAE Technical Paper, 2015. DOI: 10.4271/2015-24-2408.
- [69] K. Saha, S. Som, M. Battistoni, Y. Li, E. Pomraning and P. K. Senecal, "Numerical Investigation of Two-Phase Flow Evolution of In- and Near-Nozzle Regions of a Gasoline Direct Injection Engine During Needle Transients," *SAE Int. J. Engines*, vol. 9 (2), pp. 1230-1240, 2016. DOI: 10.4271/2016-01-0870.
- [70] DIN ISO 9276-2, *Representation of results of particle size analysis - Part 2: Calculation of average particle sizes/diameters and moments from particle size distributions*, 2006.
- [71] AVL List GmbH, *FIRE v2014.2 – Spray Module Manual*, Graz, 2016.
- [72] AVL List GmbH, *FIRE v2017.0 - Combustion Module*, Graz, 2017.